# Response of Reinforced Concrete Reservoir Walls Subjected to Blast Loading

by

Jin FAN

Thesis submitted to the
Faculty of Graduate and Postdoctoral Studies
in partial fulfillment of the requirements for the degree of

**Master of Applied Science**

in Civil Engineering

Under the auspices of the Ottawa-Carleton Institute for Civil Engineering

University of Ottawa
April 2014

# Abstract

Recent events including deliberate terrorist attacks and accidental explosions have highlighted the need for comprehensive research in the area of structural response to blast loading. Research in this area has recently received significant attention by the civil engineering community. Reinforced Concrete (RC) water reservoir tanks are an integral part of the critical infrastructure network of urban centers and are vulnerable to blast loading. However, there is a lack of research and knowledge on the performance of RC reservoir walls under blast loading. The objective of this research study is to experimentally investigate the performance of reinforced concrete reservoir walls subjected to blast loading and to analyze the structural response. This study provides experimental test data on the performance of reinforced concrete reservoir walls under blast loading and complementary analytical predictions using the Singe-Degree-Of-Freedom (SDOF) analysis method.

The reservoir walls in this study were designed according to the water volume capacity using the Portland Cement Association (PCA 1993) methodology. The design was validated using software SAP 2000. The experimental program involved the construction and simulated blast testing of two RC reservoir wall specimens with different support conditions: (1) two opposite lateral edges fixed, bottom edge pinned and top edge free; and (2) two opposite lateral edges fixed, and bottom and top edges free. The first boundary condition was intended to promote two-way bending action, while the second was dominated by one-way bending. The two specimens were each subjected to a total of six consecutive incrementally increasing blast tests. The experimental program was conducted in the shock tube testing facility that is housed in the University of Ottawa. Wall displacements, reinforcement strains, and reflected pressures and impulses were measured during testing.

Analytical calculations were conducted using the equivalent SDOF method to simulate the dynamic response of the RC reservoir wall specimens under different blast loadings. Published tables, charts and coefficients contained in Biggs (1964) and UFC 3-340-02 (2008) were adopted in the equivalent SDOF calculations. The analytical results were compared against the

experimental data. The SDOF method predicted smaller displacements than those recorded during testing. The approximate nature of the parameters and tables used in the equivalent SDOF calculations contributed to the discrepancy between the analytical and experimental results. Furthermore, assumptions regarding the support conditions and neglecting residual damage from previous blast tests contributed to the underestimation of the displacements.

# Acknowledgements

I would like to thank my thesis supervisors, Dr. Dan Palermo and Dr. Ioan Nistor, for their continued guidance and encouragement through this research study.

I would like to thank my fellow graduate students, Mr. Eric Jacques, Mr. Alan Lloyd and Mr. Leonardo Cortes, for their assistances in the laboratory, providing valuable advice and sharing many intellectual discussions in the entire course of the research study.

My thanks also go to Mr. Muslim Majeed at University of Ottawa and Mr. Stanley Conley at Carleton University for their assistances in the laboratory work.

Finally, I would like to thank my wife for her support through many years of the study.

# Table of Contents

# List of Figures

# List of Tables

# Notations

## Acronym Definition

| | |
|---|---|
| ACI | American Concrete Institute |
| DIF | Dynamic Increase Factor |
| LVDT | Linear variable displacement transducer |
| PCA | Portland Cement Association |
| PI | Pressure-impulse |
| RC | Reinforced concrete |
| UFC | Unified Facilities Criteria |
| SDOF | Single degree of freedom |

## Symbol Definition

| | |
|---|---|
| $A$ | Area |
| $A_l$ | Load area |
| $A_s$ | Area of reinforcing steel |
| $C$ | Shrinkage coefficient of concrete |
| $D$ | Diameter of inside of tank |
| $d$ | Effective depth |
| $d_b$ | Diameter of bend of steel bar |
| $E_c$ | Modulus of elasticity of concrete |
| $E_s$ | Modulus of elasticity of steel |
| $f_c$ | Tensile stress of concrete |
| $f_c'$ | Specified compressive stress of concrete |
| $f_{dc}'$ | Dynamic compressive stress of concrete |
| $f_{ds}$ | Dynamic steel stress |
| $f_{dy}$ | Dynamic steel yield stress |
| $f_s$ | Allowable steel stress |

| | |
|---|---|
| $f_u$ | Ultimate steel stress |
| $f_y$ | Static steel yield stress |
| $H$ | Tank wall height |
| $I$ | Impulse; Moment of inertia |
| $I^-$ | Impulse during the negative pressure phase |
| $I_a$ | Moment of inertia |
| $I_r$ | Reflected impulse |
| $K$ | Elastic spring constant |
| $K_E$ | Equivalent elastic unit stiffness of system |
| $K_L$ | Load transformation factor |
| $K_{LM}$ | Load-mass transformation factor |
| $K_M$ | Mass transformation factor |
| $L$ | Length |
| $L_d$ | Driver length |
| $M$ | Moment |
| $M_t$ | Mass of reinforced wall/slab |
| $m$ | Mass |
| $m^0_{P_{sa}}$ | Bending strength unit wall/slab width |
| $\bar{m}$ | Distribute mass |
| $n$ | Ratio of moduli of elasticity |
| $P$ | Pressure |
| $P_d$ | Driver pressure |
| $P_o$ | Ambient pressure |
| $P_r$ | Reflected pressure |
| $P_{so}$ | Peak incident overpressure of the shock front |
| $P_{so}^-$ | Peak incident underpressure of the shock front |
| $t$ | Time; Wall/slab thickness |
| $t_A$ | The arrival time of blast wave |
| $t_d$ | Positive phase duration |
| $t_d^-$ | Negative phase duration |

| | |
|---|---|
| $t_{max}$ | Time at maximum displacement |
| $T_{max}$ | Maximum ring tensile stress of steel |
| $T_n$ | Natural period |
| $u, u(t)$ | Displacement |
| $\dot{u}, \dot{u}(t)$ | Velocity |
| $\ddot{u}, \ddot{u}(t)$ | Acceleration |
| $u_{max}$ | Maximum displacement |
| $u_{res}$ | Residual displacement |
| $u_0, u(0)$ | Initial displacement |
| $u_{t_d}$ | Displacement at time $t_d$ |
| $V$ | Tank volume; Shear at base of wall |
| $v_0, v(0)$ | Initial velocity |
| $v_{t_d}$ | Velocity at time $t_d$ |
| $W$ | Equivalent explosive mass of TNT |
| $w$ | Unit weight of water |
| $R$ | Distance from the centre of the explosive charge; Resistance |
| $R_E$ | Elastic resistance |
| $R_m$ | Maximum resistance |
| $R(u)$ | Nonlinear resistance function |
| $Z$ | Scaled distance |
| $\gamma$ | Unit weight |
| $\varepsilon$ | Strain |
| $\varepsilon_{max}$ | Maximum strain |
| $\dot{\varepsilon}$ | Strain rate |
| $\dot{\varepsilon}_s$ | Static strain rate |
| $\theta$ | Support rotation |
| $\theta_{max}, \theta_m$ | Maximum support rotation |
| $\rho_s$ | Reinforcing steel ratio of wall/slab |
| $\omega$ | Natural frequency |
| $\emptyset(x)$ | Shape function |

| | |
|---|---|
| $\mu$ | Ductility factor |

# Chapter 1 Introduction

## 1.1 General

Terrorist activity carried out with bomb attacks has become more frequent on a global scale. These activities have demonstrated that commercial centres, governmental buildings, critical infrastructure, industrial facilities, and residential buildings are vulnerable to such terrorist attacks. Water reservoirs are part of the critical infrastructure and can be attractive targets for terrorist activity. In many structures, Reinforced Concrete (RC) walls are common structural members. For reservoirs, an RC wall can be used as a structural element to protect reservoirs against potential blast loading. Reinforced concrete reservoirs have been used extensively in municipal and industrial facilities for several decades. Figure 1.1 is a circular concrete reservoir for storage of clean water.

Figure 1.1: A circular concrete reservoir
(AMCO Water 2014)

Generally, when a blast event occurs, the exterior walls of a structure are subjected to direct, reflected pressures from the blast. The high explosives result in high overpressures of a very short duration. As a consequence, such explosions lead to highly dynamic loadings on reinforced concrete walls and structures. The overpressures, as a result of the shock wave, will propagate through the atmosphere and arrive at the target structure. The fragments generated by the

explosion and the shock loads produced by the energy of the detonation can cause damage to walls and structures. The damage level experienced by walls subjected to blast loading can be severe. Therefore, it is of interest to understand the behaviour of the RC walls under blast loading.

The two key blast parameters that most directly impact the blast environment are the explosive weight or charge weight $W$ and the stand-off distance $R$ between the blast source and the target structure. In a design or analysis procedure, the characteristics of the dynamic loading, in terms of pressure and impulse, are determined by these two parameters. Given that full-scale testing of realistic explosive effects is economically not viable and time consuming, small-scale experimental testing is accepted as a well-proven alternative to assess blast loading. This is possible since many blast parameters can be scaled for charge masses ranging from milligrams to tons. The most widely used method of blast scaling is on the basis of the Crank-Hopkinson's "cube-root" law for scaled distance, time and impulse (Loiseau et al. 2008). All blast parameters such as peak pressure, time and impulse are primarily dependent on the amount of energy released by a detonation of charge in the form of a blast wave and the distance from the explosion. The Hopkinson-Cranz law provides a universal normalized description of the blast effects in terms of scaled distance, where the scaled distance is based on a constant of proportionality between stand-off distances and charge weights that result in the same incident pressures. The Hopkinson-Cranz law permits experimental testing over very wide ranges of explosive energies and distances, including very strong shock conditions. A scaled distance is commonly used when considering different blast wave parameters in free air as stated by $Z = \frac{R}{W^{1/3}}$, where $R$ is the distance from the centre of the explosive charge to a target structure and $W$ is the mass of a standard explosive in TNT (Trinitrotoluene) equivalents. The peak incident pressure, $P_{so}$, is given as a function of the scaled distance $Z$. With the two parameters defined, the response of the structure can be analyzed. Structural analysis of the effects of an explosion on RC walls consists of two phases: (1) computation of the blast loading; and (2) evaluation of the wall resistance.

Structural displacements are one of the measures of direct damage to structures attributable to air blast effects. The term ductility refers to the ability of a material or structure to absorb energy

inelastically without degradation in the load carrying capacity. The ductility capacity plays an important role, in addition to strength and energy dissipation capacities, to provide resistance to a structure against failure. Structures/materials which are brittle have poor ductility and fail suddenly. Such structures may fail prior to reaching their flexural yield capacity or shortly thereafter. There are two main aspects to ductility to be considered. When a force is applied to a material, the initial deformation is elastic. Within the elastic range, the material will recover its original form when the load is removed. If the material is stressed by the load beyond the elastic limit, the material passes into the plastic range. In this state, the material does not recover completely after removal of the load; some deformation is permanent, but failure is not imminent. The state of failure can be assumed to occur when the stress causes the structure/material to attain its ultimate displacement capacity. Note, that for a ductile element, the ultimate displacement is typically defined as the displacement corresponding to a drop of approximately 20% of the ultimate strength capacity. One of the challenges in blast-resistant design, therefore, is to determine how much permanent (plastic) deformation is acceptable to ensure a structure is serviceable. Although deformation to the point of collapse is not desirable, some lesser deformation may not seriously interfere with the continued use of the structure (Glasstone and Dolan 1977).

The Single-Degree-Of-Freedom (SDOF) method has been widely used to predict the dynamic flexural response of concrete structures and in the design of protective structures subjected to blast loading. The widely accepted procedure to assess structural damage is through pressure-impulse $(P-I)$ interaction diagrams (Ambrosini *et al.* 2005). Once the maximum value of response parameters (displacement, ductility, etc.) associated with a specific damage level has been determined, the $P-I$ diagram is used to relate the corresponding combination of pressures and impulses imposed on the structural element. A $P-I$ diagram can be obtained from SDOF analysis, advanced numerical simulations (Lan and Crawford 2003), or blast testing.

In the case of reinforced concrete walls, the yield line analysis method is an alternative technique, which provides an upper bound load at failure. Its main benefit is that no matter how complex the wall shape or loading, it is always possible to obtain a collapse load. It is relatively simple to apply using concepts of virtual work. Many of the solutions predicted by this method

have been substantiated experimentally. The yield analysis method is used extensively throughout the blast design and analysis community to ensure sufficient strength of reinforced concrete structural elements to resist blast overpressures (Wager 1994).

Design of reservoir walls is different from regular reinforced concrete structures. One of the differences is that the concrete should not crack and, hence, tensile stresses in concrete should be within permissible limits. In this research study, reinforced concrete reservoir walls were designed based on the Portland Cement Association (PCA) design procedures. Increasing levels of blast loading were experimentally simulated using the shock tube in the University of Ottawa blast research facility. By increasing the blast loading in terms of combinations of pressure and impulse, the corresponding increase in damage experienced by the RC walls were investigated as a function of the different levels of blast loading.

## 1.2 Research Significance

Reservoirs are considered to be part of the stock of critical infrastructure that societies require for day-to-day activities. Since they are lifeline structures and play an important role in the economy of the country, their vulnerability to extreme loading, such as blast, should be considered in the design process. Reservoirs are easily accessible to the public, making them more vulnerable to terrorist attacks. If reservoirs are targeted, the resulting damage can be critical, can render the stored water unusable or can destroy the water supply infrastructure. Furthermore, the damage resulting from terrorist attacks on reservoirs would cause ripple effects leading to the disruption of the functions of society and a loss in the economy.

In many structures, Reinforced Concrete (RC) walls are common structural members and if used as an exterior element, would be subjected to direct and reflected pressures from any potential blast loads. With an increase in terrorist incidents over the past decade, blast research on RC walls/slabs/panels has become increasingly important and has received significant attention by the civil engineering community. However, very limited information is available on the response of RC reservoir walls under blast loading. A thorough review of the literature on blast research on walls/slabs/panels reveals that research work focused on the response of reinforced concrete

reservoir walls subjected to blast loading is non-existent. To the best of the author's knowledge, this research work is the only blast test conducted on reinforced concrete reservoir walls.

As a result of a lack of knowledge, this study is focused on experimental and analytical research on the performance of RC reservoir walls subjected to blast loading. The study includes design of RC reservoir walls; laboratory blast testing; and analysis of the walls using the SDOF method. Relative to structural walls found in other structures, reservoir walls have different boundary conditions and they are designed to be more resilient to cracking under service loads. Furthermore, given the nature of the loading, including the effect of retained water, reinforcement used in reservoir walls must resist bending and ring tension forces.

## 1.3 Objectives

The main objective of the research presented in this thesis is to experimentally and theoretically study the blast performance of RC reservoir walls. In detail, the objectives of the study are:

- To design reinforced concrete reservoir walls using the Portland Cement Association (PCA) method "Circular Concrete Tanks Without Prestressing";
- To investigate the response of the RC reservoir walls subjected to increasing levels of blast loads generated by the shock tube in the blast research facility at the University of Ottawa;
- To analyze the structural response of the RC walls subjected to blast loading to assess the level of structural damage;
- To generate experimental data which is used to compare against the analytical model; and
- To provide information for future research in this field of study.

## 1.4 Scope

This research study focuses on blast loading, and displacement capacity and damage modes of two RC reservoir walls. One wall is controlled by two-way bending action while a second wall behaves as a one-way reinforced concrete element. The boundary conditions for the two-way wall consist of two fixed opposite lateral edges, a hinged bottom edge and a free edge at the top.

The boundary conditions for the one-way wall include two fixed opposite lateral edges, and free bottom and top edges.

The following forms a summary of the scope of this study:

- Review of previous research in the area of response of reinforced concrete walls/slabs subjected to blast loading;
- Design, construction and instrumentation of two RC reservoir walls, one with two-way boundary conditions and the other with one-way boundary conditions;
- Experimental testing of two RC walls under blast loading generated by a shock tube;
- Evaluation of the test data and reporting of test results; and
- SDOF analyses of the RC walls based on the laboratory recorded blast pressures.

## 1.5 Thesis Structure

This thesis is organized as follows. Chapter 2 provides a thorough literature review of previous blast research on reinforced concrete walls/slabs/panels. Chapter 3 provides a theoretical background of blast loading effects and structural response, as well as dynamic response analysis using the SDOF method, and yield line analysis for RC reservoir walls. Chapter 4 describes the design of the RC reservoir walls. Chapter 5 details the experimental program including the construction of the wall specimens, the material properties of the specimens, and the instrumentation used during the experimental tests. Chapter 6 reports the experimental test results. Chapter 7 compares the experimental results with the SDOF analytical results and includes discussions. Finally, Chapter 8 provides conclusions and recommendations for future research.

# Chapter 2 Literature Review

## 2.1 Previous Research on RC Walls or Slabs Subjected to Blast Loading

The focus of this chapter is on previous research on reinforced concrete walls or slabs subjected to blast loading.

***E. Jacques, 2011***

The research work investigated the effect of retrofit techniques to improve the blast resistance of reinforced concrete (RC) walls and slabs. The author used externally bonded Carbon Fibre Reinforced Polymer (CFRP) sheets to investigate the improvement of the flexural capacity of one-way and two-way reinforced concrete panels subjected to blast loading experimentally and analytically. The main purposes of the research were to generate experimental data on the responses of control and retrofitted RC panels subjected to shock waves; to develop an analytical model to predict RC member response to blast loading; and to propose design recommendations for CFRP retrofits of RC members such as walls, beams and slabs.

The experimental program comprised the construction and blast testing of thirteen concrete panels. The thirteen specimens included seven one-way panels and six two-way plates. The specimens were divided into five companion sets labelled as CS1 to CS5. Generally, each companion set consisted of at least one control specimen and one CFRP retrofitted specimen. These specimens were exposed to a total of sixty simulated blast loads generated by the shock tube that is housed at the University of Ottawa shock tube testing facility. The structural performance of the control and CFRP retrofitted specimens subjected to blast loading was analyzed quantitatively in terms of recorded load-deformation response and observed behaviour at all stages of testing.

To assess the experimental results of various CFRP retrofit strategies, the responses of retrofitted and control specimens subjected to blast loading were compared based on displacement-time history behaviour. For the same companion set, the specimens were subjected to the same pressure-impulse (P-I) combinations.

To generate the analytical results of responses of RC panels, the author developed software to calculate the Single-Degree-Of-Freedom (SDOF) displacement-time history responses and generate P-I diagrams of blast loaded RC panels. After comparing the experimental results with the analytical results, the author concluded that the predicted behaviour of retrofitted and control RC wall and slab specimens subjected to blast loading generated by shock tube were in general agreement with the experimental results.

***Y.S. Tai, T.L. Chu, H.T. Hu, and J.Y. Wu, 2011***

This research work focused on the analysis of propagation law of the blast wave effects. The authors performed theoretical analysis on the dynamic response and damage pattern of an RC plate subjected to different blast loads using the nonlinear finite element method (Software LS-DYNA). The experimental program consisted of a free-field explosion on an RC slab, which was orthogonally reinforced, measuring 3.6 m in length, 3.0 m in width and 0.15 m in thickness.

The accuracy of the analytical results were validated by comparing to the experimental results, namely, the pressure-time history response from the field test was compared with the results from the finite element model software. The authors utilized pressure-time history response to investigate the destructive effects on the RC slab subjected to the different amounts of explosives, different reinforcement ratios, and distance from the explosives. The analytical results demonstrated that bending damage or shear failure could occur at the center of the slab. The amount of explosive and distance from the explosion to the RC slab were cited to be important parameters.

Damage to the reinforced concrete slab was examined by changing different distances to explosion, namely from a remote explosion to a short-distance explosion. The experimental

results indicated that the distance from the explosion had a significant impact on the RC slab, which was consistent with the blast pressure wave propagation law.

The authors also concluded based on the computed analytical results that for RC slab with low reinforcement ratio, damage was more probable at the centre of the slab. The slab deformation was reduced and damage was concentrated at the supports of the RC slab with the increased reinforcement ratio.

***Y. Shi, Z. X. Li, and H. Hao, 2010***

In this study, the limitations of specific procedures for progressive collapse analysis of building structures subjected to blast loading as a result of the simplifications have been highlighted. The authors proposed a new method for progressive collapse analysis of RC frame structures by including non-zero initial conditions and initial damage to adjacent structural members under blast loading. This proposed method uses pressure-impulse (P-I) diagrams to estimate the damage to structural members affected by the direct blast loading and the equivalent SDOF model to predict the velocity and displacement of structural members at the end of the blast loading phase.

To verify the efficiency and reliability of the proposed method, the authors conducted an analysis of a three-storey, two-span RC frame. The commercial software LS-DYNA was used to perform the numerical calculations. The commonly used alternative load path method and the direct simulation method were also used to analyze the progressive collapse of this sample structural frame. The authors performed numerical simulations to validate the proposed procedures in deriving the initial condition and initial damage of RC structural members (typical RC columns were adopted). The equivalent SDOF approach was used to derive initial conditions and software LS-DYNA was utilized to analyze the initial damage of the RC columns. The initial velocity and displacement of the columns obtained by equations in the proposed procedures were compared with those values derived from the numerical simulation. These results indicated that utilization of the equivalent SDOF system could provide reliable displacement and velocity estimations of the column at the end of the blast-loading phase.

Three approaches were utilized: numerical model (using software LS-DYNA); alternative load path method based on guidelines contained in GSA and DOD; and the proposed method, to carry out the progressive collapse analysis of the example frame structure. The numerical results of the GSA nonlinear dynamic analysis were compared to the results generated from the proposed method and to the benchmark analysis (results using numerical simulations by software LS-DYNA) to verify the accuracy and reliability of the proposed method. The results demonstrated that damage and collapse of adjacent columns accelerated the collapse of the structural members, leading to total collapse of the sample structural frame. The authors argued that these observations clearly indicated that the GSA nonlinear dynamic analysis procedure overestimated the capacity of the structural frame in resisting progressive collapse as a result of the neglecting of the initial damage and non-zero initiation conditions generated by the blast loads.

It was concluded that the prediction of the structural frame collapse process responding to blast loading from the proposed method was similar to the prediction generated from the numerical simulation by directly applying the blast loads on the structural frame. Compared to the GSA nonlinear dynamic analysis method, the proposed method provided better predictions of the structural progressive collapse with minimal additional effort in determining the non-zero initial conditions and damage in structural members at the end of the blast-loading phase when the progressive collapse initiates. The proposed method incorporating non-zero initial conditions and initial damage to adjacent structural members under blast loading was efficient and reliable in simulating the progressive collapse process of RC frame structures. The authors further concluded that the proposed method would reduce the comprehensive computations substantially comparing to the direct numerical simulation approach. It provided more accurate predictions of the structural progressive collapse process compared to simplified approaches for structural progressive collapse analysis that neglect non-zero initial conditions and initial damage to adjacent structural members under blast loading.

***W. W. El-Dakhakhni et al. 2010***

In this research work, the authors focused on the analysis response of RC panels under blast loading using a simplified SDOF model and a detailed finite-element (FE) analysis approach.

The objectives were to investigate the limitations of SDOF models using advanced FE analysis techniques and to look for improvements in the modeling provisions (adopted SDOF approaches) of two-way RC panels in the UFC 3-340-02 (2008).

An SDOF model based on the guidelines of UFC 3-340-02 (2008) was used to generate pressure-impulse (P-I) diagrams to predict the response of various two-way RC panels with different dimensions, aspect ratios, reinforcement ratios and support conditions (simply supported and clamped) under blast loading. In the study, the authors used the experimental results reported by Razaqpur et al. (2006) to validate the accuracy of FEM techniques. The authors claimed that the FE modeling approach adopted in this study was accurate in analyzing the structure response subjected to blast loading. The P-I diagram predictions for different displacement levels were compared to the results of experimentally validated nonlinear explicit FE analysis. The authors found significant discrepancies between the SDOF models and the FE results in terms of deflection and shear predictions.

The authors argued that the discrepancies between the SDOF and FE results could be due to the oversimplification of SDOF models. For example, deficiencies in SDOF-based resistance functions include strength underestimation resulting from neglecting multiple yield patterns and corner effects, underestimation of strain effects on enhancing steel and concrete material properties, and neglecting higher mode contributions. In addition, SDOF resistance function neglects the simultaneous existence of flexural and tensile membrane resistances and adopts a $2^{\circ}$ panel rotation limit for the flexural strength. The study illustrated possible areas of improvement of current SDOF models with the inclusion of more-refined and more realistic resistance functions, and the adoption of higher levels of material strength enhancement. The authors also concluded that the current simplified SDOF models could generate acceptable results in analyzing RC panels under blast loading within the pressure regime by assuming that flexural failure is the governing failure mode of the panels.

The authors further concluded that the FE analysis has advantages over the SDOF models. However, the FE analysis might not be appealing to designers; the design companies may not have the knowledge and resources to analyze the complex issues as RC structural response

subjected to blast loadings. The SDOF models are typically easier to implement. The results also indicated that future research would be needed to provide more realistic methods to predict the response of two-way RC panels subjected to blast loadings.

***X. Q. Zhou and H. Hao, 2008***

In this study, the authors studied the performance of exterior RC walls under different blast loading due to a terrorist event numerically and experimentally. In the numerical calculations, the authors used empirical charts contained in TM 5-1300 (1990) to estimate coefficients required in the formulations and to generate theoretical results. The pressure-impulse (P-I) diagrams were generated from both numerical and experimental results.

The numerical model was calibrated with experimental blast test results of RC slabs. The calibrated numerical model was then utilized to simulate the response of a typical exterior RC wall under blast loadings arising from terrorist bombings. Two parameters in this studied included charge weights (TNT equivalent) and the stand-off distance. The selected TNT charge weights corresponded to typical terrorist bombs. The response of the RC exterior wall at different stand-off distances were simulated at each given TNT charge weight. The damage level of the exterior RC wall was based on Mazars' damage model (Mazars 1986), which combines tensile and compressive damage. Four concrete damage categories under blast loading were considered in this study: no-damage, slight-damage, moderate-damage and severe-damage. The authors derived critical TNT charge weight-stand-off distance curves for different damage levels.

The authors compared the theoretical results to the experimental results in form of P-I diagrams. The comparison demonstrated that the theoretical results were in satisfactory agreement with the experimental results. The authors, therefore, concluded that the numerical model discussed in this study provided reasonable predictions of exterior RC wall response subjected to blast loading in the event of terrorist bombing. Safe stand-off distance was also suggested in this study.

***J. Magnusson, 2007***

This research work studied the structural behaviour of reinforced concrete beams subjected to air blast loading theoretically and experimentally. It was stated in the study that in the design of buildings to resist the effects of air blast loading or other severe dynamic loads, that it was not economical to consider the structural response in its elastic range only. Structural elements should be permitted to sustain certain plastic deformations, which better utilizes their energies absorbing capacities if exposed to dynamic loads. It is important to design for ductile response to prevent partial or total collapse of a structure due to locally failed elements. To achieve the research objectives, the author focused on load and deflection capacities as well as failure modes of the beams.

For the experimental investigation, a total of 89 simply supported beams with various concrete strength and quantity of reinforcement were tested under static loading and air blasts. The blast tests on beams were performed with a shock tube. The experimental program focused on deflections, failure modes and loads transferred to the supports.

For the theoretical analysis, the SDOF method was employed to evaluate the response of the beams in the series of tests. The theoretical results showed that SDOF model was capable to predict the dynamic structural response of RC beams when exposed to explosive loading. The theoretical results were compared to the experimental results, which demonstrated that the SDOF analysis results were in good agreement with the experimental results regardless of concrete strength and reinforcement in the beams.

It was concluded that, in general, reinforced concrete beams with high strength concrete demonstrated higher resistance in terms of enhanced stiffness and load capacity compared to similar beams of normal strength concrete when subjected to static loading. The deformation capacity and ductility of the concrete beams were found to be independent with concrete strength given that the reinforcement ratio was kept constant. The author further concluded that all reinforced concrete beams under static loading failed in flexure, whereas similar beams could fail in flexural shear in the air blast tests. The blast tests with steel fibre reinforced concrete beams

clearly indicated that the fibre length should be reduced in combination with higher concrete strength, particularly for dynamic events.

***A. G. Razaqpur, A. Tolba and E. Constestabile, 2007***

This study investigated the dynamic response of Glass Fiber Reinforced Polymer (GFRP) retrofitted concrete panels subjected to blast loading experimentally and numerically. One of the objectives of this study was to investigate the relationship between strength and ductility; two important factors in blast resistant design. The study examined the extent of reduction in ductility of RC panels accompanied by an increase of strength as a result of the retrofitting with externally bonded GFRP.

Blast tests were performed on eight reinforced concrete panels, which were divided into two groups of four specimens (as-built control specimens and retrofitted specimens). The retrofitted panels were reinforced with two laminates of GFRP arranged in a crucifix form on each face. The reflected blast pressure and impulse were measured for each blast test and were based on similar charge size and varying stand-off distances. The experimental results provide useful data to develop rational design methods for blast-resistant design of FRP retrofitted reinforced concrete elements. The experimental results can also be used to verify the accuracy of numerical software.

The numerical results in terms of blast pressure and impulse were calculated using the software CONWEP. Comparison between theoretical and experimental results demonstrated that the theoretical results generated from the software were in reasonable agreement with experimental results.

Based on the experimental results, it was concluded that the GFRP retrofitted panels performed significantly better in resisting the blast loads relative to the control panels for a similar charge weight and stand-off distance. The post-blast analysis illustrated that the post-blast static strength of the retrofitted panel was 75 % higher than that of the companion control panel. However, the authors stated that there was no consistent trend to demonstrate that the retrofitted panels had

higher residual strength than the companion control panels. Based on the results of the panels subjected to the higher charge weight, it was difficult to draw definite conclusions about the effectiveness of GFRP bonded laminates in blast mitigation.

***C. M. Morison, 2006***

The objective of this paper was to study the accuracy of SDOF methods for analyzing dynamic response of reinforced concrete flexural members under blast or ground-shock loading. In the study, the SDOF methods were reviewed chronologically starting with the modal SDOF approach and then the equivalent SDOF method. In conducting the critical review, the author focused on the assumptions and formulas in deriving the parameters, the applications, as well as the robustness and weakness of each method.

Particular attention was given to the equivalent SDOF method for analyzing dynamic response of reinforced concrete flexural members subjected to blast loading. First, the author reviewed the theoretical basis for the approach including the basic equations for transformation factors for any deflected shape and deflected mass or load distribution. It was determined that the equivalent lumped system can be analyzed with a SDOF approach by a number of different methods such as: idealized charts in modal SDOF method to quickly calculate the amplitude and time of peak response; dynamic load factor (DLF) to calculate elastic response; solving the equation of motion of the equivalent system by a complete response history generated by using algebra for the chosen resistance function and loading function; and numerically solving the equation of motion of the equivalent system using the step-by-step calculation proposed in EM 1110-345-416 (1957).

Second, the author reviewed factors and coefficients; the two sets of tables of equivalent SDOF data; and parameters for beams, and one-way and two-way slabs in EM 1110-345-416 (1957). The methods by which the data and parameters in the tables have been derived, including sample computations were described. The analyses included beams and one-way slabs, plastic analysis, and elastic analysis of two-way spans. Discrepancies in the calculations for each analysis were listed. It was concluded that the inaccuracy of the values in the table were largely due to the

approximate nature of the derivation of the SDOF method and errors introduced by the authors. The tables from EM 1110-345-416 (1957) have been used extensively in textbooks, manuals and computer programs during 1960s to 1990s without considering the methodology, inaccurate approximations and limitations behind the actual values in the tables.

Third, the author reviewed TM 5-1300 (1969), including charts, tables and formulas for plastic analysis of uniformly loaded one-way spans and various two-way spans. Three areas of concern arose: (i) inaccuracy of some coefficients; (ii) the analysis of panels with one or two free edges was incorrect for some aspect ratios; and (iii) the TM 5-1300 (1969) did not provide formulas for calculating dynamic reactions. For the elastic analysis, the author reviewed charts and tables presented in the manual for conducting numerical elastic analysis for one-way and two-way panels of different support conditions. The areas of inaccuracy of those charts and tables were also discussed. It was stated that the TM 5-1300 (1969) did not contain data for calculating elastic reactions, but it provided one recommendation. Finally, SDOF applications in TM 5-1300 (1990), SDOF coefficients in blast computer program, and SDOF methods in other research were studied. This study concluded that revised SDOF parameters were needed to accurately apply equivalent SDOF methods for two-way spanning members.

To derive new equivalent SDOF parameters, plastic yield line analysis and elastic finite element analysis was conducted for the dynamic response of panels in the plastic phase and elastic phase with different support conditions. The dynamic responses of reinforced concrete panels using parameters in EM 1110-345-416 (1957), TM 5-1300 (1990), and the newly developed data were compared. The author recommended that the tables derived from EM 1110-345-416 (1957) and the calculations in TM 5-1300 (1990) be replaced with the newly developed tables for panels supported on four edges. In summary, it was concluded in this study that, in general, the equivalent SDOF method is an appropriate approximate analysis method. The application to one-way spanning members was satisfactory. However, it was insufficient for two-way spanning members due to some inappropriate assumptions and approximations for the purpose of simplifying the process and minimizing the effort in calculating values. The SDOF coefficients contained in EM 1110-345-416 (1957) and TM 5-1300 (1990) were inaccurate. The revised new

values for equivalent SDOF method based on finite element analysis and yield line calculations were recommended for two-way spanning members.

***K. Xu and Y. Lu, 2006***

This paper studied the response of RC walls subjected to various air blast loadings in the form of damage due to concrete spalling numerically and experimentally. The authors used a three-dimensional numerical model to simulate produce the blast loading effect in three-dimensions and global structural response during the concrete spalling process. In the simulation, dynamic material strengths and realistic explosive loading were incorporated. The enhancement factor for concrete strength was obtained from a separate study based on continuous fracture mechanics and relevant experimental data. Also, the respective limit criterion in the form of critical charge weight – stand-off distance relations were obtained from a parametric calculation using the numerical model. In numerical analysis, predictions of facture locations and spall velocities of the RC walls were computed. The numerical results were presented in three-dimensions with different charge-weight and stand-off distance scenarios for three spall damage categories.

The numerical results were compared with the experimental results. The comparison illustrated reasonably good agreement. Based on the numerical results, the authors further proposed empirical equations, including: spallation criteria for no-damage, and threshold spalling and medium spall categories.

***X. Quan, 2005***

The objective of this paper was to study the response of steel-reinforced concrete walls, used as barriers in areas requiring protection, subjected to the blast loading from terrorist attacks. The study investigated the response of steel RC walls under two scenarios: (1) blast analysis on one steel-reinforced concrete wall from the explosion of a truck bomb; and (2) analysis of two RC walls impacted by a Boeing 747 passenger jet. Three-dimensional numerical simulation models based on finite element analysis and finite difference methods were employed to simulate the response of the RC walls under such extreme loadings.

In the numerical simulations, for the blast analysis, one thick steel-reinforced concrete wall that was studied was rectangular in shape and was restrained from lateral motion at the bottom using a boundary condition. A hypothetical charge weight of 5,000 kg TNT to represent a truck bomb was assumed. A number of stand-off distances were considered: 5 m, 10 m and 20 m from the RC wall. In the three-dimensional model, the propagation, reflection and diffraction of blast wave from truck bomb, as well as the structural deformation of the RC wall were simulated. The damage of the RC wall after the explosive detonation on both front and back surfaces was presented. The author discussed the relationship between damage of the reinforced concrete wall and the stand-off distance of the truck bomb from the wall.

For the impact analysis originating from a Boeing 747 passenger jet airliner as a hypothetical impact threat, the three-dimensional numerical simulation assessed 1 m and 3 m thick steel-reinforced concrete walls. The damage to the front and back surfaces of the steel-reinforced concrete walls after the airplane impact were presented. The results demonstrated that the 1 m thick steel-reinforced concrete wall was not sufficient to sustain the impact from the airplane and, therefore, could not provide the necessary protection to serve as a physical barrier to this type of terrorist attack. The damage experienced by the 3 m thick steel-reinforced concrete was localized and concentrated in the immediate area on the impacted face. The 3 m thick wall was able to remain intact during the airplane impact. It was concluded that, to provide protection with a physical barrier against the impact of this type of airplane, the thickness of the reinforced concrete wall should be increased to 3 m (assuming the same ratio of reinforcement).

***B. Lu, P. Silva, A. Nanni, and J. Baird, 2005***

The objective of this research work was to examine the feasibility of assessing the blast-resistant capacity of RC slabs subjected to blast loading using the Displacement Based Design (DBD) method. The DBD method correlates the structural performance criteria selected from design to a measurable quantity, such as the displacement ductility, to predict blast loads in terms of blast charge weights (equivalent TNT) and stand-off distances. The predicted damage levels ranged from minor damage to completely structural failure of the RC slabs resulting from blast loading effects.

In the experimental investigation, five RC slabs were tested under blast loads in the out-of-plane direction. One specimen was used as the control slab to establish a baseline to compare the performance of the RC slabs. Two specimens were strengthened with Fiber Reinforced Polymer (FRP) and two specimens were strengthened with Steel Fiber Reinforced Polymer (SFRP). The specimens were tested in an experimental mine. The predicted blast charge weights (TNT) and stand-off distances were applied in the field tests. Each test event consisted of a specific combination of charge weight and stand-off distance.

The experimental test results illustrated that the blast charge weight and stand-off distance can be effectively estimated with the DBD method. The displacement ductility levels of the RC slabs observed from the experimental tests agreed well with the predictions from the analytical investigation. In addition, the blast-resistant capacity of the RC slabs increased by retrofitting with FRP. Furthermore, the RC slabs retrofitted on both sides demonstrated greater ability in resisting blast loading relative to the RC slabs retrofitted on one side only. It was therefore concluded that RC slabs should be retrofitted on both sides to improve the blast resistance for slabs.

***Q. M. Li and H. Meng, 2002***

In this study, the authors conducted a theoretical study of the pressure-impulse (P-I) diagram of the damage assessment for structural elements subjected to blast loading. It was stated that to have a valid P-I diagram for a broad scope of loading and structural parameters, extensive experiments would be required to test various combinations of loading and structural parameters. Such an approach would be costly. Therefore, theoretical analysis of the characteristics of P-I diagrams would be meaningful by reducing the number of experimental tests and providing a better understanding on the general features of a P-I diagram.

The objective of the study was to investigate the pulse loading shape effects on the P-I diagram based on the maximum deflection damage criterion. Three pulse loading shapes (rectangular, triangular and exponential), representing a wide variety of blast loads, were considered in the study. The blast loading was idealized as a descending pressure pulse. In the study, the P-I

diagrams were derived using both dimensional analysis and elastic Single-Degree-Of-Freedom (SDOF) model.

The analytical results illustrated that the general P-I diagram was loading shape dependent. Two important characteristics of a P-I diagram were highlighted; namely the existence of horizontal and vertical asymptotes and the variation of P with I for any descending pulse load. Based on this, it was suggested that an iso-damage P-I diagram might be divided into three regimes: (I) impulse-controlled damage, (II) peak load and impulse-controlled damage, and (III) peak load-controlled damage. These three structural response regimes could correspond to three damage regimes on a P-I diagram and would be helpful in understanding the damage identification on a P-I diagram. The results demonstrated that the effect of pulse loading shape on the P-I diagram was considerable, specifically in Regime-II when both peak load and impulse were significant for dynamic structural response. It was observed that the rectangular pulse resulted in the lowest P-I diagram and the exponential pulse caused the highest P-I diagram.

While the theoretical analysis demonstrated pulse loading shape had considerable influence on the dynamic response of structures, the authors discussed that this effect on the P-I diagram could be eliminated by introducing an effective impulse if the response of a structure or a structural member was dominated by elastic deformation and the structural damage level was controlled by a characteristic deflection. In the study, a unique effective pressure-impulse diagram was proposed by introducing effective loading parameters to eliminate the pulse loading shape effect. As a result, a loading shape independent P-I diagram was developed to define structural damage levels. It was concluded, however, that both structural parameters and critical deflections associated with certain damage levels would need to be determined experimentally and/or numerically.

***N. Duranovic, 1998***

This paper investigated structural modeling for assessing the characteristics and behaviour of RC slabs subjected to impulsive loading produced at different scales analytically and experimentally. It was stated that structural modeling has been widely used for assessing structural response of

structural elements under blast loading due to the economic and practical advantages. With modeling, structural elements can be built to a reduced scale compared to testing full size members or structures. Therefore, the response of real structures subjected to large explosive loading can be represented by smaller structures exposed to scaled loads.

The "gravity forces neglected model" was adopted to reduce a scale from full size structures to scaled size structures in order to study structural response of RC slabs exposed to close range explosions. The explosive charges and distances from the target structural element were scaled according to the cube root scaling laws in the theoretical analyses. Two types of charges were considered: large scale and small scale. The large scale charge was chosen to be 1300 g. According to cube root scaling law, the charge mass of 1300 g at a distance of R1 from the charge would produce a scaled charge mass of 78 g with the same peak overpressure and shock wave velocity at a distance of R2. For practical reasons, the same size detonator was used for both scales.

The analytical results illustrated that, although the scaled charges produced the same peak pressure and shock wave velocity at scaled distances, the positive duration and impulse resulting from the larger charge was 2.5 times greater than corresponding values from the smaller charge.

The theoretical model was designed to represent approximately 1:4 scale and 1:10 scale models of prototypes. In the experimental program, the small RC slab specimens (SE) model the large specimens (LSE) at 1:2.5 scales. Supports were fully fixed in all cases. During the blast testing, deflections, local and overall damage, and crack patterns were recorded. The experimental results highlighted that both local and overall damage were almost identical despite the fact that the scaled RC slab was 2.5 times smaller than the large RC slab. It was noted in the study that scaling of local and overall damage of the slab was more successful then scaling of slab displacements or reinforcement strains.

It was concluded that the proposed “gravity forces neglected model” could be used for dynamic modeling. However, neglecting strain rate effects was more important and can notably affect the test results. The analytical results are not affected by neglecting gravitational forces. The

experimental test results demonstrated that the displacements obtained on the small scale RC slab specimens were smaller than on the full scale RC slab specimens. The local and overall damage was almost identical in appearance for both size of RC slabs which indicated that the failure mechanism was the same for real structure and scaled model.

***F. Toutlemonde, P. Rossi, C. Boulay, and C. Guedon, 1995***

The authors conducted an experimental study to investigate the dynamic behaviour of concrete slabs subjected to shock loading generated by shock tube. The objectives were to better understand the behaviour of concrete under high loading rates; better control the shock (blast, impact, and impulsive loading) resistance of concrete structures; provide reliable experimental data to develop numerical models; and compare different types of structural response with respect to impulsive loading.

A series of slabs were experimentally tested in to analyze the effect of free water, porosity and reinforcement on the dynamic strength of a typical concrete structure. The concrete slabs were subjected to successive impulsive shots with increasing intensity until failure. Six types of slabs were tested with the shock tube; each subjected to 5-15 successive tests by the shock tube.

The experimental results included loads at the initiation of cracking and failure that were observed for the first series of tests on different slabs. The recorded test results provided upper and lower bound loads. The true critical loads lied somewhere between these two boundary values.

## 2.2 Discussion and Justification of This Study

To summarize, the state-of-the-art review has shown that the dynamic response of RC walls/slabs subjected to blast loading has been studied analytically, numerically and experimentally by the structural engineering community and reported in the literature. However, none of the research focused on the blast performance of RC reservoir/tank walls. The dynamic response of RC reservoir walls/slabs subjected to blast loading, to the researcher's best

knowledge, has not been experimentally tested to date. There is a lack of information on blast-resistant design procedures in this area. The experimental and numerical work presented in this thesis aims to advance knowledge in this area with experimental data and through an assessment of the applicability of the SDOF approach.

# Chapter 3 Blast Loading and Structural Response

## 3.1 General

In blast-resistant design of reinforced concrete structures to resist the effects of accidental explosions, the principal effects of the explosive output to be considered are blast pressures, fragments generated by the explosion, and the shock loads produced by the shock wave while propagating outward through the surrounding air or ground (Ahmad et al. 2012).

The explosion is a phenomenon of a large-scale, rapid and abrupt release of energy. The shock or blast wave is generated when the atmosphere surrounding the explosion is forcibly pushed back by the hot gases produced from the explosion source. The front of the wave, called the shock front, is like a wall of highly compressed air having an overpressure much greater than that in the region behind it. The blast effects of an explosion are presented in a shock wave of high intensity shock front that expands outward from the explosive source to the surrounding air. As the shock wave propagates through the air, the wave front encircles the structures in its path such that the entire structures are exposed to the blast pressure. The magnitude and distribution of the blast loading on the structure depends on the following factors: (1) the type of explosive material, energy released (size of detonation) and weight of explosive; (2) the detonation location relative to the structure; and (3) the intensity and magnification of the pressure due to the interaction with the ground or the structure.

Structural response to blast wave loading is a transient dynamic problem. The combination of external loading and inertia forces are resisted by internal elastic and damping forces within the structure and structural members. The relationship between natural period of the global structure, natural period of structural members, duration of the blast wave loading, geometry of the structure, and location of the loading are significant in determining how the structure will respond.

## 3.2 Blast Loading

### 3.2.1 Explosions and blast phenomenon

An explosion is defined as a large-scale, rapid and sudden release of energy. The detonation of the explosive generates a significant amount of energy, which causes the explosive gas to expand forcing the surrounding air out of the space. Consequently, a compressed layer of this air, known as shock front, is formed at the instant of the detonation. It contains most of the energy released from the explosion and expands outwards at supersonic speed. As the blast wave propagates, it decays in strength, extends in duration and decreases in shock front velocity and temperature, and propagates quickly away from the blast source.

For the purpose of the design of protective structures to resist the effects of blast loading, the principal explosion effects to be considered are blast pressures, fragments generated by the explosion and the shock loads produced by the shock wave transmitted through the air or ground (Magnusson 2007). Of these three parameters, the blast pressures are usually the governing factor in determining structural response. Many design guides provide charts and tables that can be used to determine the structure's response to a certain blast pressure profile. Detonation produces an overpressure peak. Thereafter, as the blast wave propagates outward from the explosion source to the sounding air, the pressure decreases and drops. The blast wave is characterized by a sudden increase in pressure to a value above ambient atmospheric, followed by a decrease to an atmospheric pressure. This duration is referred to as the positive phase. After a short period of time, the pressure behind the shock front falls below the atmospheric pressure (negative phase). The variation of blast wave pressure with distance from explosion is presented in Figure 3.1.

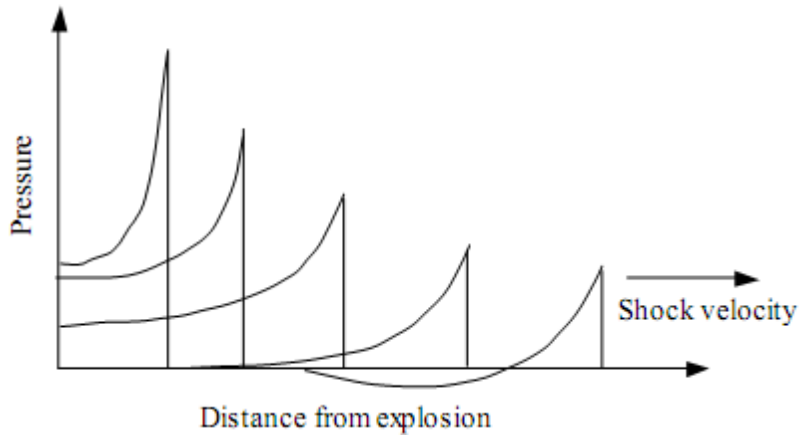


Figure 3.1: Blast wave propagation (Ngo et al. 2007)

As the shock wave travels outward from the charge, the peak pressure which forms at the shock front of the wave steadily decreases in velocity. To analyze the blast loading, it is necessary to determine the initial reduction of the dynamic pressure with time as blast effects on structures depend on the pressure-time history in addition to the peak pressure. At large a distance from the detonation, the peak pressure is insignificant, and the blast wave can be treated as a sound wave.

### 3.2.2 Characteristic of blast loads

To study the blast effects on a given structure, the characteristics of the blast wave must be known. The explosive wave is characterized by a sudden increase in pressure to peak, followed by a decrease to an atmospheric pressure (positive phase), and then a further decrease in pressure below the atmospheric pressure (negative phase). The typical pressure-time history of the blast waveform generated by a free-air detonation from an explosive at some stand-off distance is given in Figure 3.2.

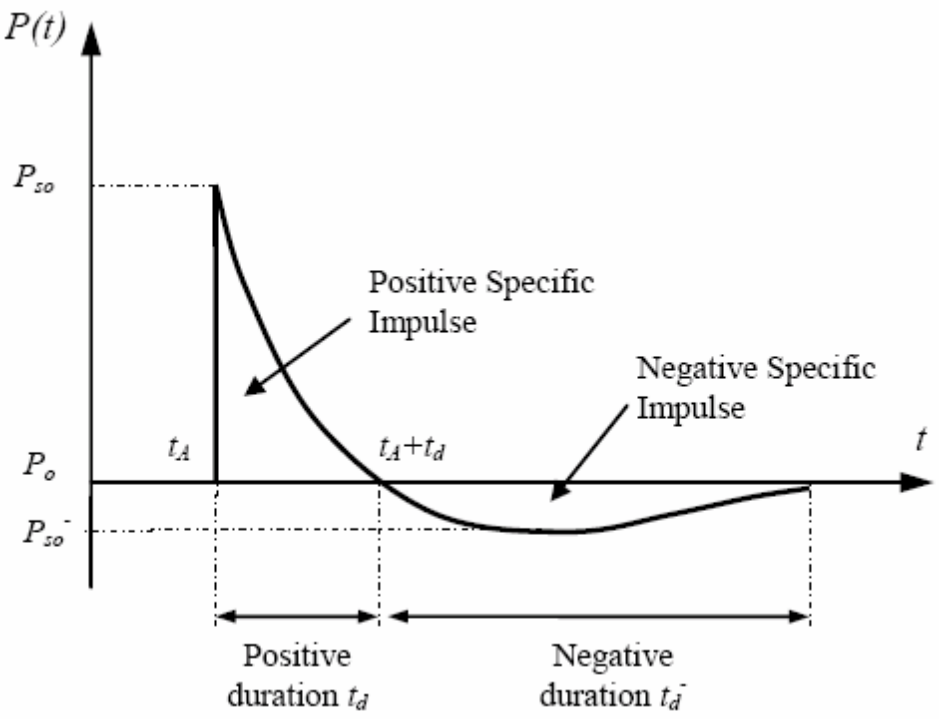


Figure 3.2: Blast pressure versus duration behaviour (Magnusson 2007)

The main characteristics of the development of this pressure wave are the following: the arrival time $t_A$ of the blast wave; the peak overpressure $P_{so}$; the ambient pressure $P_o$; the positive phase duration time $t_d$; the maximum negative pressure $P_{so}^-$; and the duration of the negative phase $t_d^-$. The positive impulse is determined from the area bounded by the peak overpressure and the positive phase duration $t_d$.

At the arrival time $t_A$ of the blast wave, the pressure suddenly increases in an extremely short rise-time to attain its peak overpressure $P_{so}$ over the ambient pressure $P_o$. The pressure then starts decreasing until it reaches the ambient pressure $P_o$ at time $t_d$. After this point, the pressure decays below the ambient pressure until it reaches the maximum negative pressure $P_{so}^-$ and then eventually returns to ambient condition in the duration of the negative phase denoted as $t_d^-$.

The blast shock wave propagates as a sphere of compressed gas that rapidly moves outwards from the explosive source. When the incident pressure wave impinges on a surface of a structure that is not parallel to the projection of the shock wave, the pressure is reflected and increasing in magnitude, producing what is known as the reflected pressure. The reflected pressure is always

greater than the incident pressure for the same distance from the explosion. Ngo et al. (2007) stated that when the shock wave encounters any structure in its path, the incident peak overpressure $P_{so}$ is magnified by a reflection factor that depends on the intensity of the shock wave. The reflected pressure varies with the angle of incidence of the shock wave. When the shock wave impinges on a structure surface that is perpendicular to the direction it is traveling, the impacted structure surface will experience the maximum reflected pressure. When the reflecting surface is parallel to the blast wave, the minimum reflected pressure or incident pressure will be reached.

The following paragraph is based on the work of Ngo et al. (2007). The pressure generated during a blast wave is a function of time and has two distinct phases which impose two different types of pressures on structures in its path. The two phases are: portion above ambient pressure which is called positive phase duration, $t_d$; and the portion below ambient pressure which is called negative phase duration, $t_d^-$. Comparing to the positive phase, the negative phase is longer in duration but with a lower magnitude of pressure. The impulse arising from the pressure wave measures the blast energy from an explosion transmitted to structure. Both the negative and positive phases of the pressure-time waveform contribute to impulse. As the stand-off distance increases, the duration of the positive phase increases resulting in lower peak amplitude. Therefore, explosive charges located extremely close to a target structure impose a highly impulsive, high intensity pressure load over a localized region of the target structure. Charges located farther away from the target structure produce a lower-intensity, longer-duration uniform pressure distribution over the entire structure. Eventually, the entire structure is immersed within the shock wave. The magnitude and distribution of blast loads imposed on a target structure vary greatly depending on explosive properties (type of material, energy output, and quantity of explosive); location of the detonation relative to the target structure; and magnification of the pressure pulse through its interaction with the ground or structure (reflection effects). The reflected pressure and the reflected impulse are the forces to which the target structure ultimately responds. During the negative phase, impact from fragments as a result of the initial positive phase may cause secondary damage on the already weakened structure.

### 3.2.3 Blast wave scaling laws

Blast parameters are primarily dependent on an explosive charge weight by a detonation in the form of a blast wave and the distance from the explosion. To characterize the properties of blast waves generated by explosives in free-air, extensive experiments have been conducted by researchers for many decades. The test results suggest that the blast waves follow scaling laws. Many blast wave parameters can be scaled for charge masses ranging from a few grams up to several tons.

The most common form of blast scaling is Hopkinson or 'cube-root' scaling law. The Hopkinson-Cranz law provides a universal normalized description of the blast effects in terms of scaled distance, where the scaled distance is the constant of proportionality between stand-off distances and charge weights that result in the same incident pressures. For example, two different weights of the same explosive detonated in similar atmospheric conditions, produce similar blast waves at some identical scaled distance. The scaled distance is an important parameter to determine the air-blast pressure and impulse. Other blast parameters can conveniently be plotted against the scaled distance. The Hopkinson-Cranz law is also useful for conducting experimental testing over a very wide range of explosive energies and distances, including very strong shock conditions. The usefulness is in the sense that the scaling law can be employed to find data for explosions to be tested in experiments to measure the properties of the blast wave.

In the study conducted by Luccioni et al. (2004), the Hopkinson-Cranz Scaling Law states that similar explosive waves are produced at identical scaled distances when two different charges of the same explosive and with the same geometry are detonated in the same atmosphere. Thus, any distance $R$ from an explosive charge $W$ could be transformed into a characteristic scaled distance $\left(Z = \frac{R}{W^{1/3}}\right)$, where $W$ is the charge mass expressed in kilograms of TNT. The use of $Z$ allows a concise and efficient representation of blast wave parameters for a wide range of real situations. Huntington-Thresher and Cullis (2001) stated that different explosives are generally compared through their TNT equivalency both in terms of peak pressure and impulse. The TNT

equivalency of an explosive is defined as the ratio of the mass of TNT to the mass of the explosive such that both result in the same magnitude of pressure or impulse.

Scaling laws provide parametric correlation relationships between a particular explosion and a standard charge of the same substance. The basic characteristics of the explosion and blast wave phenomena are presented together with a discussion of TNT equivalency and blast scaling laws. In general practice, prediction of blast pressure is based on scaled distance. All parameters of the pressure-time curve are also normally written in terms of a scaled distance.

### 3.2.4 Dynamic blast loading on structures

Blast loading is a short duration load also known as impulsive loading. The blast loading can be treated mathematically as an equivalent triangular load. If a blast wave strikes a structure, the structure is experiences loading from two components: static overpressure and the dynamic pressure. Both static overpressure and dynamic pressure are a function of time and stand-off distance to the charge center. Time and distance are accompanied by the velocity at which the blast wave is propagating, although the velocity is not constant. Due to the combination of the time and distance, the component of translational pressure as a result of the static overpressure depends on the size of the target structure compared to the positive phase duration of the blast. The translational pressure is defined as the net pressure due to blast loading. The structural response to blast loading depends on the natural period of vibration and the degree of ductility (deformation capacity). Structural elements constructed with ductile structural materials, such as steel and reinforced concrete, can absorb significant amount of strain energy and, therefore, are more resistant to the blast loading. On the other hand, brittle structural materials, such as timber, masonry and monolithic glass, are not ductile. Consequently, structures with brittle properties could fail abruptly when subjected to the blast loading.

The blast effects of an explosion on structures are in the form of a wave composed of a high-intensity shock front, like a wall of highly compressed air, which travels outward from the surface of the explosive into the surrounding air. As the shock wave expands, the peak overpressure decays in strength, lengthens in duration and decreases in velocity (Ahmad et al.

2012). When the incident blast wave strikes a solid structural surface, the wave is reflected. This leads to the air particle velocity dropping to zero at the reflecting surface while the pressure, density and temperature are increased. The actual pressure developed through this process is a function of the following factors: (1) the peak overpressure of the incident blast wave; and (2) the angle between the direction of motion of the wave and the face of the structure, i.e. the angle of incidence. The largest increase in the reflected overpressure will be for normal reflection where the direction of motion of the wave is perpendicular to the surface at the point of incidence. Normal reflection of weak incident blast wave will result in a reflected overpressure having about twice the value of the incident wave. However, the reflected pressure for strong incident blast wave can be several times greater in magnitude compared to that of the incident pressure. In extreme cases, the reflected pressure has the ability to reach up to twenty times that of the incident pressure (Magnusson 2007). The pressure increases during reflection is due to the conversion of the kinetic energy of the air immediately behind the shock front into internal energy as the moving air particles are decelerated at the surface of the structure (Glasstone and Dolan 1977). The impulse density (amount of impulse) will increase by reflection in a similar way as the incident pressure increases. The spherical expansion of the blast wave leads to a continuous reduction of the peak pressure and impulse density. However, the duration of the blast wave increases (Magnusson 2007).

The following paragraph is based on the work of Ngo et al. (2007). The threat from a conventional bomb is determined by two equally important elements: the bomb size, or charge weight $W$; and the stand-off distance $R$ between the detonation point and the target structure. Figure 3.3 shows the blast pressure effects on an example building structure. In the scenario where the external walls of a building are capable of resisting the blast loads, the incident shock front will penetrate through windows and door openings. As a result, the floors, ceilings, walls etc. will be damaged. Occupants within the building will be subjected to the sudden pressures and fragments from shattered windows, doors and other materials. For the case where the external walls are not capable of resisting the blast wave, the structural members will be impacted in the same manner as what has been described in previous scenario. In addition to that, building components will be fractured and fragmented by the dynamic pressure immediately after the shock front moves. Building contents and occupants will be displaced in the direction of

the blast wave propagation. Occupants in the affected building will be vulnerable to severe injuries.

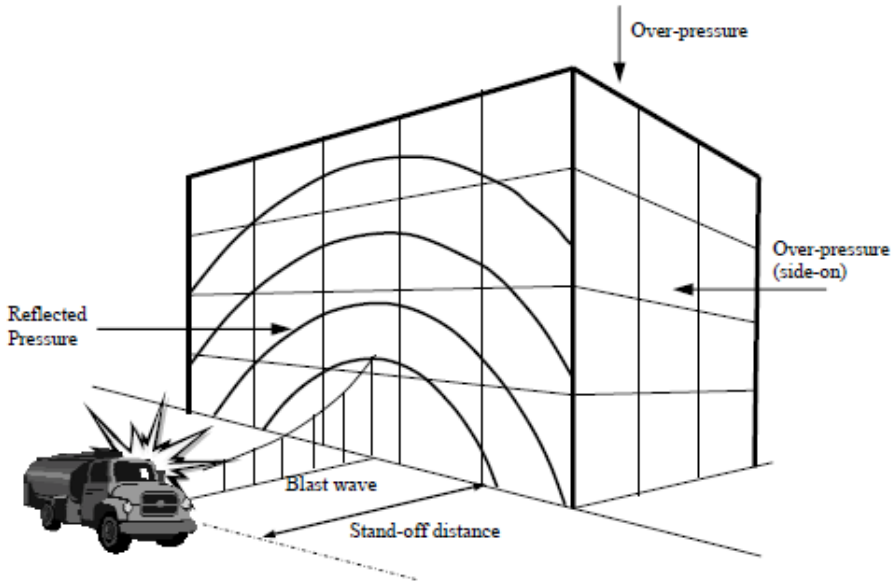


Figure 3.3: Blast loads on a building (Ngo et al. 2007)

## 3.3 Structural Response to Blast Loading

Blast loading is a short duration load resulting from the detonation of high explosives. It is described by two parameters: peak overpressure and duration. The design of structures subjected to blast loading is often treated by the assuming an equivalent triangular blast load. Blast loading is the function of distance of the structure from the explosion and the charge weight. The ductility and natural period of vibration of a structure are two important characteristics in the structural response to an explosion.

In the event of an explosion, ductile structural elements such as steel and reinforced concrete are more resistant to blast loading and less vulnerable to damage compared to brittle structural elements such as timber and masonry. Ductile structural elements can absorb significant amounts of strain energy. The peak overpressure, the positive phase duration, the incident overpressure

impulse, and the natural period of response of the structural elements are required to analyze the dynamic response to blast loading.

The following paragraph is based on the study of Priyanka and Munirudrappa (2002). The structural behaviour under blast loading can be characterized into three categories depending on the comparison between the positive duration of a blast wave and the natural period of a structure. (1) Quasi-static response: when the positive phase duration of blast wave is much longer than the natural period of the structure. For this type of response, the structure will be deformed before the blast load decays. (2) Impulsive response: when the positive duration of a blast wave is much shorter than the natural period of a structure. In this response, the deformation of the structure continues after the blast wave diminishes and ceases to act on the structure. (3) Dynamic response: when the positive phase duration of a blast wave is approximately the same as the natural period of a structure. Here the response of the structure is dependent on time and is determined by solving the equations of motion of the structural system.

The sudden application of large intensity loading due to blast on a structure causes non-linear permanent deformation of the structural components. The analysis of blast loading is therefore a non-linear dynamic analysis problem (Ngo et al. 2007).

### 3.3.1 Single-Degree-Of-Freedom (SDOF) analysis

The Single-Degree-Of-Freedom (SDOF) approach can be used as a simplified method to predict and analyze the dynamic response of structures or structural elements subjected to blast and impact loading. This analytical technique has also been utilized for the design of blast-resistant structures due to air blast loading (Mays and Smith 1995). The advantage of using the SDOF method in blast-resistant design can be attributed to its simplicity and cost-effectiveness that requires limited input data and reasonable computational effort. The SDOF methods will provide satisfactory prediction results given that an accurate response mode shape of the real structural behaviour is adopted.

All structures possess multiple degrees of freedom. The behaviour of structures subjected to blast loading can be conveniently represented with SDOF models by determining the ordinate that accurately describes the dynamic motion of a complex structural system. The simplified approximate method attempts to evaluate a structure using only one degree of freedom, the horizontal displacement. Although more detailed and complex methods of dynamic analysis are available, the basic analytical model applied in blast design is the SDOF method because this approximate analytical technique is considered to provide satisfactory response results given the uncertainties associated with blast design (Biggs 1964).

The SDOF mass-spring system is an approximation of a structural system subjected to an external forcing function. The response of the structural system with a nonlinear resistance term, $R(u)$, can be written as given by Equation 3.1 based on static equilibrium of dynamic forces:

$$m\ddot{u}(t) + R(u) = AP(t) \quad [3.1]$$

where $m$ is the mass of the system, $R(u)$ is a nonlinear resistance, $A$ is the area exposed to blast loading, $P(t)$ is the time-variant forcing function, and $u$ and $\ddot{u}$ are the displacement and acceleration of the mass, respectively. Damping is typically neglected given the short duration of structural response to blast loading (Biggs 1964).

If structural response is expected to be nonlinear or the forcing function is in the form of a set of discrete pressure-time points, numerical integration is the approach to use to solve the equation of motion (Jacques 2011).

Replacing the nonlinear resistance, $R(u)$, in Equation [3.1] with a linear resistance term, $ku(t)$, the following linear SDOF equation of motion is obtained:

$$m\ddot{u}(t) + ku(t) = AP(t) \quad [3.2]$$

where $k$ is the stiffness of the system.

A closed-form solution to the equation of motion expressed in Equation 3.2 is the most convenient method when the forcing function is simple and the resistance of the structural member or structure is proportional to the displacement of the structural system.

Jacques (2011) reported that a number of numerical techniques are available in the literature to solve this type of equation of motion. However, the average acceleration method is one approach that is very appealing due to its user-friendliness and unconditional stability in the integration method (UFC-03-340-02 2008).

Among the existing closed-form approximations of the blast pressure-time history, the most common ones are a linearly decreasing function and an exponentially decreasing function. An idealized linearly decreasing forcing function may be used to describe the first positive phase of blast loading due to its simplicity (UFC-03-340-02 2008). This forcing function, shown in Figure 3.4, can be expressed as:

$$P_r(t) = P_r\left(1 - \frac{t}{t_d}\right) \quad [3.3]$$

where $P_r$ is the peak reflected pressure and $t_d$ is the positive phase duration.

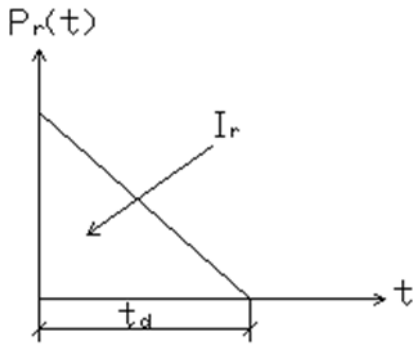


Figure 3.4: Idealized pressure-time histories

The impulse, $I$, equals the area under the pressure-time history and is defined as:

$$I = \int_0^{t_d} P_r(t)dt = \frac{P_r t_d}{2} \quad [3.4]$$

Equating Equations [3.1] and [3.3] generates the following second order differential equation:

$$m\ddot{u}(t) + ku(t) = AP_r\left(1 - \frac{t}{t_d}\right) \quad [3.5]$$

The displacement solution to Equation [3.5] during the forced-vibration phase when $0 \leq t \leq t_d$ is:

$$u(t) = \left(u_0 - \frac{Ap_r}{k}\right) cos\omega t + \frac{v_0 + {Ap_r}/{kt_d}}{\omega} sin\omega t + \frac{Ap_r}{k}\left(1 - \frac{t}{t_d}\right) \quad [3.6]$$

where $\omega = \sqrt{k/m}$ is the natural frequency of the structure, and $u_0$ and $v_0$ are the initial displacement and velocity at time $t = 0$, respectively.

The free-vibration displacement response of the system in Equation [3.5] during the free-vibration phase when $t \geq t_d$ is given by:

$$u(t) = u_{t_d} cos\omega(t - t_d) + \frac{v_{t_d}}{\omega} sin\omega(t - t_d) \quad [3.7]$$

where $u_{t_d}$ and $v_{t_d}$ are the displacement and velocity of the mass at time $t = t_d$, respectively.

### 3.3.2 Modelling structures as equivalent SDOF systems

The equivalent SDOF method is widely used in protective design against the effects of blast. This method also forms the basis of equivalent SDOF factors presented in Biggs (1964) and TM5-1300 (1990) for SDOF calculation for dynamic response. Recently, Bangash and Bangash (2006) also referred to the equivalent SDOF method for blast protective design (Syed et al. 2006).

All structures consist of more than one degree of freedom. For practical purpose, it is possible to describe the motion of a multi-degree-of-freedom structure by a single ordinate through the use of transformation factors. The problem can then be simplified by considering a single degree of freedom (SDOF) system. The use of transformation factors to approach the response of a distributed system has been well described in detail by Biggs (1964), UFC-03-340-02 (2008), and (Jacques 2011).

The response of the multi-degree-of freedom structures can be approximated to the response of an equivalent SDOF system by assuming that the response is controlled by a single mode. The displacement time-history of the equivalent SDOF system is equal to that of the real structure at the equivalent ordinate. This equivalent ordinate is typically selected at the location of maximum

displacement. In this way, the mass of the distributed system is lumped at the position of the equivalent ordinate, while the distributed force and stiffness are lumped as a series of point loads imposing on the lumped mass. Transformation factors are required to lump the real structural system as an equivalent ordinate. Transformation factors for an equivalent SDOF system are generated based on the assumption that the deflected shapes are caused by the static application of the dynamic loads (Biggs 1964).

The selection of an appropriate shape function is crucial in generating transformation factors. Shape functions must be selected in the way that they are able to capture anticipated behaviour of structural members. As a means of describing the displacement process, the formation of plastic hinges usually indicates a transition from elastic bending to rigid body motion. This behaviour must be defined by the shape function to generate adequate results (Biggs 1964).

The start of plastic behaviour will lead to a gradual change in dynamic properties of the structural system. Applying discontinuous shape functions to describe this behaviour of the structure introduces uncertainties in the calculations, even though this is generally considered as acceptable by the approximation nature of the SDOF method (Biggs 1964).

The mass factor, $K_M$, is required to transform a system with distributed mass into an equivalent SDOF system with lumped mass. The mass factor is defined as:

$$K_M = \frac{\int_0^L \bar{m}\Phi(x)^2 dx}{\bar{m}L} \qquad [3.8]$$

where $\bar{m}$ is the mass per unit length of the member and $\Phi(x)$ is the shape function of the member.

The real structure is given in Figure 3.5. It can be idealized as an equivalent SDOF system shown in Figure 3.6.

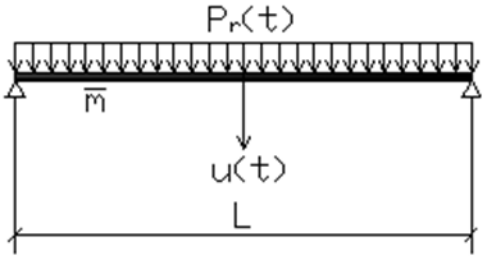


Figure 3.5: Real structure

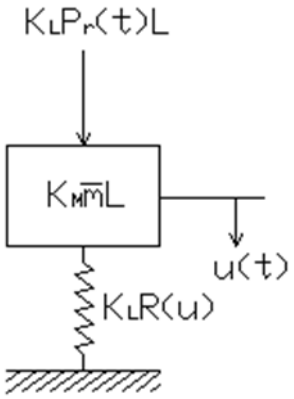


Figure 3.6: Equivalent SDOF system

The load factor, $K_L$, is used to transform distributed force and stiffness to a single point load and is computed by the following equation:

$$K_L = \frac{\int_0^L P\Phi(x)dx}{PL} \quad [3.9]$$

It is convenient to define a single load mass factor, $K_{LM}$, as the ratio of the mass factor to the load factor:

$$K_{LM} = \frac{K_M}{K_L} \quad [3.10]$$

The equation of motion of an equivalent single-degree-of-freedom system with non-linear resistance incorporating $K_{LM}$ is as follows:

$$K_{LM}m\ddot{u}(t) + R(u) = AP(t) \quad [3.11]$$

If appropriate shape functions are selected that adequately describe structural behaviour as the structural member progresses from elastic to plastic response, the above procedures in Equations 3.8 to 3.11 may be used to transform structural elements into an equivalent SDOF model (Jacques 2011).

Common transformation factors have been published in several references, notably in Biggs (1964) and UFC-03-340-02 (2008). These design aids can be applied in design of one-way and two-way flexural members with a variety of common support conditions subjected to distributed and concentrated point loads (Jacques 2011).

### 3.3.3 Pressure-Impulse (P-I) diagrams

Pressure-Impulse (P-I) diagrams or iso-damage curves can be used to estimate damage and non-damaged ranges in a structural element subjected to blast load. The pressure-impulse diagrams usually contain a group of curves with different degrees of damage. Figure 3.7 is a typical P-I diagram showing the levels of damage for a structural member. The P-I diagrams are derived based on the maximum displacement criteria. The pressure-impulse space is divided into several regions corresponding to a specific level of damage. The damage levels include low damage, medium damage, and high damage (Li and Meng 2002).

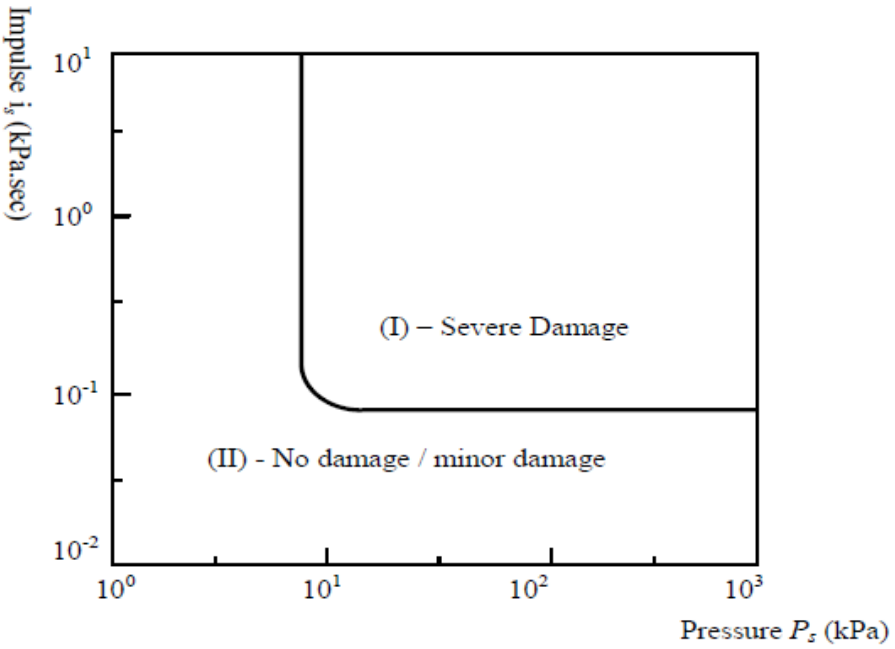


Figure 3.7: Typical Pressure-Impulse (P-I) diagram (Ngo al et. 2007)

It is important to consider the duration of blast loading along with the magnitude of blast pressure for dynamic analysis response of structural elements. P-I diagrams which incorporate both blast pressure magnitude and duration are commonly used to assess damage of structural components subjected to blast loading. The P-I diagrams or iso-damage curves are used to link the effects of blast load to the maximum response of the structural system. The difference in P-I diagrams due to various damage levels is more significant in the region where damage is dominated by pressure rather than impulse. The P-I diagrams can be readily adopted for quick damage evaluation for reinforced concrete structures. Iso-damage curves including both magnitude and duration of blast loading connect the blast load to the corresponding damage for given blast loading scenarios (Syed et al. 2006).

Currently, available design guidelines and manuals for blast protective design are, for the most part, based on the SDOF model. The P-I diagrams can often be generated based on equivalent SDOF systems. The P-I diagrams are commonly used in the blast resistant design or damage assessment of structures to establish safe response limits for given blast loading scenarios. Experimental or field blast testing results can be compared to analytical results to assess the effectiveness of P-I diagrams in blast damage assessment (Syed et al. 2006).

## 3.4 Yield Line Analysis

Yield line analysis is an ultimate load analysis approach for predicting the ultimate flexural strength of reinforced concrete structural elements, which can be adopted for blast loading. The method is used to either determine the design moments in a structural element corresponding to failure or the applied load at which a structural element will fail. The yield line theory has been used in practical and economic blast-resistant design of reinforced concrete structural elements such as reinforced concrete slabs (Wager 1994).

The majority of structures have been designed using elastic theory. In the case of slabs, elastic methods of design can be particularly challenging for slabs of irregular shape. It is difficult to establish an exact solution for the ultimate flexural strength of a one-way or two-way reinforced concrete walls/slabs with elastic analysis. The yield line analysis is an alternative technique that can assesses the load at which a slab fails.

The yield line theory provides upper bound solutions to the ultimate load capacity of reinforced concrete slabs through an assumed collapse mechanism by choosing a pattern of yield lines. The yield line analysis is an alternative technique to study the behaviour of a slab subjected to blast loading. It is an ultimate load method based on flexural response and assesses the load at which a slab will fail, known as the collapse load. It is possible to obtain a realistic value of the collapse load for any complex slab shape or loading configuration. Therefore, the ultimate load method is a powerful tool for estimating the required bending resistance of slabs subjected to blast loading, specifically for slabs of irregular shapes. It has also been assumed that the elastic deformations are negligible comparing to the plastic deformations and that the slab will not fail until a valid mechanism is formed. This means that all the deformations take place at the yield lines. When a slab is loaded to the point of failure, yield lines will form in the most highly stressed areas and develop into continuous plastic hinges. These plastic hinges form a yield line pattern. The yield lines divide the slab into individual regions. The regions pivot about their axes of rotation until maximum deflection (the ultimate moment of the yield line section) or until failure occurs. Several geometric combinations of plastic hinges can describe a valid mode for failure (failure mechanism) for a given slab, and each must be evaluated to determine the lowest failure load.

The assumption of an incorrect failure mechanism for a slab will lead to over predicting the ultimate resistance of the structural element. This phenomenon emphasizes that it is critical to evaluate all plausible failure mechanisms for a slab to ensure that the most reliable failure load is established (Wager 1994).

Two approaches are possible in yield-line theory. The first approach, known as the virtual work method, is based on an energy method with the principle that the external work done by the applied loads in causing a small virtual displacement is equal to the internal work done through rotation along the yield lines. The alternative approach is based on equilibrium method of solving various yield line patterns. Essentially, the equilibrium method is simply the work method, but presented in a different form (Kennedy and Goodchild 2003).

In this study, yield line analysis was conducted to establish the potential yield locations. This assisted in determining the location to place the reinforcing steel strain gauges in the test specimens.

# Chapter 4 Design of Reinforced Concrete Reservoir Walls

## 4.1 General

In general, there are three types of water tanks: 1) tanks resting on ground; 2) underground tanks; and 3) elevated tanks. Tanks resting on ground, such as water reservoirs, are supported directly by the ground surface. The walls of these tanks are subjected to hydrostatic pressure from the water that is retained, while the base is subjected to the weight of water and pressure of the underlying soil.

Design of reinforced concrete tanks requires specific attention to crack control, durability and serviceability performance criteria, in addition to strength. A properly designed reservoir must have sufficient capacity to sustain the applied loads without experiencing cracking to prevent leakage of the water that is retained. Therefore, the tensile stresses that develop in the concrete are required to satisfy prescribed permissible limits. Generally, a reservoir that is structurally sound will not leak. To achieve this target, certain requirements must be met including provisions prescribing a proper amount of and distribution of steel reinforcement, correct spacing and detailing of construction joints, and quality concrete placed using appropriate construction practices.

From a design perspective, tanks may be classified according to their shapes, for example, circular tanks and rectangular tanks. For the purpose of this study, the reservoir walls built for testing are representative of scaled walls from a circular tank located above ground and with either hinged or free boundary conditions at the base, and free boundary conditions at the top of the reservoir. The walls have been designed to sustain forces arising from a triangular hydrostatic loading condition.

## 4.2 Design Requirements

The structural design of environmental concrete structures such as water reservoir tanks is not covered explicitly in Canadian design standards. A variety of international documents are frequently adopted. The widely used references for the design of reinforced concrete tanks in Canada and the USA are the American Concrete Institute (ACI) 350 committee reports and the Portland Cement Association (PCA) publications (Rashed et al. 1997).

The limit states for tanks are the ultimate limit state and the serviceability limit state which includes leakage, durability and deflection limit states. The serviceability requirements typically govern the design. Within the serviceability requirements, leakage and durability generally govern over deflection limitations. Various design strategies may be used to create a structure that will satisfy all limit state requirements.

### 4.2.1 Code requirements

The ACI 318 *Building Code Requirements for Structural Concrete* represents the minimum requirements for structural concrete used in buildings for safety, serviceability and durability. The ACI 350-06 *Code Requirements for Environmental Engineering Concrete Structures*, based on the structural design provisions that conform to the ACI 318, covers the structural design, materials selection, and construction of environmental engineering concrete structures, including structures for the purpose of storing liquid, for example, reservoirs and dams. In comparison to ACI 318, the ACI 350-06 provides more rigorous requirements for structures which are subject to severe exposure conditions, and more restrictive serviceability requirements including liquid-tightness and gas-tightness testing requirements. The loads covered in ACI 350-06 include: dead and live loads, vibrating equipment, and hydrodynamic forces. Exposure conditions for concrete, such as concentrated chemicals, alternate wetting and drying, and freezing and thawing are also explicitly stated. In addition, crack widths are important parameters of performance and must be controlled to ensure contamination of ground water or the environment is limited, to prevent loss of product, and to promote durability (ACI Committee 350 2006). A properly designed tank must resist the applied loads and possibly incur some minor cracks which are not significant enough to

cause leakage. However, cracks that potentially cause leakage must be avoided in a properly designed tank. The goal of designing and constructing a structurally sound tank that will not leak is achieved by providing a proper design and materials. The objective is to produce a serviceable concrete structure that is durable, nearly impermeable, and resistant to chemicals, with limited deflections and cracking (ACI Committee 350 2006).

Historically, the Portland Cement Association (PCA) published reports on the design of rectangular and circular reinforced concrete tanks (PCA 1942, 1963, 1981 and 1993). Tables are provided to assist with structural design of various tanks. After ACI 350 was adopted, the PCA reports became consistent with the ACI 350 recommendations. However, there are still some differences between the two documents. Neither ACI 350 nor ACI 318 provides guidelines for controlling the stress in the concrete due to ring tension to prevent excessive cracking. Any significant cracking in a liquid containing tank is unacceptable. The PCA provides a minimum wall thickness for circular tanks based on constructability. Given the height of the reinforced concrete wall in contact with the liquid, the minimum thickness of the wall can be calculated. In addition, the PCA suggests that the wall thickness be such that, in the hoop direction, the wall does not crack under normal service loads. The PCA also includes an explicit allowance for concrete shrinkage in the calculations (PCA 1993).

### 4.2.2 Loading conditions

A reservoir water tank is designed to sustain the loads that it will be subjected to during its service life. Water tanks should be designed to resist induced forces and deformations without collapse or gross leakage. There is no cover on the top when the tank is full of liquid. The joint between wall and base of the tank is restrained against radial translation, but is free to rotate. In this study, it is assumed that the load applied on the reservoir wall is based on the internal pressure from stored liquid inside of the tank. It is also assumed that the tank is filled to the top with liquid. According to PCA (1993) *Circular Concrete Tanks Without Prestressing*, the assumption of a fixed base could result in an improperly designed wall. It is more reasonable to assume the base is hinged rather than fixed, which consequently leads to a more conservative design. Therefore, the model applied in this research to represent reservoir walls consists of

hinged base and free top boundary conditions and subject to a triangular load. The model is shown in Figure 4.1.

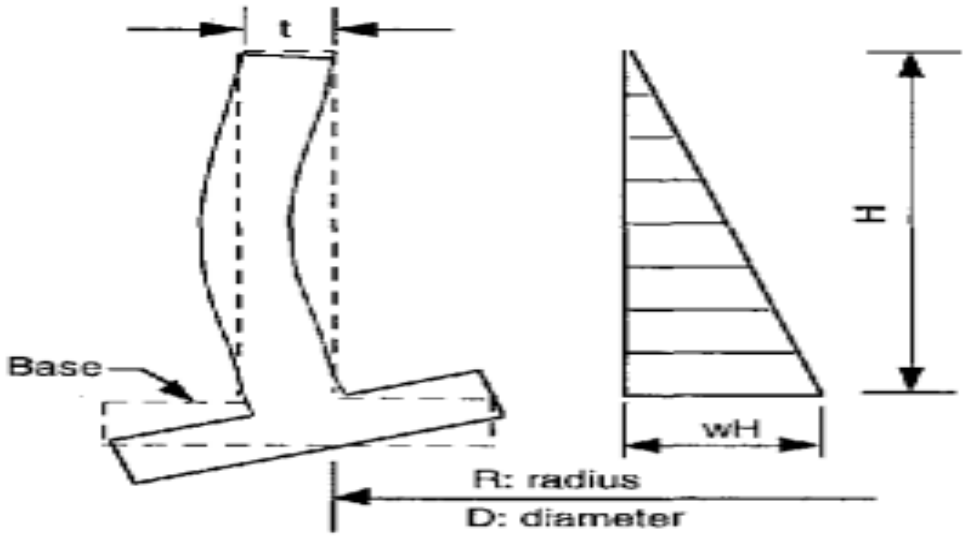


Figure 4.1: Boundary conditions: wall with hinged base and free top subjected to triangular load (Circular concrete tanks without prestressing 1993)

## 4.3 Design Method

The design method prescribed in *Circular Concrete Tanks Without Prestressing*, published by the Portland Cement Association (PCA 1993), was adopted in this study. The PCA method is based on the American Concrete Institute (ACI) 350 specifications, but with some differences in the design provisions. The PCA method is a simplified technique to design RC reservoir walls, and includes coefficients to determine bending moments, shear, tension and deflections for a variety of aspect ratios and end conditions.

For strength design, the load combinations to determine the required strength, $U$, are based on two modifications made in ACI 350 from Section 9.2 of ACI Standard 318-89 (Building Code Requirements for Reinforced Concrete):

1. The load factor to be used for liquid lateral pressure, $F$, is 1.7 rather than the 1.4 which is specified in ACI 318. The PCA (1993) suggests that reservoir tank designs should meet the requirements of ACI 350 and, therefore, recommends a load factor of 1.7; and
2. Structural members shall be designed to meet the required strength, $U$, according to ACI 318-89. The ACI 350 requires that the required strength $U$ must be increased by a sanitary coefficient. The application of sanitary coefficient will increase the design loads to provide a more conservative design with reduced cracking. The increased required strength is given by:

$$Required\ strength = Sanitary\ coefficient \times U$$

where the $Sanitary\ coefficient$ equals:

1.3 for flexure;

1.65 for direct tension; and

1.3 for shear beyond that of the capacity provided by the concrete.

For the working stress alternative design method, ACI 350 recommends it be in accordance with ACI 318.

## 4.4 Design Details

The bending moments imposed on the walls of the reservoir tank vary along the height of the wall. Therefore, an efficient design would tailor the reinforcing area and spacing to satisfy the moments. In addition, the thickness of the wall could also vary to optimize the design process, by either tapering the wall or stepping the wall. However, a simplistic design detailing approach was selected, such that the reinforcement would be consistent for the entire wall. This resulted in one reinforcing ratio to satisfy the moments along the height of the wall and one reinforcing ratio to sustain the horizontal tensile forces due to hoop tension.

The design process for the reservoir walls tested in this experimental program was initiated by assuming a thickness for the walls, the strength of the reinforcing steel, and the strength of concrete following PCA (1993) requirements. According to the loading condition, the corresponding PCA data and coefficient tables are employed to calculate the quantity, size and spacing of the tensile-resisting reinforcement, moment-resisting reinforcement, as well as the

shear reinforcement. Finally, the thickness of the reservoir wall is checked against the requirements for strength of concrete, rebar etc. If the calculated wall thickness is smaller than the assumed wall thickness, the reservoir wall design is viable. The detailed design steps are as follows:

(1) Assume wall thickness of 508 mm based on the minimum wall thickness specified in PCA (1993);
(2) Refer to PCA ratio tables to determine required tensile reinforcement in the horizontal direction;
(3) Calculate the required moment-resisting reinforcement and shear in the vertical direction;
(4) Calculate the required tensile strength of the concrete according to the horizontal and vertical reinforcement selected in the previous steps;
(5) Compare the calculated required tensile strength with the allowable concrete tensile strength. If the required tensile strength is less than the allowable concrete tensile strength, cracking will not appear in the designed RC reservoir walls.

A prototype design of a circular concrete reservoir tank was conducted using the numerical values listed below, from which scaled test specimens were derived and subjected to blast loading:

The tank volume was assumed as $V = 10000\ m^3$ after consulting the experts in the industry.

The tank wall height was selected as $H = 9\ m$ based on the suggested height range from 8 m to 10 m.

Diameter to inside of tank was calculated as $D = \sqrt{\frac{4V}{\pi h}} = 37.6\ m$

Weight of liquid, $w = 1\ g/cm^3$

Shrinkage coefficient of concrete, $C = 0.0003$

Modulus of elasticity of steel, $E_s = 200000\ MPa$

Specified compressive strength of concrete, $f_c' = 30\ MPa$

Modulus of elasticity of concrete, $E_c = 4700\sqrt{f_c'} = 25743\ MPa$

Allowable concrete tensile stress for cylindrical tank design, $0.10f_c' = 3\ MPa$

Ratio of moduli of elasticity, $n = E_s/E_c = 8$

Specified yield strength of reinforcement, $f_y = 400\ MPa$

Allowable stress in reinforcement, $f_s = 124\ MPa$

## 4.5 Validation of Design

The design results obtained from the PCA design method were validated with computer software SAP2000, specifically the tensile forces in the hoop direction and the bending moments along the height of the wall. The results from the PCA design method were in close agreement with the results using SAP2000 software. Detailed design and validation of the prototype reservoir tank are presented in Appendix A.

## 4.6 Scaling of Design

The scaling of the prototype (full size) reservoir tank concrete walls to the model size for lab testing was based on geometric factors. The height of prototype concrete wall was 9 m. The height of the opening of the shock tube is 2 m. Therefore, the scaling parameter was taken as 4.5. The intent was to ensure that the test specimens conformed to the size of the shock tube test area and that the capacity of the shock tube was capable to imposing damage to the walls. Although the size was reduced, the properties of the materials used in the design remained constant.

The scaling includes:

- height and thickness of the tank wall
- horizontal steel that resists direct tension forces
- vertical reinforcement that primarily resists bending moments

The model specimens consisted of materials that were similar to the prototype materials and geometrically similar to the prototype. Detailed scaling of the prototype design is included in Appendix A.

Note that the size of the coarse aggregate used in the test walls was 10 mm and was not scaled. A flexural-type failure was expected and, therefore, the size selected for the coarse aggregate was

not expected to affect the results. In addition, no scaling was performed on the blast loading given that the full capacity of the shock tube was intended to be exhausted.

# Chapter 5 Experimental Program

## 5.1 General

This chapter describes details of the test specimens, the construction of the test specimens, the experimental setup, instrumentation and the test procedure. The specimens were designed to investigate the structural response of reinforced concrete reservoir walls in terms of damage level due to increasing levels of blast loading. Two reinforced concrete walls representative of circular reservoir walls were tested under various combinations of pressure and impulse. The goal of the experimental program was to understand the performance of RC reservoir walls under blast loading and to provide experimental data to complement the existing literature. The test results were also used to investigate the applicability of SDOF analytical models.

## 5.2 Test Specimens

### 5.2.1 Description

Two reinforced concrete reservoir walls were designed to represent typical reinforced concrete wall segments from a circular reservoir tank. They were then scaled, constructed and tested as part of this research study. The two specimens were divided into two categories based on their boundary conditions: 1) two-way bending wall consisting of fixed supports on the two opposite lateral sides, and hinged base and free top edges; and 2) one-way bending wall with fixed two opposite lateral sides, and free base and top edges, as shown in Figure 5.1 and Figure 5.2, respectively. The fixed lateral sides were intended to simulate the continuity of the wall, while the base support condition reflects different base fixities in reservoir tanks. The free top edge represents the top of the reservoir tank. The two walls were assumed to effectively represent the behaviour of two-way and one-way walls subjected to lateral blast loading. Note that during the initial stages of the construction and instrumentation of the two wall specimens, the intent was to test both walls with the support conditions described for Wall 1 above. However, after testing the

first wall it was decided to remove the base pin support for Wall 2 to investigate the response of RC reservoir tanks with a free support at the base. Thus, as will be noted in this thesis, the location of the strain gauges was based on the assumed damage pattern (yield lines) for Wall 1.

For testing, two simplifications were implemented: (1) the test specimens were planar; and (2) the reservoir walls were tested in the absence of water. Although the prototype reservoir wall was a circular structure, a scaled section of the wall would effectively be planar. For this reason, the test specimens were planar. Given the test facility, it was not possible to include the effect of water on the walls.

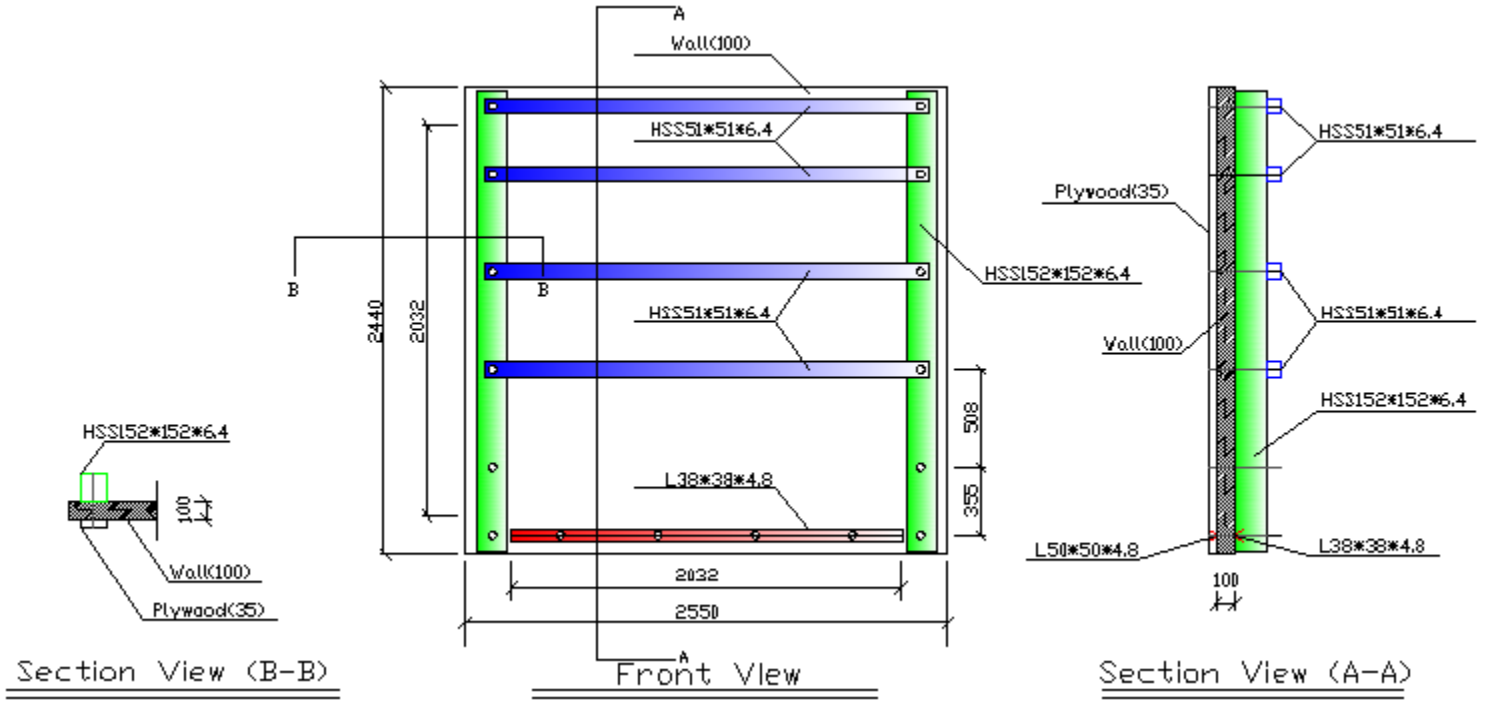


Figure 5.1: Boundary condition for wall setup 1

(all dimensions in mm)

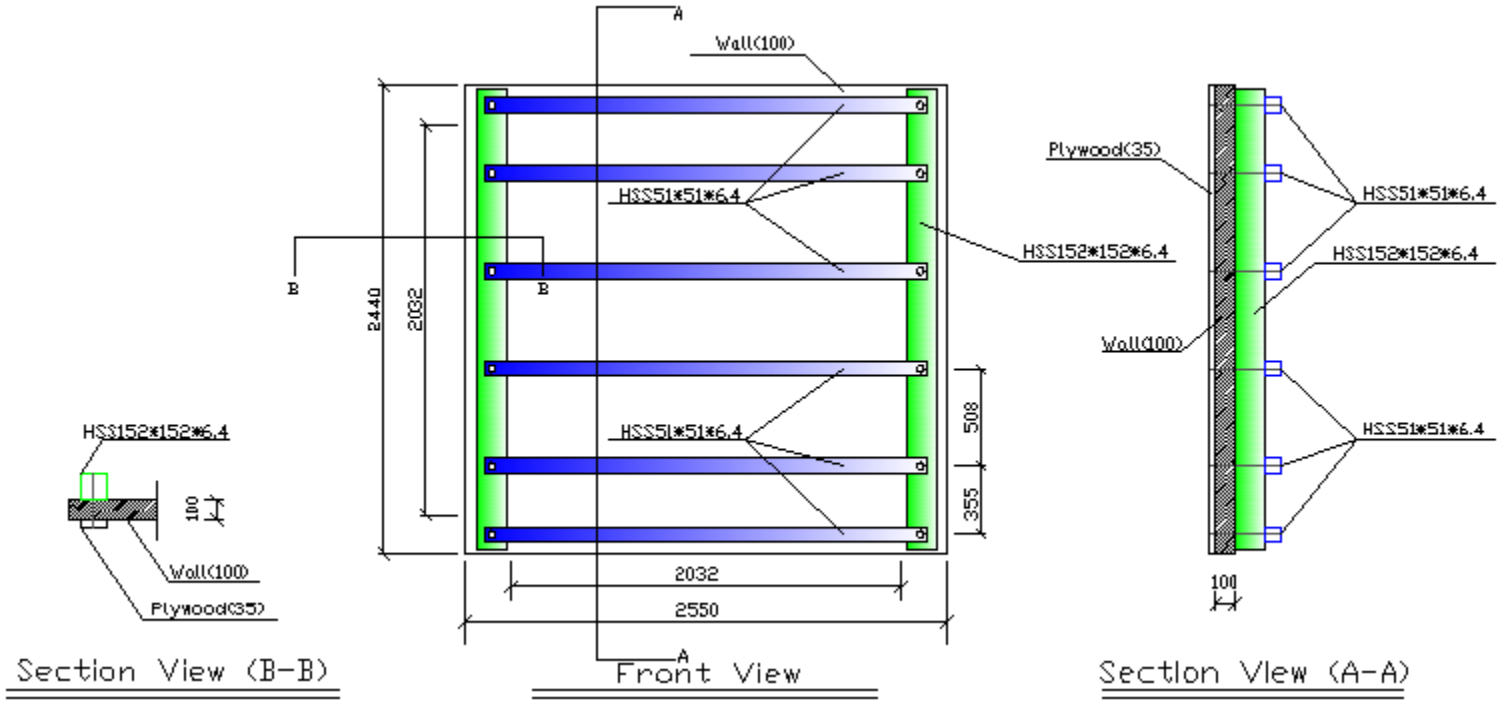


Figure 5.2: Boundary condition for wall setup 2

(all dimensions in mm)

The two reinforced concrete walls were identical with 100 mm thickness, 2550 mm length and 2440 mm height. Figures 5.3 and 5.4 are a schematic drawing and a wall cross section which provide the dimensions of the specimen with reinforcing details, respectively. The concrete walls were reinforced with two layers of rebar in two orthogonal directions. The rebar used is designated as 10*M*, which has a nominal diameter and area of 11.3 mm and 100 $mm^2$, respectively. The horizontal and vertical reinforcement were spaced at approximately 130 mm and 300 mm, respectively. The concrete had an average 28-day compressive strength of 31.5 $MPa$, with an average strength on the day of testing of 36 $MPa$. The concrete slump was 120 mm. The reinforcing steel yield stress $(f_y)$ and ultimate stress $(f_u)$ were 465 $MPa$ and 663 $MPa$, respectively.

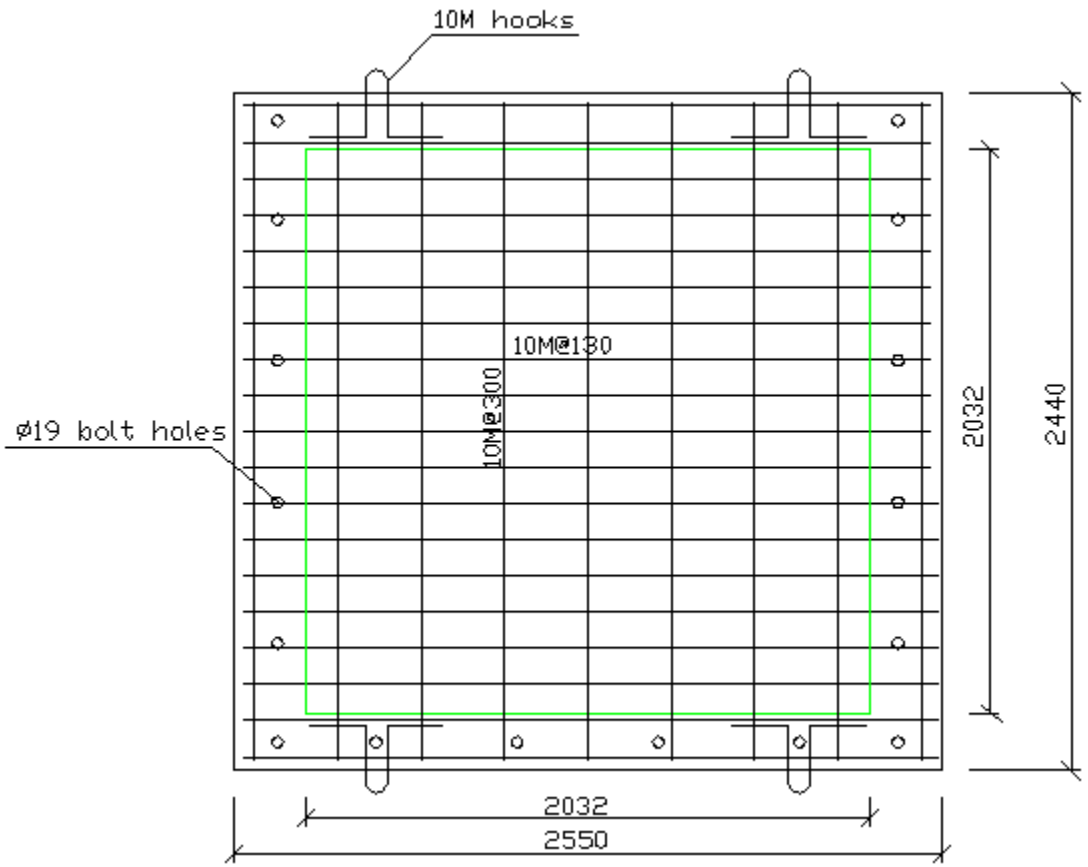


Figure 5.3: Reinforcement details for reinforced concrete walls
(all dimensions in mm)

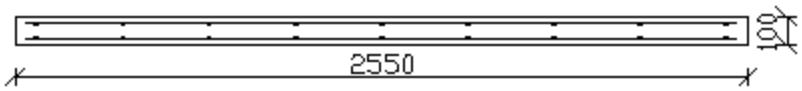


Figure 5.4: Cross section of wall

(all dimensions in mm)

Each wall specimen was subjected to 6 successive increasing blast pressures. The 6 imposed blast loads based on the driver pressure of the shock tube were 82.7 $kPa$, 206.8 $kPa$, 344.7 $kPa$, 448.2 $kPa$, 551.6 $kPa$, and 689.5 $kPa$. Ten (10) strain gauges were mounted on the reinforcing steel of each wall to record straining in the reinforcement at critical locations in the walls. Two (2) pressure sensors were placed near the side and bottom of the wall and were directly exposed to the blast loading to record the reflected pressures. Four (4) linear variable displacement transducers (LVDT) were mounted on the walls to monitor displacements.

### 5.2.2 Construction

The test specimens were constructed in the Structures Laboratory at the University of Ottawa. The reinforcing steel was supplied by a local company with the ends terminating in 180 degree bends for anchorage. The test specimens were constructed in following phases:

1. Construction of steel reinforcement cages
2. Construction of formwork
3. Installation of electrical resistance strain gauges on the steel cages
4. Concrete casting and curing of walls

The quantity, type and size of the reinforcing steel were selected prior to the construction of test specimens. The reinforcing steel was ordered to size with $180^{\circ}$ hooks at the ends with 70 mm of extension length beyond the hook. The 19 reinforcing bars placed in horizontal direction according to the tensile demand from hoop tension were spaced at approximately 130 mm. The 9 reinforcing bars placed in the vertical direction based on the moment analysis were spaced at approximately 300 mm. One layer of horizontal and vertical reinforcement were tied together to form a steel reinforcing cage. Each face of the walls contained one cage.

Formwork for the walls was constructed using $4' \times 8'$ plywood sheets of $3/4''$ thickness and $2'' \times 4''$wood studs. Wood screws were used to fasten the plywood and wood studs together for the formwork. The last step in preparing the formwork was to apply motor oil using a brush to facilitate the removal of formwork after casting. The wall reinforcing cages were then positioned within the formwork. The concrete clear cover for the top mat of steel reinforcement was maintained using plastic chairs, while small lengths of 10*M* diameter deformed steel rebar were used to maintain the clear cover for the bottom mat of steel reinforcement. The concrete cover was approximately 11 mm throughout. Thereafter, 16 PVC tubes with 19 mm diameter and 100 mm length were fastened to the formwork, along the side and bottom edges. The holes that remained at the locations of the PVC tubes after casting and removal of the formwork were used to bolt the walls to the shock tube and were also a component of the support conditions. A total of 14 strain gauges were placed on the horizontal and vertical reinforcing bars at prescribed locations to capture straining of the reinforcement at potential yield lines. The deformed reinforcing bars were made smooth using a grinder and cleaned with an acid and a base solution prior to applying the strain gauges. The strain gauges were then bonded to the reinforcing bars. After bonding, the strain gauge lead wires were insulated from the reinforcing steel using electrical tape. Two wires were then soldered to the strain gauge leads and insulated from each other using electrical tape. The wires were left outside of the formwork before casting, after which they were connected to the data acquisition system. The final measure taken was to protect the strain gauges and leads by wrapping them with a layer of electrical tape and applying a layer of silicone. Figure 5.5 illustrates the location of the strain gauges in the walls.

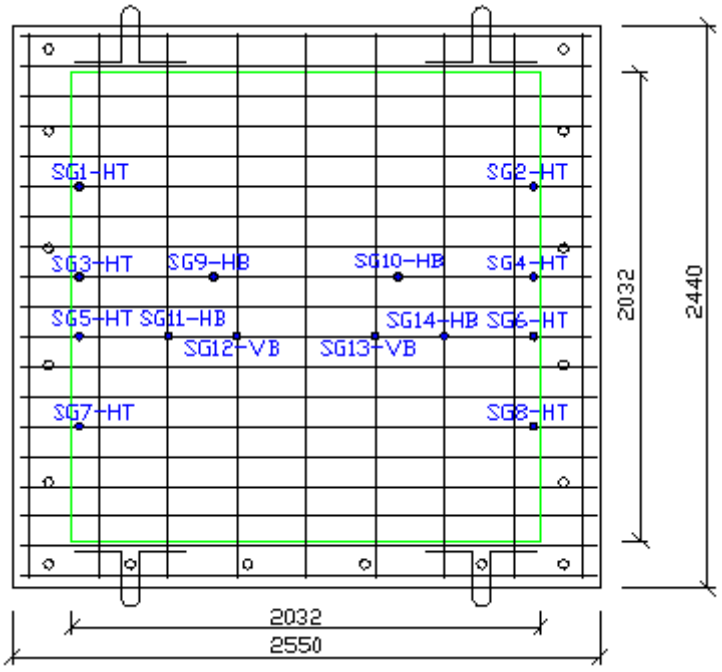


Figure 5.5: Location of strain gauges

(all dimensions in mm)

The formwork was kept moist with water prior to casting. A concrete vibrator was used to vibrate the concrete to prevent voids and ensure an even distribution of the concrete in the formwork. The walls were watered daily for seven days and covered with wet burlap to control shrinkage during curing. Figures 5.6 and 5.7 illustrate the steel cages placed in the formwork prior to casting and the wall during casting, respectively.

Figure 5.6: Wall specimen with reinforcement cage prior to casting

Figure 5.7: Reinforced concrete wall during casting

## 5.2.3 Material properties

### 5.2.3.1 Concrete

The two walls were constructed identically with a specified 28-day compressive strength of 31.5 $MPa$. The concrete for both walls contained 10 mm maximum size crushed limestone aggregates and a slump of 120 mm. The concrete strength of the specimens at the time of testing was approximately 36 $MPa$. A typical stress-strain relationship of the concrete is shown in Figure 5.8. The concrete strength was determined from an average of at least three standard cylinders with diameter of 100 *mm* and height of 200 *mm* using a Galdabini testing machine with a 600 $kN$ maximum capacity. Strain in the concrete was recorded automatically by the Galdabini testing machine.

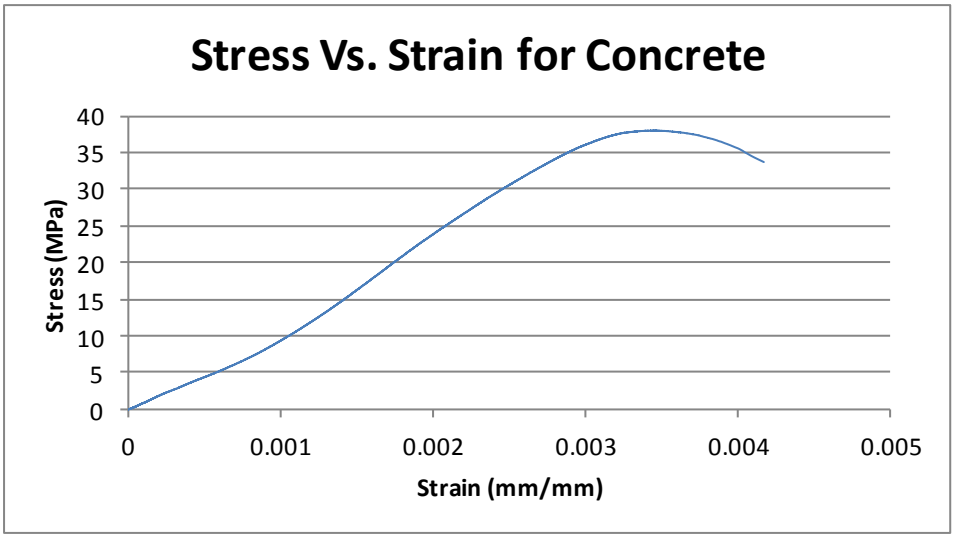


Figure 5.8: Typical stress-strain response for concrete

#### 5.2.3.2 Steel

The two wall specimens were constructed with 10$M$ (11.3 mm diameter) deformed steel with a yield strength of 465 $MPa$ and corresponding yield strain of 0.0026 mm/mm. A typical stress-strain relationship of the steel reinforcement is shown in Figure 5.9. The material properties were based on an average of three tensile coupon tests. The average ultimate strength of the steel reinforcement was 663 $MPa$ at an average ultimate strain of 0.125 mm/mm.

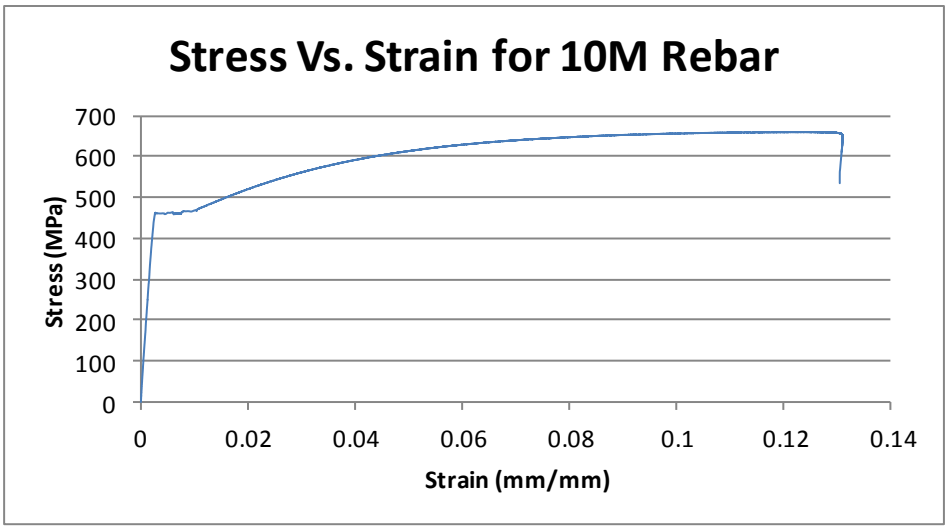


Figure 5.9: Typical stress-strain response for 10M reinforcement

## 5.3 Test Setup

### 5.3.1 Shock tube

The experimental program was conducted in the Structures Laboratory at the University of Ottawa. The blast simulator in the form of a shock tube is located in the subbasement of the Structures Laboratory. The shock tube testing facility is capable of simulating blast waves that are generated by the detonation of explosives. A wide range of pressure and impulse combinations may be produced by varying the pressure and the length of the driver section of the shock tube.

The shock tube testing facility at University of Ottawa (Figure 5.10) consists of four main components: (1) a variable length driver section with a double diaphragm firing mechanism (Figure 5.11); (2) a spool section used to control the firing with differential pressure (Figure 5.12); (3) an expansion section with sliding pressure relief vents (Figure 5.13); and (4) a rigid end test frame where test specimens are mounted (Figure 5.14). The operation of the shock tube involves charging the driver and spool sections simultaneously to the desired pressures using an air compressor. Thereafter the pressure from the spool section is drained. This results in a pressure differential between the driver and spool sections. The diaphragm that separates the two sections ruptures when this pressure differential exceeds the capacity of the diaphragm. This process triggers the firing and generation of the simulated blast load. Next, the diaphragm that separates the spool and expansion section ruptures as the pressurized air moves into the spool section. The highly pressurized air then travels through the expansion section towards the end of the shock tube where the test specimens are situated. Diaphragm combinations are chosen based on rupture pressures of the diaphragms and desired pressures in the driver (Lloyd et al. 2010). A more detailed summary of the operation and capabilities of the shock tube are described below.

Figure 5.10: Shock tube testing facility at University of Ottawa

Figure 5.11: Driver section of shock tube

Figure 5.12: Spool section of shock tube

Figure 5.13: Expansion section of shock tube

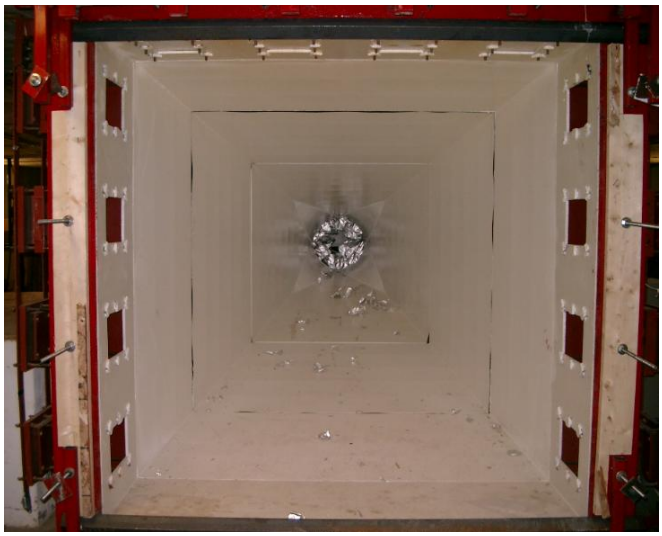

Figure 5.14: Frame section of shock tube

#### 5.3.1.1 Operation

The driver section is the main pressure vessel responsible for generating simulated blast pressure shock waves. The driver section is filled with pressurized gas and initially sealed by a diaphragm separating the driver and expansion section. Two diaphragms are employed in the operation of the shock tube to ensure the driver section is properly sealed when it is pressurized. The driver section consist of a series of 19 mm thick steel pipes, each with an inner diameter of 597 mm and outer diameter of 635 mm. The shock tube is made of six pipe sections of different lengths: two - 1525 mm in length, one - 915 mm in length, one - 610 mm in length, and two - 305 mm in length. The driver length varies from 305 mm to 5185 mm with 305 mm increments. Individual segments of pipe are combined together with twenty bolts. All of the bolt diameters are 31.75 mm. A steel plate with 12.5 mm thickness is bolted to one end of the driver section. The other end of the driver section is bolted to the spool section. The entire driver section is positioned on an inverted C-section steel tray (Lloyd et al. 2010).

The spool section is a disk holder. The flanges on the spool section are designed to mate with the flanges on the driver and the flange located between the spool and the beginning of the expansion section. The spool section is used to control firing with differential pressure (Lloyd et al. 2010). The spool section of 90 mm length is secured with bolts between the driver section and

the expansion section. Combinations of Grade 1100 aluminum diaphragms are placed between the driver-spool section and the spool-expansion section (Lloyd et al. 2010). The combinations of aluminum diaphragms are selected such that the differential pressure gradient across the driver-spool and spool-expansion sections is less than the specified rupture strength of the diaphragms for a specific driver pressure. This double diaphragm system ensures a safe and accurate control of the shock tube ignition system (Jacques 2011). The rupture strength of the diaphragms utilized during testing is presented in Table 5.1.

Table 5.1: Rupture strength of the diaphragms used during testing

| Aluminum diaphragm thickness | | Rupture strength | |
|---|---|---|---|
| *inches* | *mm* | *psi* | *kPa* |
| 3/1000" | 0.08 | 5 | 34.47 |
| 5/1000" | 0.13 | 8 | 55.16 |
| 8/1000" | 0.20 | 13 | 89.63 |
| 12/1000" | 0.30 | 20 | 137.90 |

An expansion section connects the driver and spool sections to the test frame. The testing frame, which is located at the end of the expansion section has an area of $2032\ mm \times 2032\ mm$, where specimens are placed for simulated blast testing (Lloyd et al. 2010). Twelve pressure relief vents are located at the end of the expansion section next to the test frame. These vents are controlled by the reflected pressure wave. The functions of these vents are to permit the development of the negative pressure phase and to reduce the magnitude of tertiary peaks caused by subsequent reflection of the shock wave within the shock tube. The testing frame is equipped with a 203 mm wide and 12.5 mm thick steel flange. This flange runs along the perimeter of the shock tube opening. Twenty circular bolt holes, each having a diameter of 19 mm, are distributed along the flange to provide a mechanism to secure the specimens to the shock tube (Jacques 2011).

#### 5.3.1.2 Range of operation

The shock tube has the capacity to stimulate blast-induced shock wave loading within a well-defined range of operational. A typical reflected pressure-driver pressure relationship and reflected impulse-driver pressure relationship generated during shock tube testing is provided in Figures 5.15 and 5.16, respectively. The operating range is defined in terms of peak reflected

pressure, reflected impulse and positive phase duration. The magnitude of shock wave reflected pressure is controlled by selecting an appropriate driver pressure, and the positive phase duration is controlled by the driver length. By selecting both driver length and driver pressure, the impulse imposed on the test specimens may be controlled.

The relationship between maximum reflected pressures versus driver pressures has been analyzed in a study conducted by Lloyd et al. (2010). The results illustrated that larger driver pressures resulted in larger reflected pressures. Figure 5.15 illustrates the relationship between reflected pressure and driver pressure with various driver lengths. The maximum reflected pressure achievable with the shock tube is approximately 100 $kPa$ (14.5 $psi$). Furthermore, the driver length only has a minor impact on the reflected pressure except for the smallest driver length. The reflected pressures were significantly lower at the smallest driver length relative to the trend from all other driver lengths.

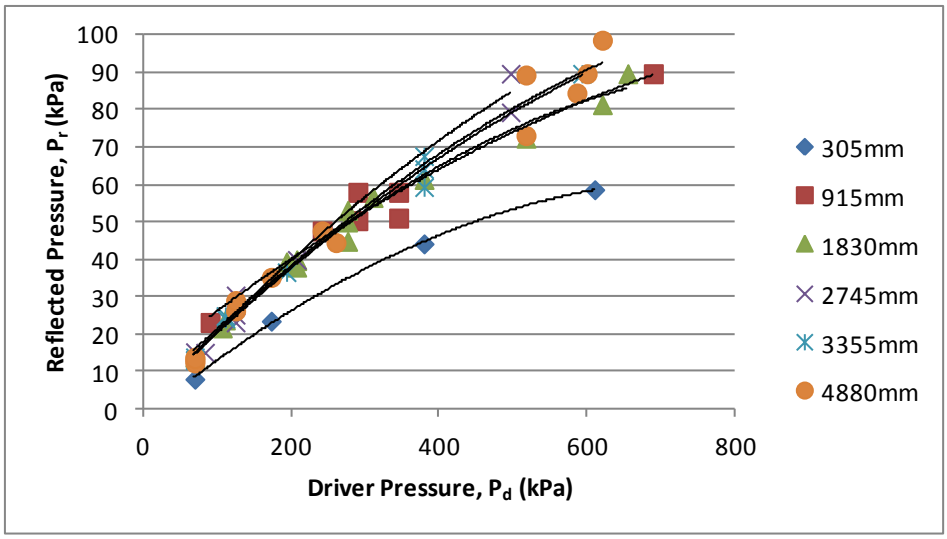


Figure 5.15: Reflected pressure-driver pressure relationship based on various driver lengths for shock tube (Lloyd et al. 2010)

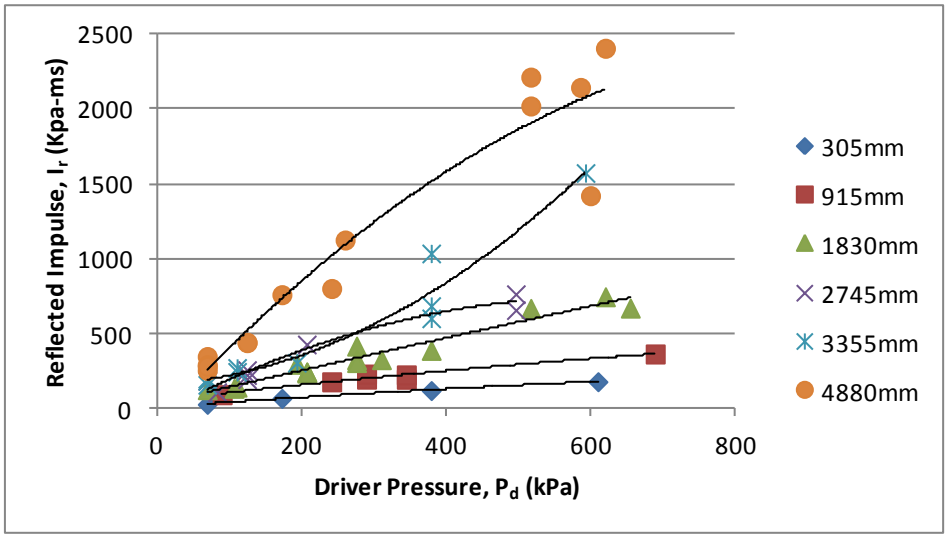


Figure 5.16: Reflected impulse-driver pressure relationship based on various driver lengths for shock tube (Lloyd et al. 2010)

This study also examined the relationship between the reflected impulses during the positive phase versus driver pressure. The results indicated that longer driver lengths produced shock waves with longer positive phase durations. Figure 5.16 provides the relationship between reflected impulse and driver pressure with various driver lengths. The maximum reflected impulse for the positive phase that can be achieved in the shock tube is approximately 2200 $kPa - ms$ (319 $psi - ms$). Maximum values for reflected pressures and corresponding impulses for five shock tube driver lengths were also provided in tabular form in the study.

Lloyd et al. (2010) reported that the shock tube is planar at the location of the testing frame; a deviation of only 8 % in the arrival time of the shock front was observed. In addition, it was determined in the study that the velocity of the shock wave front ranged between 340 m/s and 410 m/s. The velocity of wave front increases with an increase in driver pressure. Lloyd et al. (2010) also reported that the shock tube does not provide a sufficient testing apparatus for diffraction loading due to the low particle velocities associated with the shock wave.

## 5.3.2 Support conditions

### 5.3.2.1 Two-way bending wall behaviour

The 100 mm thick two-way bending wall was tested with the two opposite lateral sides fixed, the base edge hinged and the top edge free. Two $152\,mm \times 152\,mm \times 6.4\,mm$ hollow steel sections (HSS $152 \times 152 \times 6.4$) were used to fix the two opposite lateral sides of specimen to the shock tube testing frame. Twelve 19 mm diameter bolts were used to clamp together the HSS section with the test specimen and the test frame. In addition, four hollow steel sections with dimensions of $51\,mm \times 51\,mm \times 6.4\,mm$ (HSS $51 \times 51 \times 6.4$) were placed horizontally and in front of the test specimen and connected to the two $152\,mm \times 152\,mm \times 6.4\,mm$ hollow steel sections with eight-19 mm diameter bolts. The objective was to restrain rotation of the HSS $152 \times 152 \times 6.4$ steel sections to ensure the fixed boundary condition was achieved. One-$38\,mm \times 38\,mm \times 4.8\,mm$ angle was used on the front face of the specimen and one-$50\,mm \times 50\,mm \times 4.8\,mm$ angle on the back face of the specimen at the base to construct a hinged support condition. Holes were drilled in the angles corresponding to the locations of bolt holes in the flange of the shock tube test frame. At the base, the wall was clamped by bolting the wall between the back-to-back angles and shock tube test frame. Schematic details and the support conditions are illustrated in Figure 5.1 and Figure 5.17.

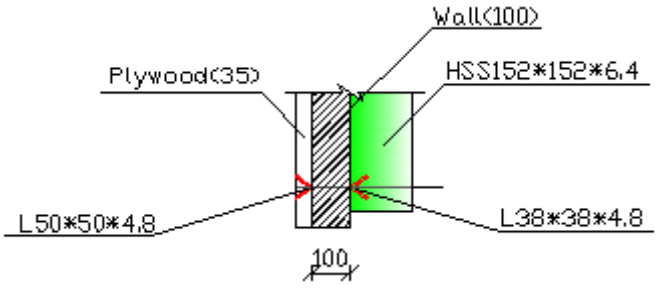


Figure 5.17: Pin connections at the base
(all dimensions in mm)

#### 5.3.2.2 One-way bending wall behaviour

The 100 mm thick one-way bending wall was tested with the two opposite lateral side edges fixed and free base and top edges. Two-$152\ mm \times 152\ mm \times 6.4\ mm$ hollow steel sections (HSS$152 \times 152 \times 6.4$) were used to fix the two opposite lateral sides of the specimen to the shock tube test frame with the aid of twelve-19 mm diameter bolts. In addition, six hollow steel sections (HSS $51 \times 51 \times 6.4$) were connected to the two $152\ mm \times 152\ mm \times 6.4\ mm$ hollow steel sections with twelve-19 mm diameter bolts to retrain the HSS$152 \times 152 \times 6.4$ from rotating. Schematic details of the support conditions are illustrated in Figure 5.2.

## 5.4 Instrumentation

The experimental data was recorded by a data acquisition system. It included: strain gauges to record the strains experienced by the reinforcement; piezoelectric dynamic pressure sensors to capture the reflected pressures imposed on the test specimens; and linear variable displacement transducers to monitor the displacement of the wall panels. In addition, a video recording system was used to record the wall response to blast loading.

### 5.4.1 Data acquisition system

The experimental data was recorded by a Yokogawa SL1000 High-Speed Data Acquisition Unit recording at *100,000 samples per second*. This data acquisition unit can lead to a sample being recorded every 10 $\mu s$. The SL1000 data acquisition unit was equipped to have the capacity to record ten strain channels and six low-voltage channels. Excitation was provided by a Kistler *24V*-16 channel power supply unit. The data acquisition unit and the high-speed video camera were triggered when one of the pressure sensors recorded a pressure which was greater than a predetermined threshold level. Data was recorded for 1 *s* with a pre-trigger time of 0.1 *s*. The experimental data from the SL1000 data acquisition unit was saved to a Windows PC. A second PC was used to run the high-speed camera which was used to monitor and record shock wave propagation and structural response subjected to blast loading.

#### 5.4.1.1 Strain gauges

Each wall was instrumented with strain gauges located on selected vertical and horizontal reinforcing bars to record the strain-time histories. Tokyo Sokki Kenkyujo Co., Ltd. FLA-6-350-11 (350 $\Omega$) electrical resistance strain gauges of 6 mm length were used. The location of the strain gauges was based on an assumed line yield line pattern for Wall 1. Twelve strain gauges were placed on the horizontal reinforcing bars and two strain gauges were placed on vertical reinforcing bars in each wall at various locations along the width and height (see Figure 5.4). Eight of the strain gauges were located on four of the horizontal reinforcing bars (five gauges connected to the data acquisition) near the assumed negative yield lines at the sides of the walls. The remaining six strain gauges were located on two horizontal reinforcing bars (four gauges connected to the data acquisition) and two vertical reinforcing bars (one gauge connected to the data acquisition) near the predicted positive yield lines. The strain-time histories from the gauges were used to determine the degree of yielding of the reinforcement.

#### 5.4.1.2 Piezoelectric dynamic pressure sensors

The reflected pressure-time histories experienced by the wall specimens and resulting from the shock wave were measured with two independent dynamic piezoelectric pressure sensors (PCB Piezotronics Model #112A22). The pressure sensors were placed within the expansion section of the shock and 50 mm from the wall specimens. One sensor was placed near the bottom of the shock tube opening and the other near mid-height.

#### 5.4.1.3 Linear variable displacement transducers

One type of linear variable displacement transducer (LVDT), namely Celesco CLWG – 300, was used to measure the displacements of the two RC walls. The LVDTs were connected to the walls at one end and to a support stand at the other end in a manner that permitted rotation of the LVDTs at both ends. The LVDTs were installed on the walls using aluminum brackets and were supported on rigid shoring jacks. Each LVDT was calibrated prior to the first blast shot on each specimen.

Figure 5.18 shows the LVDTs attached to one of the walls. Four Celesco CLWG – 300 LVDTs with a stroke of 300 mm were used during testing. The LVDTs were connected where maximum displacements were expected to occur, such as at mid-span and along yield lines. In addition, LVDTs were also placed near the supports. Figure 5.19 shows the four LVDTs attached to Wall 1: LVDT-Top at the maximum displacement location; LVDT-Mid at mid-span; LVDT-Rig along the assumed positive yield line; and LVDT-Lef near the left support. Figure 5.20 illustrates the four LVDTs attached to Wall 2: LVDT-Mid and LVDT-Bot at the maximum displacement locations; and LVDT-Lef and LVDT-Rig approximately half the distance from the maximum displacement location to the edges of the fixed supports.

Figure 5.18: LVDTs attached to wall specimen

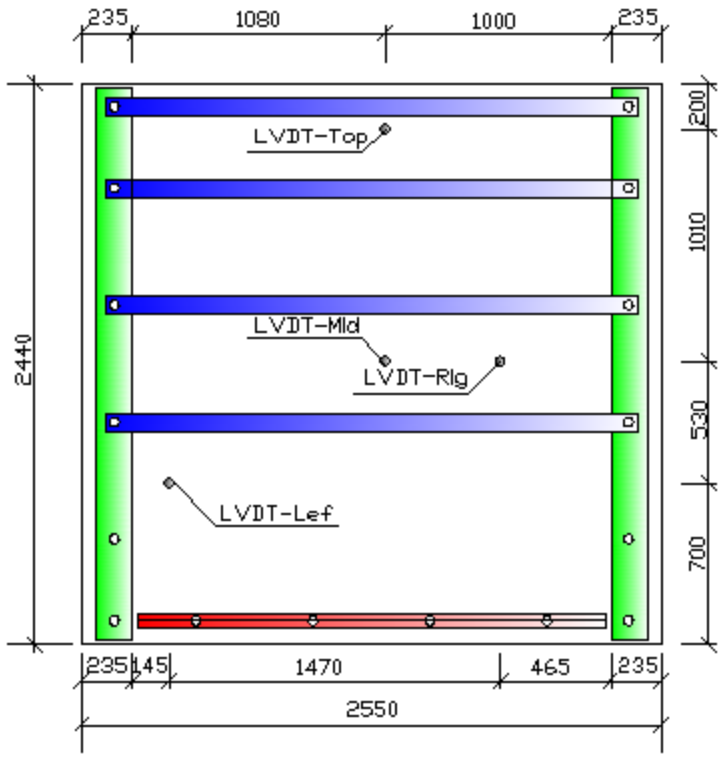


Figure 5.19: LVDT locations for Wall 1

(all dimensions in mm)

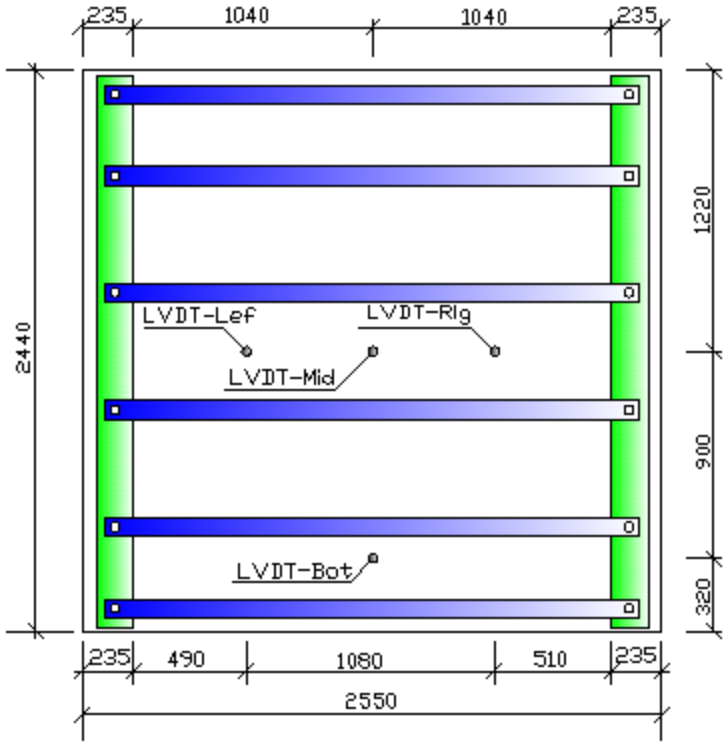


Figure 5.20: LVDT locations for Wall 2

(all dimensions in mm)

### 5.4.2 Video recording system

The wall specimens were attached directly over the end frame of the shock tube; therefore, a uniformly distributed pressure was applied directly on the specimens. A high-speed video camera was placed at the side of the walls during testing, and recorded the response of the walls to blast loading at a maximum of 1000 *frames per second* with a resolution of 800 × 600 pixels. The camera was triggered by the SL1000 data acquisition unit. Three 1000 W studio lights were used to lighten the specimens. The high-speed camera was monitored by a windows PC. The camera was located 2500 mm from the edge of the wall in each test. The displacement profile of the specimens under smaller blast pressures was recorded by the above mentioned camera location. However, the camera was located further away from the shock tube when the specimens were subjected to higher and destructive blast pressures.

## 5.5 Test Procedure and Loading Program

### 5.5.1 Test procedure

The two wall specimens were bolted to the shock tube to simulate two different boundary conditions: two-way and one-way bending behaviours. As a result of the different boundary conditions, the damage level experienced by the two walls were not necessarily similar for the various test blast pressures applied on walls. Six blast tests with different reflected pressures and impulses were imposed on each specimen. The following procedure was typically followed during the blast testing:

(1) Install the supports prior to mounting the walls into position;
(2) Position the walls at the end of the shock tube to complete the installation of the support conditions;
(3) Install the instrumentation: connect the strain gauge lead wires to the data acquisition unit; connect the four LVDTs; adjust the high-speed camera and studio lights; and calibrate the data acquisition system;

(4) Select the appropriate driver length and aluminum foils according to the desired reflected pressure and reflected impulse;
(5) Conduct a trigger check prior to each specimen test to ensure the data acquisition system was properly configured; and
(6) Photograph the specimens before and after each blast test to document progression of damage.

### 5.5.2 Test program

The objective of the test program was to compare the blast performance of reinforced concrete reservoir walls with different support conditions. The first setup included two fixed opposite lateral sides, hinged base and free top edge. The second setup consisted of two fixed opposite lateral sides, and free bottom and top edges. The two wall specimens were exposed to same driver length (4880 mm) with the six different blast tests. However, given the different boundary conditions for the two walls, the test results were different. The same blast test generated different levels of damage for the different boundary conditions. A number of the blast tests were intended to promote elastic response, while others were intended to push the walls into the inelastic range. Tables 5.2 and 5.3 provide the different blast tests for each wall specimen, including driver pressure, and reflected pressures and impulses experienced by the walls. In addition, corresponding scaled distances, standoff distances and equivalent charge weight are also included, which correspond to the tests on the specimens.

Table 5.2: Blast wave characteristics for Wall 1

| Test order | Driver pressure $P_d$ $kPa$ | Reflected pressure $P_r$ $kPa$ | Reflected impulse $I_r$ $kPa-ms$ | TNT charge weight $W$ $kg$ | Stand-off distance $R$ $m$ | Scaled distance $Z$ $m/kg^{1/3}$ |
|---|---|---|---|---|---|---|
| 1 | 82.7 | 12.1 | 244.1 | 1064.5 | 208.9 | 20.5 |
| 2 | 209.6 | 41.9 | 751.1 | 1881.3 | 101.0 | 8.2 |
| 3 | 352.3 | 59.4 | 1245.2 | 4470.3 | 108.3 | 6.6 |
| 4 | 448.8 | 72.5 | 1267.6 | 3207.3 | 86.4 | 5.9 |
| 5 | 556.4 | 77.2 | 1900.1 | 9630.0 | 120.3 | 5.7 |
| 6 | 717.1 | 100.9 | 2369.2 | 12789.1 | 115.5 | 4.9 |

Table 5.3: Blast wave characteristics for Wall 2

| Test order | Driver pressure $P_d$ $kPa$ | Reflected pressure $P_r$ $kPa$ | Reflected impulse $I_r$ $kPa-ms$ | TNT charge weight $W$ $kg$ | Stand-off distance $R$ $m$ | Scaled distance $Z$ $m/kg^{1/3}$ |
|---|---|---|---|---|---|---|
| 1 | 117.2 | 22.4 | 367.8 | 854.8 | 120.5 | 12.7 |
| 2 | 212.4 | 41.0 | 670.6 | 1402.1 | 92.9 | 8.3 |
| 3 | 351.6 | 64.8 | 1102.2 | 2625.7 | 86.2 | 6.2 |
| 4 | 406.8 | 66.2 | 1304.1 | 4166.2 | 99.2 | 6.2 |
| 5 | 552.3 | 89.0 | 1794.7 | 6667.4 | 98.9 | 5.3 |
| 6 | 710.8 | 100.1 | 2122.4 | 9299.5 | 104.2 | 5.0 |

# Chapter 6 Experimental Results

## 6.1 General

This chapter presents experimental results recorded from the shock tube-induced blast loading applied on the two RC reservoir walls and the observed behaviour of the two specimens. Six successive blast tests with the same driver length and varying driver pressures were imposed on each specimen. The results presented herein include the reflected pressure, reflected impulse, displacement, and reinforcement strain-time histories. Both wall specimens were instrumented with 10 strain gauges on the reinforcement; however, only the strains recorded from gauges SG9-HB and SG10-HB are illustrated in this chapter. The data recorded from the remaining strain gauges are provided in Appendix B and Tables 6.5 and 6.6. Photos showing the extent of the damage after each test are also provided. Lastly, comparisons between wall one and two are presented in this chapter.

As part of this test program, each wall was subjected to multiple blast pressures. This permitted for additional test data to be collected. Previous tests result in the accumulation of damage, which causes a reduction in the stiffness of the test specimens and, therefore, an increase in the displacements relative to a specimen tested in its virgin condition.

## 6.2 Wall Specimen 1

Specimen one was supported to promote two-way bending action. The two opposite lateral sides of the wall were fixed, the base edge was hinged and the top edge was free. It was assumed that the side supports were fully fixed. The wall was subjected to six successive blast tests with increasing driver pressures while maintaining a constant driver length. The progression of damage after each blast test is illustrated in Figures 6.4, 6.8, 6.12, 6.16, 6.20 and 6.24. A summary of the experimental results including shock tube firing parameters and shock wave properties are listed in Table 6.1. A summary of maximum displacements, maximum support

rotations and residual displacements measured by the four LVDTs is available in Table 6.3, and a summary of the reinforcement strain gauge data is provided in Table 6.5.

### 6.2.1 Blast Test 1

The first blast test was generated with a driver length of *4880 mm* and a driver pressure of *82.7 $kPa$*. The resulting shock wave had a peak reflected pressure of *12.1 $kPa$,* reflected impulse of *244.1$kPa-ms$* and positive phase duration of *43.2 $ms$*. The reflected pressure was recorded by a pressure transducer located on the right side of the expansion section of the shock tube and 50 mm from the wall specimen. This pressure transducer was situated near the mid height level of the wall specimen. The maximum displacement recorded by Top LVDT was *1.44 mm* (maximum support rotation of *0.08*° relative to the right side fixed edge) which occurred at a time of *14.6 $ms$*. The rotation was determined by dividing the displacement recorded by Top LVDT by the distance of the LVDT to the right support of the specimen. The maximum residual displacement from Top LVDT was *0.58 mm*. The reflected pressure- and impulse-time histories are presented in Figure 6.1. The displacement-time histories recorded by the LVDTs are plotted in Figure 6.2. Note that due to problems with the instrumentation, the results for LVDT designated "right" are omitted in the results presented for Wall 1.

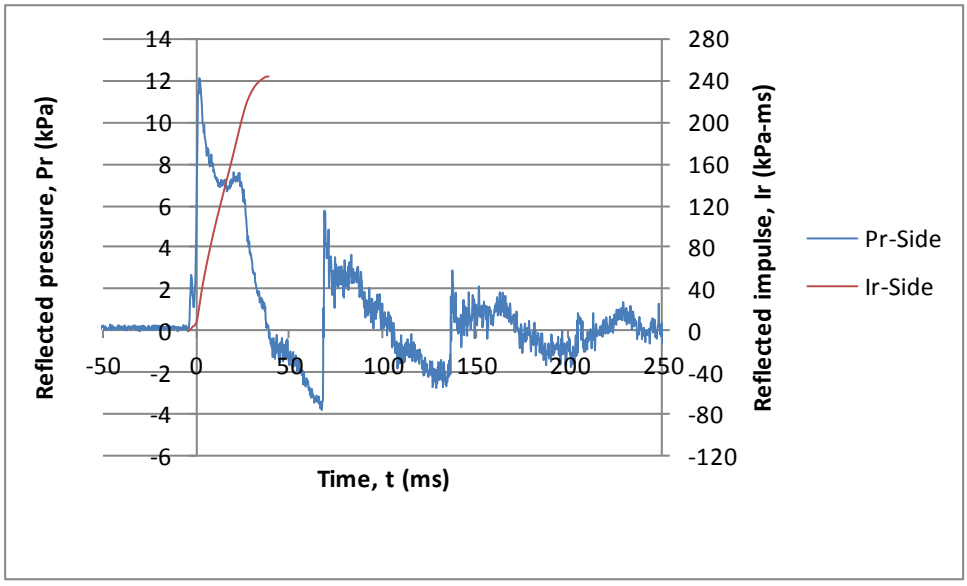


Figure 6.1: Test 1 reflected pressure- and impulse-time histories for Wall 1

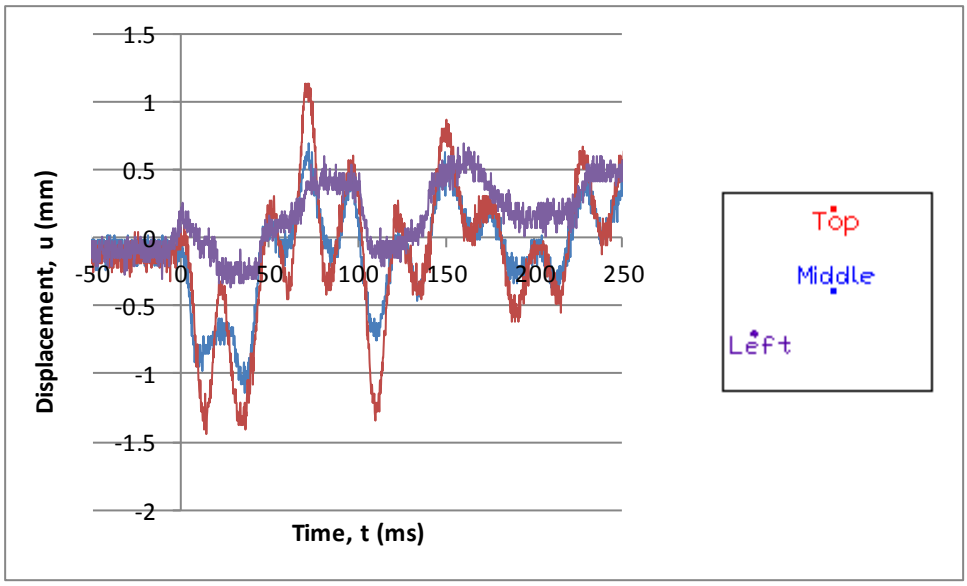


Figure 6.2: Test 1 displacement-time histories of Wall 1

The strain recorded by Gauge SG9-HB located at 1/3$^{rd}$ of the width of the wall from the side support and at mid height was *0.0043 %* at a time of *12.8 ms*, corresponding to a strain-rate of *0.0034* $s^{-1}$. The residual strain recorded by Gauge SG9-HB was *-0.0005 %*. The strain captured by Gauge SG10-HB positioned at 1/3$^{rd}$ of the width of the wall and at mid height was *0.0064 %* at a time of *10.2 ms*, corresponding to a strain-rate of *0.0063* $s^{-1}$. The residual strain in Gauge SG10-HB was *-0.0001 %*. The strain-time histories for Gauges SG9-HB and SG10-HB for test 1 of Wall 1 are shown in Figure 6.3.

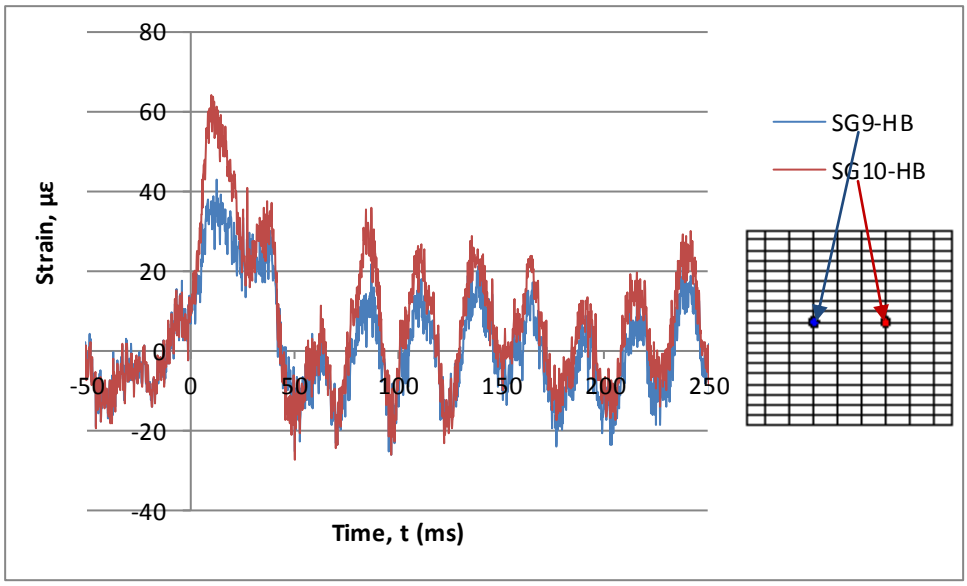


Figure 6.3: Test 1 strain-time histories for Gauges SG9-HB and SG10-HB of Wall 1

The wall remained elastic after the first test and no damage or cracking was observed. The condition of Wall 1 after this test is illustrated in Figure 6.4.

Figure 6.4: Condition of Wall 1 after test 1

### 6.2.2 Blast Test 2

The second blast test was generated with a driver length of *4880 mm* and a driver pressure of *209.6 kPa*. The resulting shock wave had a peak reflected pressure of *41.9 kPa*, reflected impulse of *751.1 kPa − ms* and positive phase duration of *52.2 ms*. The maximum displacement recorded by Top LVDT was *5.34 mm* (maximum support rotation of *0.31°*) which occurred at a time of *17.4 ms*. The maximum residual displacement from Left LVDT was *0.45 mm*. The reflected pressure- and impulse-time histories are presented in Figure 6.5. The displacement-time histories for the LVDTs are illustrated in Figure 6.6.

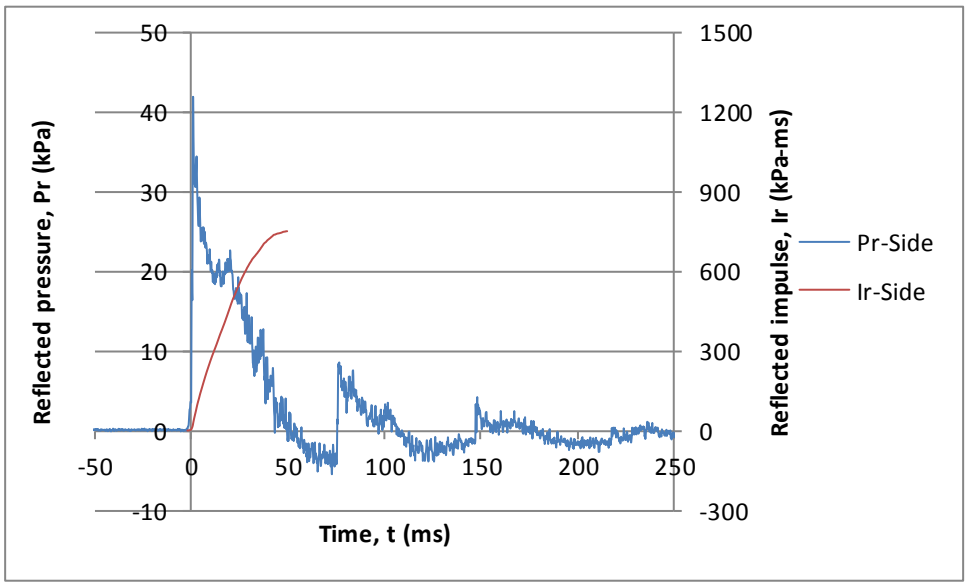


Figure 6.5: Test 2 reflected pressure- and impulse-time histories for Wall 1

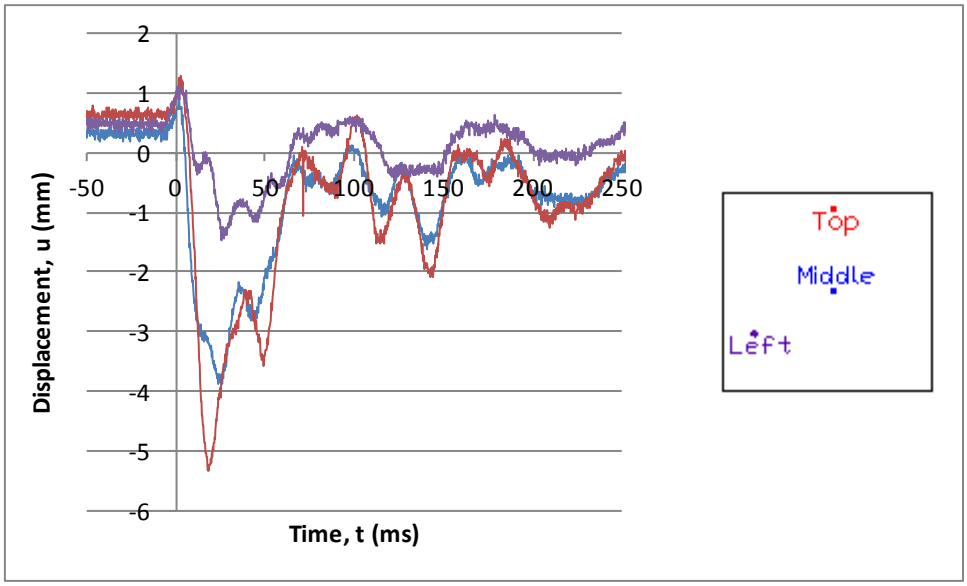


Figure 6.6: Test 2 displacement-time histories of Wall 1

The strain recorded by Gauge SG9-HB was *0.0140 %* at a time of *15.0 ms*, corresponding to a strain-rate of *0.0094* $s^{-1}$. The residual strain in Gauge SG9-HB was *0.0026 %*. The strain captured by Gauge SG10-HB was *0.0412 %* at a time of *21.6 ms*, corresponding to a strain-rate of *0.0191* $s^{-1}$. The residual strain in Gauge SG10-HB was *0.0199 %*. The strain-time histories for Gauges SG9-HB and SG10-HB for test 2 of Wall 1 are shown in Figure 6.7.

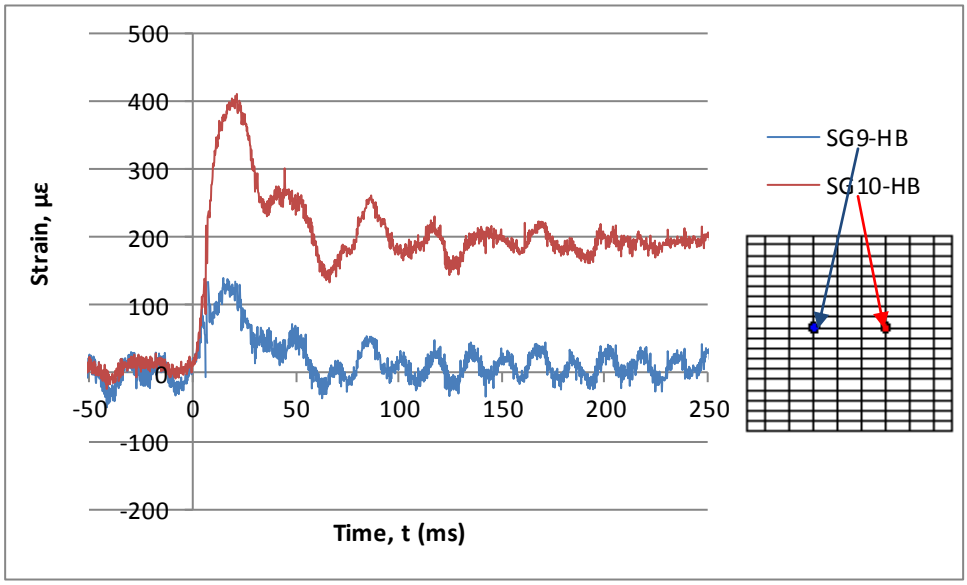


Figure 6.7: Test 2 strain-time histories for Gauges SG9-HB and SG10-HB of Wall 1

Several cracks surfaced after this test. Four vertical cracks formed and were concentrated in the middle one-third of the width of the wall. The maximum crack length was $1600\ mm$ and the shortest length was $600\ mm$. A single horizontal crack was evident at the bottom one-third of the height of the wall. The length of the crack was $1060\ mm$. The extent of damage to Wall 1 after this test is illustrated in Figure 6.8.

Figure 6.8: Condition of Wall 1 after test 2

### 6.2.3 Blast Test 3

The third blast test was generated with a driver length of *4880 mm* and a driver pressure of *352.3* $kPa$. The resulting shock wave had a peak reflected pressure of *59.4* $kPa$, reflected impulse of *1245.2* $kPa - ms$ and positive phase duration of *56.6* $ms$. The maximum displacement recorded by Top LVDT was *11.31 mm* (maximum support rotation *0.65°*) which occurred at a time of *20.0* $ms$. The maximum residual displacement from Left LVDT was *1.10 mm*. The reflected pressure- and impulse-time histories are presented in Figure 6.9. The displacement-time histories for the LVDTs are illustrated in Figure 6.10.

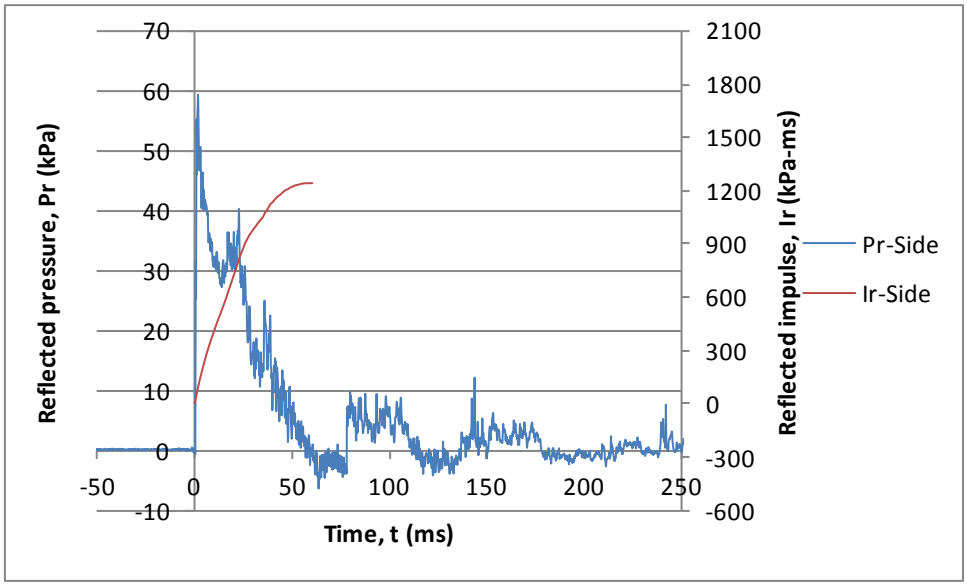


Figure 6.9: Test 3 reflected pressure- and impulse-time histories for Wall 1

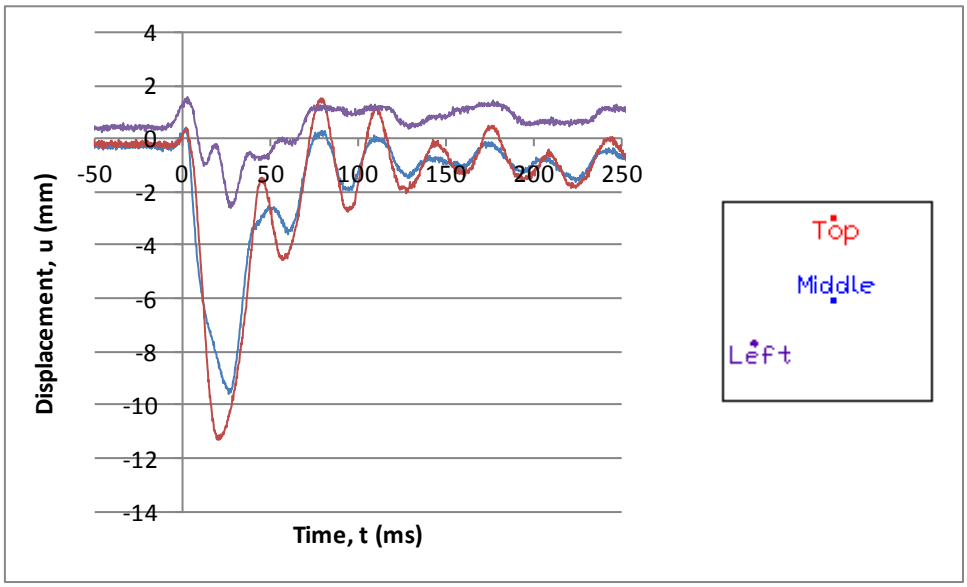


Figure 6.10: Test 3 displacement-time histories of Wall 1

The strain recorded by Gauge SG9-HB was *0.0638 %* at a time of *23.8 ms*, corresponding to a strain-rate of *0.0268* $s^{-1}$. The residual strain in Gauge SG9-HB was *0.0193 %*. The strain captured by Gauge SG10-HB was *0.1052 %* at a time of *24.2 ms*, corresponding to a strain-rate of *0.0435* $s^{-1}$. The residual strain in Gauge SG10-HB was *0.0357 %*. The strain-time histories for Gauges SG9-HB and SG10-HB for test 3 of Wall 1 are shown in Figure 6.11.

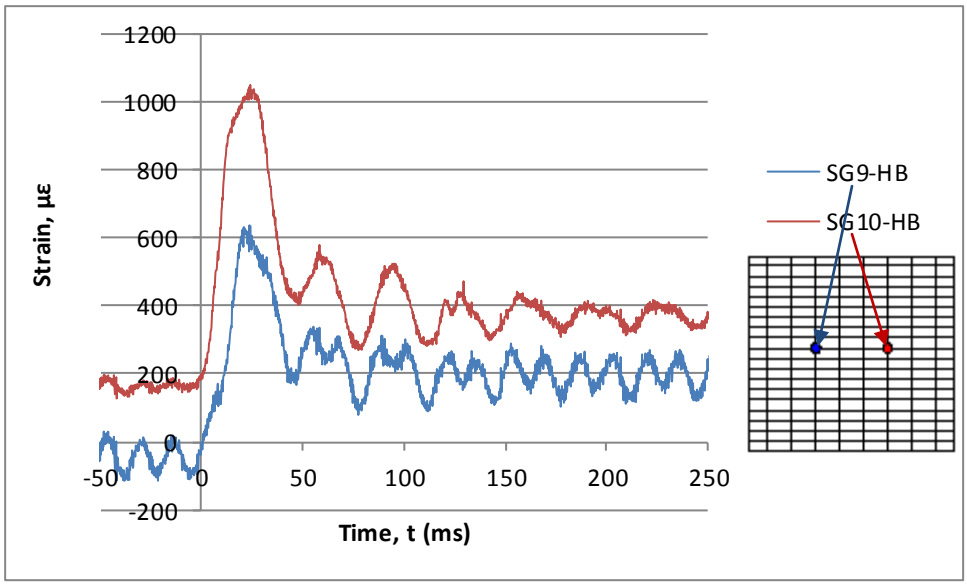


Figure 6.11: Test 3 strain-time histories for Gauges SG9-HB and SG10-HB of Wall 1

After this test, five cracks at an angle of 45° developed and propagated from the bottom one-third of the wall height towards the center of the wall. One and four cracks surfaced on the left and the right sides of the centerline of the wall, respectively. Their lengths were between $600 - 1050\ mm$. Two vertical cracks also formed; one of them was $1080\ mm$ in length and surfaced at the top one-third of the height of the wall, while the other was $620\ mm$ in length and was situated in the middle one-third of the height of the wall. One horizontal crack became visible at the middle one-third of the wall height and had a length of $600\ mm$. The horizontal cracks intersected with the 45° inclined cracks. The extent of damage to Wall 1 after this test is illustrated in Figure 6.12.

Figure 6.12: Condition of Wall 1 after test 3

### 6.2.4 Blast Test 4

The fourth blast test was generated with a driver length of *4880 mm* and a driver pressure of *448.8* $kPa$. The resulting shock wave had a peak reflected pressure of *72.5* $kPa$, reflected impulse of *1267.6* $kPa-ms$ and positive phase duration of *60.4* $ms$. The maximum displacement recorded by Top LVDT was *15.22 mm* (maximum support rotation *0.87*°) which occurred at a time of *22.2* $ms$. The maximum residual displacement from Left LVDT was *1.97 mm.* The reflected pressure- and impulse-time histories are presented in Figure 6.13. The displacement-time histories for the LVDTs are illustrated in Figure 6.14.

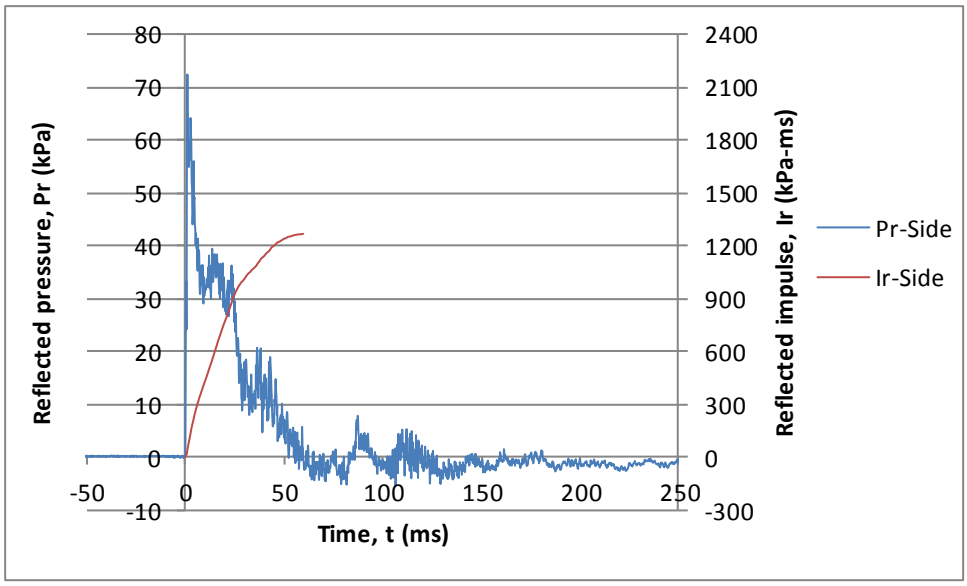


Figure 6.13: Test 4 reflected pressure- and impulse-time histories for Wall 1

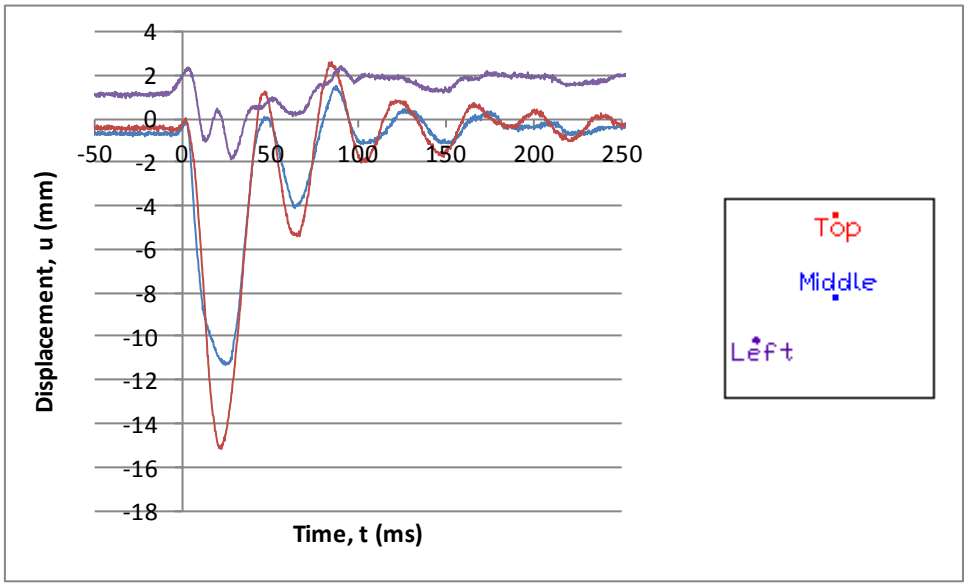


Figure 6.14: Test 4 displacement-time histories of Wall 1

The strain recorded by Gauge SG9-HB was *0.1098 %* at a time of *21.2 ms*, corresponding to a strain-rate of *0.0518* $s^{-1}$. The residual strain in Gauge SG9-HB was *0.0338 %*. The strain captured by Gauge SG10-HB was *0.1432 %* at a time of *13.2 ms*, corresponding to a strain-rate of *0.1085* $s^{-1}$. The residual strain in Gauge SG10-HB was *0.0454 %*. The strain-time histories for Gauges SG9-HB and SG10-HB for test 4 of Wall 1 are shown in Figure 6.15.

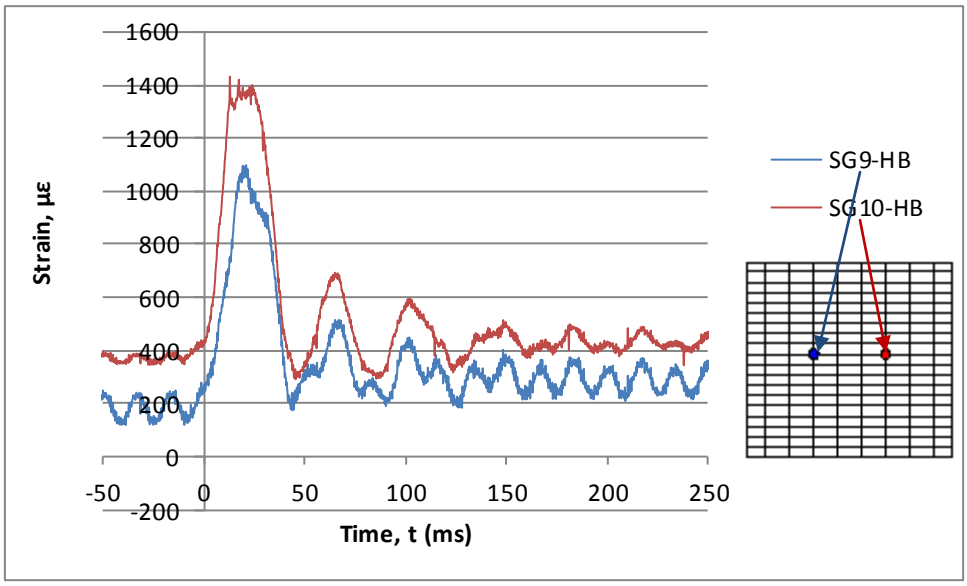


Figure 6.15: Test 4 strain-time histories for Gauges SG9-HB and SG10-HB of Wall 1

After the fourth test, the existing vertical and horizontal cracks extended further in length. Three new cracks formed at angles of 45°. Their lengths ranged from $250 - 400\ mm$. For the vertical cracks, the maximum length exceeded $1800\ mm$, while the longest horizontal crack was more than $1500\ mm$ in length. For the 45° inclined cracks, the maximum length was approximately $1600\ mm$. The extent of damage in Wall 1 after this test is illustrated in Figure 6.16.

Figure 6.16: Condition of Wall 1 after test 4

### 6.2.5 Blast Test 5

The fifth test was generated with a driver length of *4880 mm* and a driver pressure of *556.4 $kPa$*. The resulting shock wave had a peak reflected pressure of *77.2 $kPa$,* reflected impulse of *1900.1 $kPa-ms$* and positive phase duration of *64.6 $ms$*. The maximum displacement recorded by Top LVDT was *26.38 mm* (maximum support rotation *1.51°*) which occurred at a time of *26.8 $ms$*. The maximum residual displacement from Top LVDT was *3.33 mm*. The reflected pressure- and impulse-time histories are presented in Figure 6.17. The displacement-time histories for the LVDTs are illustrated in Figure 6.18.

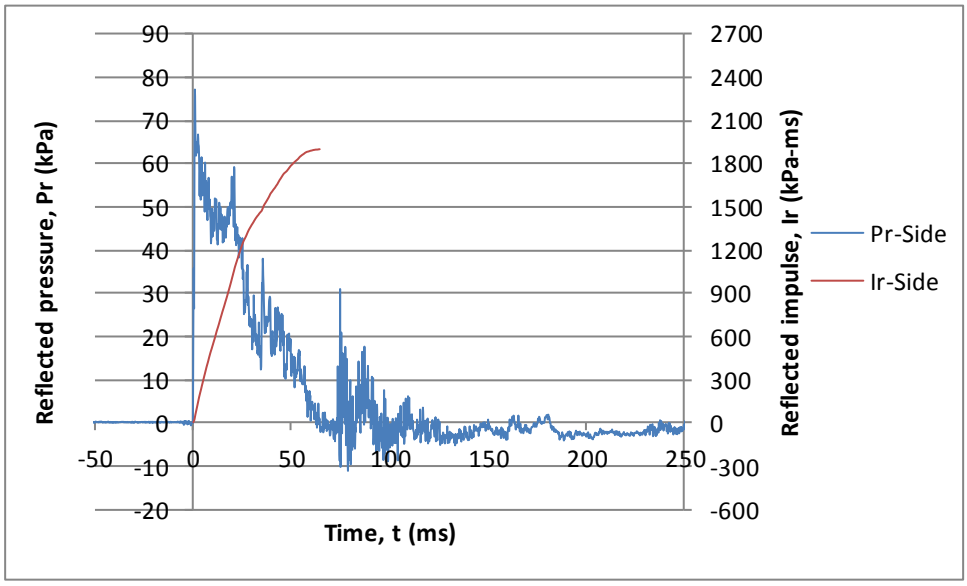


Figure 6.17: Test 5 reflected pressure- and impulse-time histories for Wall 1

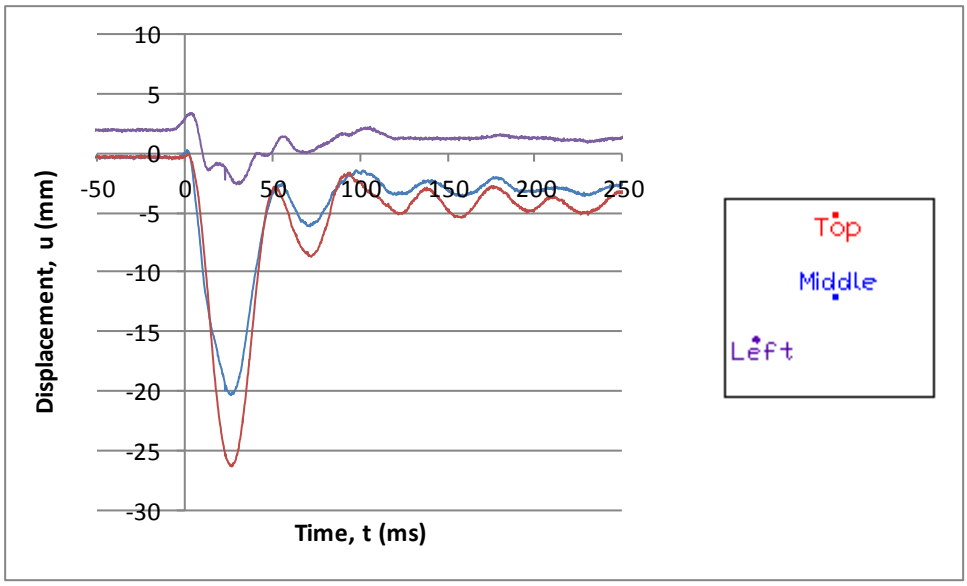


Figure 6.18: Test 5 displacement-time histories of Wall 1

The strain recorded by Gauge SG9-HB was *0.1801 %* at a time of *24.2 ms*, corresponding to a strain-rate of *0.0744* $s^{-1}$. The residual strain in Gauge SG9-HB was *0.0444 %*. The strain captured by Gauge SG10-HB was *0.2567 %* at a time of *26.6 ms*, corresponding to a strain-rate of *0.0965* $s^{-1}$. The residual strain in Gauge SG10-HB was *0.0692 %*. The strain-time histories for Gauges SG9-HB and SG10-HB for test 5 of Wall 1 are shown in Figure 6.19. The green horizontal dashed line highlights the yield strain of the reinforcement.

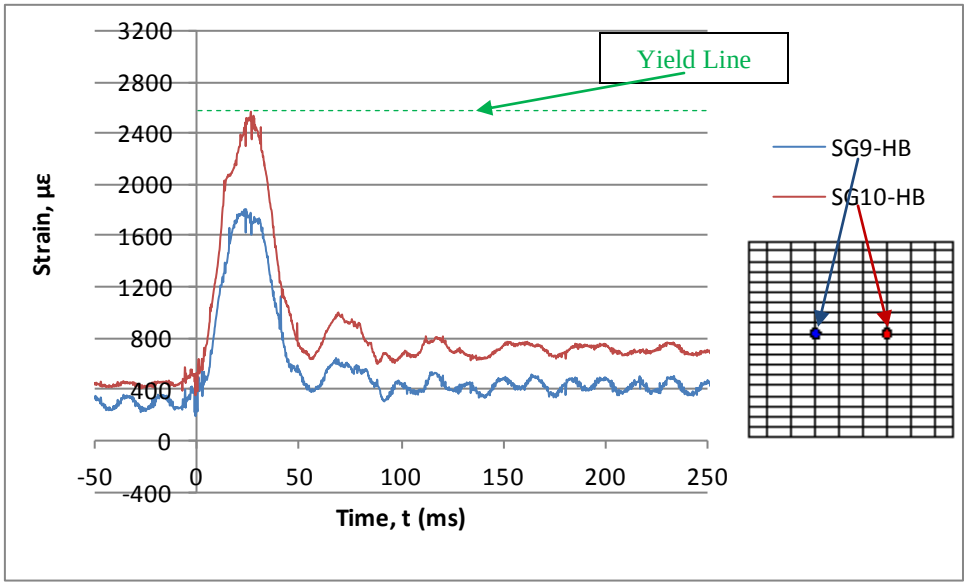


Figure 6.19: Test 5 strain-time histories for Gauges SG9-HB and SG10-HB of Wall 1

Additional cracking inclined at 45° surfaced after this test. They extended from the bottom-right and bottom-left corners towards the top of the wall. Existing vertical cracks further propagated and extended to the top and bottom of the wall. New cracking became evident in the horizontal direction. Five of the 45° angle cracks were located near the left corner and the other five 45° angle cracks were concentrated at the right corner of the wall. All of the 45° angle cracks travelled from the bottom of the wall towards the top area of the wall. The extent of damage to Wall 1 after this test is illustrated in Figure 6.20.

Figure 6.20: Condition of Wall 1 after test 5

### 6.2.6 Blast Test 6

The sixth test was generated with a driver length of *4880 mm* and a driver pressure of $717.1\ kPa$. The resulting shock wave had a peak reflected pressure of $100.9\ kPa$, reflected impulse of $2369.2\ kPa - ms$ and positive phase duration of $61.4\ ms$. The maximum displacement recorded by Top LVDT was *34.59 mm* (maximum support rotation *1.98*°) which occurred at a time of $28.2\ ms$. The maximum residual displacement from Top LVDT was *3.63 mm.* The reflected pressure- and impulse-time histories are presented in Figure 6.21. The displacement-time histories for the LVDTs are illustrated in Figure 6.22.

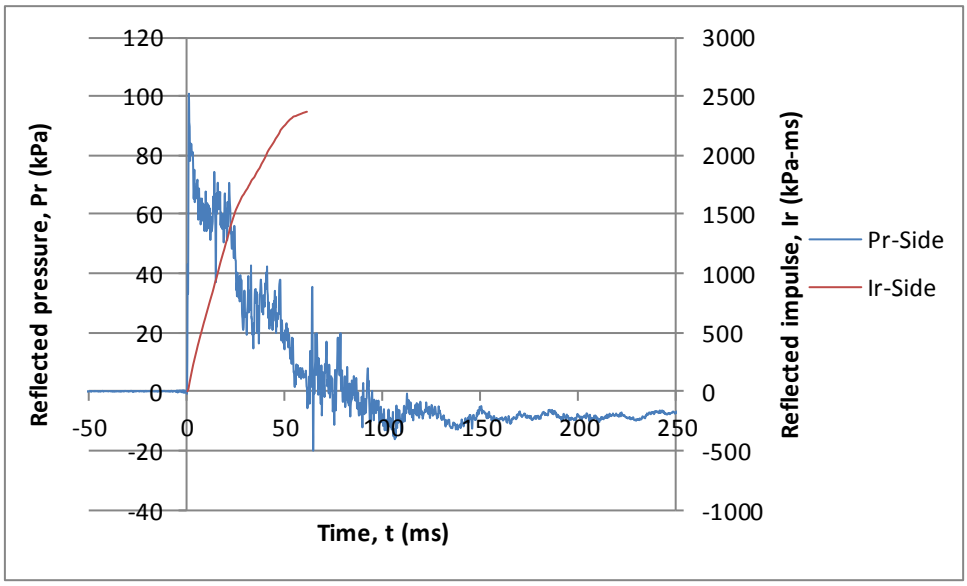


Figure 6.21: Test 6 reflected pressure- and impulse-time histories for Wall 1

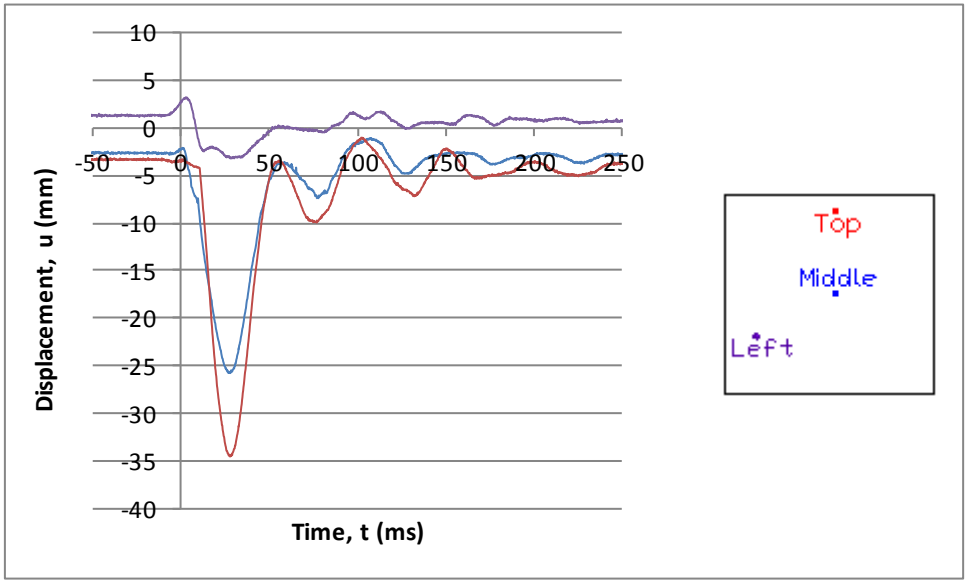


Figure 6.22: Test 6 displacement-time histories of Wall 1

The strain recorded by Gauge SG9-HB was *0.2507 %* at a time of *25.6 ms*, corresponding to a strain-rate of *0.0979* $s^{-1}$. The residual strain in Gauge SG9-HB was *0.0594 %*. The strain captured by Gauge SG10-HB was *0.3834 %* at a time of *27.2 ms*, corresponding to a strain-rate of *0.1410* $s^{-1}$. The residual strain in Gauge SG10-HB was *0.1459 %*. The strain-time histories for Gauges SG9-HB and SG10-HB for test 6 of Wall 1 are shown in Figure 6.23. The green horizontal dashed line highlights the yield strain of the reinforcement.

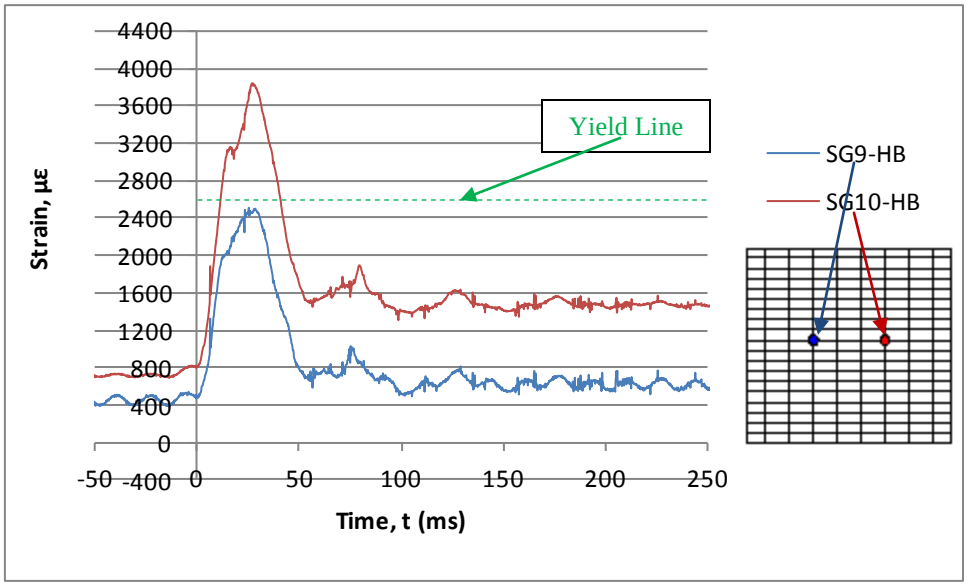


Figure 6.23: Test 6 strain-time histories for Gauges SG9-HB and SG10-HB of Wall 1

Most of the existing cracks developed further in length and width. The vertical cracks within the middle one-third of the wall width had the largest widths. Many of the 45° angle cracks extended further from the bottom left and right corners of the wall upwards to the top of the specimen. The extent of damage to Wall 1 after this test is illustrated in Figure 6.24.

Figure 6.24: Condition of Wall 1 after test 6

## 6.3 Wall Specimen 2

Specimen 2 was supported to promote one-way bending action. The two opposite lateral sides of the wall were fixed, while the base and top edges were free. It was assumed that the side supports were fully fixed. The wall was subjected to six successive blast tests with increasing driver pressures while maintaining a constant driver length. The progression of damage after each test is illustrated in Figures 6.28, 6.32, 6.36, 6.40, 6.44 and 6.48. A summary of the experimental results including shock tube firing parameters and shock wave properties are listed in Table 6.2. A summary of maximum displacements, maximum support rotations and residual displacements measured by the four LVDTs is available in Table 6.4, and a summary of the reinforcement strain gauge data is provided in Table 6.6.

### 6.3.1 Blast Test 1

The first blast test was generated with a driver length of *4880 mm* and a driver pressure of *117.2* $kPa$. The resulting shock wave had a peak reflected pressure of *22.4* $kPa$, reflected impulse of *367.8* $kPa - ms$ and positive phase duration of *45.4* $ms$. The reflected pressure was recorded by a pressure transducer located on the right side of the expansion section of the shock tube and 50 mm from the wall specimen. This pressure transducer was situated near the mid height level of the wall. The maximum displacement recorded by Left LVDT was *1.52 mm* (maximum support rotation *0.18°* relative to the left side fixed edge) which occurred at a time of *42.2* $ms$. The rotation was determined by dividing the displacement recorded by Left LVDT by the distance of the LVDT to the left support of the specimen. The maximum residual displacement from Bottom LVDT was *0.12 mm*. The reflected pressure- and impulse-time histories are presented in Figure 6.25. The displacement-time histories recorded by the LVDTs are plotted in Figure 6.26. Note that due to problems with the instrumentation, the results for LVDT designed "right" were omitted for all blast tests and LVDT "left" for blast tests 3-6 in the results presented for Wall 2.

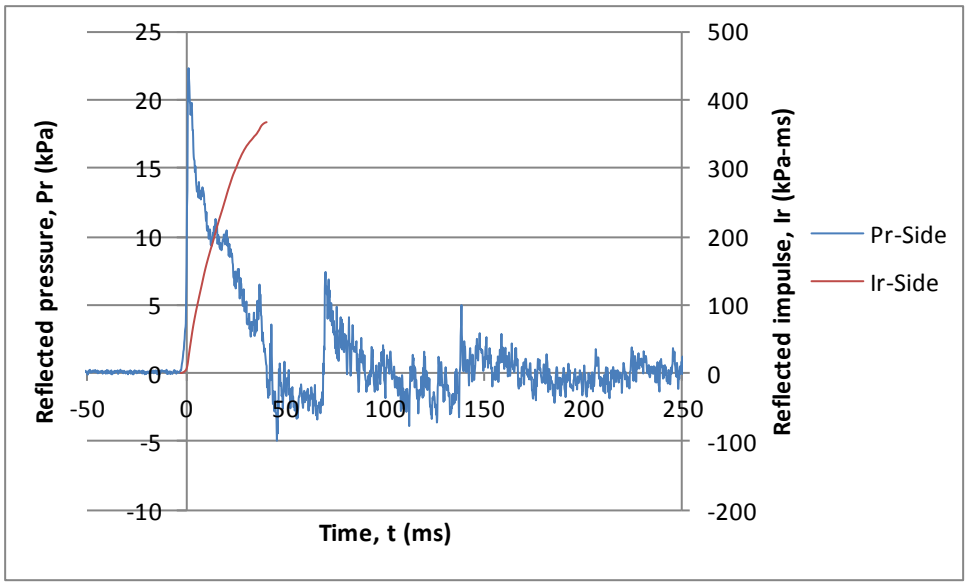


Figure 6.25: Test 1 reflected pressure- and impulse-time histories for Wall 2

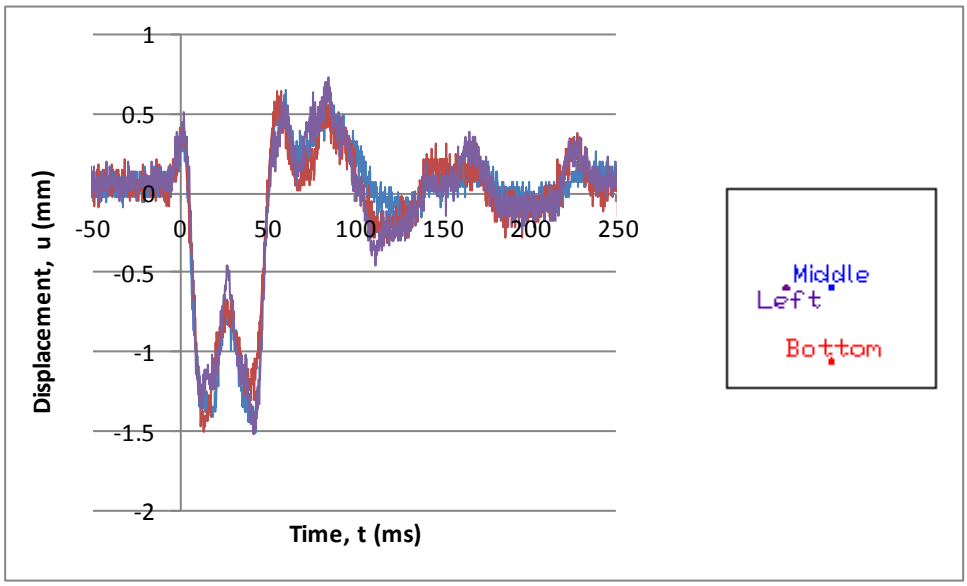


Figure 6.26: Test 1 displacement-time histories of Wall 2

The strain recorded by Gauge SG9-HB located at 1/3$^{rd}$ of the width of the wall from the side support and at mid height was *0.0112 %* at a time of *14.6 ms*, corresponding to a strain-rate of *0.0076* $s^{-1}$. The residual strain recorded by Gauge SG9-HB was *0.0017 %*. The strain captured by Gauge SG10-HB positioned at 1/3$^{rd}$ of the width of the wall and at mid height was *0.0073 %* at a time of *14.8 ms*, corresponding to a strain-rate of *0.0049* $s^{-1}$. The residual strain in Gauge SG10-

HB was *-0.0007 %*. The strain-time histories for Gauges SG9-HB and SG10-HB for test 1 of Wall 2 are shown in Figure 6.27.

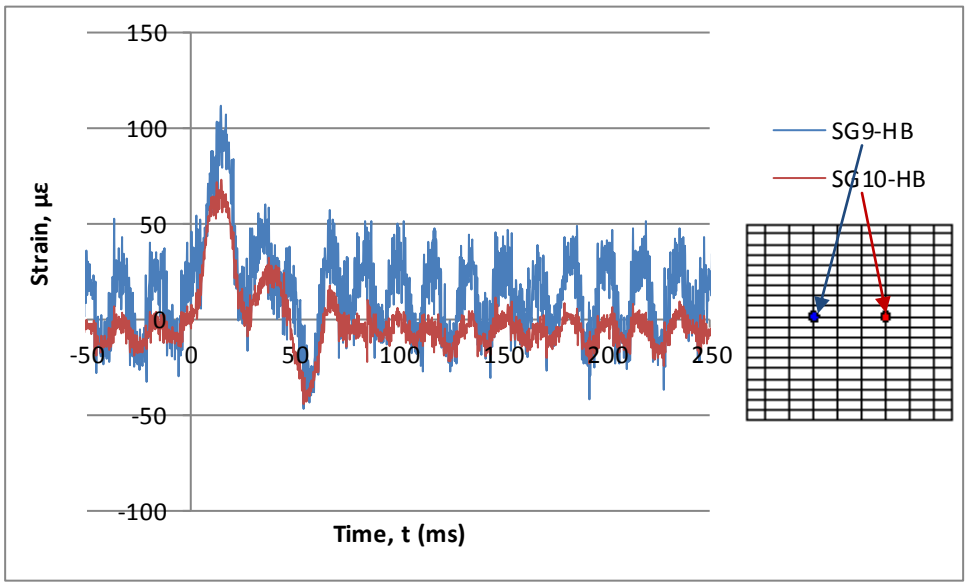


Figure 6.27: Test 1 strain-time histories for Gauges SG9-HB and SG10-HB of Wall 2

The wall remained elastic after testing and no damage or cracking was observed. The condition of Wall 2 after this test is illustrated in Figure 6.28.

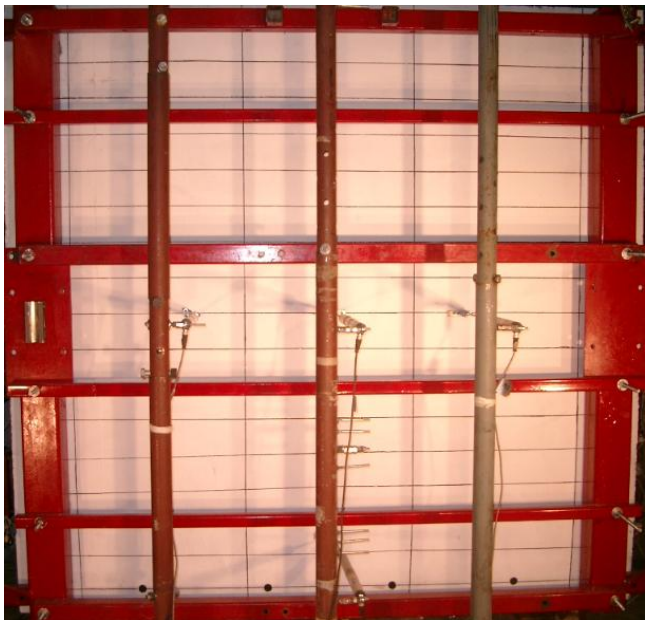

Figure 6.28: Condition of Wall 2 after test 1

### 6.3.2 Blast Test 2

The second blast test was generated with a driver length of *4880 mm* and a driver pressure of *212.4 kPa*. The resulting shock wave had a peak reflected pressure of *41.0 kPa,* reflected impulse of *670.6 kPa − ms* and positive phase duration of *57.6 ms*. The maximum displacement recorded by Middle LVDT was *3.68 mm* (maximum support rotation *0.20°*) which occurred at a time of *18.8 ms*. The maximum residual displacement from Middle LVDT was *0.54 mm.* The reflected pressure- and impulse-time histories are presented in Figure 6.29. The displacement-time histories for the LVDTs are illustrated in Figure 6.30.

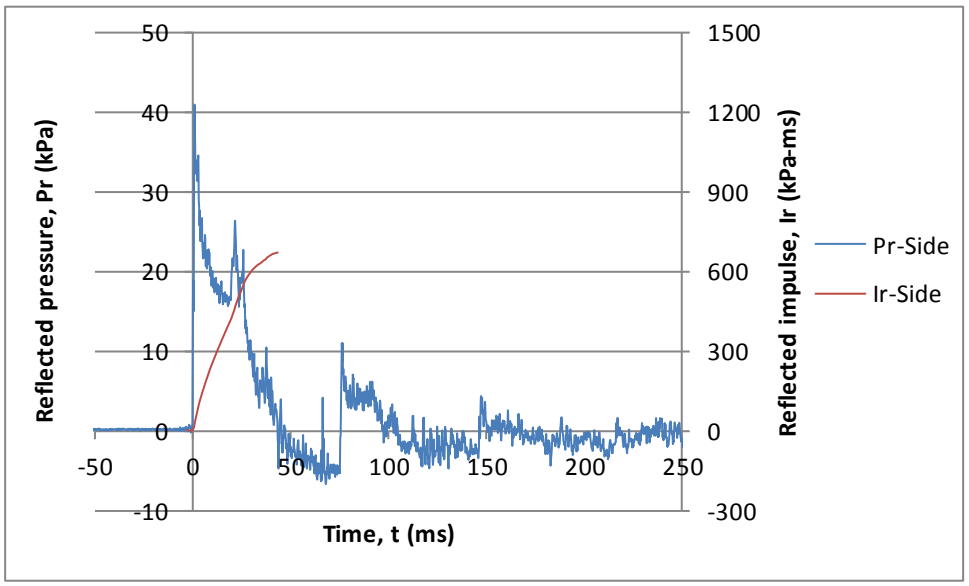


Figure 6.29: Test 2 reflected pressure- and impulse-time histories for Wall 2

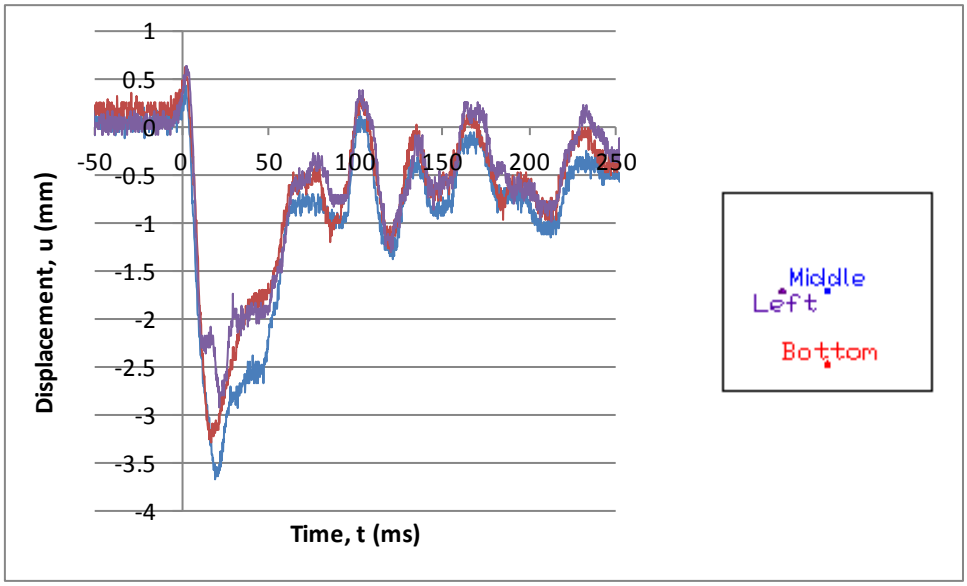


Figure 6.30: Test 2 displacement-time histories of Wall 2

The strain recorded by Gauge SG9-HB was *0.0210 %* at a time of *14.0 ms*, corresponding to a strain-rate of *0.0150* $s^{-1}$. The residual strain in Gauge SG9-HB was *0.0053 %*. The strain captured by Gauge SG10-HB was *0.0169 %* at a time of *13.6 ms*, corresponding to a strain-rate of *0.0124* $s^{-1}$. The residual strain in Gauge SG10-HB was *0.0021 %*. The strain-time histories for Gauges SG9-HB and SG10-HB for test 2 of Wall 2 are shown in Figure 6.31.

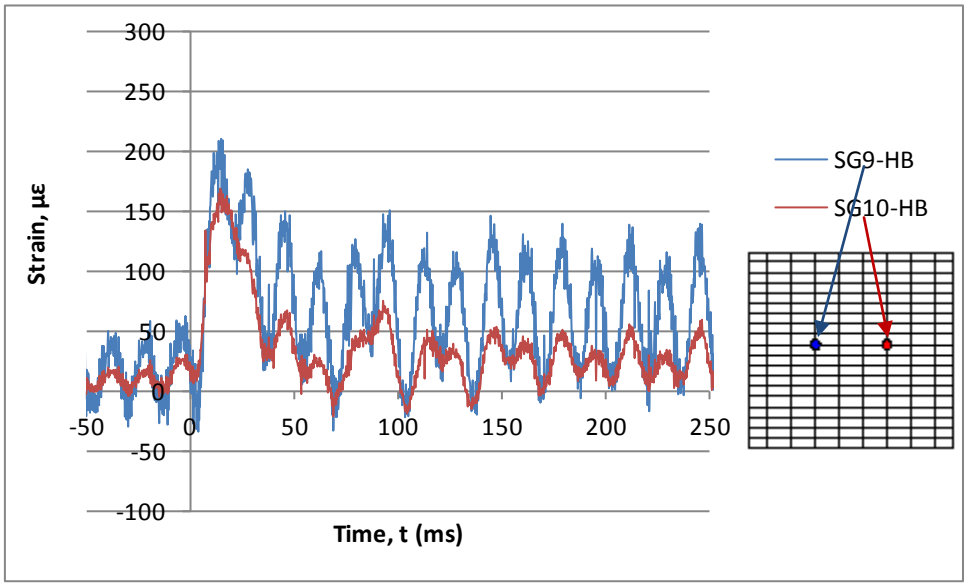


Figure 6.31: Test 2 strain-time histories for Gauges SG9-HB and SG10-HB of Wall 2

Two vertical cracks formed near the middle one-third of the wall width with lengths of approximately $150\ mm$. The extent of damage to Wall 2 after this test is illustrated in Figure 6.32.

Figure 6.32: Condition of Wall 2 after test 2

### 6.3.3 Blast Test 3

The third blast test was generated with a driver length of *4880 mm* and a driver pressure of *351.6* $kPa$. The resulting shock wave had a peak reflected pressure of *64.8* $kPa$, reflected impulse of *1102.2* $kPa - ms$ and positive phase duration of *52.8* $ms$. The maximum displacement recorded by Middle LVDT was *9.85 mm* (maximum support rotation *0.54°*) which occurred at a time of *22.6* $ms$. The maximum residual displacement from Bottom LVDT was *1.89 mm.* The reflected pressure- and impulse-time histories are presented in Figure 6.33. The displacement-time histories for the LVDTs are illustrated in Figure 6.34.

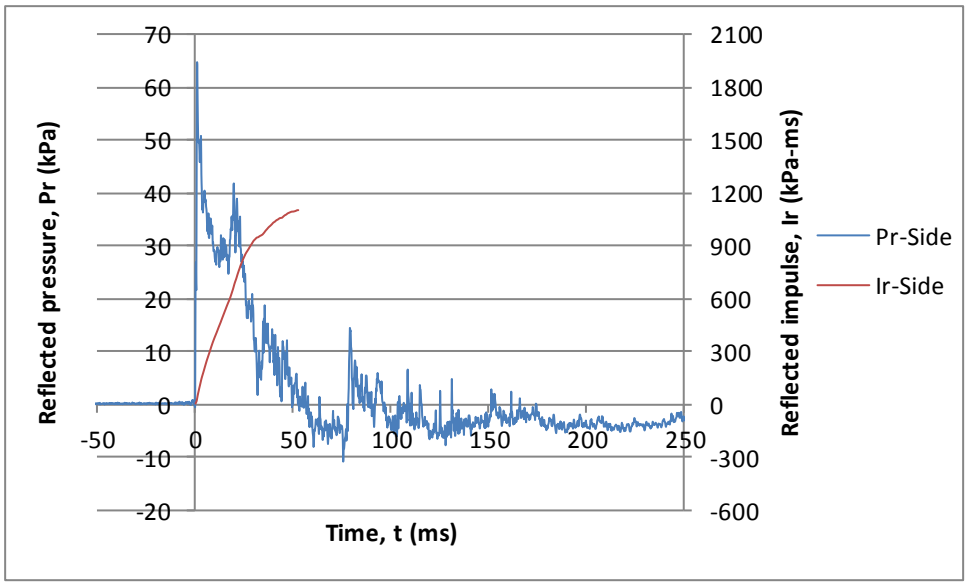


Figure 6.33: Test 3 reflected pressure- and impulse-time histories for Wall 2

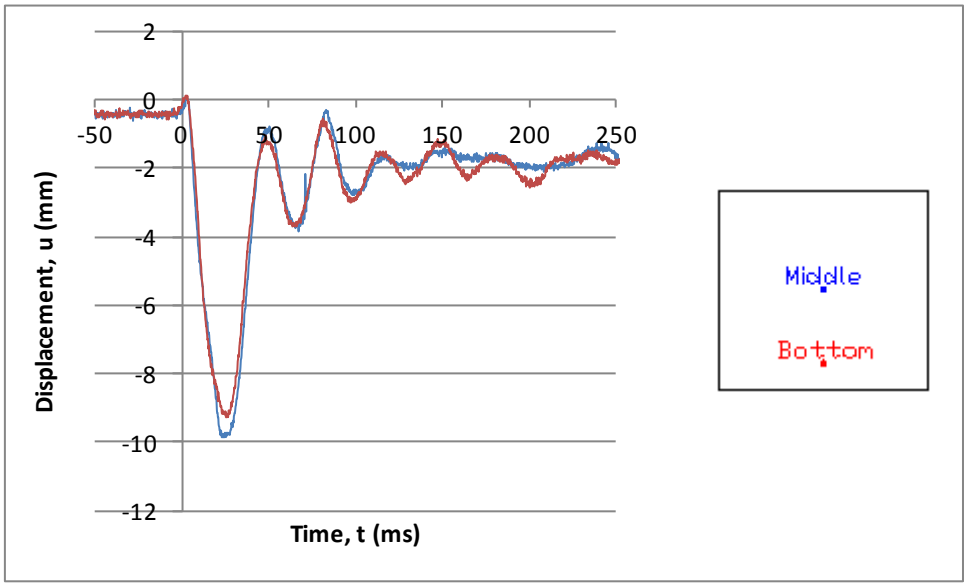


Figure 6.34: Test 3 displacement-time histories of Wall 2

The strain recorded by Gauge SG9-HB was *0.0414 %* at a time of *13.0 ms*, corresponding to a strain-rate of *0.0318* $s^{-1}$. The residual strain in Gauge SG9-HB was *0.0185 %*. The strain captured by Gauge SG10-HB was *0.1006 %* at a time of *22.2 ms*, corresponding to a strain-rate of *0.0453* $s^{-1}$. The residual strain in Gauge SG10-HB was *0.0209 %*. The strain-time histories for Gauges SG9-HB and SG10-HB for test 3 of Wall 2 are shown in Figure 6.35.

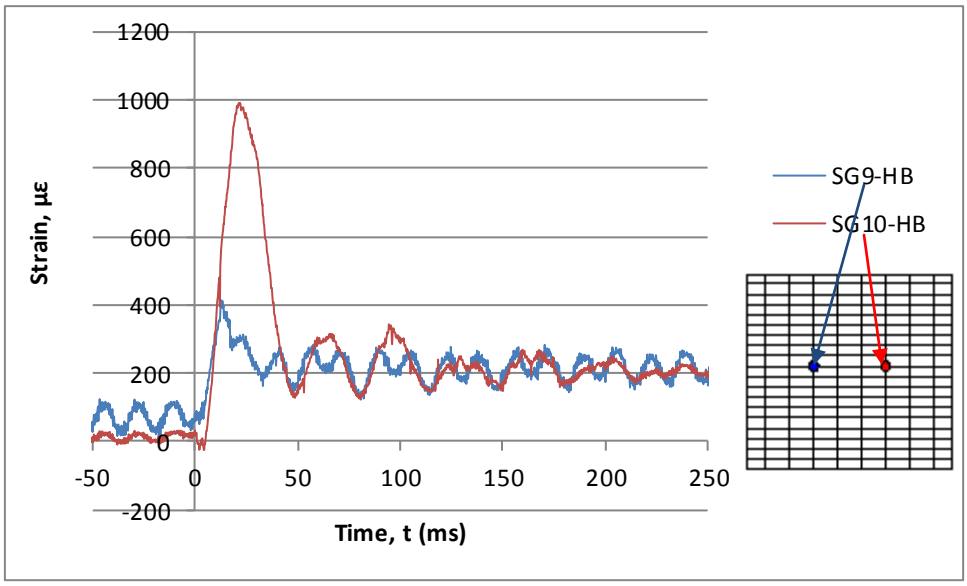


Figure 6.35: Test 3 strain-time histories for Gauges SG9-HB and SG10-HB of Wall 2

Four new vertical cracks surfaced in the middle one-third width of the wall with approximate lengths of 150 *mm*, 180 *mm*, and 210 *mm*. The two existing vertical cracks propagated further towards the top and bottom of the wall, and their lengths reached 900 *mm* and 700 *mm*. On the pressure side of the wall, two horizontal cracks were discovered, both located in the middle one-third height of the wall with lengths of 300 *mm* and 400 *mm*. The extent of damage to Wall 2 after this test is illustrated in Figure 6.36.

Figure 6.36: Condition of Wall 2 after test 3

### 6.3.4 Blast Test 4

The fourth blast test was generated with a driver length of *4880 mm* and a driver pressure of *406.8 kPa*. The resulting shock wave had a peak reflected pressure of *66.2 kPa,* reflected impulse of *1304.1* $kPa-ms$ and positive phase duration of *57.6* $ms$. The maximum displacement recorded by Middle LVDT was *14.35 mm* (maximum support rotation *0.79*°) which occurred at a time of *23.6* $ms$. The maximum residual displacement from Bottom LVDT was *2.65 mm.* The reflected pressure- and impulse-time histories are presented in Figure 6.37. The displacement-time histories for the LVDTs are illustrated in Figure 6.38.

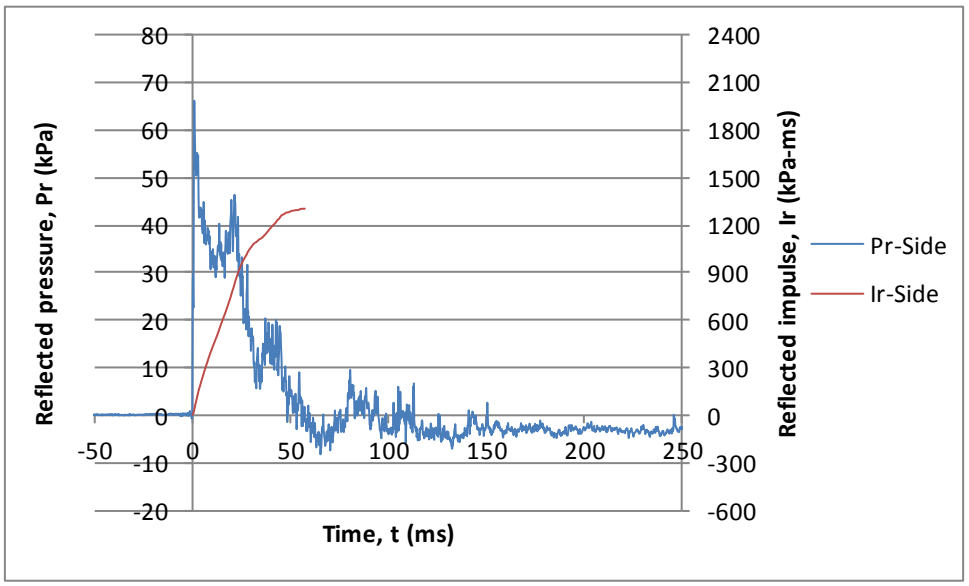


Figure 6.37: Test 4 reflected pressure- and impulse-time histories for Wall 2

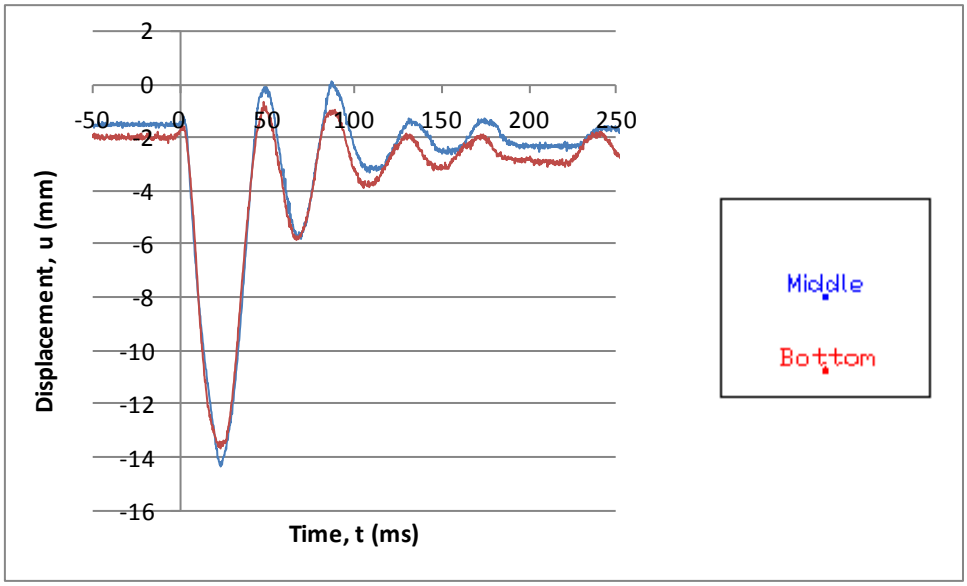


Figure 6.38: Test 4 displacement-time histories of Wall 2

The strain recorded by Gauge SG9-HB was *0.0430 %* at a time of *39.8 ms*, corresponding to a strain-rate of *0.0108* $s^{-1}$. The residual strain in Gauge SG9-HB was *0.0256 %*. The strain captured by Gauge SG10-HB was *0.1467 %* at a time of *20.8 ms*, corresponding to a strain-rate of *0.0705* $s^{-1}$. The residual strain in Gauge SG10-HB was *0.0283 %*. The strain-time histories for Gauges SG9-HB and SG10-HB for test 4 of Wall 2 are shown in Figure 6.39.

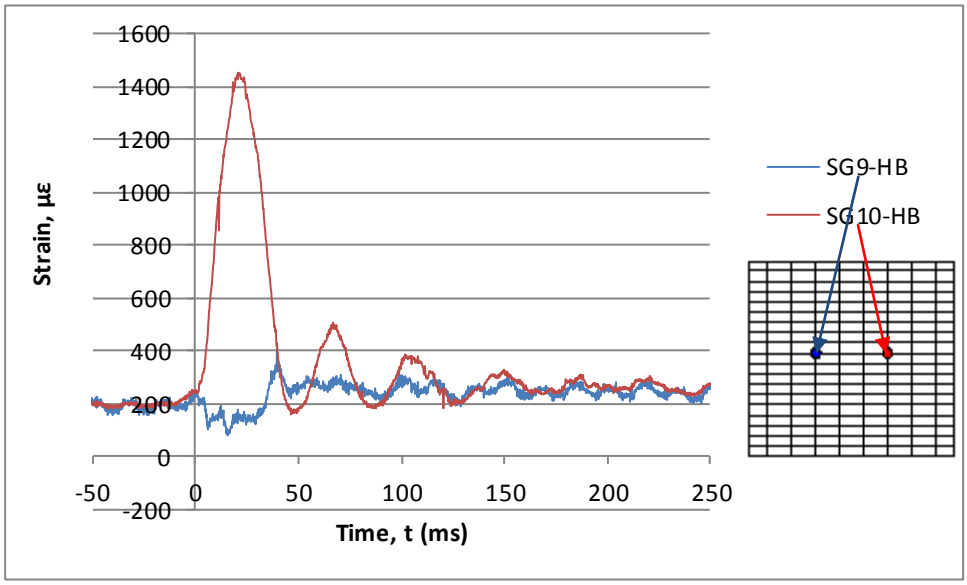


Figure 6.39: Test 4 strain-time histories for Gauges SG9-HB and SG10-HB of Wall 2

After this test, a significant number of vertical cracks formed near the middle one-third width of the wall. The longest crack was approximately 1300 $mm$ and was located in the center of the wall. A 900 $mm$ long vertical crack formed to the left of the longest crack, while a 1000 $mm$ long vertical crack developed to the right. The length of the vertical cracks moving towards the left and right supports was progressively shorter in length. The extent of damage to Wall 2 after this test is illustrated in Figure 6.40.

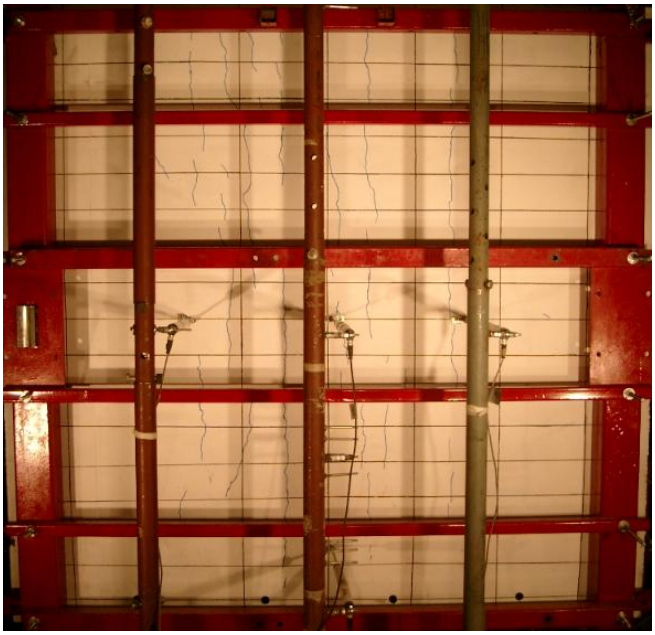

Figure 6.40: Condition of Wall 2 after test 4

### 6.3.5 Blast Test 5

The fifth blast test was generated with a driver length of *4880 mm* and a driver pressure of *552.3* $kPa$. The resulting shock wave had a peak reflected pressure of *89.0* $kPa$, reflected impulse of *1794.7* $kPa - ms$ and positive phase duration of *59.2* $ms$. The maximum displacement recorded by Middle LVDT was *21.67 mm* (maximum support rotation *1.19*°) which occurred at a time of *26.0* $ms$. The maximum residual displacement from Bottom LVDT was *4.41 mm.* The reflected pressure- and impulse-time histories are presented in Figure 6.41. The displacement-time histories for the LVDTs are illustrated in Figure 6.42.

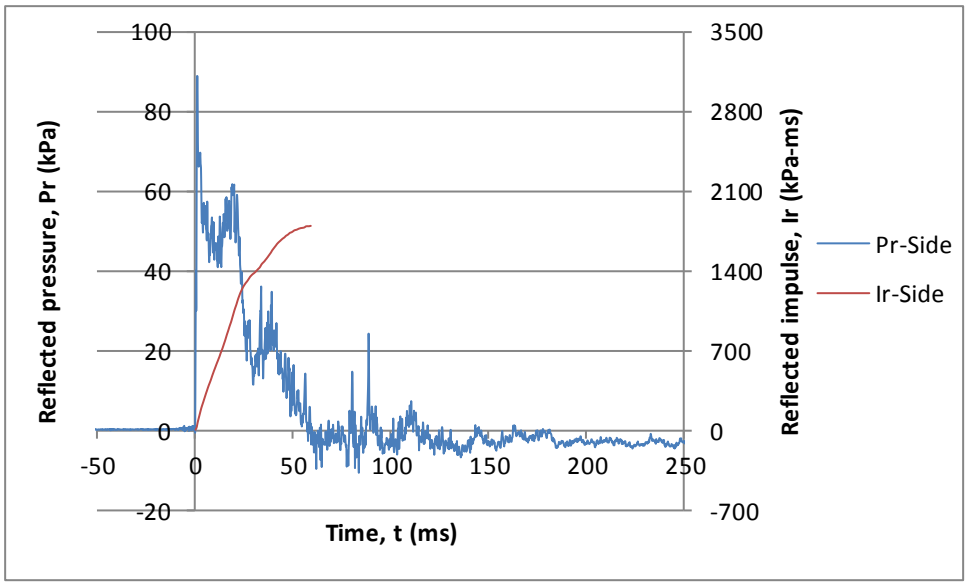


Figure 6.41: Test 5 reflected pressure- and impulse-time histories for Wall 2

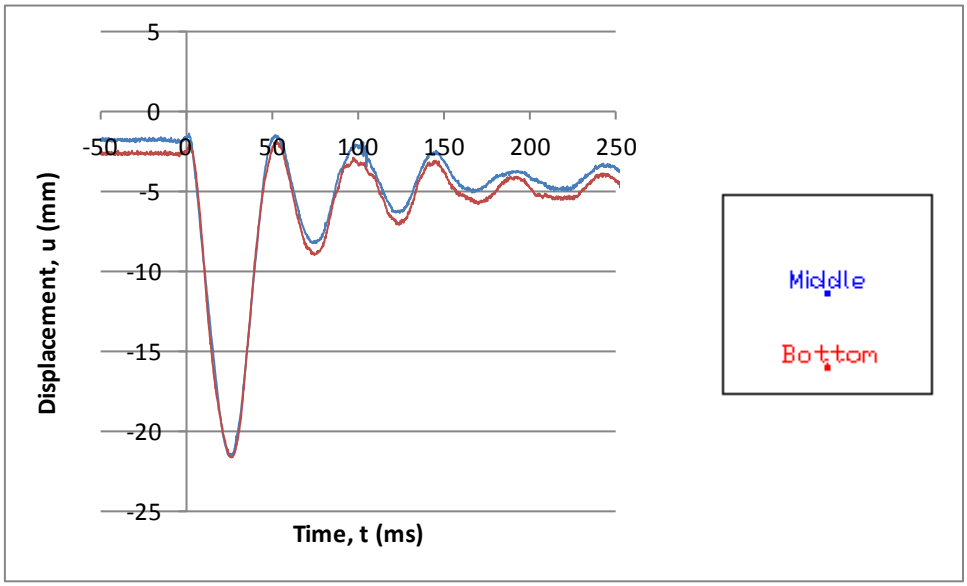


Figure 6.42: Test 5 displacement-time histories of Wall 2

The strain recorded by Gauge SG9-HB was *0.0916 %* at a time of *32.4 ms*, corresponding to a strain-rate of *0.0283* $s^{-1}$. The residual strain in Gauge SG9-HB was *0.0379 %*. The strain captured by Gauge SG10-HB was *0.2030 %* at a time of *20.4 ms*, corresponding to a strain-rate of *0.0995* $s^{-1}$. The residual strain in Gauge SG10-HB was *0.0345 %*. The strain-time histories for Gauges SG9-HB and SG10-HB for test 5 of Wall 2 are shown in Figure 6.43. The green horizontal dashed line highlights the yield strain of the reinforcement.

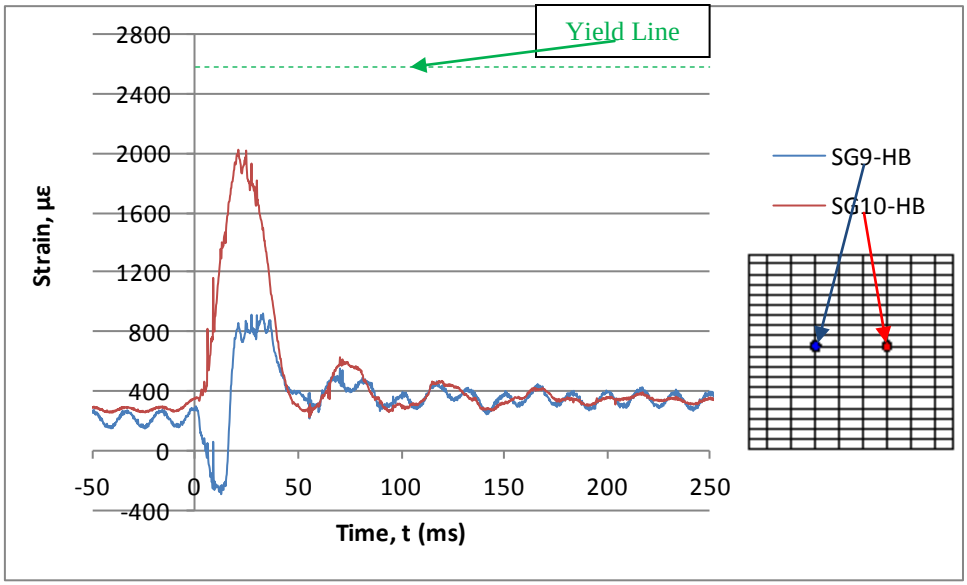


Figure 6.43: Test 5 strain-time histories for Gauges SG9-HB and SG10-HB of Wall 2

Four new vertical cracks appeared near the middle one-third width of the wall, ranging in length from $400 - 700\,mm$. The existing vertical cracks continued to propagate towards the top and bottom of the wall. A major vertical crack at the centerline of the wall extended through the entire height of the wall. The remaining existing vertical cracks exceeded $1800\,mm$ in length. The extent of damage to Wall 2 after this test is illustrated in Figure 6.44.

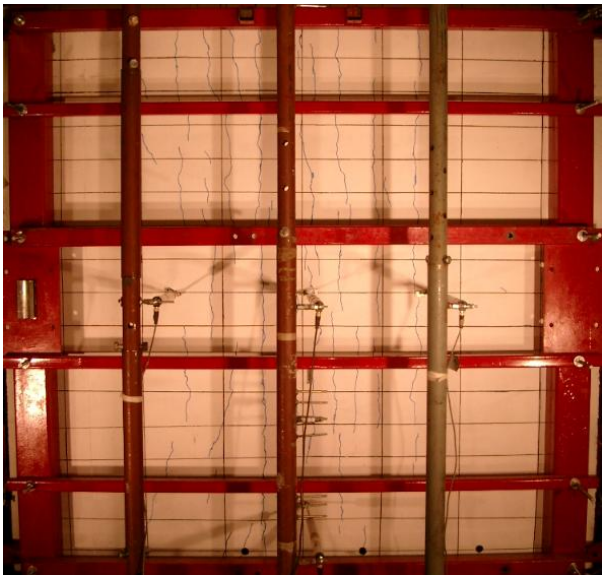

Figure 6.44: Condition of Wall 2 after test 5

### 6.3.6 Blast Test 6

The sixth blast test was generated with a driver length of *4880 mm* and a driver pressure of *710.8 $kPa$*. The resulting shock wave had a peak reflected pressure of *100.1 $kPa$,* reflected impulse of *2122.4 $kPa - ms$* and positive phase duration of *54.4 $ms$*. The maximum displacement recorded by Middle LVDT was *33.74 mm* (maximum support rotation *1.86*°) which occurred at a time of *26.6 $ms$*. The maximum residual displacement from Bottom LVDT was *12.18 mm.* The reflected pressure- and impulse-time histories are presented in Figure 6.45. The displacement-time histories for the LVDTs are illustrated in Figure 6.46.

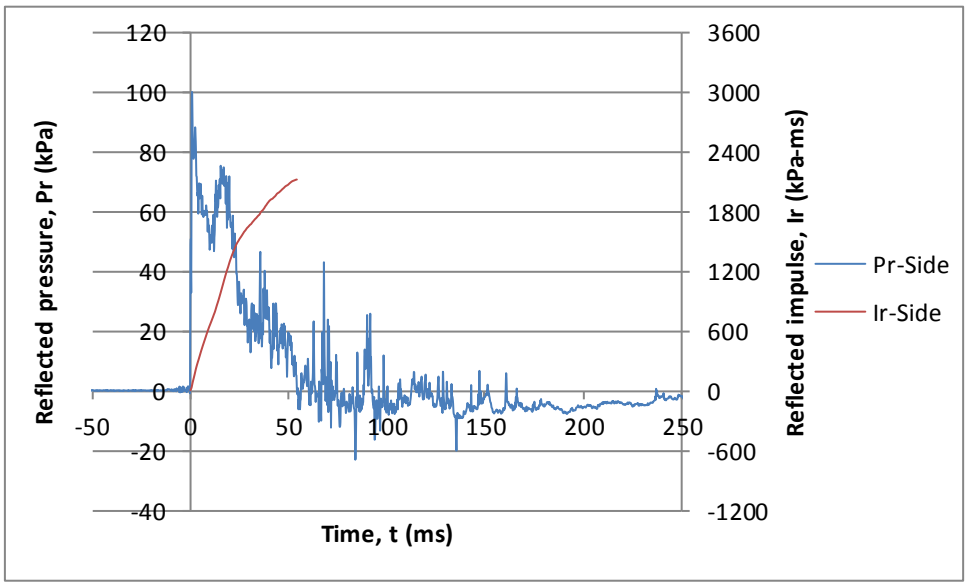


Figure 6.45: Test 6 reflected pressure- and impulse-time histories for Wall 2

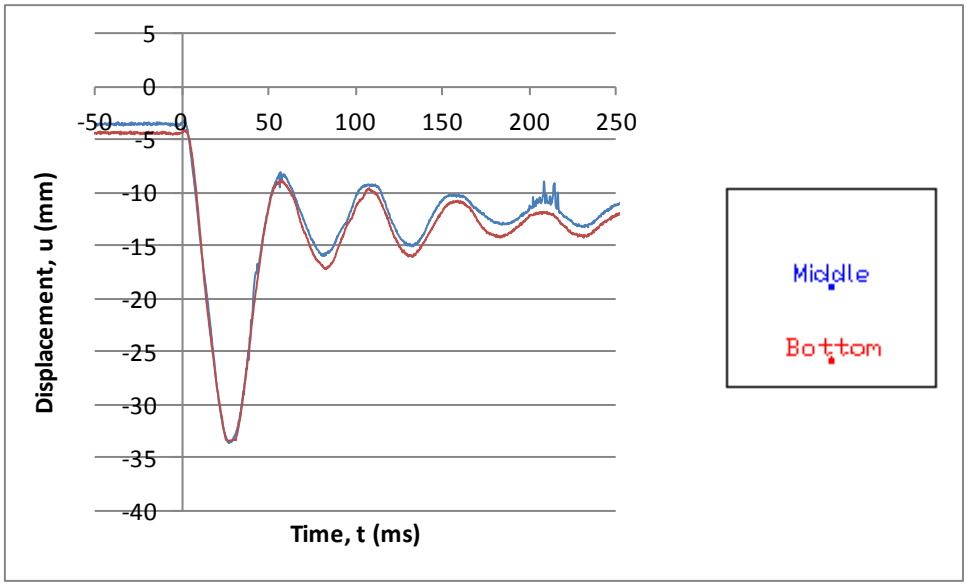


Figure 6.46: Test 6 displacement-time histories of Wall 2

The strain recorded by Gauge SG9-HB was *0.1511 %* at a time of *26.6 ms*, corresponding to a strain-rate of *0.0568* $s^{-1}$. The residual strain in Gauge SG9-HB was *0.0414 %*. The strain captured by Gauge SG10-HB was *0.2259 %* at a time of *21.6 ms*, corresponding to a strain-rate of *0.1046* $s^{-1}$. The residual strain in Gauge SG10-HB was *0.0379 %*. The strain-time histories for Gauges SG9-HB and SG10-HB for test 6 of Wall 2 are shown in Figure 6.47. The green horizontal dashed line highlights the yield strain of the reinforcement.

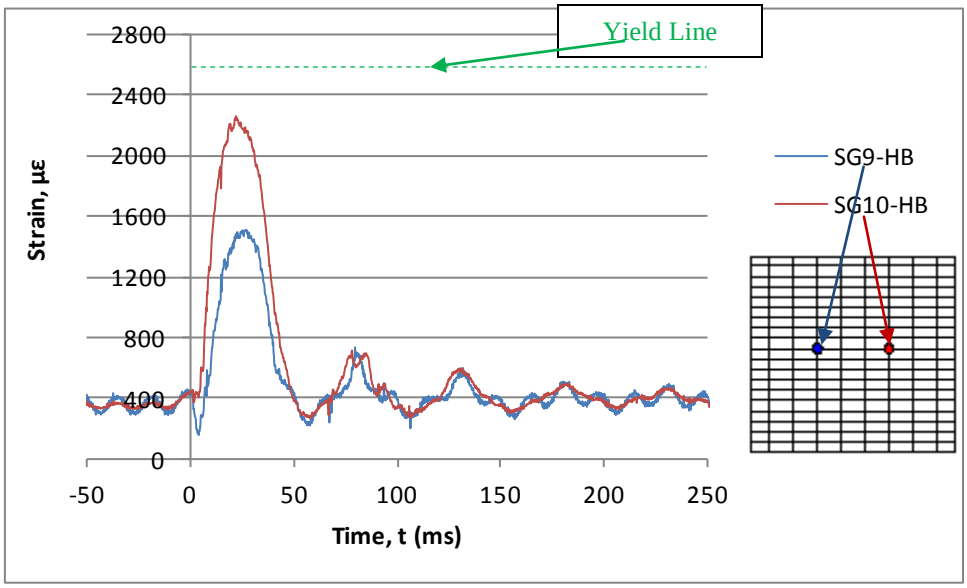


Figure 6.47: Test 6 strain-time histories for Gauges SG9-HB and SG10-HB of Wall 2

The existing vertical cracks near the middle of the wall extended through the entire height of the wall. Two of the vertical cracks, one located at the left and the other at the right of the one-third width of the wall, were approximately $2250\ mm$ and $2000\ mm$ in length, respectively. At the back of the wall (on the pressure side), nine horizontal cracks were visible, with lengths ranging from $300\ mm$ to $2000\ mm$. The extent of damage to the Wall 2 after this test is illustrated in Figure 6.48.

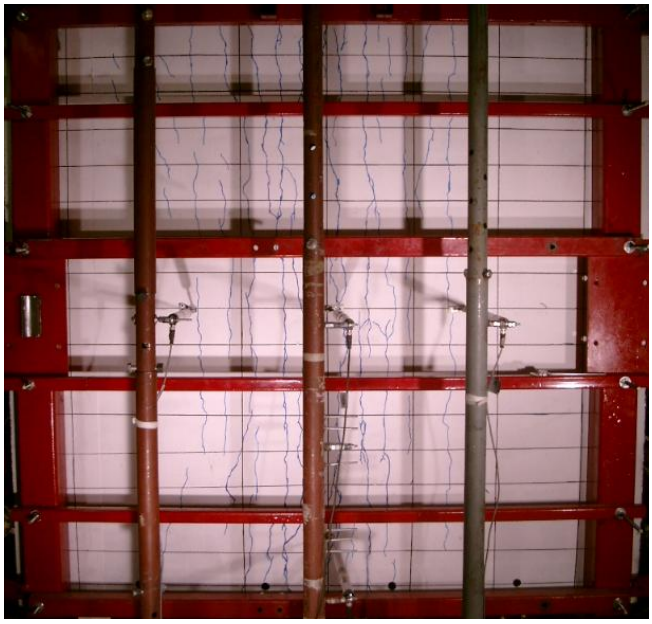

Figure 6.48: Condition of Wall 2 after test 6

## 6.4 Performance of Wall Specimens

The experimental results of the two-way and one-way bending RC reservoir walls are compared in this section. The maximum displacements recorded by the LVDTs are provided in Tables 6.3 and 6.4, and maximum reinforcement strains captured by the strain gauges are given in Tables 6.5 and 6.6.

### 6.4.1 Shock tube firing parameters and shock wave response

The imposed pressures on Walls 1 and 2 were generated by the same driver length and nearly similar driver pressures. Figures 6.49 and 6.50 illustrate the relationship between reflected pressure and driver pressure, and reflected impulse and driver pressure, respectively. Figure 6.49 demonstrates that the reflected pressure is positively correlated with driver pressure among the six blast tests for the two walls. The reflected pressures were similar for the two walls for similar driver pressures. The only significant difference between the two walls arose for a driver pressure of approximately 550 $kPa$, which corresponded to blast test 5. It is clearly evident that an increase in the driver pressure resulted in an increase in the reflected pressure. The response in Figure 6.50 between the reflected impulse and drive pressure also highlights the positive correlation among the six blast tests for the two walls. An increase in the driver pressure resulted in an increase in the reflected impulse. For the most part, Wall 1 experienced greater reflected impulse than Wall 2.

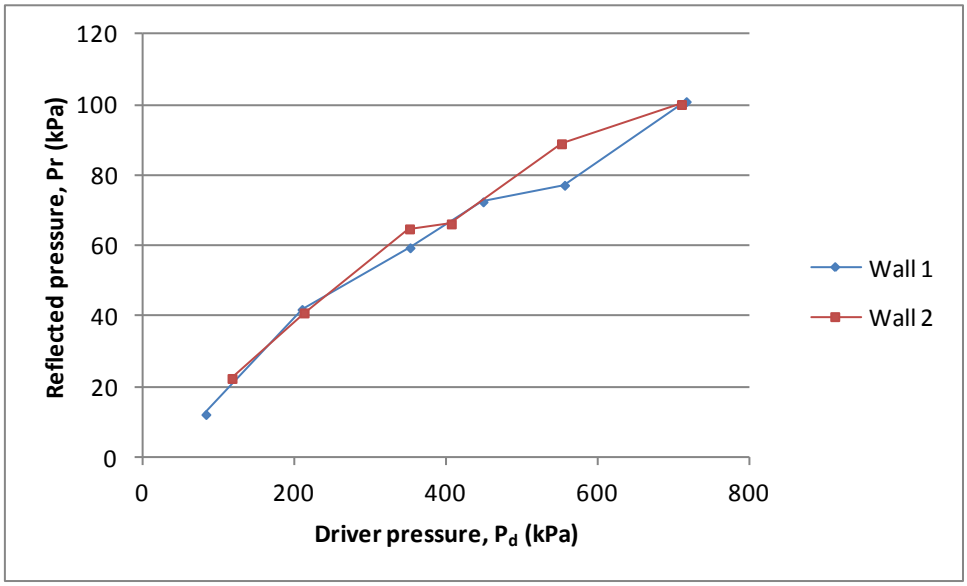


Figure 6.49: Relationship between reflected pressure and driver pressure for Wall 1 and Wall 2

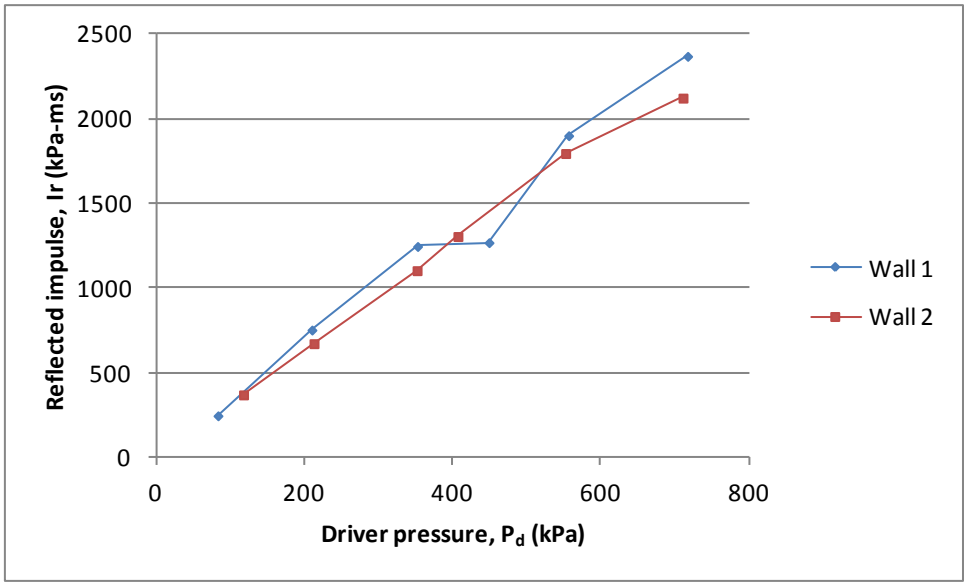


Figure 6.50: Relationship between reflected impulse and driver pressure for Wall 1 and Wall 2

Figure 6.51 demonstrates that the reflected impulse is positively correlated with reflected pressure among the six blast tests for two walls. An increase in the reflected pressure resulted in an increase in the reflected impulse. For the most part, Wall 1 experienced greater reflected impulse than Wall 2.

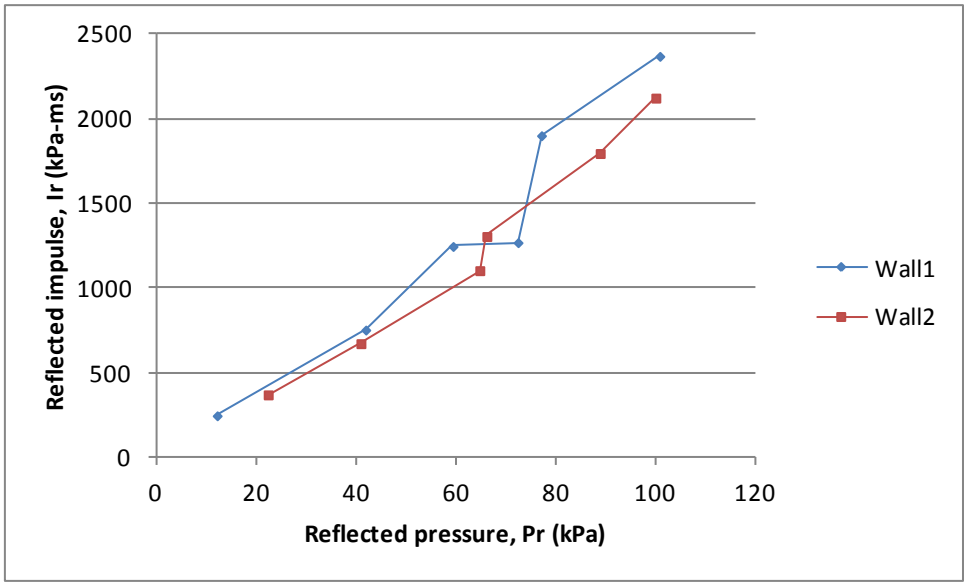


Figure 6.51: Relationship between reflected impulse and reflected pressure for Wall 1 and Wall 2

### 6.4.2 Maximum displacements

The maximum displacement in Wall 1 was *34.59 mm* after test 6 (driver length of 4880 *mm* and driver pressure of 717.1 $kPa$). The maximum displacement in Wall 2 was *33.74 mm* after test 6 (driver length of 4880 *mm* and driver pressure of 710.8 $kPa$). The corresponding reflected pressures and impulses were *100.9* $kPa$ and *2369.2* $kPa-ms$, and *100.1* $kPa$ and *2122.4* $kPa-ms$ for Wall 1 and Wall 2, respectively. Figure 6.52 provides a plot of reflected pressure and maximum displacement. The results include readings from Top LVDT and Middle LVDT, which recorded the maximum displacements in Wall 1 and Wall 2, respectively. The response demonstrates that the reflected pressures are positively correlated with maximum displacements for the six blast tests for the two walls. Furthermore, the maximum displacements recorded by the middle LVDT for Wall 1 are included to provide a direct comparison to the middle LVDT in Wall 2. Figure 6.53 illustrates the relationship between reflected impulse and maximum displacements for the same LVDTs. Similar behaviours are evident where the reflected impulses are positively correlated with maximum displacements among the six blast tests for the two walls.

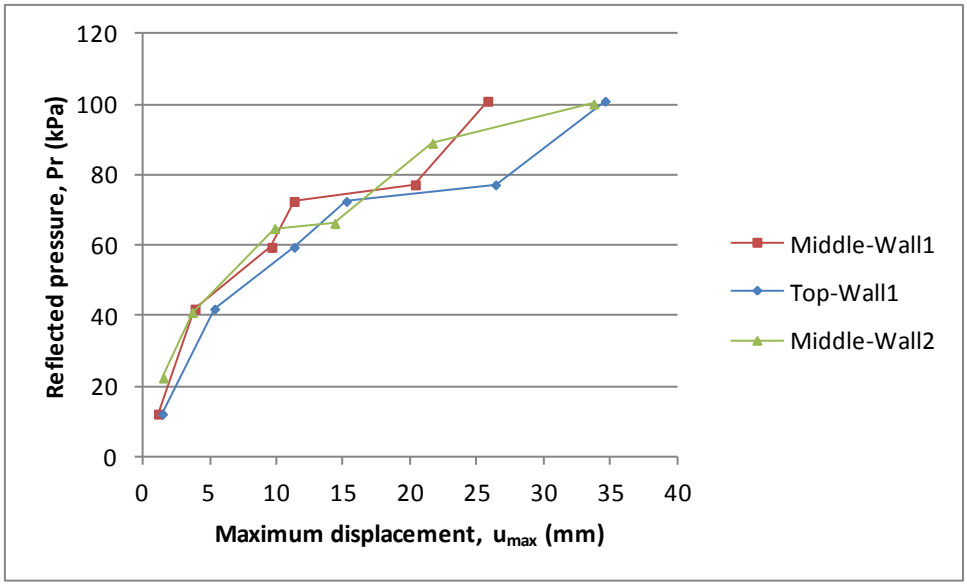


Figure 6.52: Relationship between reflected pressure and displacements of Wall 1 and Wall 2

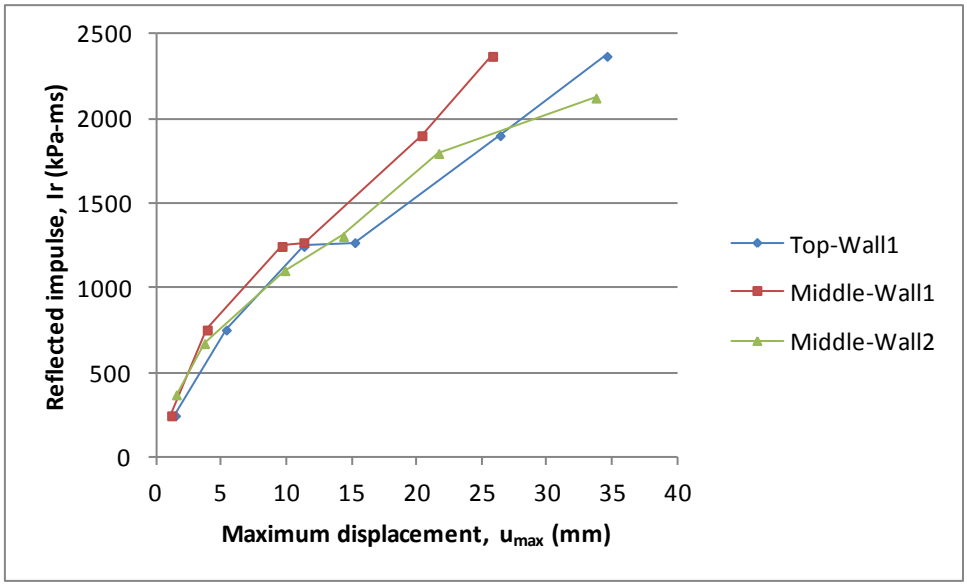


Figure 6.53: Relationship between reflected impulse and displacements of Wall 1 and Wall 2

The experimental results illustrate that the displacements were slightly larger for the two-way bending wall (Wall 1) relative to the one-way wall (Wall 2) for similar blast loading after blast test 1. This was contrary to expectations. A probable cause was the actual degree of restraint provided by the side edge supports that were intended to be fully fixed. For Wall 1 four HSS steel sections were used to span the wall and tie the edge supports, while six HSS sections were used for Wall 2. The additional horizontal tie members seem to stiffen the edge supports, thus providing more fixity. In addition, the impulse experienced by Wall 1 was, in general, greater than Wall 2 resulting in increased displacements for Wall 1.

### 6.4.3 Maximum reinforcement strains

For Wall 1, the reinforcing steel yielded after test 5 (reflected pressure of 77.2 $kPa$ and reflected impulse of 1900.1 $kPa - ms$). The maximum strain in Gauge SG10-HB was *0.26 %*, which just slightly exceeded the yield strain of *0.26 %* obtained from coupon tensile testing. Strains of *0.18 %*, *0.17 %* and *0.21 %* were recorded by Gauges SG9-HB, SG11-HB and SG14-HB, below the yield limit. After test 6, the maximum strain in Gauge SG10-HB was *0.38 %*, which exceeded the yield strain, while the strains recorded by SG9-HB, SG11-HB and SG14-HB were *0.25 %*, just slightly below the yield limit. Recall that the location of the strain gauges was based on an

assumed yield line pattern for Wall 1. As such, it appears that the gauges were properly positioned to capture yielding.

For Wall 2, the strain gauges did not record strains in excess of yielding. After test 6 (reflected pressure of 100.1 $kPa$ and reflected impulse of 2122.4 $kPa - ms$) a maximum strain of *0.23 %* was captured by Gauge SG10-HB. It is probable that the strain gauges did not record yielding due to their location in the wall, which was based on an assumed yield line for Wall 1. The damage to Wall 2 was more confined at the midspan of the specimen; however, this zone was deficient of strain gauges.

Figures 6.54 and 6.55 provide plots of the reflected pressure and reflected impulse against the strain recorded by Gauge SG10-HB, respectively. This gauge recorded the highest strains in Walls 1 and 2.

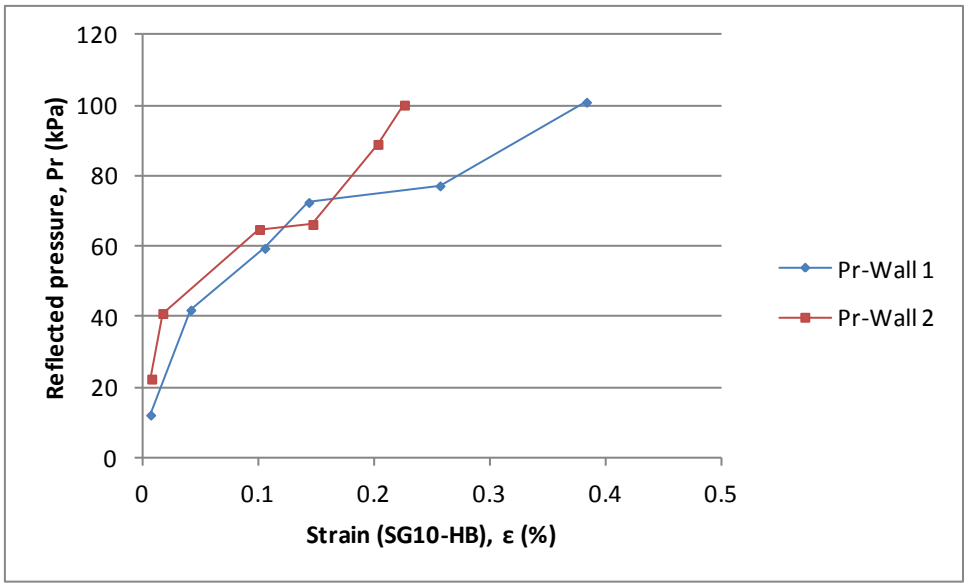


Figure 6.54: Relationship between reflected pressure and strain (SG10-HB) of Wall 1 and Wall 2

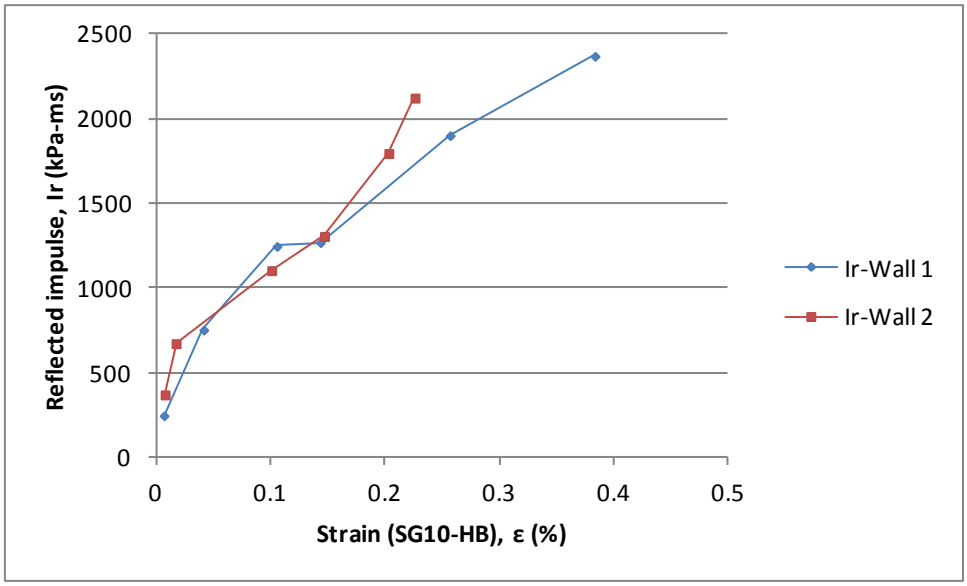


Figure 6.55: Relationship between reflected impulse and strain (SG10-HB) of Wall 1 and Wall 2

## 6.5 Summary

Walls 1 and 2 were exposed to increasing levels of blast loading while maintaining a constant driver length of 4880 mm in the shock tube setup. The testing investigated the response of the walls with different support conditions subjected to blast loading. Wall 1 responded within the elastic regime for Tests 1-4, corresponding to a range in reflected pressures of 12.1 - 72.5 $kPa$. For Tests 5 and 6 (reflected pressures of 77.2 $kPa$ and 100.9 $kPa$, respectively), Wall 1 was pushed into the elastic-plastic range. Yielding of Wall 1 commenced during Test 5. The shock waves imposed on Wall 1 for Tests 1-4 were equivalent to a range in charge weights of 1064.5 - 3207.3 $kg$, and a range in stand-off distances of 208.9 - 86.4 $m$. The shock waves for Tests 5 and 6 were equivalent to the charge weights of 9630.0 $kg$ and 12789.1 $kg$, and stand-off distances of 120.3 $m$ and 115.5 $m$, respectively.

For Wall 2, the behaviour was elastic for all 6 tests, corresponding to a reflected pressure ranging between 22.4 $kPa$ and 100.1 $kPa$. The shock waves imposed on Wall 2 for Tests 1-6 were equivalent to a range in charge weights of 854.8 - 9299.5 $kg$, and a range in stand-off distances of 120.5 - 86.2 $m$.

For the levels of blasting loading imposed in this testing program, RC reservoir walls similar to those tested can be expected to respond within the elastic to elastic-plastic regime.

Wall 1 was supported to promote two-way bending action. The two opposite sides of the wall were fixed, the base edge was hinged and the top edge was free. Wall 2 was supported to promote one-way bending action. The two opposite sides of the wall were fixed, and the base and the top edges were free. Testing demonstrated that the support conditions influenced the test results. This phenomenon will be investigated in Chapter 7 with Single-Degree-Of-Freedom analyses.

Table 6.1: Shock tube firing parameters, shock wave properties and experimental results for Wall 1

| Blast test | Driver length $L_d$ $mm$ | Driver pressure $P_d$ $kPa$ | Reflected pressure $P_r$ $kPa$ | Reflected impulse $I_r$ $kPa-ms$ | Positive phase duration $t_d$ $ms$ |
|---|---|---|---|---|---|
| 1 | 4880 | 82.7 | 12.1 | 244.1 | 43.2 |
| 2 | 4880 | 209.6 | 41.9 | 751.1 | 52.2 |
| 3 | 4880 | 352.3 | 59.4 | 1245.2 | 56.6 |
| 4 | 4880 | 448.8 | 72.5 | 1267.6 | 60.4 |
| 5 | 4880 | 556.4 | 77.2 | 1900.1 | 64.6 |
| 6 | 4880 | 717.1 | 100.9 | 2369.2 | 61.4 |

Table 6.2: Shock tube firing parameters, shock wave properties and experimental results for Wall 2

| Blast test | Driver length $L_d$ $mm$ | Driver pressure $P_d$ $kPa$ | Reflected pressure $P_r$ $kPa$ | Reflected impulse $I_r$ $kPa-ms$ | Positive phase duration $t_d$ $ms$ |
|---|---|---|---|---|---|
| 1 | 4880 | 117.2 | 22.4 | 367.8 | 45.4 |
| 2 | 4880 | 212.4 | 41.0 | 670.6 | 57.6 |
| 3 | 4880 | 351.6 | 64.8 | 1102.2 | 52.8 |
| 4 | 4880 | 406.8 | 66.2 | 1304.1 | 57.6 |
| 5 | 4880 | 552.3 | 89.0 | 1794.7 | 59.2 |
| 6 | 4880 | 710.8 | 100.1 | 2122.4 | 54.4 |

Table 6.3: Maximum displacements, maximum support rotations and residual displacements for Wall 1

| Blast test | Driver length $L_d$ $mm$ | Driver pressure $P_d$ $kPa$ | LVDT-Middle | | | | LVDT-Top | | | |
|---|---|---|---|---|---|---|---|---|---|---|
| | | | Maximum displacement $u_{Mid.-max}$ $mm$ | Time to maximum $t_{Mid.-max}$ $ms$ | Maximum support rotation $\theta_{Mid.-max}$ ° | Residual displacement $u_{Mid.-res.}$ $mm$ | Maximum displacement $u_{Top-max}$ $mm$ | Time to maximum $t_{Top-max}$ $ms$ | Maximum support rotation $\theta_{Top-max}$ ° | Residual displacement $u_{Top-res.}$ $mm$ |
| 1 | 4880 | 82.7 | -1.14 | 36.4 | 0.07 | 0.35 | -1.44 | 14.6 | 0.08 | 0.58 |
| 2 | 4880 | 209.6 | -3.88 | 23.2 | 0.22 | -0.20 | -5.34 | 17.4 | 0.31 | -0.15 |
| 3 | 4880 | 352.3 | -9.63 | 26.4 | 0.55 | -0.68 | -11.31 | 20.0 | 0.65 | -0.48 |
| 4 | 4880 | 448.8 | -11.30 | 24.6 | 0.65 | -0.22 | -15.22 | 22.2 | 0.87 | -0.25 |
| 5 | 4880 | 556.4 | -20.37 | 26.2 | 1.17 | -2.58 | -26.38 | 26.8 | 1.51 | -3.33 |
| 6 | 4880 | 717.1 | -25.80 | 27.4 | 1.48 | -2.80 | -34.59 | 28.2 | 1.98 | -3.63 |

Table 6.3: Maximum displacements, maximum support rotations and residual displacements for Wall 1 (continued)

| Blast test | Driver length $L_d$ $mm$ | Driver pressure $P_d$ $kPa$ | LVDT-Right | | | | LVDT-Left | | | |
|---|---|---|---|---|---|---|---|---|---|---|
| | | | Maximum displacement $u_{Rig.-max}$ $mm$ | Time to maximum $t_{Rig.-max}$ $ms$ | Maximum support rotation $\theta_{Rig.-max}$ ° | Residual displacement $u_{Rig.-res.}$ $mm$ | Maximum displacement $u_{Lef.-max}$ $mm$ | Time to maximum $t_{Lef.-max}$ $ms$ | Maximum support rotation $\theta_{Lef.-max}$ ° | Residual displacement $u_{Lef.-res.}$ $mm$ |
| 1 | 4880 | 82.7 | No data | No data | No data | No data | 0.70 | 160.4 | 0.28 | 0.54 |
| 2 | 4880 | 209.6 | No data | No data | No data | No data | -1.46 | 25.0 | 0.58 | 0.45 |
| 3 | 4880 | 352.3 | No data | No data | No data | No data | -2.59 | 27.6 | 1.02 | 1.10 |
| 4 | 4880 | 448.8 | No data | No data | No data | No data | 2.69 | 27.6 | 1.06 | 1.97 |
| 5 | 4880 | 556.4 | No data | No data | No data | No data | 3.41 | 4.0 | 1.35 | 1.37 |
| 6 | 4880 | 717.1 | No data | No data | No data | No data | 3.68 | 3.0 | 1.45 | 0.69 |

Note: negative displacements are recorded when the LVDTs are compressed and positive displacements when the LVDTs are extended.

Table 6.4: Maximum displacements, maximum support rotations and residual displacements for Wall 2

| Blast test | Driver length $L_d$ $mm$ | Driver pressure $P_d$ $kPa$ | LVDT-Middle | | | | LVDT-Bottom | | | |
|---|---|---|---|---|---|---|---|---|---|---|
| | | | Maximum displacement $u_{Mid.-max}$ $mm$ | Time to maximum $t_{Mid.-max}$ $ms$ | Maximum support rotation $\theta_{Mid.-max}$ $^\circ$ | Residual displacement $u_{Mid.-res.}$ $mm$ | Maximum displacement $u_{Bot.-max}$ $mm$ | Time to maximum $t_{Bot.-max}$ $ms$ | Maximum support rotation $\theta_{Bot.-max}$ $^\circ$ | Residual displacement $u_{Bot.-res.}$ $mm$ |
| 1 | 4880 | 117.2 | -1.51 | 43.6 | 0.08 | 0.07 | -1.51 | 13.6 | 0.08 | 0.12 |
| 2 | 4880 | 212.4 | -3.68 | 18.8 | 0.20 | -0.54 | -3.30 | 16.6 | 0.18 | -0.35 |
| 3 | 4880 | 351.6 | -9.85 | 22.6 | 0.54 | -1.58 | -9.28 | 25.0 | 0.51 | -1.89 |
| 4 | 4880 | 406.8 | -14.35 | 23.6 | 0.79 | -1.78 | -13.68 | 23.6 | 0.75 | -2.65 |
| 5 | 4880 | 552.3 | -21.67 | 26.0 | 1.19 | -3.58 | -21.64 | 26.2 | 1.19 | -4.41 |
| 6 | 4880 | 710.8 | -33.74 | 26.6 | 1.86 | -11.10 | -33.53 | 26.4 | 1.85 | -12.18 |

Table 6.4: Maximum displacements, maximum support rotations and residual displacements for Wall 2 (continued)

| Blast test | Driver length $L_d$ $mm$ | Driver pressure $P_d$ $kPa$ | LVDT-Right | | | | LVDT-Left | | | |
|---|---|---|---|---|---|---|---|---|---|---|
| | | | Maximum displacement $u_{Rig.-max}$ $mm$ | Time to maximum $t_{Rig.-max}$ $ms$ | Maximum support rotation $\theta_{Rig.-max}$ $^\circ$ | Residual displacement $u_{Rig.-res.}$ $mm$ | Maximum displacement $u_{Lef.-max}$ $mm$ | Time to maximum $t_{Lef.-max}$ $ms$ | Maximum support rotation $\theta_{Lef.-max}$ $^\circ$ | Residual displacement $u_{Lef.-res.}$ $mm$ |
| 1 | 4880 | 117.2 | No data | No data | No data | No data | -1.52 | 42.2 | 0.18 | 0.04 |
| 2 | 4880 | 212.4 | No data | No data | No data | No data | -2.93 | 21.2 | 0.34 | -0.24 |
| 3 | 4880 | 351.6 | No data | No data | No data | No data | No data | No data | No data | No data |
| 4 | 4880 | 406.8 | No data | No data | No data | No data | No data | No data | No data | No data |
| 5 | 4880 | 552.3 | No data | No data | No data | No data | No data | No data | No data | No data |
| 6 | 4880 | 710.8 | No data | No data | No data | No data | No data | No data | No data | No data |

Note: negative displacements are recorded when the LVDTs are compressed and positive displacements when the LVDTs are extended.

Table 6.5: Experimental strain data for Wall 1

| Blast test | SG1-HT | | | | SG3-HT | | | | SG4-HT | | | | SG7-HT | | | |
|---|---|---|---|---|---|---|---|---|---|---|---|---|---|---|---|---|
| | $\varepsilon_{max}$ | $t_{max}$ | $\dot{\varepsilon}_{SG1}$ | $\sum\varepsilon_{res.}$ | $\varepsilon_{max}$ | $t_{max}$ | $\dot{\varepsilon}_{SG3}$ | $\sum\varepsilon_{res.}$ | $\varepsilon_{max}$ | $t_{max}$ | $\dot{\varepsilon}_{SG4}$ | $\sum\varepsilon_{res.}$ | $\varepsilon_{max}$ | $t_{max}$ | $\dot{\varepsilon}_{SG7}$ | $\sum\varepsilon_{res.}$ |
| | % | $ms$ | $s^{-1}$ | % | % | $ms$ | $s^{-1}$ | % | % | $ms$ | $s^{-1}$ | % | % | $ms$ | $s^{-1}$ | % |
| 1 | 0.0023 | 28.6 | 0.0008 | 0.0002 | 0.0047 | 27.6 | 0.0017 | 0.0007 | 0.0011 | 27.8 | 0.0004 | 0.0004 | 0.0027 | 27.6 | 0.0010 | 0.0006 |
| 2 | 0.0037 | 52.8 | 0.0007 | 0.0013 | 0.0063 | 4.6 | 0.0136 | 0.0024 | 0.0011 | 58.2 | 0.0002 | 0.0002 | 0.0048 | 51.2 | 0.0009 | 0.0025 |
| 3 | 0.0056 | 36.6 | 0.0015 | -0.0027 | 0.0084 | 6.0 | 0.0140 | -0.0024 | 0.0032 | 115.6 | 0.0003 | 0.0014 | 0.0120 | 36.6 | 0.0033 | 0.0039 |
| 4 | 0.0112 | 50.2 | 0.0022 | 0.0056 | 0.0127 | 51.8 | 0.0025 | 0.0051 | 0.0104 | 48.2 | 0.0022 | 0.0035 | 0.0208 | 32.0 | 0.0065 | 0.0126 |
| 5 | 0.0169 | 233.8 | 0.0007 | 0.0077 | 0.0219 | 32.2 | 0.0068 | 0.0098 | 0.0152 | 49.2 | 0.0031 | 0.0085 | 0.0346 | 26.6 | 0.0130 | 0.0160 |
| 6 | 0.0252 | 162.8 | 0.0015 | -0.0302 | 0.0467 | 25.6 | 0.0182 | 0.0218 | 0.0312 | 75.8 | 0.0041 | 0.0226 | 0.0511 | 25.6 | 0.0200 | 0.0206 |

Note: $\varepsilon_{max}$ is the maximum strain; $t_{max}$ is the time to maximum strain; $\dot{\varepsilon}_{SG}$ is the strain rate; and $\sum\varepsilon_{res.}$ is the cumulative residual strain.

Table 6.5: Experimental strain data for Wall 1 (continued)

| Blast test | SG8-HT | | | | SG9-HB | | | | SG10-HB | | | | SG11-HB | | | |
|---|---|---|---|---|---|---|---|---|---|---|---|---|---|---|---|---|
| | $\varepsilon_{max}$ | $t_{max}$ | $\dot{\varepsilon}_{SG8}$ | $\sum\varepsilon_{res.}$ | $\varepsilon_{max}$ | $t_{max}$ | $\dot{\varepsilon}_{SG9}$ | $\sum\varepsilon_{res.}$ | $\varepsilon_{max}$ | $t_{max}$ | $\dot{\varepsilon}_{SG10}$ | $\sum\varepsilon_{res.}$ | $\varepsilon_{max}$ | $t_{max}$ | $\dot{\varepsilon}_{SG11}$ | $\sum\varepsilon_{res.}$ |
| | % | $ms$ | $s^{-1}$ | % | % | $ms$ | $s^{-1}$ | % | % | $ms$ | $s^{-1}$ | % | % | $ms$ | $s^{-1}$ | % |
| 1 | 0.0009 | 47.6 | 0.0002 | 0.0003 | 0.0043 | 12.8 | 0.0034 | -0.0005 | 0.0064 | 10.2 | 0.0063 | -0.0001 | 0.0039 | 28.6 | 0.0014 | -0.0005 |
| 2 | 0.0024 | 69.2 | 0.0003 | 0.0006 | 0.0140 | 15.0 | 0.0094 | 0.0026 | 0.0412 | 21.6 | 0.0191 | 0.0199 | 0.0123 | 15.0 | 0.0082 | 0.0010 |
| 3 | 0.0050 | 168.0 | 0.0003 | -0.0012 | 0.0638 | 23.8 | 0.0268 | 0.0193 | 0.1052 | 24.2 | 0.0435 | 0.0357 | 0.0445 | 24.2 | 0.0184 | 0.0133 |
| 4 | 0.0273 | 51.4 | 0.0053 | 0.0013 | 0.1098 | 21.2 | 0.0518 | 0.0338 | 0.1432 | 13.2 | 0.1085 | 0.0454 | 0.0871 | 21.4 | 0.0407 | 0.0246 |
| 5 | 0.0304 | 49.2 | 0.0062 | 0.0045 | 0.1801 | 24.2 | 0.0744 | 0.0444 | 0.2567 | 26.6 | 0.0965 | 0.0692 | 0.1658 | 23.4 | 0.0708 | 0.0424 |
| 6 | 0.0320 | 75.8 | 0.0042 | 0.0150 | 0.2507 | 25.6 | 0.0979 | 0.0594 | 0.3834 | 27.2 | 0.1410 | 0.1459 | 0.2487 | 28.6 | 0.0869 | 0.0632 |

Table 6.5: Experimental strain data for Wall 1 (continued)

| Blast test | SG12-VB | | | | SG14-HB | | | |
|---|---|---|---|---|---|---|---|---|
| | $\varepsilon_{max}$ | $t_{max}$ | $\dot{\varepsilon}_{SG12}$ | $\sum\varepsilon_{res.}$ | $\varepsilon_{max}$ | $t_{max}$ | $\dot{\varepsilon}_{SG14}$ | $\sum\varepsilon_{res.}$ |
| | % | $ms$ | $s^{-1}$ | % | % | $ms$ | $s^{-1}$ | % |
| 1 | 0.0026 | 39.4 | 0.0007 | 0.0005 | 0.0083 | 9.4 | 0.0089 | 0.0003 |
| 2 | 0.0080 | 6.6 | 0.0121 | 0.0023 | 0.0467 | 21.6 | 0.0216 | 0.0194 |
| 3 | 0.0106 | 21.0 | 0.0051 | -0.0016 | 0.1078 | 24.2 | 0.0446 | 0.0330 |
| 4 | 0.0291 | 32.0 | 0.0091 | 0.0067 | 0.1361 | 21.6 | 0.0630 | 0.0417 |
| 5 | 0.0696 | 21.6 | 0.0322 | 0.0189 | 0.2067 | 26.6 | 0.0777 | 0.0499 |
| 6 | 0.1216 | 25.6 | 0.0475 | 0.0363 | 0.2518 | 17.2 | 0.1464 | 0.0599 |

Table 6.6: Experimental strain data for Wall 2

| Blast test | SG1-HT/SG5-HT | | | | SG3-HT | | | | SG4-HT | | | | SG7-HT | | | |
|---|---|---|---|---|---|---|---|---|---|---|---|---|---|---|---|---|
| | $\varepsilon_{max}$ % | $t_{max}$ $ms$ | $\dot{\varepsilon}_{SG1}$ $s^{-1}$ | $\sum\varepsilon_{res.}$ % | $\varepsilon_{max}$ % | $t_{max}$ $ms$ | $\dot{\varepsilon}_{SG3}$ $s^{-1}$ | $\sum\varepsilon_{res.}$ % | $\varepsilon_{max}$ % | $t_{max}$ $ms$ | $\dot{\varepsilon}_{SG4}$ $s^{-1}$ | $\sum\varepsilon_{res.}$ % | $\varepsilon_{max}$ % | $t_{max}$ $ms$ | $\dot{\varepsilon}_{SG7}$ $s^{-1}$ | $\sum\varepsilon_{res.}$ % |
| 1 | 0.0299 | 2.4 | 0.1247 | 0.0042 | 0.0065 | 45.0 | 0.0015 | 0.0028 | 0.0011 | 55.0 | 0.0002 | -0.0001 | 0.0053 | 67.0 | 0.0008 | 0.0022 |
| 2 | 0.0394 | 0.8 | 0.4929 | -0.0005 | 0.0131 | 27.0 | 0.0049 | 0.0007 | 0.0017 | 66.0 | 0.0003 | -0.0001 | 0.0118 | 27.0 | 0.0044 | 0.0024 |
| 3 | 0.0098 | 41.4 | 0.0024 | -0.0021 | 0.0147 | 41.8 | 0.0035 | -0.0027 | 0.0027 | 44.4 | 0.0006 | -0.0009 | 0.0123 | 38.6 | 0.0032 | 0.0013 |
| 4 | 0.0130 | 39.2 | 0.0033 | 0.0005 | 0.0153 | 37.4 | 0.0041 | -0.0021 | 0.0032 | 49.8 | 0.0007 | -0.0006 | 0.0137 | 37.0 | 0.0037 | 0.0018 |
| 5 | 0.0136 | 32.4 | 0.0042 | 0.0015 | 0.0163 | 32.4 | 0.0050 | -0.0007 | 0.0061 | 49.4 | 0.0012 | 0.0005 | 0.0148 | 32.4 | 0.0046 | 0.0029 |
| 6 | 0.0149 | 30.2 | 0.0049 | 0.0062 | 0.0175 | 30.2 | 0.0058 | 0.0049 | 0.0066 | 21.4 | 0.0031 | 0.0031 | Strain Gauge Damaged | | | |

Note: Tests 1 and 2 for SG1-HT, Tests 3, 4, 5 and 6 for SG5-HT.

Table 6.6: Experimental strain data for Wall 2 (continued)

| Blast test | SG8-HT | | | | SG9-HB | | | | SG10-HB | | | | SG11-HB | | | |
|---|---|---|---|---|---|---|---|---|---|---|---|---|---|---|---|---|
| | $\varepsilon_{max}$ % | $t_{max}$ $ms$ | $\dot{\varepsilon}_{SG8}$ $s^{-1}$ | $\sum\varepsilon_{res.}$ % | $\varepsilon_{max}$ % | $t_{max}$ $ms$ | $\dot{\varepsilon}_{SG9}$ $s^{-1}$ | $\sum\varepsilon_{res.}$ % | $\varepsilon_{max}$ % | $t_{max}$ $ms$ | $\dot{\varepsilon}_{SG10}$ $s^{-1}$ | $\sum\varepsilon_{res.}$ % | $\varepsilon_{max}$ % | $t_{max}$ $ms$ | $\dot{\varepsilon}_{SG11}$ $s^{-1}$ | $\sum\varepsilon_{res.}$ % |
| 1 | 0.0029 | 67.0 | 0.0004 | 0.0000 | 0.0112 | 14.6 | 0.0076 | 0.0017 | 0.0073 | 14.8 | 0.0049 | -0.0007 | 0.0105 | 14.4 | 0.0073 | 0.0015 |
| 2 | 0.0076 | 29.0 | 0.0026 | 0.0002 | 0.0210 | 14.0 | 0.0150 | 0.0053 | 0.0169 | 13.6 | 0.0124 | 0.0021 | 0.0198 | 13.6 | 0.0145 | 0.0052 |
| 3 | 0.0082 | 38.6 | 0.0021 | -0.0014 | 0.0414 | 13.0 | 0.0318 | 0.0185 | 0.1006 | 22.2 | 0.0453 | 0.0209 | 0.0335 | 93.0 | 0.0036 | 0.0213 |
| 4 | 0.0087 | 18.4 | 0.0047 | -0.0012 | 0.0430 | 39.8 | 0.0108 | 0.0256 | 0.1467 | 20.8 | 0.0705 | 0.0283 | 0.0958 | 18.4 | 0.0521 | 0.0275 |
| 5 | 0.0109 | 29.4 | 0.0037 | 0.0019 | 0.0916 | 32.4 | 0.0283 | 0.0379 | 0.2030 | 20.4 | 0.0995 | 0.0345 | 0.1166 | 24.2 | 0.0482 | 0.0317 |
| 6 | 0.0400 | 30.2 | 0.0132 | 0.0268 | 0.1511 | 26.6 | 0.0568 | 0.0414 | 0.2259 | 21.6 | 0.1046 | 0.0379 | 0.1707 | 26.0 | 0.0656 | 0.0358 |

Table 6.6: Experimental strain data for Wall 2 (continued)

| Blast test | SG12-VB | | | | SG14-HB | | | |
|---|---|---|---|---|---|---|---|---|
| | $\varepsilon_{max}$ % | $t_{max}$ $ms$ | $\dot{\varepsilon}_{SG12}$ $s^{-1}$ | $\sum\varepsilon_{res.}$ % | $\varepsilon_{max}$ % | $t_{max}$ $ms$ | $\dot{\varepsilon}_{SG14}$ $s^{-1}$ | $\sum\varepsilon_{res.}$ % |
| 1 | 0.0073 | 67.0 | 0.0011 | 0.0045 | 0.0083 | 12.6 | 0.0066 | 0.0002 |
| 2 | 0.0163 | 27.0 | 0.0060 | 0.0048 | 0.0122 | 13.6 | 0.0090 | -0.0001 |
| 3 | 0.0280 | 170.8 | 0.0016 | 0.0173 | 0.0472 | 23.8 | 0.0198 | 0.0089 |
| 4 | 0.0308 | 68.6 | 0.0045 | 0.0211 | 0.0957 | 23.8 | 0.0402 | 0.0180 |
| 5 | 0.0389 | 29.4 | 0.0132 | 0.0243 | 0.1549 | 20.4 | 0.0759 | 0.0243 |
| 6 | 0.0483 | 29.0 | 0.0167 | 0.0306 | 0.1746 | 18.4 | 0.0949 | 0.0240 |

# Chapter 7 Single-Degree-Of-Freedom Analysis of RC Reservoir Walls

## 7.1 General

The scaled RC reservoir walls that were tested under simulated blast loading were modelled using the Single-Degree-Of-Freedom (SDOF) method. The SDOF procedure is a simple and cost-effective method which requires limited input data and computation. The SDOF model is widely used to predict the dynamic response of reinforced concrete structures subjected to blast loading. The SDOF analysis in this research work was only based on one scenario: two opposite lateral edges fixed, and base and top free to represent Wall 2. The resistance-displacement response used as input to the SDOF analysis was generated based on known and calculated strengths and stiffness values of the concrete and reinforcement. The analysis results are presented in Sections 7.3, 7.4 and 7.5. The analytical results were compared against the experimental data to validate the SDOF model for predicting the dynamic response of the RC reservoir walls subjected to the blast loading. In addition, the intent of SDOF was to investigate the influence of the assumed support conditions.

## 7.2 Dynamic Single-Degree-Of-Freedom (SDOF) Analysis

The following paragraph is based on the study of Ngo et al. (2007). The dynamic response of structures subjected to blast loading is a complex phenomenon. It is typically a nonlinear problem that involves dynamics, high strain-rate effects, large deformation, non-linear material properties and complex structural interaction. However, the analysis can be simplified through assumptions and simplifications related to the response of the structure (equivalent SDOF system) and the blast loads (triangular pulse). These assumptions and simplifications have been widely accepted and usually result in close approximations to the actual dynamic structural response. When dealing with dynamic load effects, it is common to transform the affected structure into a SDOF system. By doing this, the calculations are simplified, but the computed

results remain sufficiently accurate. For SDOF analysis of blast loads, a link is established between the positive phase duration and the natural period of the structure. This leads to blast load idealization and simplifies the classification of the blast loading regimes.

### 7.2.1 Equivalent SDOF systems

The *Single Degree-Of-Freedom* (SDOF) system is the simplest vibratory system. It can be described by a single mass connected to a spring which is permitted to deform only along the axis of the spring. In real structures, the structural members have distributed masses and multiple degrees of freedom. To use SDOF approximations to solve such problems, the real structure is transformed into a dynamically equivalent SDOF system. To convert the real structure to the equivalent SDOF system, it is necessary to incorporate transformation factors: mass factor $(K_M)$ and load factor $(K_L)$, which can be applied to the real mass and load to establish equivalent values. According to the study of Ngo et al. (2007), the actual structure can be transformed into an equivalent SDOF system, which has one concentrated mass and one weightless spring. This equivalent SDOF system represents the resistance of the structure against deformation. Figure 7.1 provides this idealized system as discussed in Section 3.3.1.

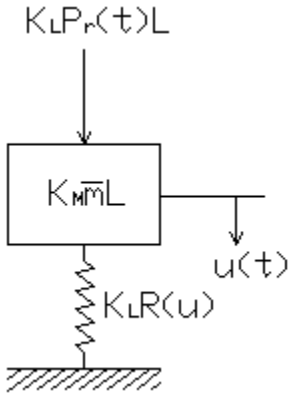


Figure 7.1: Equivalent SDOF system

The blast load, which an equivalent SDOF system is subjected to, can be idealized as a triangular pulse delivering a peak force $P_r$. The positive phase duration of the blast load is $t_d$. The idealized loading function is illustrated in Figure 7.2. The forcing function is given as:

$$P_r(t) = P_r\left(1 - \frac{t}{t_d}\right) \quad [7.1]$$

where $P_r$ is the peak reflected pressure and $t_d$ is the duration of the first positive phase.

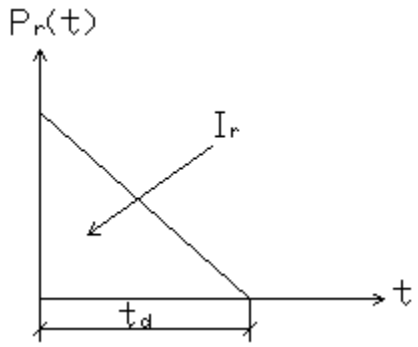


Figure 7.2: Idealized pressure-time histories

The impulse, $I$, equals the area under the pressure-time history and is defined as:

$$I = \int_0^{t_d} P_r(t)dt = \frac{P_r t_d}{2} \quad [7.2]$$

Based on static equilibrium of dynamic forces, the response of the SDOF system without damping can be written as:

$$m\ddot{u}(t) + ku(t) = AP(t) \quad [7.3]$$

Equating Equations [7.3] and [7.1] generates the following second order differential equation:

$$m\ddot{u}(t) + ku(t) = AP_r\left(1 - \frac{t}{t_d}\right) \quad [7.4]$$

The displacement solution to Equation [7.4] during the forced-vibration phase when $0 \leq t \leq t_d$ is:

$$u(t) = \left(u_0 - \frac{Ap_r}{k}\right) cos\omega t + \frac{v_0 + {Ap_r}/{kt_d}}{\omega} sin\omega t + \frac{Ap_r}{k}\left(1 - \frac{t}{t_d}\right) \quad [7.5]$$

where $\omega = \sqrt{k/m}$ is the natural frequency of the structure, and $u_0$ and $v_0$ are the initial displacement and velocity at time $t = 0$, respectively.

The free-vibration displacement response of the system in Equation [7.4] when $t \geq t_d$ is given by:

$$u(t) = u_{t_d} cos\omega(t - t_d) + \frac{v_{t_d}}{\omega} sin\omega(t - t_d) \quad [7.6]$$

where $u_{t_d}$ and $v_{t_d}$ are the displacement and velocity of the mass at time $t = t_d$, respectively.

### 7.2.2 Elastic-plastic SDOF systems

Structural elements (e.g. wall) are expected to undergo large inelastic deformation under blast load. The deformations of the material are mostly recoverable while the response is in the elastic range. When the load exceeds the yield limit, permanent deformations can be expected. When the load is removed, the unloading response of the wall follows a path defined by elastic stiffness and deformations decrease from the previous maximum value to the permanent deformation. If the wall is reloaded, the response again follows the elastic stiffness to the previous maximum deformation until the yield limit is reached and, thereafter, the plastic deformations continue to increase. Ngo et al. (2007) reported that the use of a step-by-step numerical solution which requires nonlinear dynamic finite-element software is the only method to conduct an exact analysis of dynamic structural response. However, there is substantial uncertainty in the loading and understanding the predicted deformations. Therefore, the solution from an equivalent elastic-plastic SDOF system (Biggs 1964) is commonly used. The interpretation of displacement is based on the ductility factor $\mu = \frac{y_m}{y_e}$.

The resistance of reinforced concrete elements subjected to blast loading is highly nonlinear. In practice, a resistance-displacement relationship (resistance function) can be used to predict the resistance in a dynamic test. In the test of a simply supported wall or slab element bending in one way under uniform loading with the assumption that a single plastic hinge will form at center span of the panel, the displacement of such a panel is represented by an elastic-perfectly plastic response. The resistance function is simplified as illustrated in Figure 7.3. At a certain displacement, the wall or slab element will continuously yield at near constant resistance until it reaches the ultimate displacement limit, the point at which the wall or slab element will eventually fail. Therefore, it is important to adopt an accurate resistance response function which represents the actual behaviour of the structure to obtain an accurate prediction of the dynamic response of the structure under blast loading.

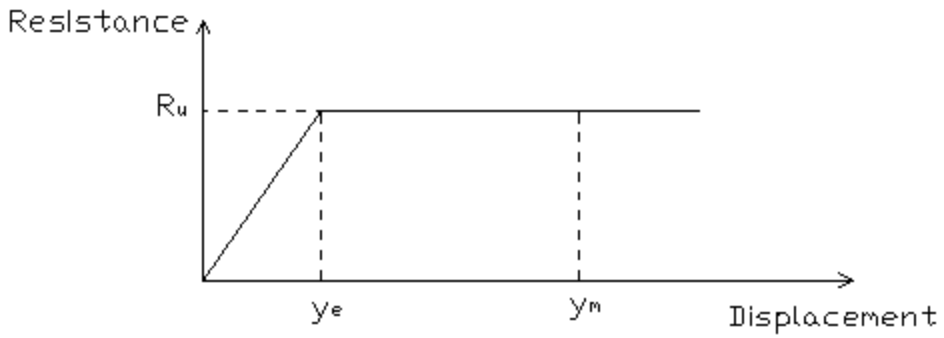


Figure 7.3: Simplified resistance function of an elastic-plastic SDOF system (Ngo et al. 2007)

### 7.2.3 Resistance-displacement curves

The resistance-displacement curve relates the load that is resisted as a function of the displacement experienced by the blast-loaded structural component. It can be derived with conventional static calculation methods, including applicable DIFs (Dynamic Increase Factors). The load in the resistance-displacement response has the same spatial distribution as the applied blast load, typically a uniformly distributed pressure load. In a ductile reinforced concrete component, the load resistance increases approximately linearly with displacement until the reinforcing steel yields in the maximum moment regions, and then the resistance remains relatively constant with increasing displacement until failure. As described in the subsequent sections, piecewise linear resistance curves, $R(u)$, were generated with material dynamic increase factors (DIFs) corresponding to an assumed strain-rate of $0.1\ s^{-1}$ as recommended by UFC 3-340-02 (2008) for explosions in the far-design range.

The equivalent resistance-displacement function for Wall 2 that experienced one-way bending was based on Biggs (1964) and UFC 3-340-02 (2008).

### 7.2.4 Transformation factors

In developing the equation of motion for the equivalent SDOF system, transformation factors are used to determine the equivalent mass, stiffness, resistance, and load. The transformation factors,

or the load factors, mass factors, and load-mass factors are defined in Biggs (1964) and UFC 3-340-02 (2008).

The piecewise linear load-mass transformation factors, $K_{LM}$, for one-way bending wall/slab, along with the load-mass transformation factors defined as step functions based on Biggs (1964) and UFC 3-340-02 (2008), respectively, were used in the dynamic analysis conducted in this research. For example, the load-mass factors for the one-way bending wall (two opposite lateral sides fixed, and base and top edges free) for the three ranges of behaviour (elastic, elastic-plastic and plastic) are 0.77, 0.78 and 0.66. For the analyses of the one-way bending wall/slab, the load-mass factor was taken as a weighted average of the three ranges of behaviour.

### 7.2.5 System mass

The wall mass was calculated based on the volume of the specimen that was bounded by the supports and subjected to blast pressures; the participation of mass located outside of the supports was assumed to be negligible. The unit weight, $\gamma_c$, of the reinforced concrete wall specimens was assumed to be $2400\ kg/m^3$. Note that the support system was connected to the shock tube frame through the ends of the wall outside of the blast loaded area. Therefore, the mass of the support system was judged not to contribute to the mass subjected to blast loading.

### 7.2.6 Loaded area

The area impacted by the blast-induced pressure wave is known as the loaded area, $A_l$. This area was calculated based on the area of the shock tube opening on the blast loaded face of the wall specimens. The loaded area for the two wall specimens was $4.13\ m^2$.

### 7.2.7 Pressure-time history

The reflected pressure-time history used as the load-time function input for the dynamic analysis was recorded by two pressure sensors. Both sensors were placed approximately 50 mm away from the test specimens and connected to the side wall of the expansion section of the shock

tube. One sensor was placed at the mid-height level of the wall specimens and the other near the base of the specimens. The side pressure gauge was used as the primary recording device, while the bottom gauge was used as a backup. The reflected pressures recorded by the side pressure gauge provided the primary data source for the load-time function used in the dynamic analysis. The discrepancy in the SDOF results by using either the side or bottom pressure gauge data is generally negligible.

### 7.2.8 Selection of time-step

The time step used for the numerical integration was $2 \times 10^{-4}$s ($0.2\,ms$) which was found to give acceptable results. It results in convergence in the solution.

## 7.3 Detailed Analysis for One-Way Bending Wall

The analysis for Wall 2, which was controlled by one-way bending, adopted the equivalent SDOF method in a step-by-step calculation subjected to blast loads using tables and figures published in Biggs (1964) and UFC 3-340-02 (2008) to simplify the procedure.

### 7.3.1 Design parameters

The dynamic response under blast load is a function of the applied load, the maximum resistance of the element experiencing the loading, and its geometry and yield line response. Analyses performed in accordance with UFC 3-340-02 (2008) is based on an external load consisting of only a shock loading phase; typically a triangular pulse, with an instantaneous rise to the peak pressure followed by a linear decay.
The geometry and support conditions of the wall specimen are important parameters in analyzing dynamic response subjected to the blast load.

The geometry and support conditions of the wall specimen are as follows:

a) Geometry of Wall 2

b = 2550 mm  a = 2440 mm  h = 100 mm

b) Support conditions

Fixed on opposite lateral sides, and free on the top and bottom edges

c) Diagram of boundary conditions and load-time function

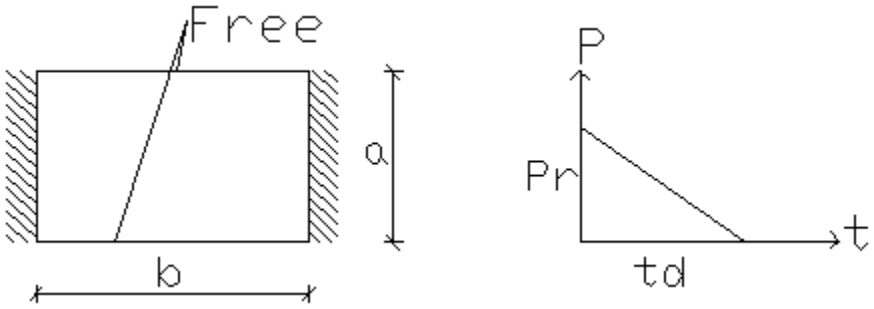


Figure 7.4: Boundary conditions for one-way wall and load-time function

## 7.3.2 Dynamic material strength of reinforcing steel and concrete

The dynamic concrete and reinforcing steel strengths are based on the approach in UFC 3-340-02 (2008), which allows the material strengths to be increased for higher strain-rate effects. Table 7.1 provides the dynamic increase factor (DIF) for design of reinforced concrete elements. The reinforcing steel yield strength and the concrete compressive cylinder strength, as provided in Chapter 5 were:

$f_y = 465.2\ MPa$, and $f_c' = 35.9\ MPa$

Table 7.1: Dynamic increase factor (DIF) for design of reinforced concrete elements (UFC 3-340-02 2008)

| TYPE OF STRESS | FAR DESIGN RANGE | | | CLOSE-IN DESIGN RANGE | | |
|---|---|---|---|---|---|---|
| | Reinforcing Bars | | Concrete | Reinforcing Bars | | Concrete |
| | $f_{dy}/f_y$ | $f_{du}/f_u$ | $f'_{dc}/f'_c$ | $f_{dy}/f_y$ | $f_{du}/f_u$ | $f'_{dc}/f'_c$ |
| Bending | 1.17 | 1.05 | 1.19 | 1.23 | 1.05 | 1.25 |
| Diagonal Tension | 1.00 | ------ | 1.00 | 1.10 | 1.00 | 1.00 |
| Direct Shear | 1.10 | 1.00 | 1.10 | 1.10 | 1.00 | 1.10 |
| Bond | 1.17 | 1.05 | 1.00 | 1.23 | 1.05 | 1.00 |
| Compression | 1.10 | ------ | 1.12 | 1.13 | ------ | 1.16 |

The dynamic strength of materials (reinforcing steel and concrete) accounting for strain-rate effects according to Table 7.1 is:

$f_{dy} = DIF \times f_y = 1.17 \times 465.2 = 544.3\ MPa$

$f'_{dc} = DIF \times f'_c = 1.19 \times 35.9 = 42.7\ MPa$

The DIFs are based on the far-design range and bending stresses due to the level of blast loading imposed on the wall specimens and the main response mode of the specimens, respectively.

### 7.3.3 Moment of inertia and modulus of elasticity of concrete

The moment of inertia and the modulus of elasticity of concrete were calculated as follows:

a) Reinforcing steel ratio of Wall 2, $\rho_s$:

$\rho_s = \frac{A_s}{ad} = \frac{19\times2\times100}{2440\times83} = 0.0188$

Note that this reinforcement ratio includes both tension and compression reinforcement and is used to determine the moment of inertia of the section.

b) The effective depth of Wall 2, $d$:

$d = 83\ mm$

Using the empirical expression (Biggs 1964), the moment of inertia is as follows:

$I_a = \frac{bd^3}{2}(5.5\rho_s + 0.083) = \frac{1 \times 83^3}{2} \times (5.5 \times 0.0188 + 0.083) = 53290.5\ mm^4/mm$

The modulus of elasticity of concrete, $E_c$, was based on the Canadian Standards Association Standard A23.3-04 (Design of Concrete Structures):

$E_c = 4500\sqrt{f'_{dc}} = 4500\sqrt{42.7} = 29408.0\ MPa$

### 7.3.4 Equivalent elastic unit stiffness of system and load-mass factor

The clear distance between supports, $b_s$:

$b_s = 2080\ mm$

From Table 7.2 (Biggs 1964), the equivalent elastic unit stiffness $K_E$ is calculated:

$K_E = \frac{307 E_c I_a}{{b_s}^2} = \frac{307 \times 29408.0 \times 53290.5}{2080^2} = 111200\ N/mm = 111200000\ N/m$

From Table 7.2 (Biggs 1964), the load-mass factors for uniformly distributed loading for the three ranges of behaviour (elastic, elastic-plastic and plastic) are 0.77, 0.78 and 0.66, respectively. The load-mass factor for the system is the average of the load-mass factors in the three ranges of behaviour. Since the behaviour was assumed to be primarily elastic, a value near that for the elastic range is used based on the following weighted average: $K_{LM} = \frac{0.77+\frac{0.78+0.66}{2}}{2} = 0.745$

Table 7.2: Transformation factors for beams and one-way slabs (Biggs 1964)

| *Loading diagram* | *Strain range* | *Load factor* $K_L$ | *Mass factor* $K_M$ | | *Load-mass factor* $K_{LM}$ | | *Maximum resistance* $R_m$ | *Spring constant* $k$ | *Effective spring constant* $k_E$† | *Dynamic reaction* $V$ |
|---|---|---|---|---|---|---|---|---|---|---|
| | | | *Concentrated mass** | *Uniform mass* | *Concentrated mass** | *Uniform mass* | | | | |
| $F = pL$ <br> $L$ | Elastic | 0.53 | ... | 0.41 | ... | 0.77 | $\frac{12\mathfrak{M}_P}{L}$ | $\frac{384EI}{L^3}$ | ..... | $0.36R + 0.14F$ |
| | Elastic-plastic | 0.64 | ... | 0.50 | ... | 0.78 | $\frac{8}{L}(\mathfrak{M}_P + \mathfrak{M}_{P_m})$ | $\frac{384EI}{5L^3}$ | $\frac{307EI}{L^3}$ | $0.39R + 0.11F$ |
| | Plastic | 0.50 | .. | 0.33 | ... | 0.66 | $\frac{8}{L}(\mathfrak{M}_P + \mathfrak{M}_{P_m})$ | 0 | ..... | $0.38R_m + 0.12F$ |
| $F$ <br> $\frac{L}{2}$ $\frac{L}{2}$ | Elastic | 1.0 | 1.0 | 0.37 | 1.0 | 0.37 | $\frac{4}{L}(\mathfrak{M}_P + \mathfrak{M}_{P_m})$ | $\frac{192EI}{L^3}$ | ..... | $0.71R - 0.21F$ |
| | Plastic | 1.0 | 1.0 | 0.33 | 1.0 | 0.33 | $\frac{4}{L}(\mathfrak{M}_P + \mathfrak{M}_{P_m})$ | 0 | ..... | $0.75R_m - 0.25F$ |

### 7.3.5 Mass, loaded area, natural frequency, and natural period of the system

The mass, loaded area, natural frequency, and natural period of the system were calculated as follows:

a) Mass

Assume density of reinforced concrete, $\gamma$:

$\gamma = 2400\ kg/m^3$

Mass of wall that was subjected to blast pressures was bounded by the side fixed supports and the top and bottom free edges, $M_w$:

$M_w = \gamma V_s = \gamma a b_s h = 2400 \times 2.440 \times 2.080 \times 0.1 = 1218.0\ kg$

b) Loaded area

Loaded area, $A_l$:

$A_l = a_l \times b_l = 2.032 \times 2.032 = 4.129\ m^2$

c) Natural frequency

Natural frequency of system, $\omega$:

$$\omega = \sqrt{\frac{K_E}{K_{LM} M_w}} = \sqrt{\frac{111200000}{0.745 \times 1218.0}} \div 10^3 = 0.3501\ ms^{-1}$$

d) Natural period

The natural period of the system, $T_n$:

$$T_n = 2\pi \sqrt{\frac{K_{LM} M_w}{K_E}} = 2\pi \sqrt{\frac{0.745 \times 1218.0}{111200000}} \times 10^3 = 17.9\ ms$$

### 7.3.6 Bending strength of wall specimen

The bending strength of Wall 2 was based on the dynamic strength of the reinforcement, $f_{ds}$ and the concrete, $f'_{dc}$, provided in Table 7.3. [Note: the bending strength was only based on

contribution from the tension reinforcement; the compression reinforcement provided negligible bending strength.]

a) The value of $\alpha_1$:

$\alpha_1 = 0.85 - 0.0015 f'_{dc} = 0.85 - 0.0015 \times 42.7 = 0.79$

b) Depth of equivalent rectangular stress block, $a'$:

$$a' = \frac{A_s f_{dy}}{\alpha_1 a f'_{dc}} = \frac{(19 \times 100) \times 544.3}{0.79 \times 2440 \times 42.7} = 12.56\ mm$$

c) Assume maximum support rotation, $\theta_m$:

If $0^\circ < \theta_m \leq 2^\circ$, then $f_{ds} = f_{dy}$

d) The bending unit strength of the wall, $m^0_{Psb}$:

$$m^0_{Psb} = \frac{A_s f_{dy}}{a}\left(d - \frac{a'}{2}\right) = \frac{(19 \times 100) \times 544.3}{2440} \times \left(83 - \frac{12.56}{2}\right) = 32.52\ kN.mm/mm$$

Table 7.3: Dynamic design stresses for reinforcement and concrete

(UFC 3-340-02 2008)

| TYPE OF STRESS | TYPE OF REINFORCEMENT | MAXIMUM SUPPORT ROTATION, $\theta_m$ (DEGREES) | DYNAMIC DESIGN STRESS | |
|---|---|---|---|---|
| | | | REINFORCEMENT, $f_{ds}$ | CONCRETE, $f_{dc}$ |
| Bending | Tension and Compression | $0 < \theta_m \leq 2$<br>$2 < \theta_m \leq 6$<br>$6 < \theta_m \leq 12$ | $f_{dy}$ (1)<br>$f_{dy} + (f_{du} - f_{dy})/4$<br>$(f_{dy} + f_{du})/2$ | $f_{dc}$<br>(2)<br>(2) |
| Diagonal Tension | Stirrups | $0 < \theta_m \leq 2$<br>$2 < \theta_m \leq 6$<br>$6 < \theta_m \leq 12$ | $f_{dy}$<br>$f_{dy}$<br>$f_{dy}$ | $f_{dc}$<br>$f_{dc}$<br>$f_{dc}$ |
| Diagonal Tension | Lacing | $0 < \theta_m \leq 2$<br>$2 < \theta_m \leq 6$<br>$6 < \theta_m \leq 12$ | $f_{dy}$<br>$f_{dy} + (f_{du} - f_{dy})/4$<br>$(f_{dy} + f_{du})/2$ | $f_{dc}$<br>$f_{dc}$<br>$f_{dc}$ |
| Direct Shear | Diagonal Bars | $0 < \theta_m \leq 2$<br>$2 < \theta_m \leq 6$<br>$6 < \theta_m \leq 12$ | $f_{dy}$<br>$f_{dy} + (f_{du} - f_{dy})/4$<br>$(f_{dy} + f_{du})/2$ | $f_{dc}$<br>(3)<br>(3) |
| Compression | Column | (4) | $f_{dy}$ | $f_{dc}$ |

### 7.3.7 Resistance of wall specimen

Using the bending unit strength of the wall, the resistance was determined as follows:

a) The resistance, $R_E$, based on the equivalent stiffness and the displacement is as follows:

$$R_E = K_E u \quad [7\text{-}7]$$

b) The ultimate moment capacity at the support and midspan are equivalent, leading to:

$$m_{Ps} = m_{Pm} = a m_{Psb}^0 \quad [7\text{-}8]$$

c) Using Table 7.2, the maximum resistance of the wall based on an elastic-plastic response, $R_m$ is:

$$R_m = \frac{8}{b_s}(m_{Ps} + m_{Pm}) = \frac{8}{b_s}(a m_{Psb}^0 + a m_{Psb}^0) = \frac{16 a m_{Psb}^0}{b_s} \quad [7\text{-}9]$$

$$R_m = \frac{16 \times 2440 \times 32.52}{2080} = 610.4\ kN$$

### 7.3.8 Equivalent SDOF equation of motion

The equation of motion for an equivalent SDOF system to determine the dynamic response to blast loading is as follows:

$$K_{LM} M_w \ddot{u}(t) + K_E u(t) = A_l p_r(t) \quad [7\text{-}10]$$

$$K_{LM} M_w \ddot{u}(t) + K_E u(t) = A_l p_r \left(1 - \frac{t}{t_d}\right) \quad [7\text{-}11]$$

The loading function on the right side of the equation is based on a triangular representation as illustrated in Figure 7.4.

### 7.3.9 Reflected pressure and displacement-time history response

The reflected pressure is based on a triangular pressure distribution to represent the actual reflected pressure and is determined from the following:

when $0 \le t \le t_d$ $\quad p_r(t) = p_r \left(1 - \frac{t}{t_d}\right)$ [7-12]

when $t > t_d$ $\quad p_r(t) = 0$ [7-13]

The displacement of the SDOF system that is experienced during the forced vibration phase is:

$$u(t) = \left(u_0 - \frac{A_l p_r}{K_E}\right) cos\omega t + \frac{\left(v_0 + {}^{A_l p_r}/_{K_E t_d}\right)}{\omega} sin\omega t + \frac{A_l p_r}{K_E}\left(1 - \frac{t}{t_d}\right) \quad \text{when } 0 \le t \le t_d \quad [7\text{-}14]$$

The displacement of the SDOF system that is experienced during the free vibration phase is:

$$u(t) = u_{t_d} cos\omega(t - t_d) + \frac{v_{t_d}}{\omega} sin\omega(t - t_d) \quad \text{when } t > t_d \quad [7\text{-}15]$$

## 7.3.10 Sample calculation for Wall 2: one-way bending

The following parameters were used as input to the SDOF calculations:

*Test 6:* $p_r = 100.1\ k\ Pa$, and $I_r = 2122.4\ kPa - ms$

The duration of the triangular blast load: $t_{df} = \frac{2I_r}{p_r} = \frac{2\times2122.4}{100.1} = 42.4\ ms$

Initial time: $t_0 = 0\ ms$

Time step: $\Delta t = \frac{T_n}{90} = \frac{17.9}{90} = 0.20\ ms$

Time: $t_{i+1} = t_i + \Delta t$

Initial displacement: $u(0) = u_0 = 0\ mm$

Initial velocity: $v(0) = v_0 = 0\ mm/ms$

Displacement when $0 \le t \le t_d$:

$$u(t) = \left(u_0 - \frac{A_l p_r}{K_E}\right) cos\omega t + \frac{\left(v_0 + {}^{A_l p_r}/_{K_E t_d}\right)}{\omega} sin\omega t + \frac{A_l p_r}{K_E}\left(1 - \frac{t}{t_d}\right)$$

Displacement when $t > t_d$:

$$u(t) = u_{t_d} cos\omega(t - t_d) + \frac{v_{t_d}}{\omega} sin\omega(t - t_d)$$

The outcome of the SDOF analysis is a displacement-time history. The displacement response can be used to develop a resistance-displacement response as provided in Figure 7.5. The resistance is determined from the stiffness of the system and the displacement and is capped by the maximum resistance ($R = K_E u \le R_m$). Figure 7.5 provides the response for blast test 6. Point B in the response provides the yield point ($u_{yield}$, $R_m$), while the maximum displacement is given by point C ($u_{max}$, $R_m$). The maximum displacement calculated with SDOF for blast test 6

was 6.69 mm (Point C). Note that this displacement does not consider damage that was experienced by the wall during previous blast loading.

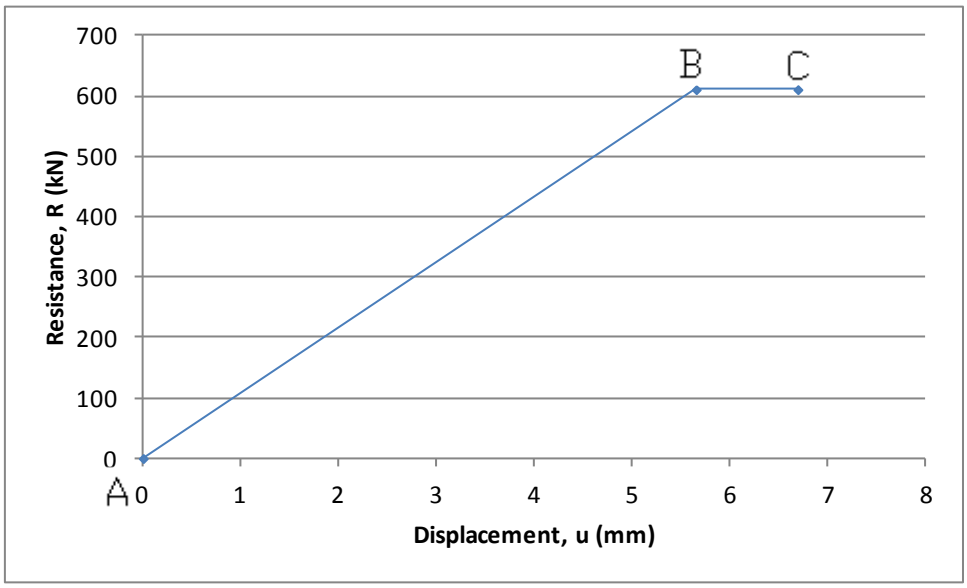


Figure 7.5: Resistance-displacement response for Wall 2 subjected to blast test 6 ($P_r = 100.1$ kPa and $I_r = 2122.4$ kPa $-$ ms)

## 7.4 Analytical Results

The analytical results are presented in the following sections.

### 7.4.1 Equivalent SDOF and experimental maximum displacements

For the one-way bending wall (Wall 2), the reflected pressure was 64.8 $kPa$ and the reflected impulse was 1102.2 $kPa - ms$ for blast test 3. The displacement according to the SDOF method was 4.21 $mm$. The relative displacements experienced during testing were 9.31 $mm$ at the middle LVDT and 8.93 $mm$ at the bottom LVDT. For blast test 6, the reflected pressure was 100.1 $kPa$ and the reflected impulse was 2122.4 $kPa - ms$. The displacement calculated using the SDOF method was 6.69 $mm$, while the relative displacements from testing were 30.16 $mm$ at the middle LVDT and 29.12 $mm$ at the bottom LVDT. The SDOF analysis procedure underestimated the displacements for blast tests 3-6. Discrepancies can be attributed to the

assumption of fully fixed side supports and not accounting for previous damage from prior blast tests. In addition, it is probable that assumptions in the SDOF modelling contributed to the discrepancies in the results. This includes treating the response of an actual structural element with distributed mass by a single concentred mass, and using a weighted average of the three different behavioural ranges to determine the transformation factors.

Table 7.4 provides a comparison of the maximum displacements between the SDOF analysis and testing.

Table 7.4: Comparison of maximum displacements based on the SDOF analysis (fixed-fixed) and recorded experimentally for Wall 2

| Blast test | Wall 2 | | |
|---|---|---|---|
| | Equivalent SDOF method displacement $mm$ | Experimental method displacement $mm$ | Ratio (SDOF/Test) |
| 1 | 1.45 | 1.52 | 0.95 |
| 2 | 2.65 | 3.75 | 0.71 |
| 3 | 4.21 | 9.31 | 0.45 |
| 4 | 4.39 | 12.77 | 0.34 |
| 5 | 5.91 | 19.89 | 0.30 |
| 6 | 6.69 | 30.16 | 0.22 |

For the one-way bending (Wall 2), the ratio of the maximum displacements from the SDOF method to the test results ranged from approximately 0.22 to 0.95.

## 7.4.2 Equivalent SDOF predicted and experimental yielding of wall specimen

According to the equivalent SDOF analysis, yielding was predicted to occur during test 5 with a reflected pressure of 89.0 $kPa$, and a reflected impulse of 1794.7 $kPa-ms$. In Figure 7.6, yielding is defined by Point B. The strain gauge data from testing indicated that yielding was not experienced by the end of testing corresponding to blast test 6 (reflected pressure of 100.1 $kPa$ and reflected impulse of 2122.4 $kPa-ms$). The maximum strain gauge (SG10-HB) reading during test 6 was 2259 $\mu\varepsilon$, which was slightly smaller than the yield strain (2550 $\mu\varepsilon$). Note, however, that the midpan region of Wall 2 where cracking/damage was concentrated did not

contain strain gauges as a result of the strain gauge location based on the assumed damage pattern for Wall 1. Therefore, it is probable that the reinforcement at midspan did experience yielding.

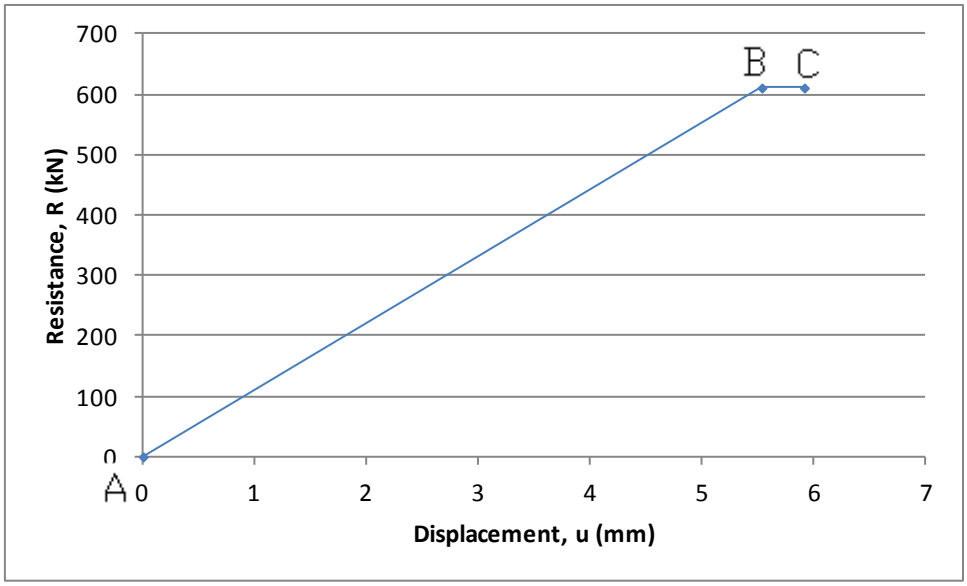


Figure 7.6: Resistance-displacement response of Wall 2 for blast test 5 ($P_r = 89.0$ kPa and $I_r = 1794.7$ kPa $-$ ms)

## 7.5 Effect of Assumed Supports Conditions

A parametric SDOF analysis was performed to investigate the degree of fixity of the side supports, which were initially assumed to be fully fixed during testing. Furthermore, the previous analysis results were also based on the assumption of full fixity. The analysis was based solely on Wall 2, which only had supports on the two opposite lateral sides. The parametric analysis was conducted assuming that the side supports were pinned. Table 7.5 provides the SDOF results along with those recorded during testing.

Table 7.5: Comparison of maximum displacements based on the SDOF analysis (pinned-pinned) and recorded experimentally for Wall 2

| Blast test | Wall 2 | | |
|---|---|---|---|
| | Equivalent SDOF method displacement $mm$ | Experimental method displacement $mm$ | Ratio (SDOF/Test) |
| 1 | 5.02 | 1.52 | 3.30 |
| 2 | 9.19 | 3.75 | 2.45 |
| 3 | 14.70 | 9.31 | 1.58 |
| 4 | 15.59 | 12.77 | 1.22 |
| 5 | 21.06 | 19.89 | 1.06 |
| 6 | 23.97 | 30.16 | 0.79 |

The results illustrate that the assumption of pinned side supports is reasonably accurate for blast tests 4-6. In comparison with Table 7.4, the SDOF analysis provides better results when the supports are assumed fully fixed for blast tests 1 and 2. The results seem to suggest that the system behaved as fixed during the first few blast tests. However, with increasing blast tests, the supports began to rotate and behaved more closely as pins.

# Chapter 8 Conclusions and Future Work

## 8.1 Summary

Experimental and complementary analytical investigations were carried out on reinforced concrete reservoir walls to study the performance and dynamic structural response subjected to the blast loading. One, two-way dominant reinforced concrete wall and one, one-way dominant reinforced concrete wall were tested under shock tube-induced blast loading. Two support conditions were investigated: (1) two opposite lateral edges fixed, base edge hinged and top edge free for the two-way bending wall; and (2) two opposite lateral edges fixed, and base and top edges free for the one-way bending wall. Each specimen was subjected to six consecutive blast tests using the same driver length and similar driver pressures. Testing was conducted using a shock tube testing facility. The performance of the one-way bending wall was analyzed with the equivalent SDOF method.

The SDOF analysis of the one-way dominant wall was conducted to determine displacement response. Force-deformation characteristics of the one-way bending wall were determined based on simplified relations (tables and figures) commonly used in design and analysis of blast-resistant structures. The force-deformation characteristics were used to perform an equivalent single-degree-of-freedom analysis to determine the displacements experienced by the wall for each blast test. The SDOF displacements were compared against the experimental recorded displacements to assess the ability to predict the dynamic response of the RC reservoir walls to blast loading.

The following conclusions were drawn for this experimental and analytical research program along with recommendations for future research.

## 8.2 Conclusions

The main purpose of this study was to experimentally and analytically investigate dynamic response of RC reservoir walls subjected to blast loading and to provide experimental test data and information for future research in this area. To achieve this objective, an experimental program was conducted using shock tube to investigate the behaviour of reinforced concrete reservoir walls subjected to blast loading. The analytical analysis was conducted using the equivalent SDOF method. The experimental results were compared to the analytical results for the one-way RC reservoir wall. This study suggests that the theoretical analysis using the equivalent SDOF method should only be used for preliminary analysis and design provided that the assumed support conditions are correct, that any previous damage is accounted for, and that assumptions inherent in the SDOF do not significantly affect the results.

Based on the experimental test results and the SDOF analyses, the following conclusions can be reached:

- The reflected pressures and impulses measured during testing for the same driver length and similar drive pressures were generally in agreement for the two walls.
- The reflected impulses were positively correlated with the reflected pressures for the six blast tests for the two walls.
- The reflected pressures and impulses were positively correlated with the maximum displacements for the six blasts tests for the two walls.
- During the last blast test, both walls experienced similar maximum displacements. However, the residual displacement in Wall 2 was significantly higher than Wall 1.
- Although the capacity of the shock tube was not sufficient to generate large inelastic behaviour in the two-way wall (Wall 1) during testing, yielding was recorded by the strain gauges during blast test 5. At this stage the wall was in elastic-plastic range.
- Although yielding was expected to occur in Wall 2 given that yielding was recorded for Wall 1, the strain gauges in Wall 2 experienced strains less than the yield strain. This was a direct result of the strain gauge location for both walls being selected based on the assumed damage pattern for Wall 1.

- The cracking pattern for Wall 1 was typical of theoretical yield line patterns for the support conditions used during testing. Wall 2 experienced typical one-way cracking patterns for walls/slabs.
- The displacements calculated using the equivalent SDOF method underestimated the displacements recorded during testing of the one-way bending wall (Wall 2), specifically from blast tests 3-6. With increasing reflected pressure and impulse, this difference became larger.
- The discrepancy between the analytical results and experimental results can be attributed to assumptions in the SDOF method, such as assuming the opposite lateral sides were fully fixed. Furthermore, the SDOF method did not incorporate residual damage in the wall due to prior blast loading, which would result in a reduction in the system stiffness leading to increased displacements due to subsequent blast loading.
- A parametric study investigating the assumed support conditions for Wall 2, demonstrated that for the initial blast tests, the assumption of full fixity was appropriate. However, for subsequent blast testing, an assumption of pinned supports provided better agreement with the experimental results.
- In general, the equivalent single-degree-of-freedom method is an approximate method for the analysis of blast-loaded reinforced concrete members. It can be used for preliminary analysis and design provided the assumed support conditions are correct.

## 8.3 Future Work

The following recommendations are intended for future research:

- Future research should consider improved support conditions during testing that can better provide full fixity for the sides of the test specimens.
- Testing should be conducted with the walls retaining water to simulate the condition when the reservoir tanks are in operation.
- Parametric SDOF studies should be conducted to include various degrees of fixity of the side supports.

- Parameters used in the equivalent SDOF method should consider more influencing factors such as concrete strength, reinforcement ratios, support conditions, and geometry of the cross section.
- More advanced nonlinear finite element modelling should be investigated that can simulate the support conditions of the four edges of the wall, specifically for cases where the support conditions are irregular.

# References

ACI Committee 350. (2006). "Code Requirements for Environmental Engineering Concrete Structures (ACI 350M-06) and Commentary". *American Concrete Institute*, Farmington Hills, MI, USA.

Ahmad, S., Taseer, M., and Pervaiz, H. (2012). "Effects of Impulsive Loading on Reinforced Concrete Structures". *Technical Journal, University of Engineering and Technology Taxila, Vibration analysis issue.*

Ambrosini, D., Luccioni, B., Jacinto, A., and Danesi, R. (2005). "Location and Mass of Explosive From Structural Damage". *Engineering Structures*. 27(2), 167-176.

AMCO Water. (2014). "A Circular Concrete Reservoir". http://www.amcowater.com.au/about-us/. Last Accessed: 2014/06/15.

Bangash, M. Y. H. & Bangash, T. (2006). "Explosion-Resistant Buildings". *Springer-Verlag Berlin Heidelberg*, London, UK.

Biggs, J. M. (1964)."Introduction to Structural Dynamics". McGraw-Hill, New York, USA.

Cement Association of Canada. (2005). "Concrete Design Handbook". *Canada Standards Association*, Mississauga, ON, Canada.

Duranovic, N. (1998). "Impulsive Loading on Reinforced Concrete Slabs – Modelling Considerations". *International Conference on Structures Under Shock and Impact*, SUSI, 817-826.

EI-Dakhakhni, W. W., Mekky, W. F., Changiz Rezaei, S. H. (2010). “Validity of SDOF Models for Analyzing Two-Way Reinforced Concrete Panels under Blast Loading”. *Journal of Performance of Constructed Facilities,* 24(4), 311-325.

Glasstone S. and Dolan, P. J. (1977). “The Effects of Nuclear Weapons”. Third Edition. Prepared and published by the United States Department of Defence and the Energy Research and Development Administration.

Holmberg, M. W. (2009). “Reinforced Concrete Tank Design”. *Structure Magazine,* 22-23.

Huntington-Thresher, W. K. E. and Cullis, I. G. (2001). "TNT Blast Scaling For Small Charges". *19th International Symposium of Ballistics, 7–11 May 2001, Interlaken, Switzerland.* Defence Evaluation and Research Agency, Fort Halstead, Sevenoaks, Kent TN14 7BP, UK.

Jacques, E. (2011). "Blast Retrofit of Reinforced Concrete Walls and Slabs". *Master of Applied Science Thesis,* University of Ottawa.

Kennedy, G. and Goodchild, C. (2003). "Practical Yield Line Design". Reinforced Concrete Council. British Cement Association, UK.

Lan, S. R. and Crawford, J. C. (2003). “Evaluation of the Blast Resistance of Metal Deck Roofs”. *In Proceeding of the fifth Asia-Pacific conference on shock & impact loads on structures.* 3–12, Changsha, Hunan, China.

Li, Q. M. and Meng, H. (2002). “Pressure-Impulse Diagram for Blast Loads Based on Dimensional Analysis and Single-Degree-of Freedom Model”. *Journal of Engineering Mechanics,* 128(1), 87-92.

Lloyd, A., Jacques, E., Saatcioglu, M., Palermo, D., Nistor, I., and Tikka, T. (2010) "Capabilities and Effectiveness of Using A Shock Tube to Simulate Blast Loading on Structures and Structural Components". Submitted for review, ACI Special Publication on Blast, Pittsburgh, PA.

Loiseau, O., Cheval, K., and Kevorkian, S. (2008). "Laboratory scale tests for the assessment of solid explosive blast effects". *Tenth International Conference on Structures Under Shock and Impact,* Algarve, Portugal.

Lu, B., Silva, P., Nanni, A., and Baird, J. (2005). "Retrofit for Blast Resistant RC Slabs With Composite Materials". *International Concrete Abstracts Portal.* American Concrete Institute (ACI). Special Publication. Vol. 230, 1345-1360.

Luccioni, B. M., Ambrosini, R. D., and Danesi, R. F. (2004). "Analysis of Building Collapse Under Blast Loads". *Engineering Structures*. 26(1), 63-71.

Magnusson, J. (2007). "Structural Concrete Elements Subjected to Air Blast Loading". Licentiate thesis, KTH, Department of Civil and Architectural Engineering, Stockholm, Sweden.

Mays, G. C. and Smith, P. D. (1995), "Blast Effects on Buildings". Thomas Telford Publications, London, UK.

Mazars, J. (1986). "A Description of Micro and Macro Scale Damage of Concrete Structures". *Engineering Fracture Mechanics*. Volume 25, Issues 5-6, 729 – 737.

Morison, Colin M. (2006). "Dynamic Response of Walls and Slabs by Single-Degree-Of-Freedom Analysis-A Critical Review and Revision". *International Journal of Impact Engineering*, 32(8), 1214-1247.

Ngo, T., Mendis, P., Gupta, A. & Ramsay, J. (2007). "Blast Loading and Blast Effects on Structures-An Overview", *EJSE Special Issue: Loading on Structures*, 76-91, University of Melbourne, Australia.

Portland Cement Association (PCA). (1993). "Circular Concrete Tanks without Prestressing". Skokie, Illinois, USA.

Priyanka, M. and Munirudrappa, N. (2012). “Blast Loading and Its Effects on Structures – A Critical Review”. *NBM Media’s Publications: NBM&CW*. New Delhi, India.

Quan, X. (2005). “Applications of a Coupled Multi-solver Approach in Evaluating Damage of Reinforced Concrete Walls from Shock and Impact”. *18th International Conference on Structural Mechanics in Reactor Technology (SMiRT 18),* 2539-2547, Beijing, China.

Rashed, A. A., Rogowsky, D. M., and Elwi, A. E. (1997). “Rational Design of Prestressed and Reinforced Concrete Tanks”. *Structural Engineering Report No. 220. Department of Alberta Department of Civil & Environmental Engineering. University of Alberta.*

Razaqpur, A. G., Tolba, A., and Contestabile, E. (2007). “Blast Loading Response of Reinforced Concrete Panels with Externally Bonded GFRP Laminates”. *Composites*, B38, 535-546.

Shi, Y. C., Li, Z. X., and Hao, H. (2010). “A New Method for Progressive Collapse Analysis of RC Frames under Blast Loading”. *Engineering Structures*, 32, 1691-1703.

Syed, Z. I., Mendis, P., Lam, N. T. K., and Ngo, T. (2006). "Concrete Damage Assessment for Blast Load Using Pressure-Impulse Diagrams". *Earthquake Engineering in Australia, Canberra,* 24-26. University of Melbourne, Australia.

Tai, Y. S., Chu, T. L., Hu, H. T., and Wu, J. Y. (2011). “Dynamic Response of A Reinforced Concrete Slab Subjected to Air Blast Load”. *Theoretical and Applied Fracture Mechanics*, 56(3), 140-147.

Toutlemonde, F., Rossi, P., Boulay, C., Gourraud, C., and Guedon, C. (1995). “Dynamic Behaviour of Concrete: Tests of Slabs with A Shock Tube”. *Materials and Structures*, 28(179), 293-298.

U.S. Army corps of engineers, Naval facilities engineering command, and Air force civil engineer support agency (2008). "Structures to Resist The Effects of Accidental Explosions". UFC3-340-02.

Wager, P. C. (1994). "Yield Line Analysis of Slabs With Covered Openings". *26th DoD Explosives Safety Seminar.* August 16 - 18. Miami, Florida, USA.

Xu, K., and Lu, Y. (2006). "Numerical Simulation Study of Spallation in Reinforced Concrete Plates Subjected to Blast Loading". *Computers & Structures*, 84(5-6), 431-438.

Zhou, X. Q., and Hao, H. (2008). "Numerical Prediction of Reinforced Concrete Exterior Wall Response to Blast Loading". *Advances in Structural Engineering*, 11(4), 355-367.

# Appendix A: Detailed Design of Regular Circular Reinforced Concrete (RC) Reservoir Walls Utilizing the PCA (1993) Design Method

This appendix contains details of the design of the RC reservoir wall specimens in Chapter 4. The aim of this appendix is to illustrate the application of the circular tank design approach proposed in PCA (1993). The prototype wall is circular in shape, above ground and with boundary conditions consisting of a hinge at the base and free at the top. The wall is designed to sustain the forces from triangular loading conditions. PCA (1993) tables for circular tanks were used for the structural analysis.

## A 1 Design Details

A prototype design of a circular concrete reservoir tank was conducted using the values listed below, from which scaled test specimens were derived and subjected to blast loading:

Tank volume, $V = 10000\ m^3 = 353146.67\ ft^3$

Tank wall height, $H = 9\ m = 29.53\ ft$

Diameter to inside of tank, $D = 37.61\ m = 123.40\ ft$

Weight of liquid, $w = 1\ g/cm^3 = 62.5\ lb/ft^3$

Shrinkage coefficient of concrete, $C = 0.0003$

Modulus of elasticity of steel, $E_s = 200000\ MPa = 29 \times 10^6\ psi$

Specified compressive strength of concrete, $f_c' = 30\ MPa = 4351\ psi$

Modulus of elasticity of concrete, $E_c = 4700\sqrt{f_c'} = 25743\ MPa = 3.73 \times 10^6\ psi$

Allowable concrete tensile stress for cylindrical tank design, $0.10f_c' = 3\ MPa = 435\ psi$

Ratio of moduli of elasticity, $n = E_s/E_c = 8$

Specified yield strength of reinforcement, $f_y = 400\ MPa = 58015\ psi$

Allowable stress in reinforcement, $f_s = 124.11\ MPa = 18000\ psi$

## A 1.1 Horizontal design of exterior wall – ring tensile forces

As a first approximation, assume the wall to be 508 mm (1.67 ft) thick. Weight of liquid, $w = 1\ g/cm^3 = 62.5\ lb/ft^3$.

According to ACI350, $w_u$ for ring tension

$w_u = sanitary\ cofficient \times (1.7 \times Lataral\ Force) = 1.65 \times (1.7 \times w)$

$= 1.65 \times (1.7 \times 62.5) = 175.3\ lb/ft^3$

$w_u = 175.3\ lb/ft^3$ $H = 9\ m = 29.53\ ft$ $R = 18.81\ m = 61.70\ ft$

$D = 37.61\ m = 123.40\ ft$ $f_s = 18000\ psi$ $H^2/Dt = 4.24$ $\emptyset = 1.0$

The ring tension per foot of height is computed by multiplying $w_u HR$ by the coefficients in Table A.1 with the value of $H^2/Dt = 4.24$.

Table A.1 is used to determine the ring tension based on a triangular load and hinged base and free top.

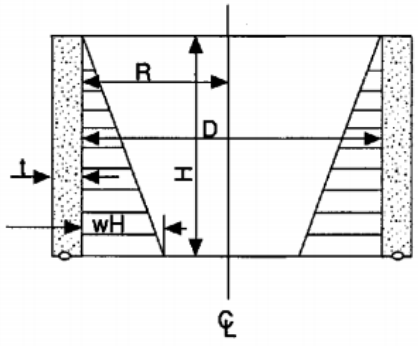


Figure A.1: Hinged base-free top under triangular load

(Circular concrete tanks without prestressing 1993)

Table A.1: Tension in circular rings for hinged base-free top under triangular load

(Circular concrete tanks without prestressing 1993)

T = coef. × wHR lb per ft

Positive sign indicates tension

| | Coefficients at point | | | | | | | | | |
|---|---|---|---|---|---|---|---|---|---|---|
| $\frac{H^2}{Dt}$ | 0.0H | 0.1H | 0.2H | 0.3H | 0.4H | 0.5H | 0.6H | 0.7H | 0.8H | 0.9H |
| 0.4 | +0.474 | +0.440 | +0.395 | +0.352 | +0.308 | +0.264 | +0.215 | +0.165 | +0.111 | +0.057 |
| 0.8 | +0.423 | +0.402 | +0.381 | +0.358 | +0.330 | +0.297 | +0.249 | +0.202 | +0.145 | +0.076 |
| 1.2 | +0.350 | +0.355 | +0.361 | +0.362 | +0.358 | +0.343 | +0.309 | +0.256 | +0.186 | +0.098 |
| 1.6 | +0.271 | +0.303 | +0.341 | +0.369 | +0.385 | +0.385 | +0.362 | +0.314 | +0.233 | +0.124 |
| 2.0 | +0.205 | +0.260 | +0.321 | +0.373 | +0.411 | +0.434 | +0.419 | +0.369 | +0.280 | +0.151 |
| 3.0 | +0.074 | +0.179 | +0.281 | +0.375 | +0.449 | +0.506 | +0.519 | +0.479 | +0.375 | +0.210 |
| 4.0 | +0.017 | +0.137 | +0.253 | +0.367 | +0.469 | +0.545 | +0.579 | +0.553 | +0.447 | +0.256 |
| 5.0 | -0.008 | +0.114 | +0.235 | +0.356 | +0.469 | +0.562 | +0.617 | +0.606 | +0.503 | +0.294 |
| 6.0 | -0.011 | +0.103 | +0.223 | +0.343 | +0.463 | +0.566 | +0.639 | +0.643 | +0.547 | +0.327 |
| 8.0 | -0.015 | +0.096 | +0.208 | +0.324 | +0.443 | +0.564 | +0.661 | +0.697 | +0.621 | +0.386 |
| 10.0 | -0.008 | +0.095 | +0.200 | +0.311 | +0.428 | +0.552 | +0.666 | +0.730 | +0.678 | +0.433 |
| 12.0 | -0.002 | +0.097 | +0.197 | +0.302 | +0.417 | +0.541 | +0.664 | +0.750 | +0.720 | +0.477 |
| 14.0 | 0.000 | +0.098 | +0.197 | +0.299 | +0.408 | +0.531 | +0.659 | +0.761 | +0.752 | +0.513 |
| 16.0 | +0.002 | +0.100 | +0.198 | +0.299 | +0.403 | +0.521 | +0.650 | +0.764 | +0.776 | +0.536 |

***Supplemental Coefficients***

| | Coefficient at point | | | | |
|---|---|---|---|---|---|
| $\frac{H^2}{Dt}$ | .75H | .80H | .85H | .90H | .95H |
| 20 | +0.812 | +0.817 | +0.756 | +0.603 | +0.344 |
| 24 | +0.816 | +0.839 | +0.793 | +0.647 | +0.377 |
| 32 | +0.814 | +0.861 | +0.847 | +0.721 | +0.436 |
| 40 | +0.802 | +0.866 | +0.880 | +0.778 | +0.483 |
| 48 | +0.791 | +0.864 | +0.900 | +0.820 | +0.527 |
| 56 | +0.781 | +0.859 | +0.911 | +0.852 | +0.563 |

Location 0.0H refers to the top of the wall and location 1.0H the base of the wall.

The ring tension is computed at intervals of 0.1H throughout the height of wall using Table A.2.

Table A.2: Tension in cylindrical rings (for tension in horizontal wall strips of 1ft height)

| Point | coef. from Table A.1 $H^2/Dt=4$ | coef. from Table A.1 $H^2/Dt=5$ | coef. from Table A.1 $H^2/Dt=4.24$ | Ring tensile force $T_u$=coef.$w_u$HR (lb/ft) Hinged | Rebar area $A_s=T_u/\varphi f_y$ ($in^2$/ft) | Rebar area $A_s=T_u/\varphi f_y$ ($mm^2$/m) |
|---|---|---|---|---|---|---|
| Top | 0.017 | -0.008 | 0.011 | 3520 | 0.06 | 128.00 |
| 0.1H | 0.137 | 0.114 | 0.131 | 42000 | 0.72 | 1524.00 |
| 0.2H | 0.253 | 0.235 | 0.249 | 79431 | 1.37 | 2899.84 |
| 0.3H | 0.367 | 0.356 | 0.364 | 116377 | 2.01 | 4254.51 |
| 0.4H | 0.469 | 0.469 | 0.469 | 149796 | 2.58 | 5461.01 |
| 0.5H | 0.545 | 0.562 | 0.549 | 175369 | 3.02 | 6392.34 |
| 0.6H | 0.579 | 0.617 | 0.588 | 187833 | 3.24 | 6858.01 |
| 0.7H | 0.553 | 0.606 | 0.566 | 180674 | 3.11 | 6582.84 |
| 0.8H | 0.447 | 0.503 | 0.460 | 147048 | 2.53 | 5355.18 |
| 0.9H | 0.256 | 0.294 | 0.265 | 84668 | 1.46 | 3090.34 |
| Bottom | 0.000 | 0.000 | 0.000 | 0 | 0.00 | 0.00 |

***Bars will be installed on both faces in the horizontal direction:***

*Top-0.40H* $A_s$=2.58 $in^2/ft = 2.58 \times 2116.67 = 5461\ mm^2/m$

*Use 35M deformed bars spaced 250 mm in each curtain of reinforcement for horizontal direction* ($A_s = 8000\ mm^2/m$).

*0.40H-0.70H* $A_s = 3.24\ in^2/ft = 3.24 \times 2116.67 = 6858\ mm^2/m$

*Use 35M deformed bars spaced 250 mm in each curtain of reinforcement for horizontal direction* ($A_s = 8000\ mm^2/m$).

*0.70H-Bottom* $A_s = 3.11\ in^2/ft = 3.11 \times 2116.67 = 6583\ mm^2/m$

*Use 35M deformed bars spaced 250 mm in each curtain of reinforcement for horizontal direction* ($A_s = 8000\ mm^2/m$).

Ratio of horizontal reinforcement:

$$\rho_h = \frac{A_s}{bt}$$

Take 1 ft height of wall ($12\ in$); the horizontal reinforcement is placed on the outside of the vertical reinforcement.

($t = 20\ in$)

$A_s = 8000\ mm^2/m = 8000 \times 0.00047244 = 3.78\ in^2/ft$

$$\rho_h = \frac{A_s}{bt} = \frac{3.78}{12 \times 20} = 0.0158$$

Maximum ring tensile stress in concrete under service loads and including the effects of shrinkage:

$C = 0.0003$

$A_g = 12t = 12 \times 20 = 240\ in^2$ (Choose 1 ft height of wall)

Maximum area of ring steel:

$$A_s = \frac{T_{max}}{\emptyset f_y} = \frac{187833}{1.0 \times 58015} = 3.24\ in^2/ft$$

Take 35M@250, $A_s = 3.78\ in^2/ft$

$E_c = 4700\sqrt{f_c'} = 4700\sqrt{30} = 25743\ MPa = 3.73 \times 10^6\ psi$

$E_s = 200000\ MPa = 29 \times 10^6\ psi$

$$n = \frac{E_s}{E_c} = \frac{29 \times 10^6}{3.73 \times 10^6} \approx 8$$

$T_{max} = 187833\ lb$

Maximum tensile stress in the concrete under service loads and including the effects of shrinkage:

$$f_c = \frac{CE_sA_s + T_{max(unfactored)}}{A_g + nA_s} = \frac{0.0003 \times 29 \times 10^6 \times 3.78 + \frac{187833}{1.65 \times 1.7}}{240 + 8 \times 3.78} = 371\ psi$$

$f_c/f_c' = 371/4351 = 8.5\ \% < 12\ \%$ OK

Since 435 psi is considered acceptable, the 20 in wall thickness is sufficient.

Check estimated thickness of wall, t:

$$t = \frac{CE_s + f_s - nf_c}{12 f_c f_s} \times T_{max(unfactored)}$$

$$= \frac{0.0003 \times 29 \times 10^6 + 18000 - 8 \times 435}{12 \times 435 \times 18000} \times \frac{187833}{1.65 \times 1.7} = 16.6\ in$$

Therefore, $t = 20\ in$ is enough for the wall thickness.

## A 1.2 Vertical flexure design of exterior wall – vertical moment and shear

The wall thickness, $t = 20\ in$

It is safe to assume that the internal fluid pressure will cause moments greater than the external soil pressure, even if the soil is saturated. The internal fluid pressure scenario will be used for the flexure design, and reinforcing will be the same on both faces.

According to ACI350, $w_u$ for flexure:

$$w_u = sanitary\ cofficient \times (1.7 \times Lataral\ Force) = 1.3 \times (1.7 \times w)$$

$$= 1.3 \times (1.7 \times 62.5) = 138.1\ lb/ft^3$$

$w_u = 138.1\ lb/ft^3$ $H = 9\ m = 29.53\ ft$ $R = 18.81\ m = 61.70\ ft$

$D = 37.61\ m = 123.40\ ft$ $H^2/Dt = 4.24$ $cover = 2\ in$

$d = t - cover - d_b - 1/2\ d_b = 15.89\ in$ $\emptyset = 1.0$

The moments in the vertical wall strips that are considered for the one foot wide strips are computed by multiplying $w_u H^3$ by the coefficients from Table A.3 with the value of $H^2/Dt = 4.24$.

Table A.3 is used to establish bending moments in circular walls subjected to triangular load and with hinged base support and free top edge. Table A.4 is also used as a design aid for bending moment reinforcement.

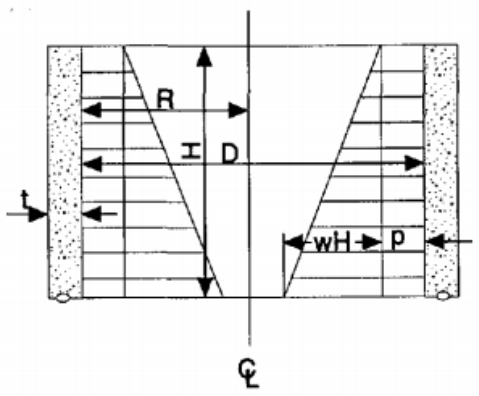


Figure A.2: Hinged base-free top under trapezoidal load

(Circular concrete tanks without prestressing 1993)

Table A.3: Moments in circular rings with hinged base-free top under trapezoidal load

(Circular concrete tanks without prestressing 1993)

Mom. = coef. × ($wH^3 + pH^2$) ft-lb per ft

Positive sign indicates tension in the outside

| $\frac{H^2}{Dt}$ | Coefficients at point | | | | | | | | | |
|---|---|---|---|---|---|---|---|---|---|---|
| | 0.1H | 0.2H | 0.3H | 0.4H | 0.5H | 0.6H | 0.7H | 0.8H | 0.9H | 1.0H |
| 0.4 | +.0020 | +.0072 | +.0151 | +.0230 | +.0301 | +.0348 | +.0357 | +.0312 | +.0197 | 0 |
| 0.8 | +.0019 | +.0064 | +.0133 | +.0207 | +.0271 | +.0319 | +.0329 | +.0292 | +.0187 | 0 |
| 1.2 | +.0016 | +.0053 | +.0111 | +.0177 | +.0237 | +.0280 | +.0296 | +.0263 | +.0171 | 0 |
| 1.6 | +.0012 | +.0044 | +.0091 | +.0145 | +.0195 | +.0236 | +.0255 | +.0232 | +.0155 | 0 |
| 2.0 | +.0009 | +.0033 | +.0073 | +.0114 | +.0158 | +.0199 | +.0219 | +.0205 | +.0145 | 0 |
| 3.0 | +.0004 | +.0013 | +.0040 | +.0063 | +.0092 | +.0127 | +.0152 | +.0153 | +.0111 | 0 |
| 4.0 | +.0001 | +.0007 | +.0016 | +.0033 | +.0057 | +.0083 | +.0109 | +.0118 | +.0092 | 0 |
| 5.0 | .0000 | +.0001 | +.0006 | +.0016 | +.0034 | +.0057 | +.0080 | +.0094 | +.0078 | 0 |
| 6.0 | .0000 | .0000 | +.0002 | +.0008 | +.0019 | +.0039 | +.0062 | +.0078 | +.0068 | 0 |
| 8.0 | .0000 | .0000 | -.0002 | .0000 | +.0007 | +.0020 | +.0038 | +.0057 | +.0054 | 0 |
| 10.0 | .0000 | .0000 | -.0002 | -.0001 | +.0002 | +.0011 | +.0025 | +.0043 | +.0045 | 0 |
| 12.0 | .0000 | .0000 | -.0001 | -.0002 | .0000 | +.0005 | +.0017 | +.0032 | +.0039 | 0 |
| 14.0 | .0000 | .0000 | -.0001 | -.0001 | -.0001 | .0000 | +.0012 | +.0026 | +.0033 | 0 |
| 16.0 | .0000 | .0000 | .0000 | -.0001 | .0002 | -.0004 | +.0008 | +.0022 | +.0029 | 0 |

***Supplemental Coefficients***

| $\frac{H^2}{Dt}$ | Coefficient at point | | | | |
|---|---|---|---|---|---|
| | .75H | .80H | .85H | .90H | .95H |
| 20 | +.0008 | +.0014 | +.0020 | +.0024 | +.0020 |
| 24 | +.0005 | +.0010 | +.0015 | +.0020 | +.0017 |
| 32 | .0000 | +.0005 | +.0009 | +.0014 | +.0013 |
| 40 | .0000 | +.0003 | +.0006 | +.0011 | +.0011 |
| 48 | .0000 | +.0001 | +.0004 | +.0008 | +.0010 |
| 56 | .0000 | .0000 | +.0003 | +.0007 | +.0008 |

Location 0.0H refers to the top of the wall and location 1.0H the base of the wall.

Table A.4: Design aid for bending moment reinforcement

(Circular concrete tanks without prestressing 1993)

| ω | .000 | .001 | .002 | .003 | .004 | .005 | .006 | .007 | .008 | .009 |
|---|---|---|---|---|---|---|---|---|---|---|
| 0.0 | 0 | .0010 | .0020 | .0030 | .0040 | .0050 | .0060 | .0070 | .0080 | .0090 |
| 0.01 | .0099 | .0109 | .0119 | .0129 | .0139 | .0149 | .0159 | .0168 | .0178 | .0188 |
| 0.02 | .0197 | .0207 | .0217 | .0226 | .0236 | .0246 | .0256 | .0266 | .0275 | .0285 |
| 0.03 | .0295 | .0304 | .0314 | .0324 | .0333 | .0343 | .0352 | .0362 | .0372 | .0381 |
| 0.04 | .0391 | .0400 | .0410 | .0420 | .0429 | .0438 | .0448 | .0457 | .0467 | .0476 |
| 0.05 | .0485 | .0495 | .0504 | .0513 | .0523 | .0532 | .0541 | .0551 | .0560 | .0569 |
| 0.06 | .0579 | .0588 | .0597 | .0607 | .0616 | .0625 | .0634 | .0643 | .0653 | .0662 |
| 0.07 | .0671 | .0680 | .0689 | .0699 | .0708 | .0717 | .0726 | .0735 | .0744 | .0753 |
| 0.08 | .0762 | .0771 | .0780 | .0789 | .0798 | .0807 | .0816 | .0825 | .0834 | .0843 |
| 0.09 | .0852 | .0861 | .0870 | .0879 | .0888 | .0897 | .0906 | .0915 | .0923 | .0932 |
| 0.10 | .0941 | .0950 | .0959 | .0967 | .0976 | .0985 | .0994 | .1002 | .1011 | .1020 |
| 0.11 | .1029 | .1037 | .1046 | .1055 | .1063 | .1072 | .1081 | .1089 | .1098 | .1106 |
| 0.12 | .1115 | .1124 | .1133 | .1141 | .1149 | .1158 | .1166 | .1175 | .1183 | .1192 |
| 0.13 | .1200 | .1209 | .1217 | .1226 | .1234 | .1243 | .1251 | .1259 | .1268 | .1276 |
| 0.14 | .1284 | .1293 | .1301 | .1309 | .1318 | .1326 | .1334 | .1342 | .1351 | .1359 |
| 0.15 | .1367 | .1375 | .1384 | .1392 | .1400 | .1408 | .1416 | .1425 | .1433 | .1441 |
| 0.16 | .1449 | .1457 | .1465 | .1473 | .1481 | .1489 | .1497 | .1506 | .1514 | .1522 |
| 0.17 | .1529 | .1537 | .1545 | .1553 | .1561 | .1569 | .1577 | .1585 | .1593 | .1601 |
| 0.18 | .1609 | .1617 | .1624 | .1632 | .1640 | .1648 | .1656 | .1664 | .1671 | .1679 |
| 0.19 | .1687 | .1695 | .1703 | .1710 | .1718 | .1726 | .1733 | .1741 | .1749 | .1756 |
| 0.20 | .1764 | .1772 | .1779 | .1787 | .1794 | .1802 | .1810 | .1817 | .1825 | .1832 |
| 0.21 | .1840 | .1847 | .1855 | .1862 | .1870 | .1877 | .1885 | .1892 | .1900 | .1907 |
| 0.22 | .1914 | .1922 | .1929 | .1937 | .1944 | .1951 | .1959 | .1966 | .1973 | .1981 |
| 0.23 | .1988 | .1995 | .2002 | .2010 | .2017 | .2024 | .2031 | .2039 | .2046 | .2053 |
| 0.24 | .2060 | .2067 | .2075 | .2082 | .2089 | .2096 | .2103 | .2110 | .2117 | .2124 |
| 0.25 | .2131 | .2138 | .2145 | .2152 | .2159 | .2166 | .2173 | .2180 | .2187 | .2194 |
| 0.26 | .2201 | .2208 | .2215 | .2222 | .2229 | .2236 | .2243 | .2249 | .2256 | .2263 |
| 0.27 | .2270 | .2277 | .2284 | .2290 | .2297 | .2304 | .2311 | .2317 | .2324 | .2331 |
| 0.28 | .2337 | .2344 | .2351 | .2357 | .2364 | .2371 | .2377 | .2384 | .2391 | .2397 |
| 0.29 | .2404 | .2410 | .2417 | .2423 | .2430 | .2437 | .2443 | .2450 | .2456 | .2463 |
| 0.30 | .2469 | .2475 | .2482 | .2488 | .2495 | .2501 | .2508 | .2514 | .2520 | .2527 |
| 0.31 | .2533 | .2539 | .2546 | .2552 | .2558 | .2565 | .2571 | .2577 | .2583 | .2590 |
| 0.32 | .2596 | .2602 | .2608 | .2614 | .2621 | .2627 | .2633 | .2639 | .2645 | .2651 |
| 0.33 | .2657 | .2664 | .2670 | .2676 | .2682 | .2688 | .2694 | .2670 | .2706 | .2712 |
| 0.34 | .2718 | .2724 | .2730 | .2736 | .2742 | .2748 | .2754 | .2760 | .2766 | .2771 |
| 0.35 | .2777 | .2783 | .2789 | .2795 | .2801 | .2807 | .2812 | .2818 | .2824 | .2830 |
| 0.36 | .2835 | .2841 | .2847 | .2853 | .2858 | .2864 | .2870 | .2875 | .2881 | .2887 |
| 0.37 | .2892 | .2898 | .2904 | .2909 | .2915 | .2920 | .2926 | .2931 | .2937 | .2943 |
| 0.38 | .2948 | .2954 | .2959 | .2965 | .2970 | .2975 | .2981 | .2986 | .2992 | .2997 |
| 0.39 | .3003 | .3003 | .3013 | .3019 | .3024 | .3029 | .3035 | .3040 | .3045 | .3051 |

Design: Using factored moment $M_u$, enter table with $M_u/\phi f'_c bd^2$; find ω and compute steel percentage ρ from $\rho = \omega f'_c / f_y$

Investigation: Enter table with ω from $\omega = \rho f_y / f'_c$ ; find value of $M_n / f'_c bd^2$ and solve for nominal strength $M_n$.

Bending moments are computed at intervals of 0.1H throughout the height of wall using Table A.5.

Table A.5: Moments in cylindrical wall (for moments in vertical wall strips of 1ft width)

| Point | coef. from Table A.3 $H^2/Dt=4$ | coef. from Table A.3 $H^2/Dt=5$ | coef. from Table A.3 $H^2/Dt=4.24$ | Moments $M_u=coef.w_uH^3$ (lbft/ft) |
|---|---|---|---|---|
| Top | 0.0000 | 0.0000 | 0.0000 | 0 |
| 0.1H | 0.0001 | 0.0000 | 0.0001 | 271 |
| 0.2H | 0.0007 | 0.0001 | 0.0006 | 1979 |
| 0.3H | 0.0016 | 0.0006 | 0.0014 | 4839 |
| 0.4H | 0.0033 | 0.0016 | 0.0029 | 10288 |
| 0.5H | 0.0057 | 0.0034 | 0.0051 | 18312 |
| 0.6H | 0.0083 | 0.0057 | 0.0077 | 27302 |
| 0.7H | 0.0109 | 0.0080 | 0.0102 | 36293 |
| 0.8H | 0.0118 | 0.0094 | 0.0112 | 39918 |
| 0.9H | 0.0092 | 0.0078 | 0.0089 | 31523 |
| Bottom | 0.0000 | 0.0000 | 0.0000 | 0 |

The required vertical reinforcement for the outside face of the wall for a maximum moment of $39918\ lbft/ft$ is:

$$\frac{M_u}{\emptyset f_c' bd^2} = \frac{39918 \times 12}{1.0 \times 4351 \times 12 \times 15.89^2} = 0.0363$$

From standard design aid of Table A.4:

$\omega = 0.0381$

$$A_s = \frac{\omega bd f_c'}{f_y} = \frac{0.0381 \times 12 \times 15.89 \times 4351}{58015} = 0.54\ in^2$$

$$\rho = \frac{A_s}{bd} = \frac{0.54}{12 \times 15.89} = 0.0029$$

$$\rho_{min} = \frac{200}{f_y} = \frac{200}{58015} = 0.0034 > 0.0029$$

Take $\rho_{min} = 0.0034$ to find $A_{smin}$

$A_{smin} = \rho_{min} bd = 0.0034 \times 12 \times 15.89 = 0.64\ in^2$

Use 20M@180 for inside vertical rebar

$A_s = 1666.67\ mm^2/m = 1666.67 \times 0.00047244 = 0.79\ in^2/in$

Use 20M@180 for inside vertical rebar

Ratio of inside vertical reinforcement:

$\rho_v = \frac{A_s}{bd} = \frac{0.79}{12 \times 15.89} = 0.0042 > \rho_{min}$ OK

Table A.6 was utilized to determine the shear forces at the base of cylindrical wall for a triangular load with a hinged base.

Table A.6: Shear at base of cylindrical wall

(Circular concrete tanks without prestressing 1993)

$$V = \text{coef.} \times \begin{cases} wH^2 \text{ lb. (triangular)} \\ pH \text{ lb. (rectangular)} \\ M/H \text{ lb. (moment at base)} \end{cases}$$

Positive sign indicates shear acting inward

| $\frac{H^2}{DI}$ | Triangular load, fixed base | Rectangular load, fixed base | Triangular or rectangular load, hinged base | Moment at edge |
|---|---|---|---|---|
| 0.4 | +0.436 | +0.755 | +0.245 | -1.58 |
| 0.8 | +0.374 | +0.552 | +0.234 | -1.75 |
| 1.2 | +0.339 | +0.460 | +0.220 | -2.00 |
| 1.6 | +0.317 | +0.407 | +0.204 | -2.26 |
| 2.0 | +0.299 | +0.370 | +0.189 | -2.57 |
| 3.0 | +0.262 | +0.310 | +0.158 | -3.18 |
| 4.0 | +0.236 | +0.271 | +0.137 | -3.68 |
| 5.0 | +0.213 | +0.243 | +0.121 | -4.10 |
| 6.0 | +0.197 | +0.222 | +0.110 | -4.49 |
| 8.0 | +0.174 | +0.193 | +0.096 | -5.18 |
| 10.0 | +0.158 | +0.172 | +0.087 | -5.81 |
| 12.0 | +0.145 | +0.158 | +0.079 | -6.36 |
| 14.0 | +0.135 | +0.147 | +0.073 | -6.88 |
| 16.0 | +0.127 | +0.137 | +0.068 | -7.36 |
| 20.0 | +0.114 | +0.122 | +0.062 | -8.20 |
| 24.0 | +0.102 | +0.111 | +0.055 | -8.94 |
| 32.0 | +0.089 | +0.096 | +0.048 | -10.36 |
| 40.0 | +0.080 | +0.086 | +0.043 | -10.62 |
| 48.0 | +0.072 | +0.079 | +0.039 | -12.76 |
| 56.0 | +0.067 | +0.074 | +0.036 | -13.76 |

The shear capacity of a 20 inch wall with $f_c' = 4351\ psi$ is:

$V_c = 2\sqrt{f_c'} b_w d = 2 \times \sqrt{4351} \times 12 \times 15.89 = 25155\ kips$

$\emptyset V_c = 1.0 \times 25155 = 25155\ kips$

The applied shear is given by multiplying $w_u H^2$ by the coefficient of 0.133 from Table A.7.

The value $w_u$ is determined using a sanitary coefficient of 1.0 if $V_u$ is less than $\emptyset V_c$:

$w_u = sanitary\ cofficient \times (1.7 \times Lataral\ Force) = 1.0 \times (1.7 \times w)$

$= 1.0 \times (1.7 \times 62.5) = 106.3\ lb/ft^3$

The resulting shear for triangular load is:

$V_u = coefficient \times w_u H^2 = 0.133 \times 106.3 \times 29.53^2 = 12337\ kips < 25155\ kips$

Compute shear at base of wall using Table A.7.

Table A.7: Shear at base of cylindrical wall (20 inch wide wall)

| Point | coef. from Table A.6 $H^2/Dt=4$ | coef. from Table A.6 $H^2/Dt=5$ | coef. from Table A.6 $H^2/Dt=4.24$ | Shear forces at base $V=coef.w_uH^2$ (lb/ft) |
|---|---|---|---|---|
| Bottom | 0.137 | 0.121 | 0.133 | 12337 |

***Bars will be installed on both faces in the vertical direction.***

*Use 20M deformed bars spaced at 180 mm in two curtains of reinforcement for the vertical direction.*

# A 2 Validation of the Design

The design forces were verified with SAP2000 and are presented in Table A.8 and Table A.9.

Table A.8: Ring tensions in cylindrical direction using SAP2000

| Point | Ring tensile forces (kip/ft) | Ring tensile forces (lb/ft) |
|---|---|---|
| Top | 0.4483 | 448.31 |
| 0.1H | 38.9981 | 38998.08 |
| 0.2H | 77.2890 | 77289.02 |
| 0.3H | 114.3672 | 114367.18 |
| 0.4H | 148.0000 | 147999.98 |
| 0.5H | 174.2462 | 174246.21 |
| 0.6H | 187.3712 | 187371.18 |
| 0.7H | 180.4479 | 180447.94 |
| 0.8H | 147.1201 | 147120.10 |
| 0.9H | 85.0705 | 85070.46 |
| Bottom | 1.7361 | 1736.13 |

Table A.9: Bending moments in cylindrical wall using SAP2000

| Point | Moments (kipft/ft) | Moments (lbft/ft) |
|---|---|---|
| Top | 0.0132 | 13.19 |
| 0.1H | 0.2021 | 202.09 |
| 0.2H | 1.3800 | 1380.03 |
| 0.3H | 4.2889 | 4288.88 |
| 0.4H | 9.5275 | 9527.50 |
| 0.5H | 17.2583 | 17258.32 |
| 0.6H | 26.7526 | 26752.58 |
| 0.7H | 35.7471 | 35747.14 |
| 0.8H | 39.6939 | 39693.92 |
| 0.9H | 31.1180 | 31117.98 |
| Bottom | 0.2198 | 219.80 |

## A 2.1 Validation results

Table A.10 provides a comparison of the tensile forces in the ring direction between the PCA method and SAP2000, while Figure A.3 provides a plot for the results of the two methods.

Table A.10: Ring tension force comparison between the PCA method and SAP2000

| Point | Point height (H) | PCA method tensile forces (kip/ft) | SAP2000 tensile forces (kip/ft) | PCA/SAP2000 |
|---|---|---|---|---|
| Top | 1.0 | 3.5195 | 0.4483 | 7.85 |
| 0.1H | 0.9 | 41.9996 | 38.9981 | 1.07 |
| 0.2H | 0.8 | 79.4314 | 77.2890 | 1.03 |
| 0.3H | 0.7 | 116.3771 | 114.3672 | 1.02 |
| 0.4H | 0.6 | 149.7958 | 148.0000 | 1.01 |
| 0.5H | 0.5 | 175.3686 | 174.2462 | 1.01 |
| 0.6H | 0.4 | 187.8325 | 187.3712 | 1.00 |
| 0.7H | 0.3 | 180.6744 | 180.4479 | 1.00 |
| 0.8H | 0.2 | 147.0478 | 147.1201 | 1.00 |
| 0.9H | 0.1 | 84.6683 | 85.0705 | 1.00 |
| Bottom | 0.0 | 0.0000 | 1.7361 | 0.00 |

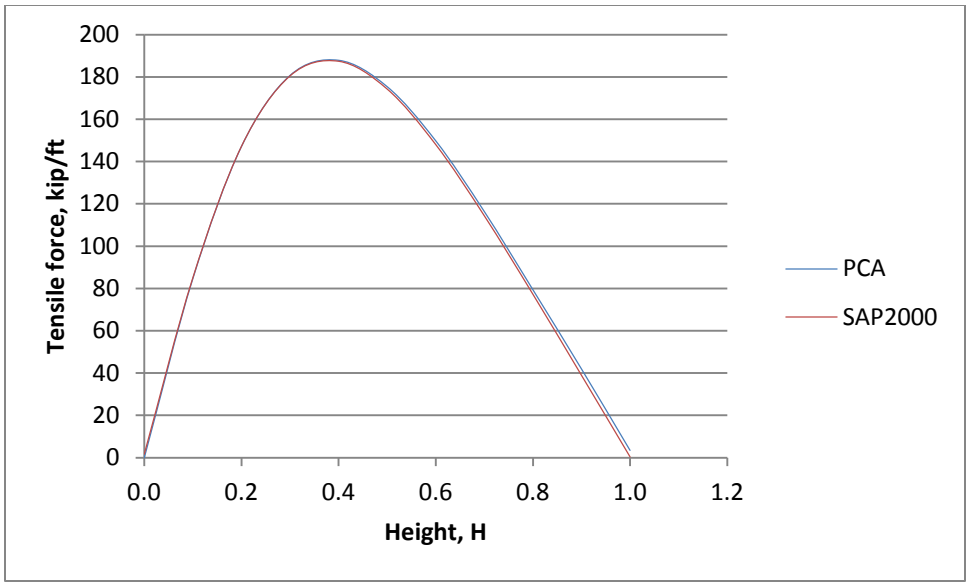


Figure A.3: Ring tension forces using PCA method and SAP2000

Table A.11 provides the bending moments computed by the PCA method and SAP2000. Figure A.4 provides a plot of the bending moments computed using the two approaches, and Figure A.5 is a schematic of the final design.

Table A.11: Comparison of bending moments between the PCA method and SAP2000

| Point | Point height (H) | PCA method moments (kipft/ft) | SAP2000 moments (kipft/ft) | PCA/SAP2000 |
|---|---|---|---|---|
| Top | 1.0 | 0.0000 | 0.0132 | 0.00 |
| 0.1H | 0.9 | 0.2705 | 0.2021 | 1.34 |
| 0.2H | 0.8 | 1.9787 | 1.3800 | 1.43 |
| 0.3H | 0.7 | 4.8388 | 4.2889 | 1.13 |
| 0.4H | 0.6 | 10.2884 | 9.5275 | 1.08 |
| 0.5H | 0.5 | 18.3122 | 17.2583 | 1.06 |
| 0.6H | 0.4 | 27.3024 | 26.7526 | 1.02 |
| 0.7H | 0.3 | 36.2925 | 35.7471 | 1.02 |
| 0.8H | 0.2 | 39.9182 | 39.6939 | 1.01 |
| 0.9H | 0.1 | 31.5235 | 31.1180 | 1.01 |
| Bottom | 0.0 | 0.0000 | 0.2198 | 0.00 |

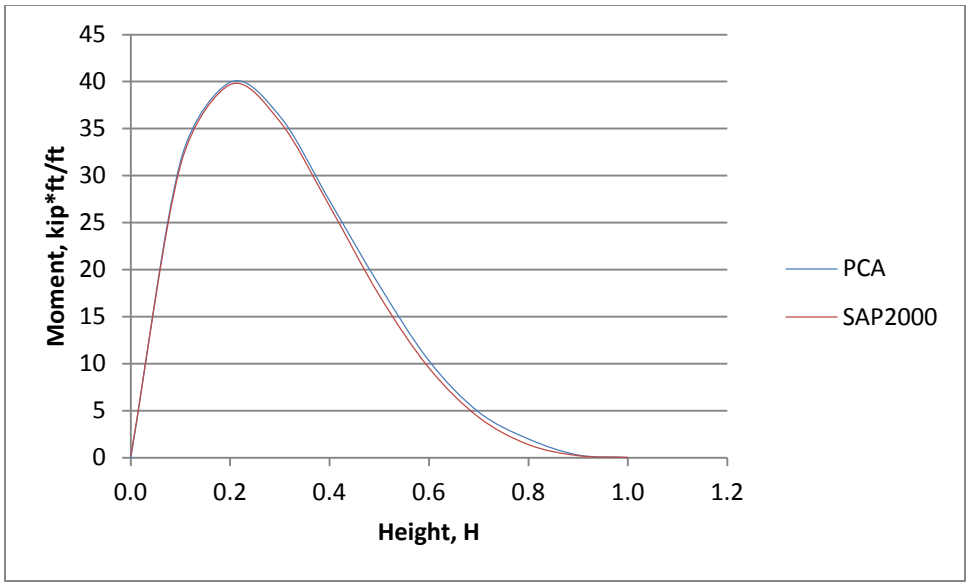


Figure A.4: Bending moments computed by the PCA method and SAP2000

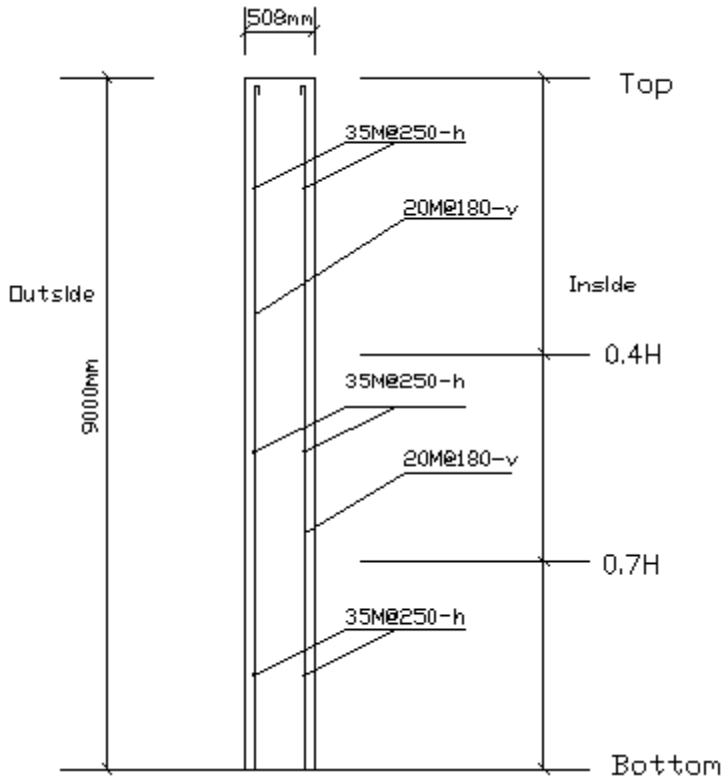


Figure A.5: Reservoir wall section

## A 3 Scaling of the Design

The prototype reservoir walls were scaled to the model size for experimental testing. The scaling parameter was chosen such that the scaled size was $1/4.5$ of the prototype design size. This was selected to ensure that the model walls would fit within the testing limits of the shock tube. Assuming full-scale wall thickness of 20 inches, the scaled-size wall thickness is $20 \times \frac{1}{4.5}\ inches$.

Model parameters:

$Scaling\ parameter = 4.5$

$Height\ of\ wall = {}^{9}/_{4.5} = 2\ m = 2000\ mm$ (equivalent to the opening of the test section of the shock tube)

$Height\ of\ wall = 2440\ mm$ (extended height to permit bolting of the wall to the shock tube)

$Thickness\ of\ wall = {}^{20}/_{4.5} = 4.44\ in$: therefore use $Thickness\ of\ wall = 4\ in = 100\ mm$

Assume $Width\ of\ wall = L = 2000\ mm$

Actual $Width\ of\ wall = L + 2l_{dh}$: from A4 $l_{dh} = 250\ mm$; $Width\ of\ wall = 2000 + 2 \times 250 = 2500\ mm$; therefore use $Width\ of\ wall = 2550\ mm$

$Concrete\ cover\ of\ wall = {}^{2}/_{4.5} = 0.4444\ in = 11.29\ mm$

For the reinforcing steel, the same reinforcement ratio was maintained.

**Ratio of horizontal reinforcement (Prototype):**

$\rho_h = \frac{A_s}{bt} = 0.0158$

Scaling for testing: 10M@130

For 1ft height of wall section: $b = 12\ in$

($t = 4\ in$)

$A_s = 1538.46\ mm^2/m = 1538.46 \times 0.00047244 = 0.73\ in^2/ft$

Ratio of horizontal reinforcement (Scaling):

$\rho_h = \frac{A_s}{bt} = \frac{0.73}{12 \times 4} = 0.0152$ OK

*Reinforcing bars were placed on both faces in the horizontal direction.*

*Use 10M deformed bars spaced at 130 mm in two curtains of reinforcement for the horizontal direction.*

**Ratio of vertical reinforcement (Prototype):**

$\rho_v = \frac{A_s}{bd} = 0.0042$

Scaling for testing: 10M@300

For 1 ft width of wall section: $b = 12\ in$, $d = t - cover - d_b - 1/2d_b = 2.89\ in$

$A_s = 333.33\ mm^2/m = 333.33 \times 0.00047244 = 0.16\ in^2/ft$

Ratio of outside and inside vertical reinforcement (Scaling):

$\rho_v = \frac{A_s}{bd} = \frac{0.16}{12 \times 2.89} = 0.0045$ OK

*Reinforcing bars were placed on both faces in the vertical direction.*

*Use 10M deformed bars spaced at 300 mm in two curtains of reinforcement for the vertical direction.*

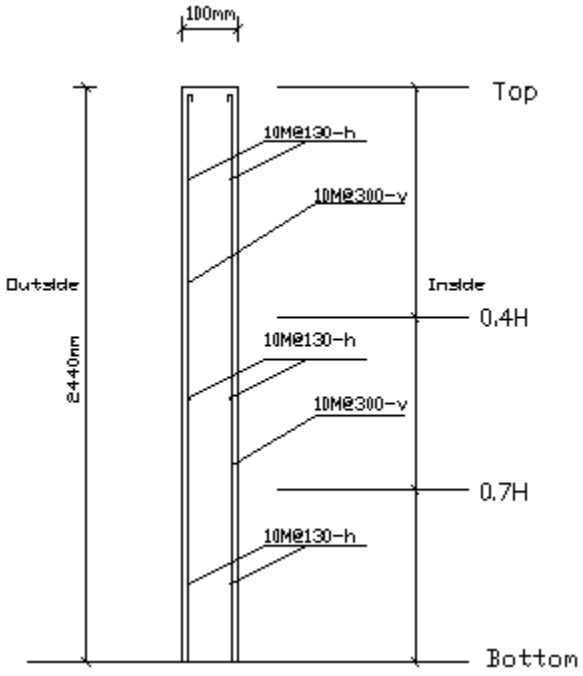


Figure A.6: Reservoir wall section (scaled)

# A 4 Development of Standard Hooks in Tension (Horizontal Rebar)

ACI350-06, Cl12.5.2, for No.19 and smaller bars:

Development length of standard hook in tension

$$l_{dh} = \left(\frac{0.24\beta\lambda f_y}{\sqrt{f_c'}}\right) d_b = \left(\frac{0.24 \times 1.0 \times 1.0 \times 500}{\sqrt{30}}\right) \times 11.3 = 247.57\ mm$$

ACI350-06, Cl12.5.1, $l_{dh} \geq 8d_b$ and $l_{dh} \geq 150\ mm$

Check $l_{dh} = 247.57\ mm \geq 8d_b = 8 \times 11.3 = 90.4\ mm$ and $l_{dh} = 247.57\ mm \geq 150\ mm$

Therefore, $l_{dh} = 250\ mm$

*Standard hooks* of 180° *bend*

ACI350-06, Cl7.2.1

Diameter of bend (10M Rebar)-inside

$6d_b = 6 \times 11.3 = 67.8\ mm$

*Extension (10M rebar)*

ACI350-06, Cl7.1.1

$4d_b = 4 \times 11.3 = 45.2\ mm < 65\ mm$ , take $4d_b = 70\ mm$

$Length\ of\ horizontal\ rebar$ (180°)

$$= L + 2\left[l_{dh} - 4d_b + \pi\left(\frac{6d_b}{2} + \frac{d_b}{2}\right) + extension\right]$$

$$= 2000 + 2 \times \left[250 - 4 \times 11.3 + \pi \times \left(\frac{6 \times 11.3}{2} + \frac{11.3}{2}\right) + 70\right] = 2798.10\ mm$$

$Length\ of\ horizontal\ rebar$ (180°) $= 2800\ mm$

Development length of standard hook in tension

CSA A23.1-04, Cl12.5.2 & Cl12.5.3

$$l_{dh} = \frac{100d_b}{\sqrt{f_c'}}\frac{f_y}{400} = \frac{100 \times 11.3}{\sqrt{30}} \times \frac{500}{400} = 257.89\ mm$$

CSA A23.1-04, Cl12.5.1, $l_{dh} \geq 8d_b$ and $l_{dh} \geq 150\ mm$

Check $l_{dh} = 257.89\ mm \geq 8d_b = 8 \times 11.3 = 90.4\ mm$ and

$l_{dh} = 257.89\ mm \geq 150\ mm$

Therefore, $l_{dh} = 260\ mm$

**Length of horizontal rebar**

*Standard hooks* of 180° *bend*

CSA A23.1-04, Annex A, Cl6.6.2.3 and Table16

Diameter of bend (10M Rebar)-inside

$D = 70\ mm$

*Extension (10M rebar)*

CSA A23.1-04, Annex A, Cl6.6.2.2

$4d_b = 4 \times 11.3 = 45.2\ mm < 60\ mm$, take $4d_b = 70\ mm$

$Length\ of\ horizontal\ rebar$ (180°)

$$= L + 2\left[l_{dh} - \frac{D}{2} - d_b + \pi\left(\frac{D}{2} + \frac{d_b}{2}\right) + extension\right]$$

$$= 2000 + 2 \times \left[260 - \frac{70}{2} - 11.3 + \pi \times \left(\frac{70}{2} + \frac{11.3}{2}\right) + 70\right] = 2822.81\ mm$$

$Length\ of\ horizontal\ rebar$ (180°) $= 2900\ mm$

Comparing the results from ACI350-06 and CSA A23.1-04 for 180° hooks:

$Length\ of\ horizontal\ rebar$ (180°) $= 2900\ mm$

**Length of vertical rebar**

*Standard hooks of* 180° *bend*

ACI350-06, Cl7.2.1

Diameter of bend (10M Rebar)-inside

$6d_b = 6 \times 11.3 = 67.8\ mm$

ACI350-06, Cl7.1.1

*Extension (10M rebar)*

$4d_b = 4 \times 11.3 = 45.2\ mm < 65\ mm$, take $4d_b = 70\ mm$

$Length\ of\ vertical\ rebar$ (180°)

$$= L - 2cover - 2\left(\frac{6d_b}{2} + d_b\right) + 2\left[\pi\left(\frac{6d_b}{2} + \frac{d_b}{2}\right) + extension\right]$$

$$= 2440 - 2 \times 15 - 2 \times \left(\frac{6 \times 11.3}{2} + 11.3\right) + 2 \times \left[\pi \times \left(\frac{6 \times 11.3}{2} + \frac{11.3}{2}\right) + 70\right]$$

$Length\ of\ vertical\ rebar\ (180°) = 2708.10\ mm$

$Length\ of\ vertical\ rebar\ (180°) = 2710\ mm$

*Standard hooks of* 180° *bend*

CSA A23.1-04, Annex A, Cl6.6.2.3 & Table16

Diameter of bend (10M Rebar)-inside

$D = 70\ mm$

*Extension (10M rebar)*

CSA A23.1-04, Annex A, Cl6.6.2.2

$4d_b = 4 \times 11.3 = 45.2\ mm < 60\ mm$, take $4d_b = 70\ mm$

$Length\ of\ vertical\ rebar\ (180°)$

$$= H - 2cover - 2\left(\frac{D}{2} + d_b\right) + 2\left[\pi\left(\frac{D}{2} + \frac{d_b}{2}\right) + extension\right]$$

$$= 2440 - 2 \times 15 - 2 \times \left(\frac{70}{2} + 11.3\right) + 2 \times \left[\pi \times \left(\frac{70}{2} + \frac{11.3}{2}\right) + 70\right]$$

$$= 2712.81\ mm$$

$Length\ of\ vertical\ rebar\ (180°) = 2720\ mm$

Comparing the results from ACI350-06 and CSAA23.1-04 for 180° hooks:

$Length\ of\ vertical\ rebar\ (180°) = 2720\ mm$

# Appendix B: Strain-time Histories

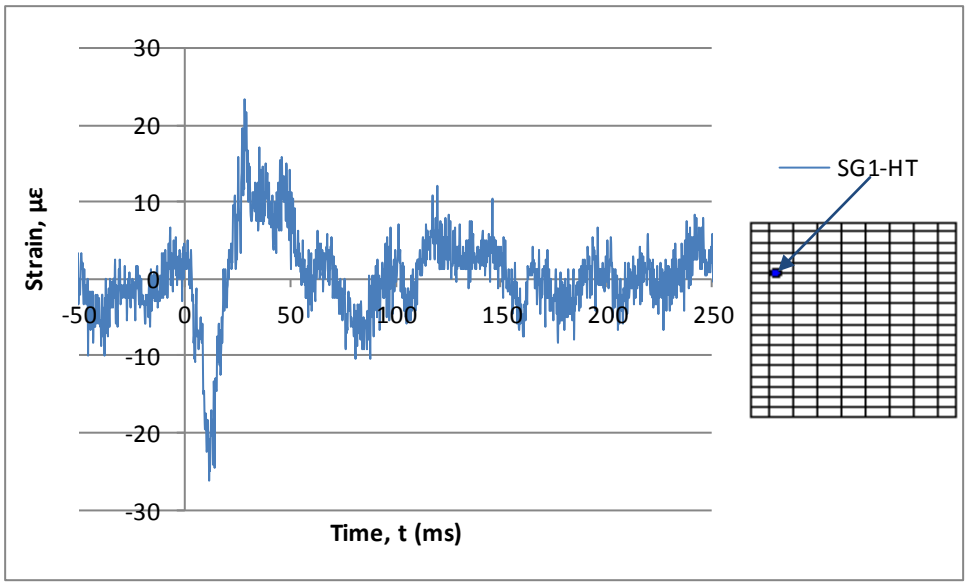


Figure B.1: Test 1 strain-time history for Gauge SG1-HT of Wall 1

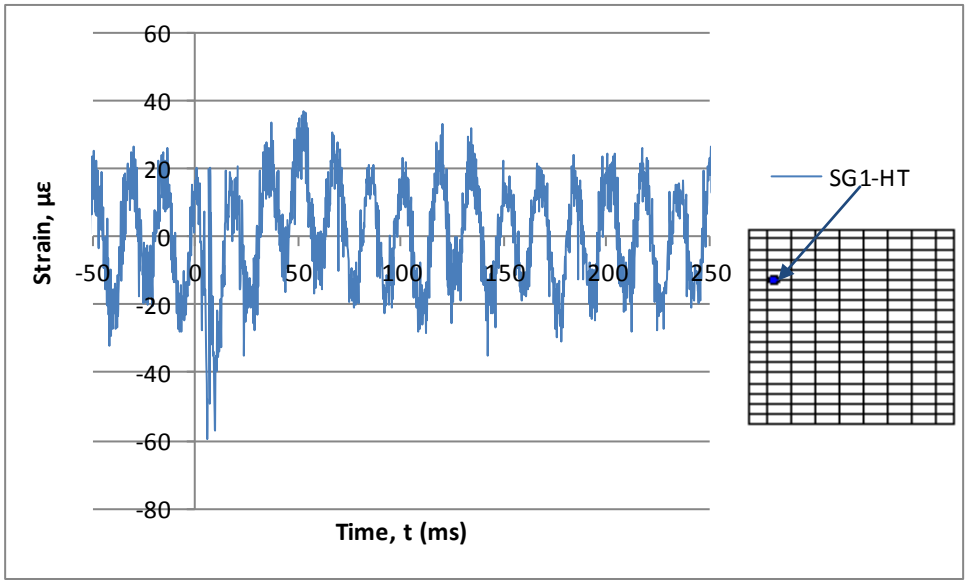


Figure B.2: Test 2 strain-time history for Gauge SG1-HT of Wall 1

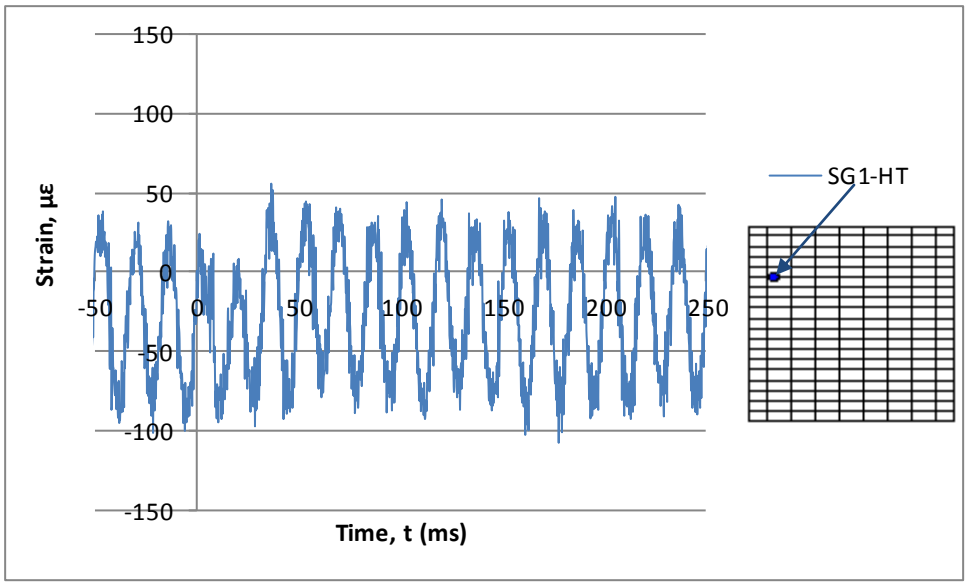


Figure B.3: Test 3 strain-time history for Gauge SG1-HT of Wall 1

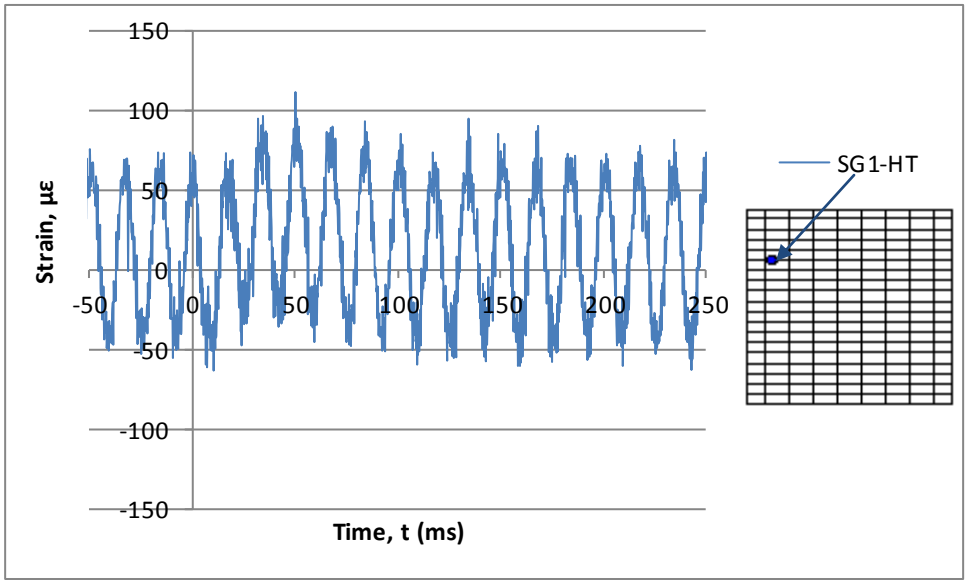


Figure B.4: Test 4 strain-time history for Gauge SG1-HT of Wall 1

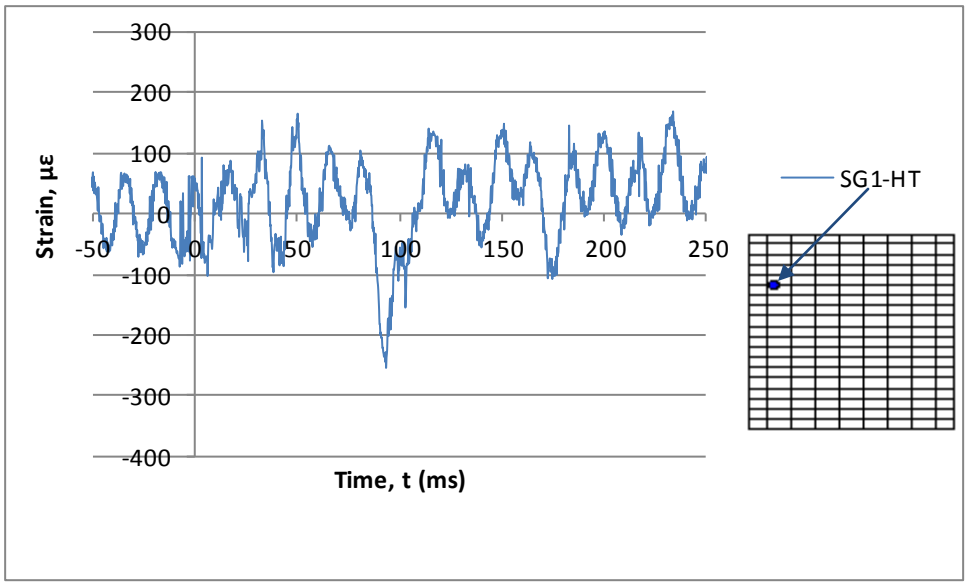


Figure B.5: Test 5 strain-time history for Gauge SG1-HT of Wall 1

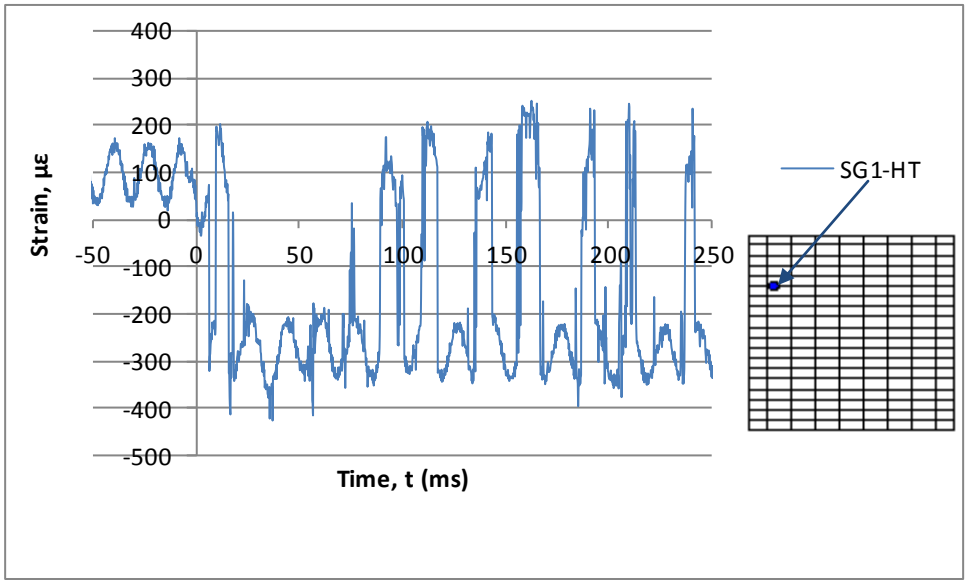


Figure B.6: Test 6 strain-time history for Gauge SG1-HT of Wall 1

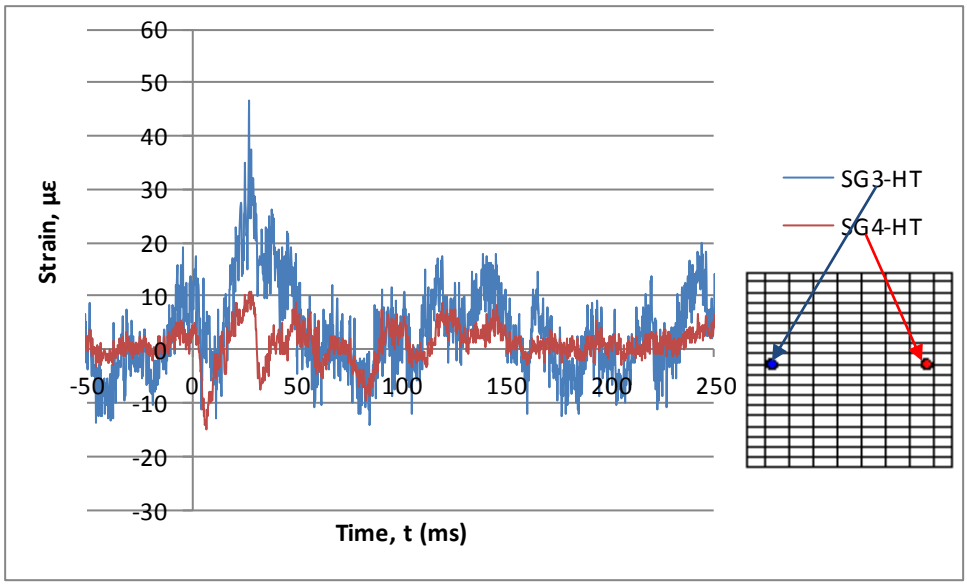


Figure B.7: Test 1 strain-time histories for Gauges SG3-HT and SG4-HT of Wall 1

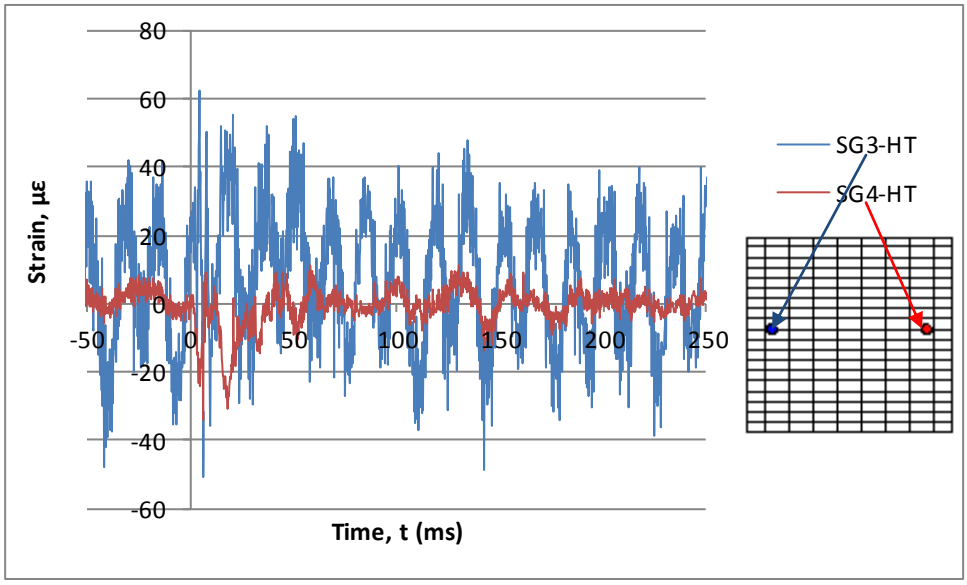


Figure B.8: Test 2 strain-time histories for Gauges SG3-HT and SG4-HT of Wall 1

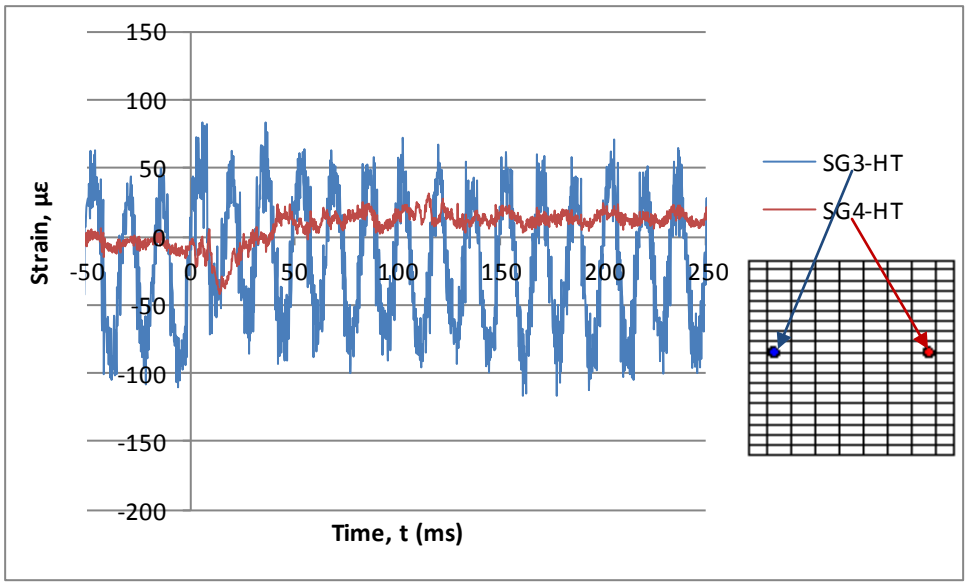


Figure B.9: Test 3 strain-time histories for Gauges SG3-HT and SG4-HT of Wall 1

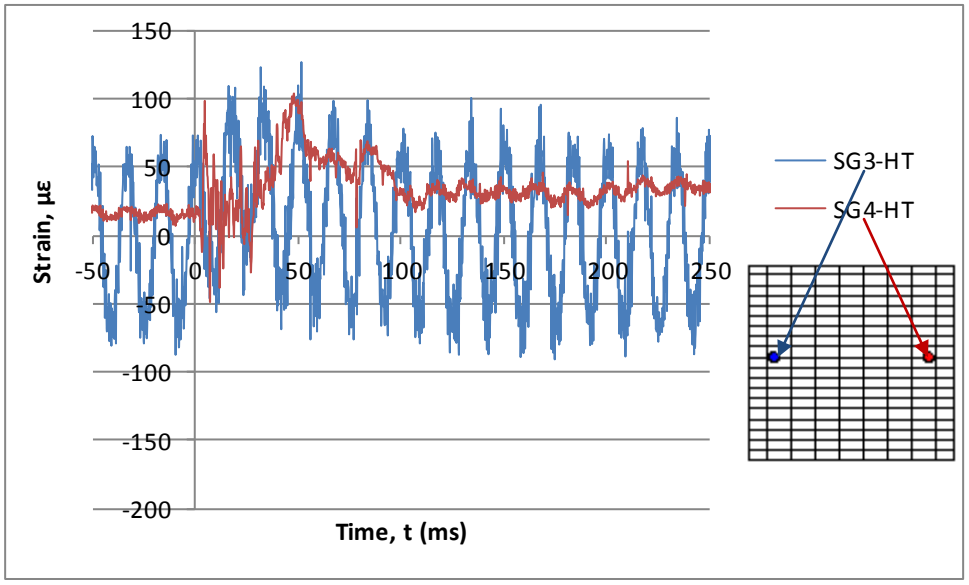


Figure B.10: Test 4 strain-time histories for Gauges SG3-HT and SG4-HT of Wall 1

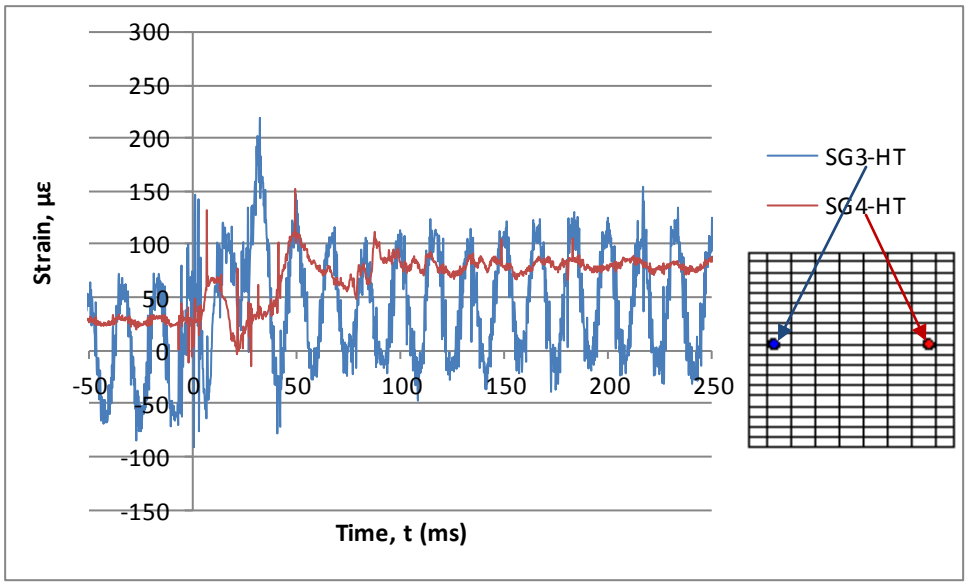


Figure B.11: Test 5 strain-time histories for Gauges SG3-HT and SG4-HT of Wall 1

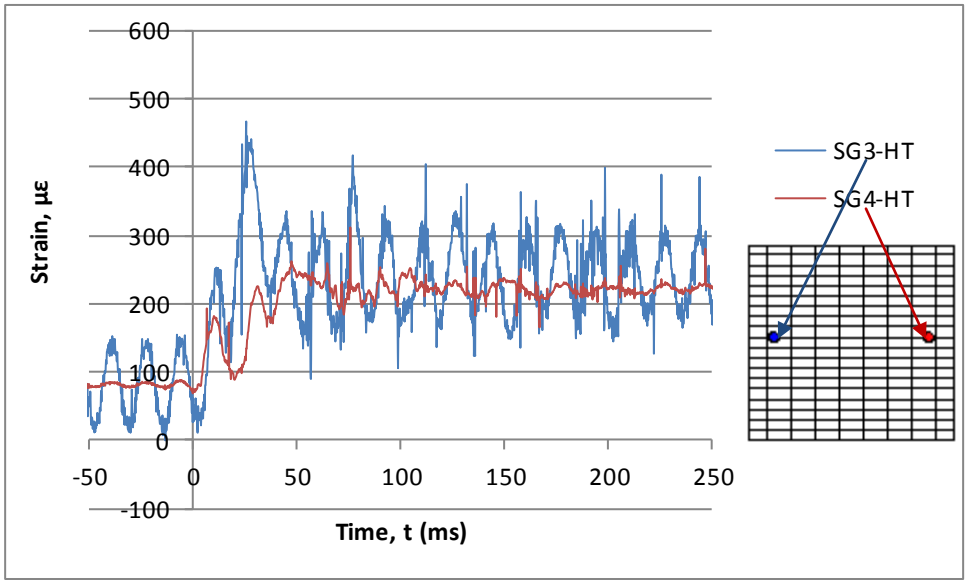


Figure B.12: Test 6 strain-time histories for Gauges SG3-HT and SG4-HT of Wall 1

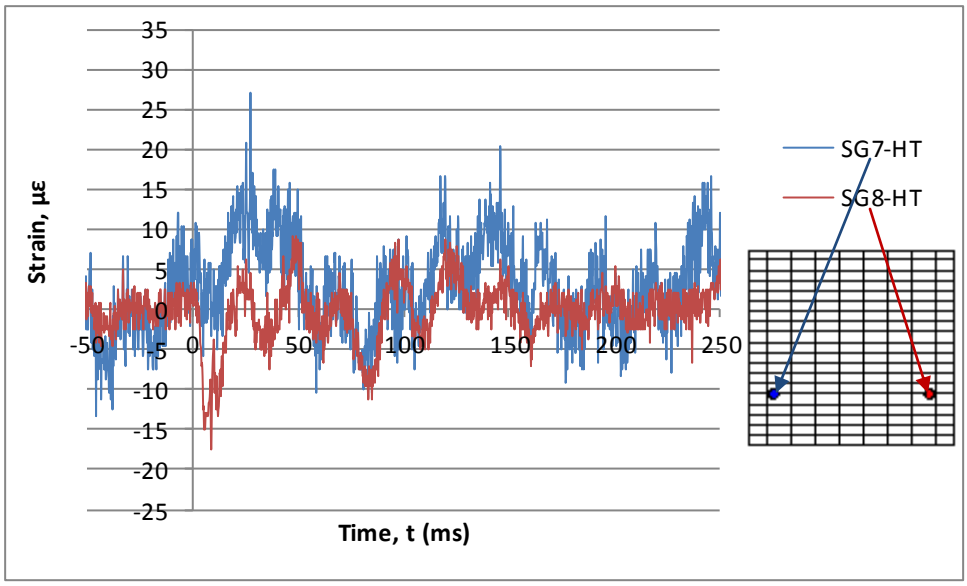


Figure B.13: Test 1 strain-time histories for Gauges SG7-HT and SG8-HT of Wall 1

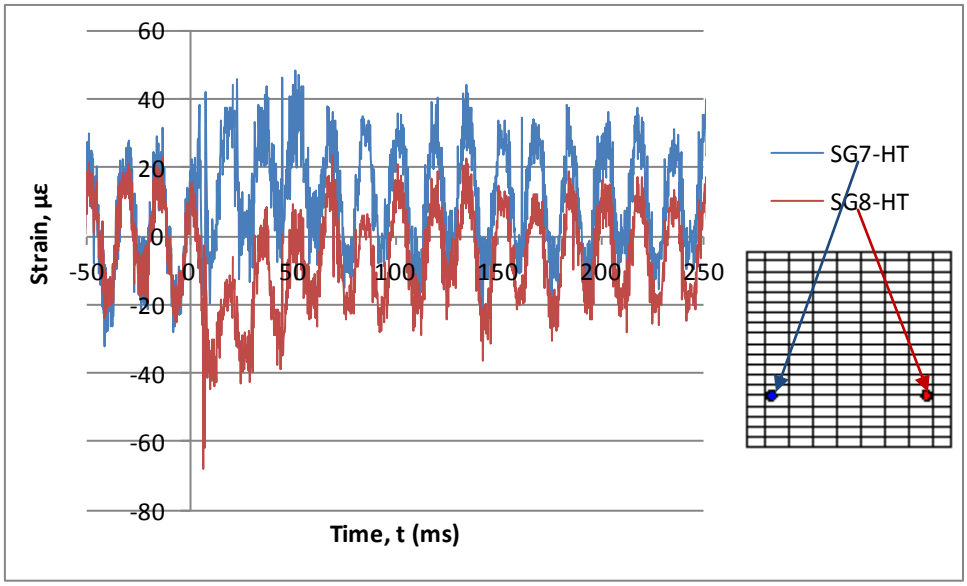


Figure B.14: Test 2 strain-time histories for Gauges SG7-HT and SG8-HT of Wall 1

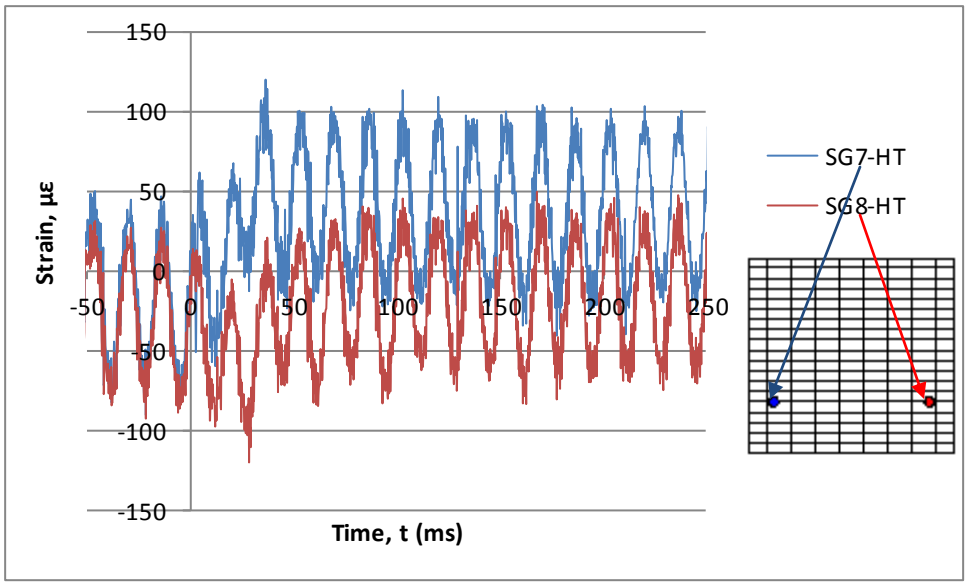


Figure B.15: Test 3 strain-time histories for Gauges SG7-HT and SG8-HT of Wall 1

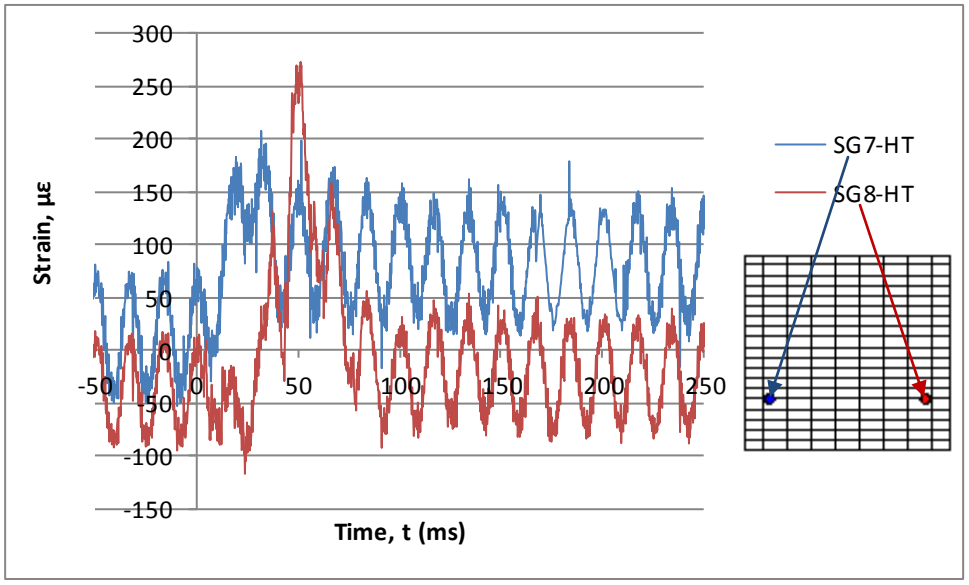


Figure B.16: Test 4 strain-time histories for Gauges SG7-HT and SG8-HT of Wall 1

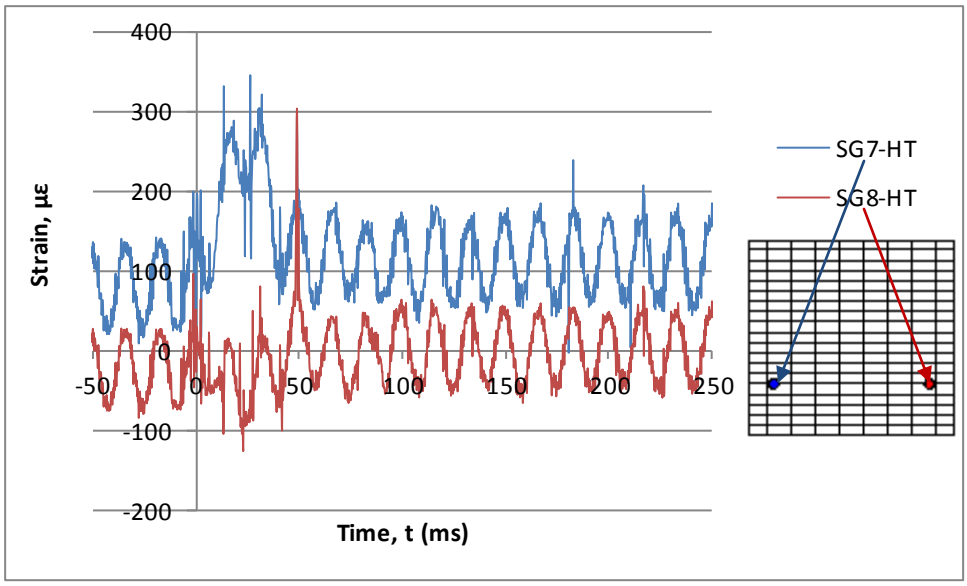


Figure B.17: Test 5 strain-time histories for Gauges SG7-HT and SG8-HT of Wall 1

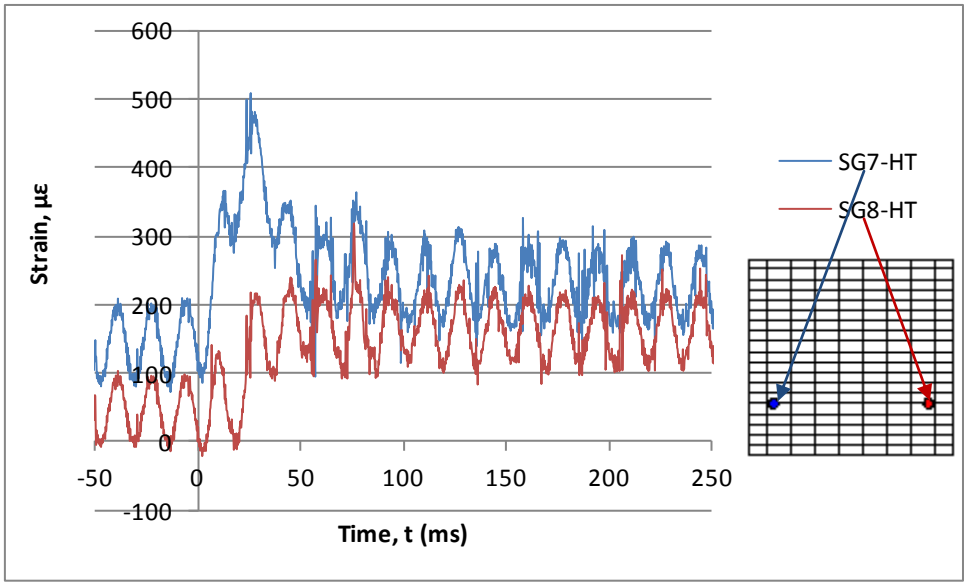


Figure B.18: Test 6 strain-time histories for Gauges SG7-HT and SG8-HT of Wall 1

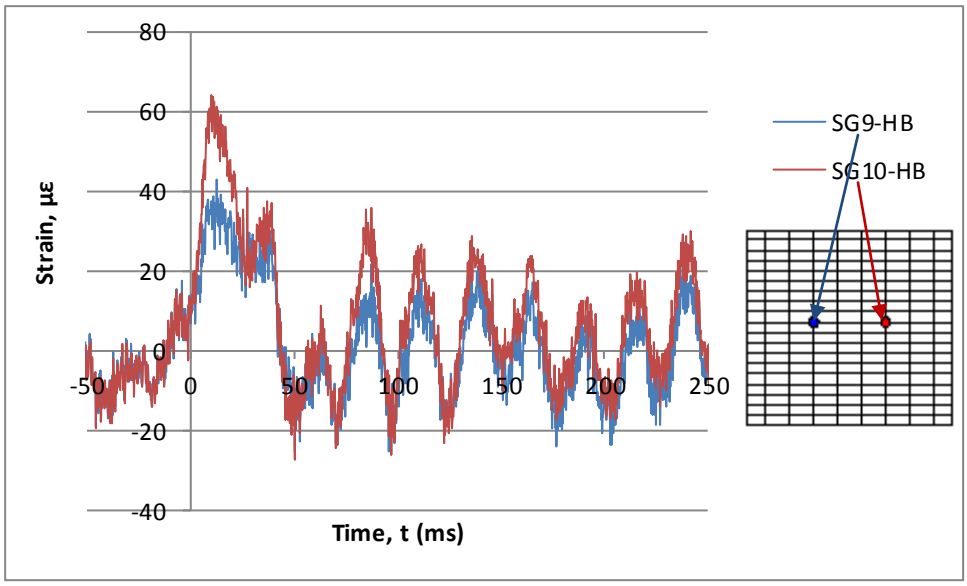


Figure B.19: Test 1 strain-time histories for Gauges SG9-HB and SG10-HB of Wall 1

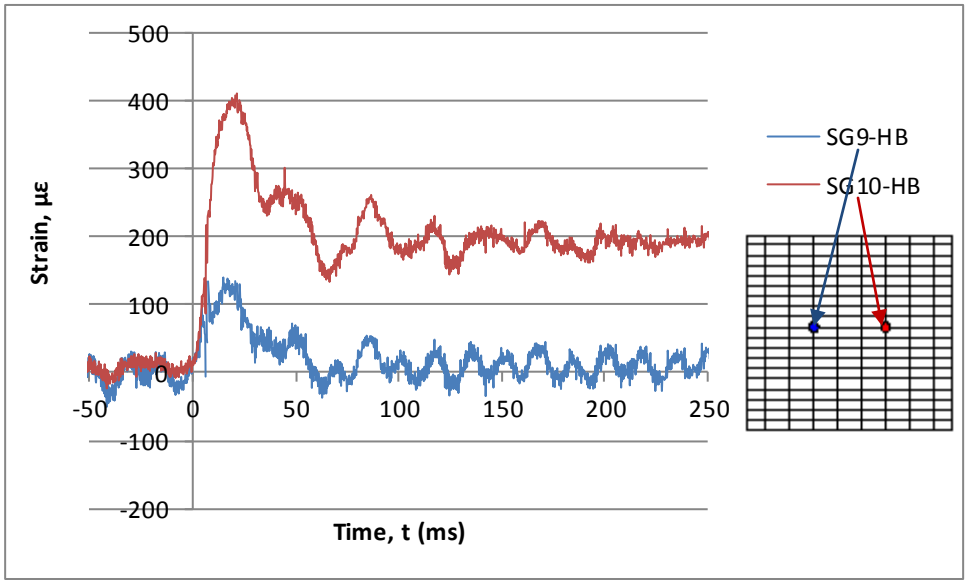


Figure B.20: Test 2 strain-time histories for Gauges SG9-HB and SG10-HB of Wall 1

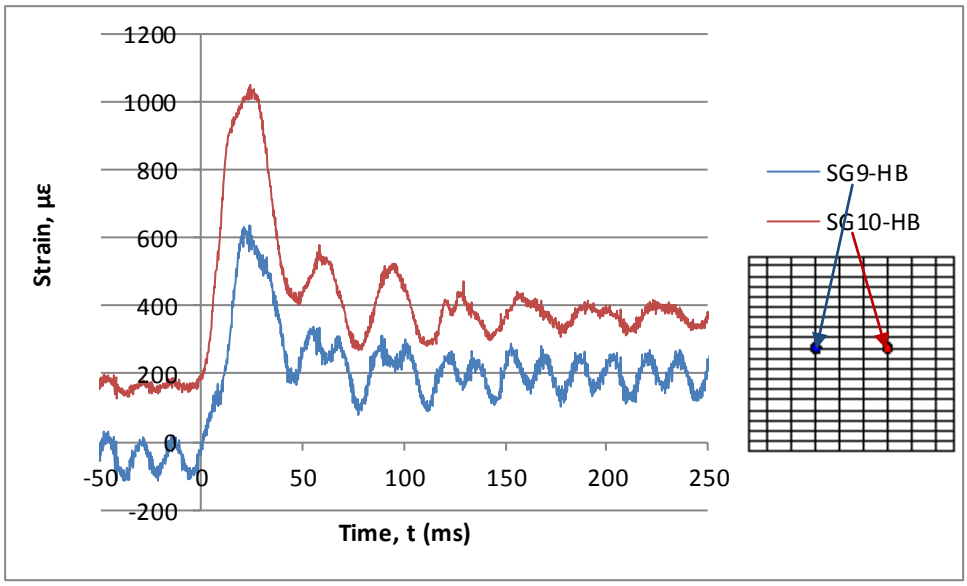


Figure B.21: Test 3 strain-time histories for Gauges SG9-HB and SG10-HB of Wall 1

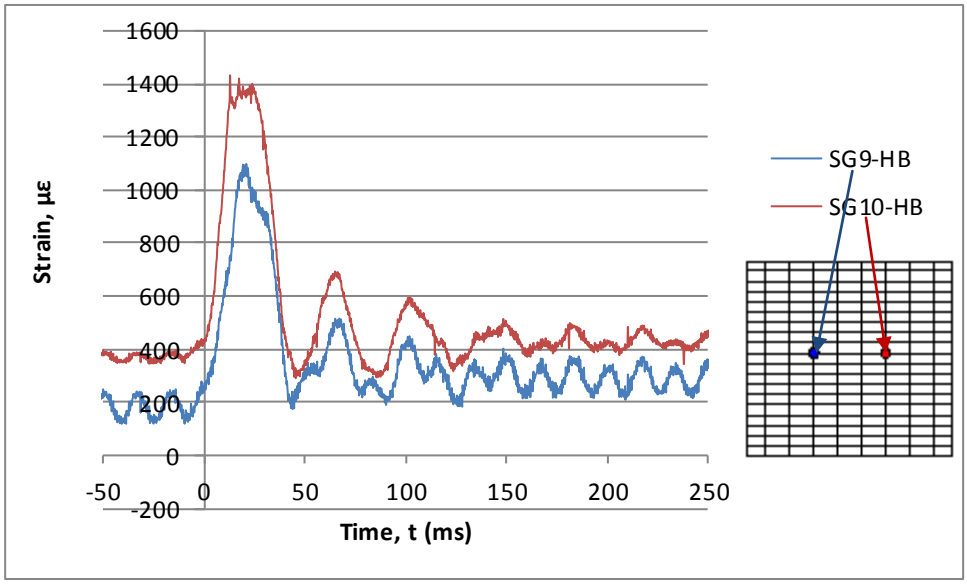


Figure B.22: Test 4 strain-time histories for Gauges SG9-HB and SG10-HB of Wall 1

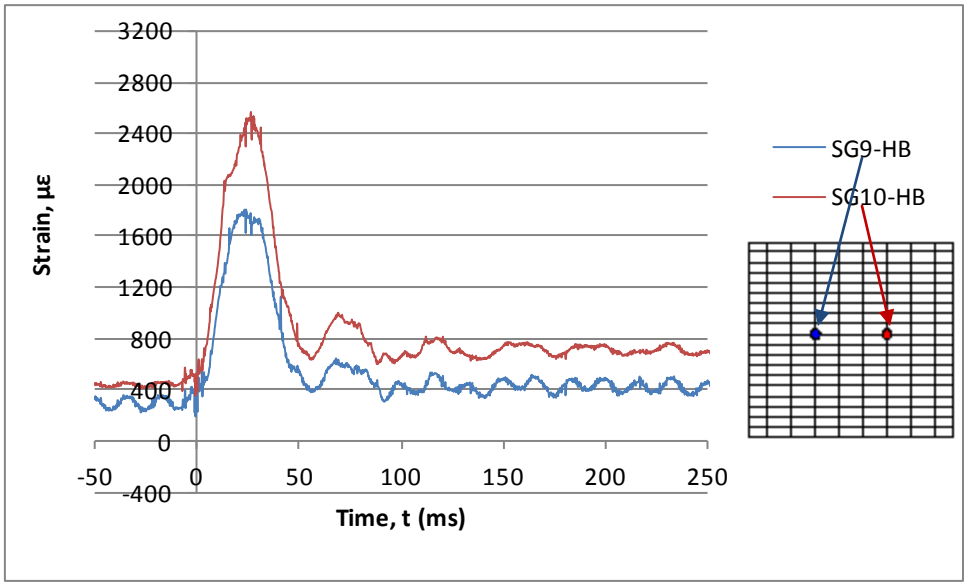


Figure B.23: Test 5 strain-time histories for Gauges SG9-HB and SG10-HB of Wall 1

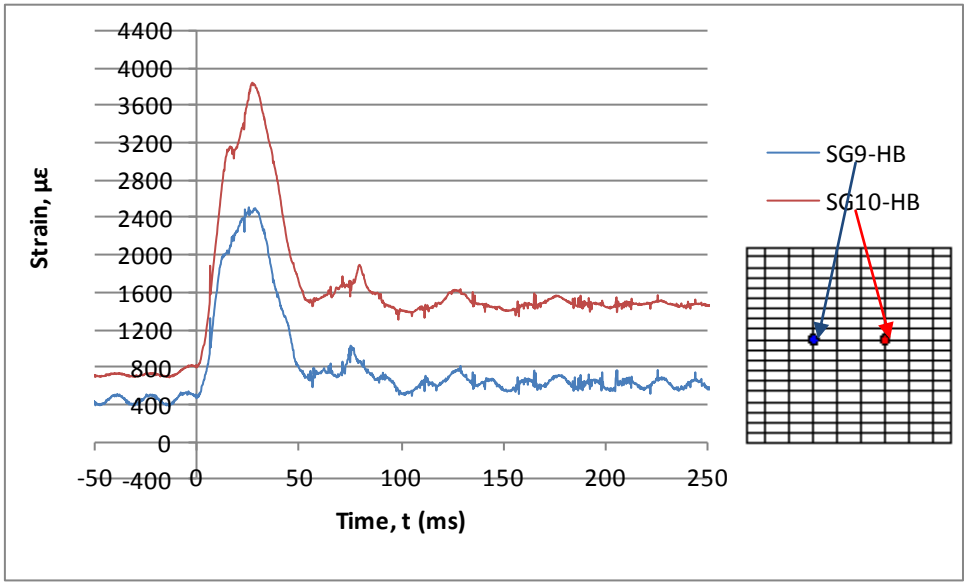


Figure B.24: Test 6 strain-time histories for Gauges SG9-HB and SG10-HB of Wall 1

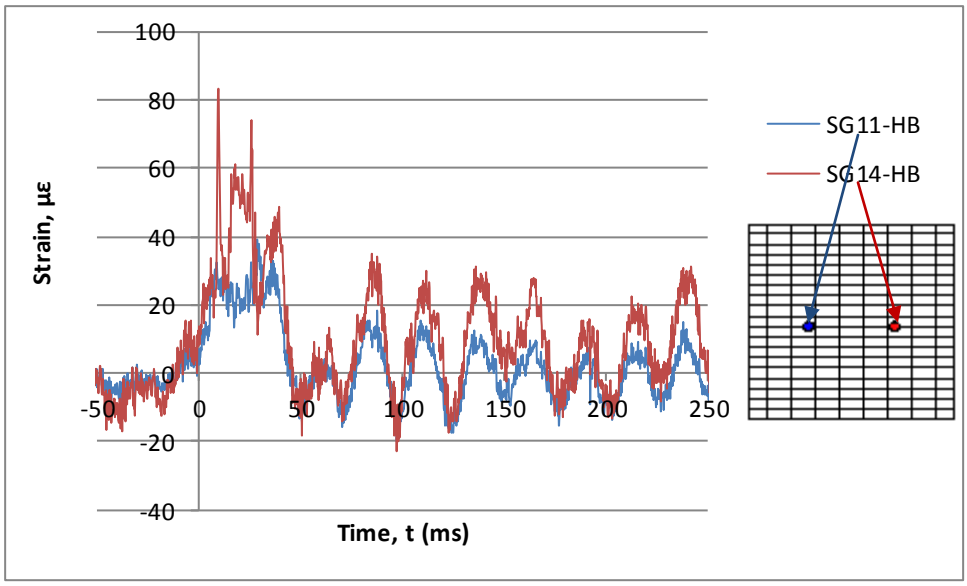


Figure B.25: Test 1 strain-time histories for Gauges SG11-HB and SG14-HB of Wall 1

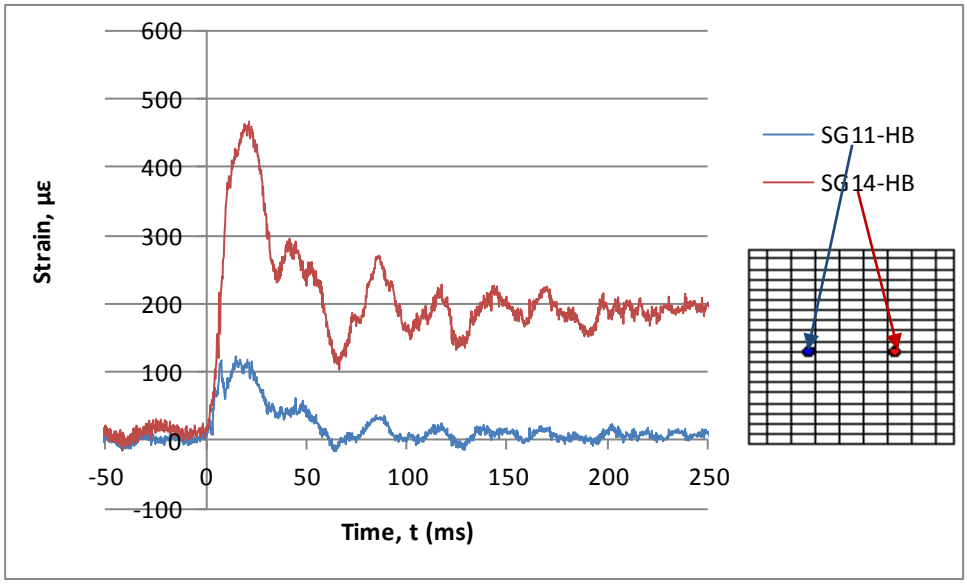


Figure B.26: Test 2 strain-time histories for Gauges SG11-HB and SG14-HB of Wall 1

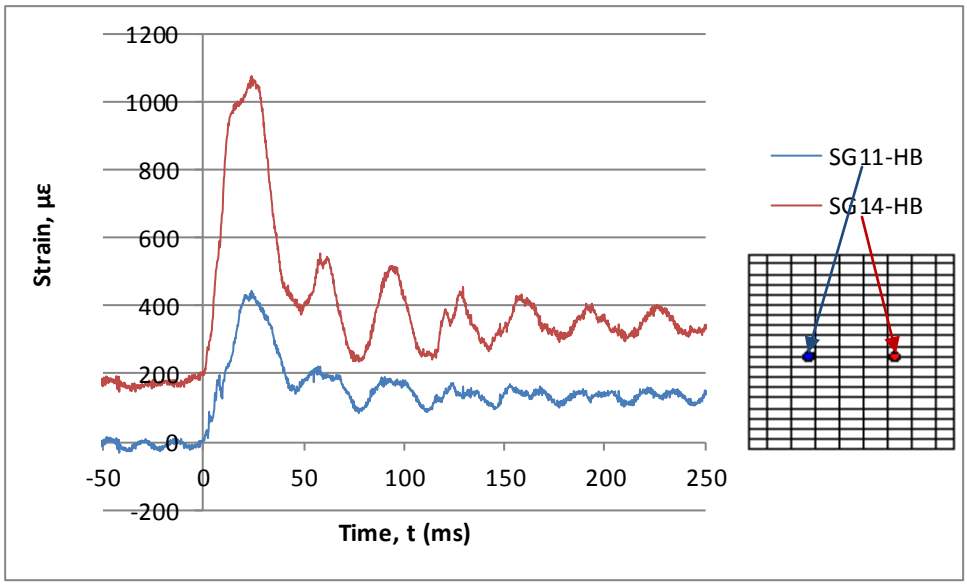


Figure B.27: Test 3 strain-time histories for Gauges SG11-HB and SG14-HB of Wall 1

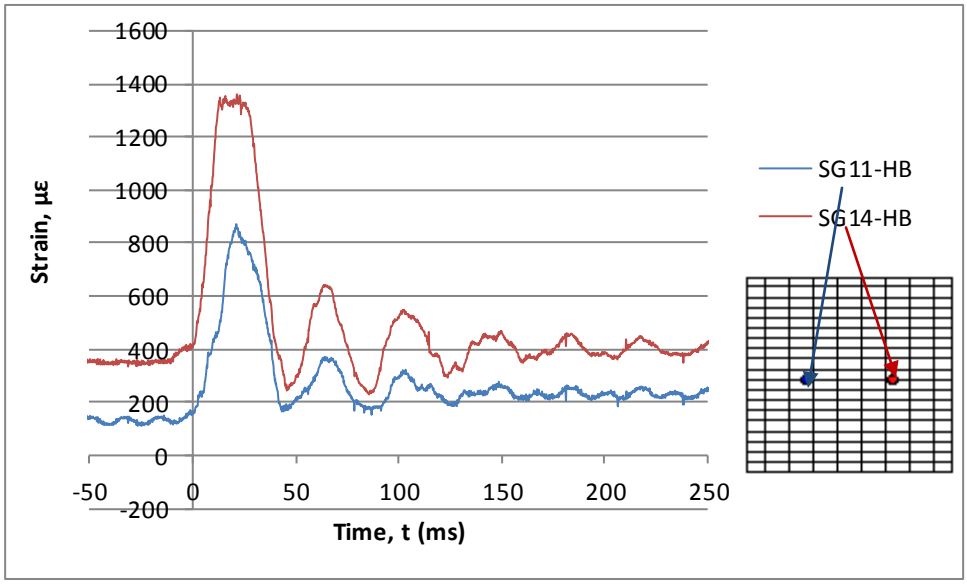


Figure B.28: Test 4 strain-time histories for Gauges SG11-HB and SG14-HB of Wall 1

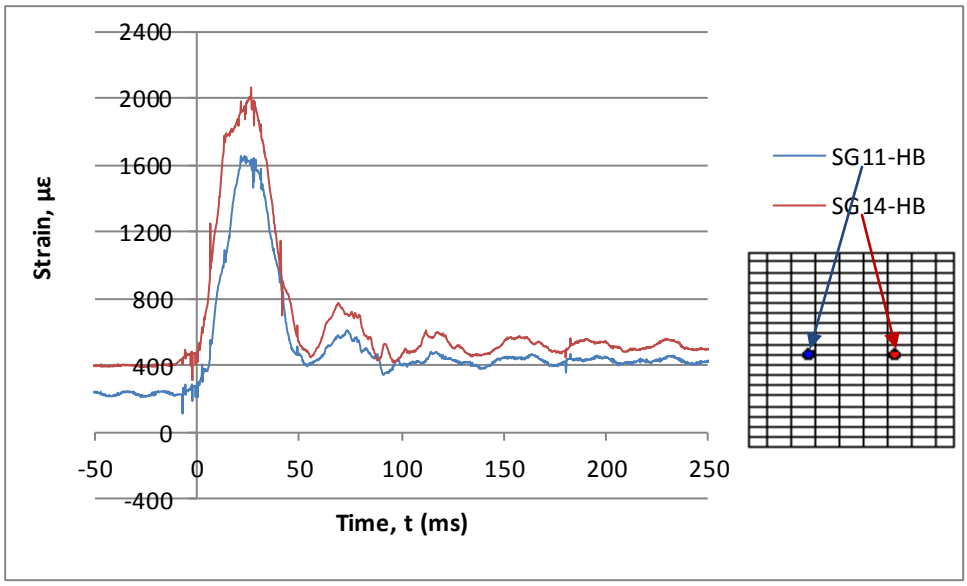


Figure B.29: Test 5 strain-time histories for Gauges SG11-HB and SG14-HB of Wall 1

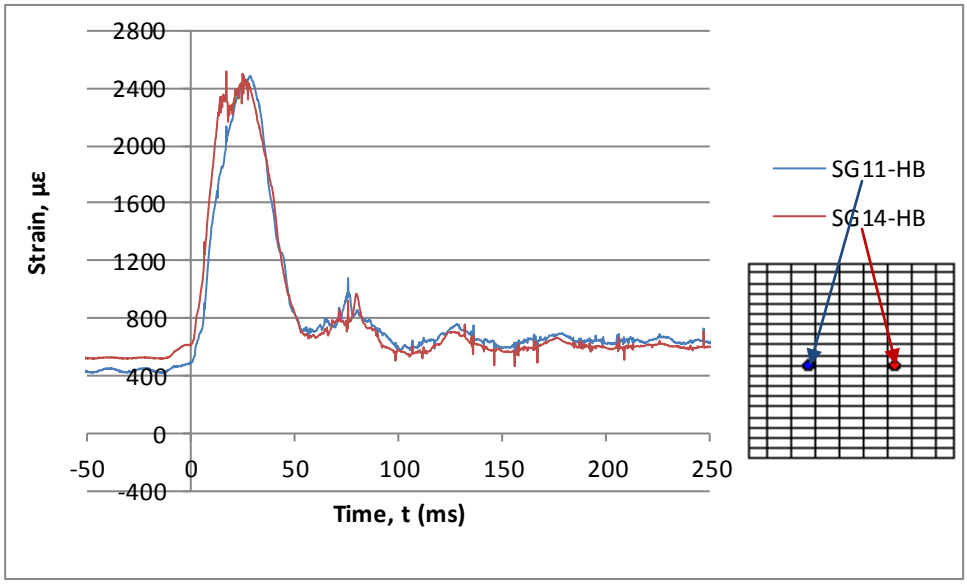


Figure B.30: Test 6 strain-time histories for Gauges SG11-HB and SG14-HB of Wall 1

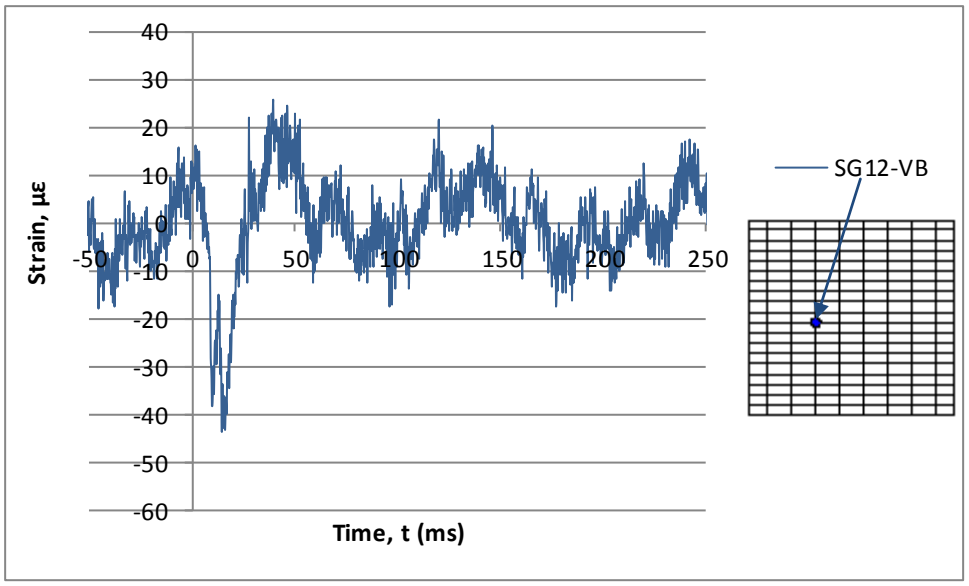


Figure B.31: Test 1 strain-time history for Gauge SG12-VB of Wall 1

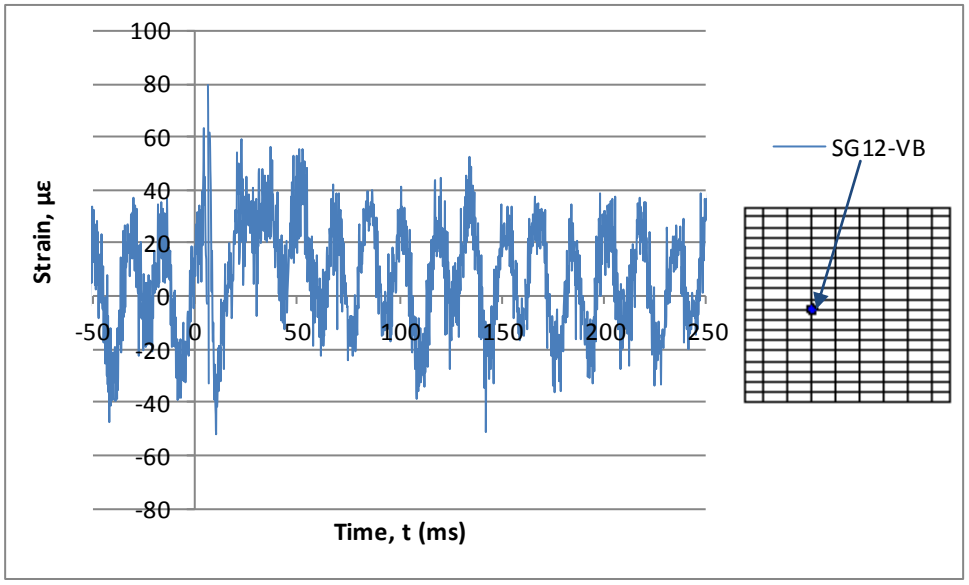


Figure B.32: Test 2 strain-time history for Gauge SG12-VB of Wall 1

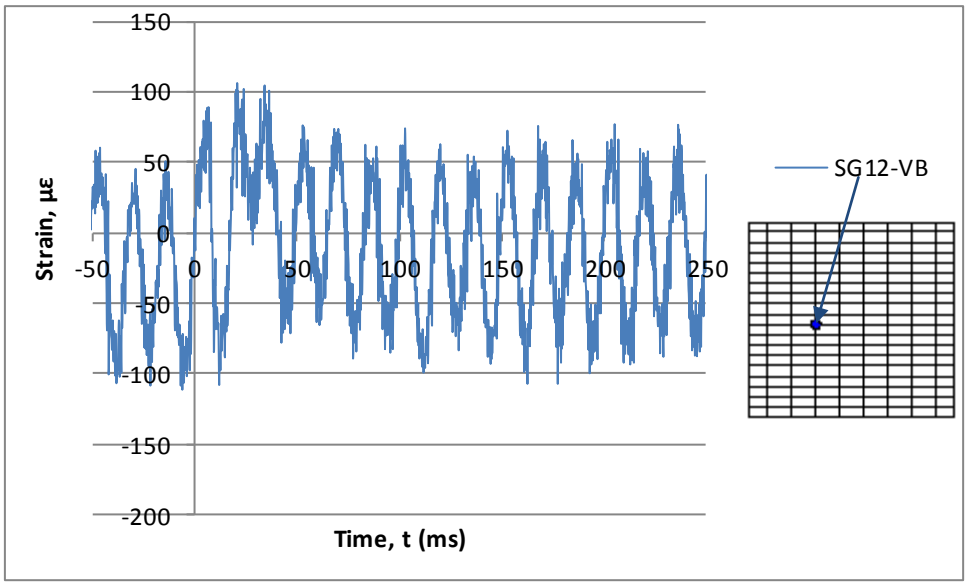


Figure B.33: Test 3 strain-time history for Gauge SG12-VB of Wall 1

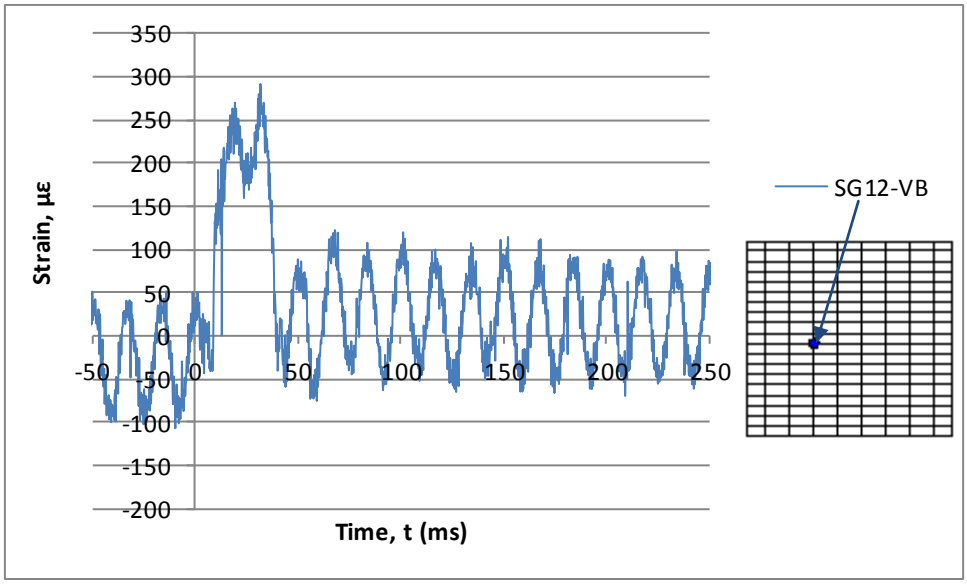


Figure B.34: Test 4 strain-time history for Gauge SG12-VB of Wall 1

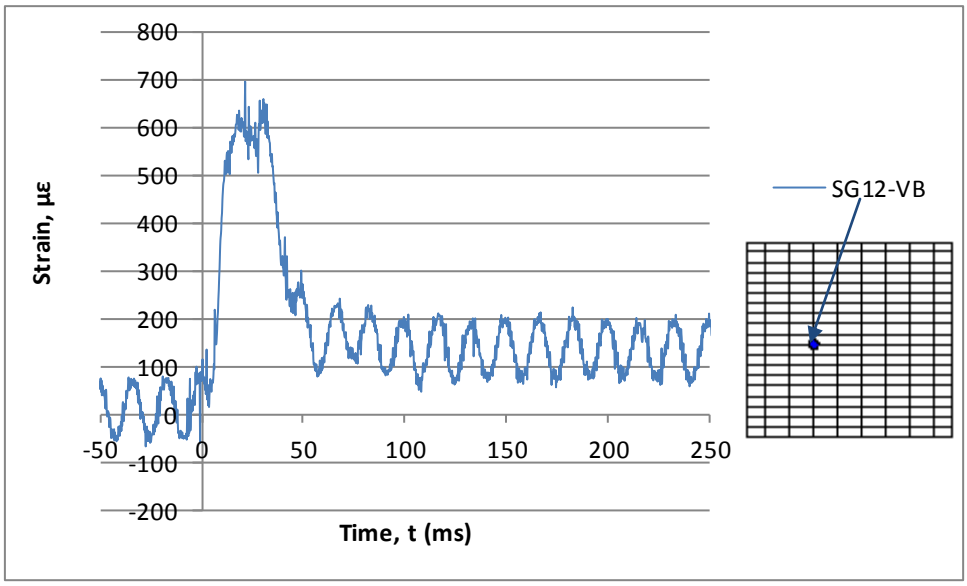


Figure B.35: Test 5 strain-time history for Gauge SG12-VB of Wall 1

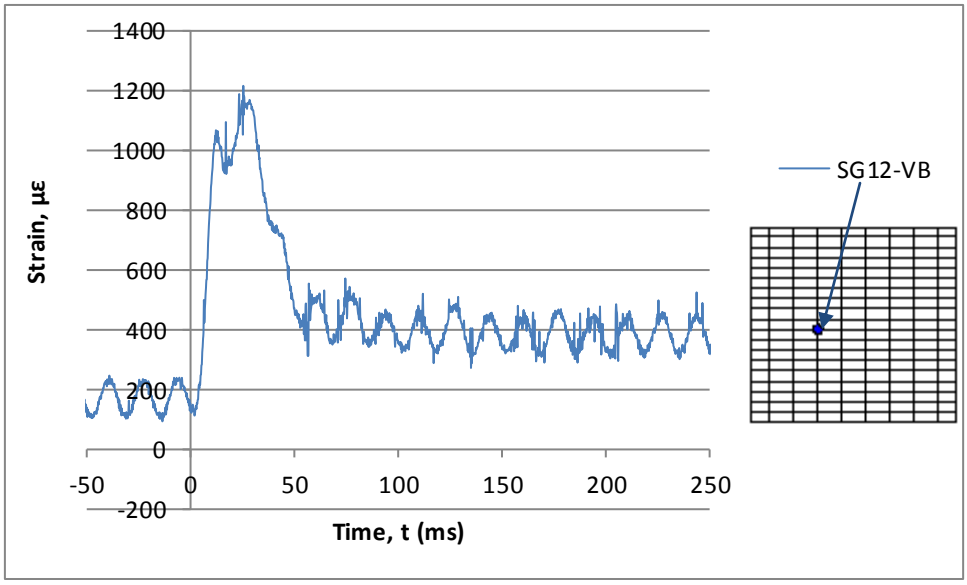


Figure B.36: Test 6 strain-time history for Gauge SG12-VB of Wall 1

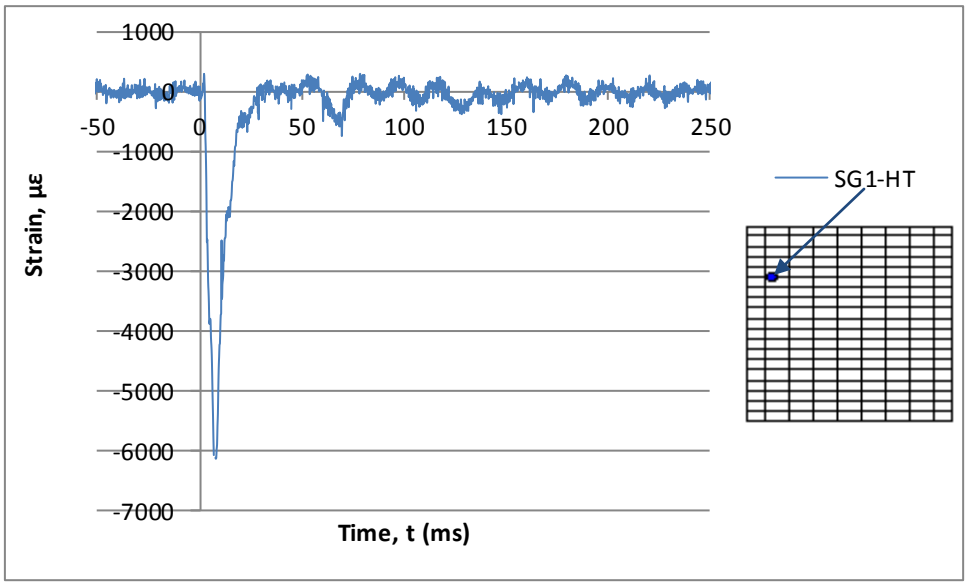


Figure B.37: Test 1 strain-time history for Gauge SG1-HT of Wall 2

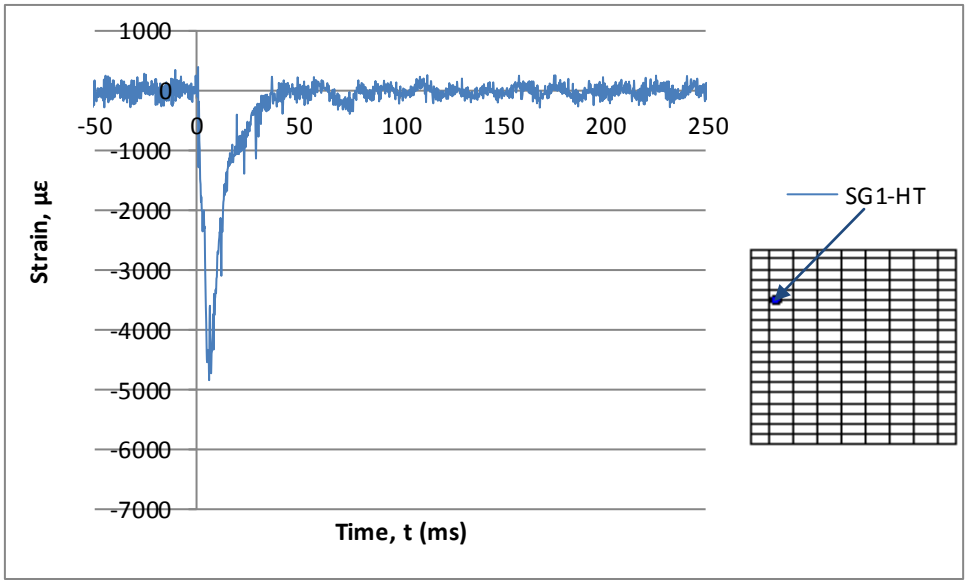


Figure B.38: Test 2 strain-time history for Gauge SG1-HT of Wall 2

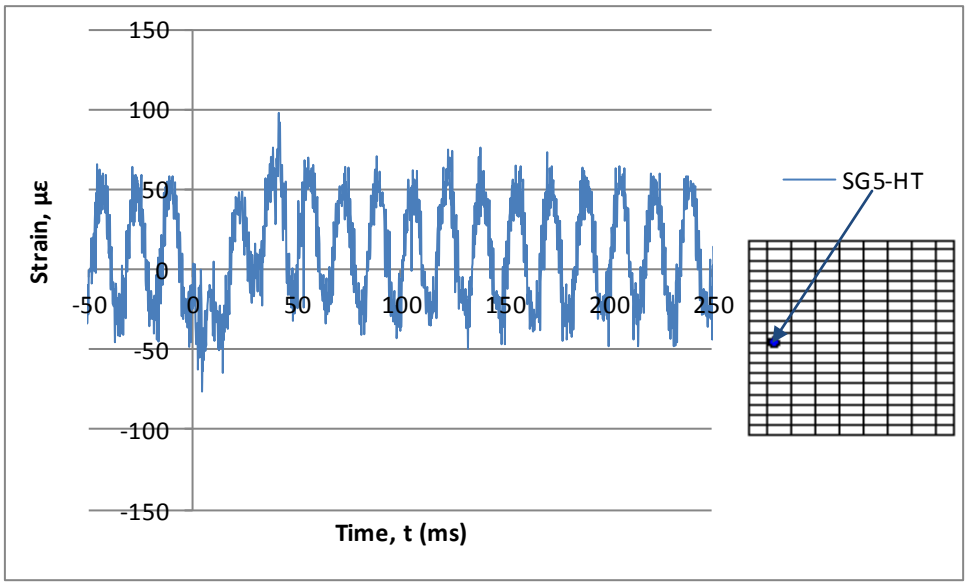


Figure B.39: Test 3 strain-time history for Gauge SG5-HT of Wall 2

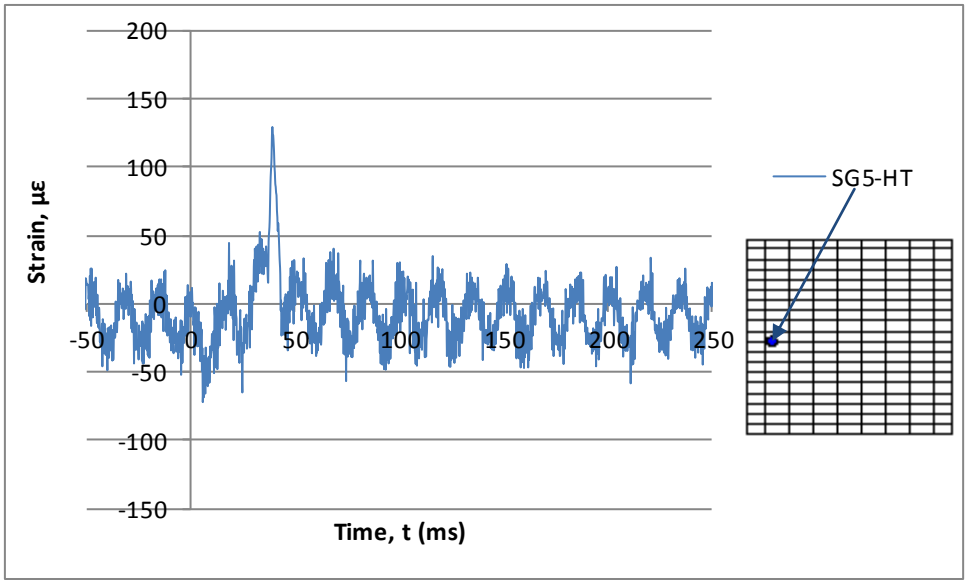


Figure B.40: Test 4 strain-time history for Gauge SG5-HT of Wall 2

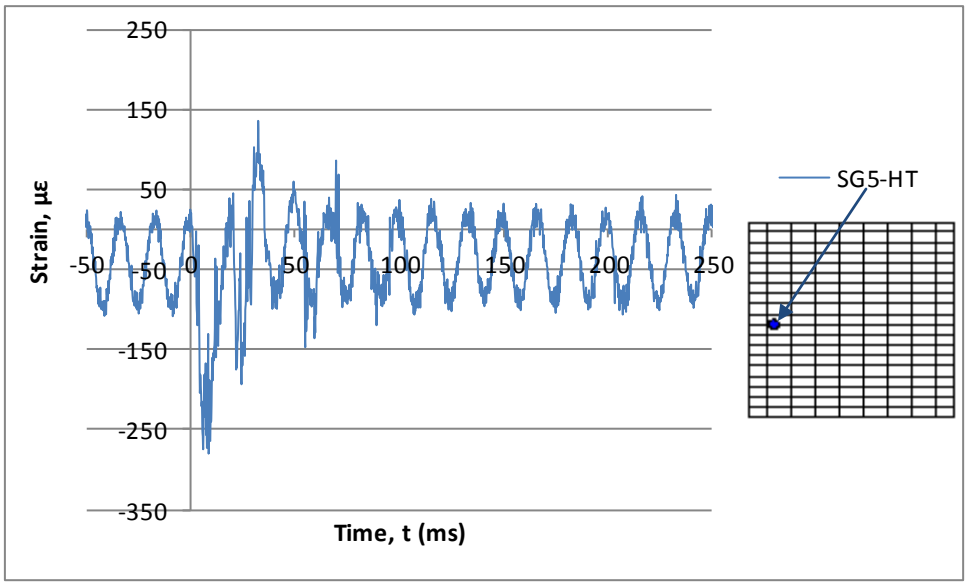


Figure B.41: Test 5 strain-time history for Gauge SG5-HT of Wall 2

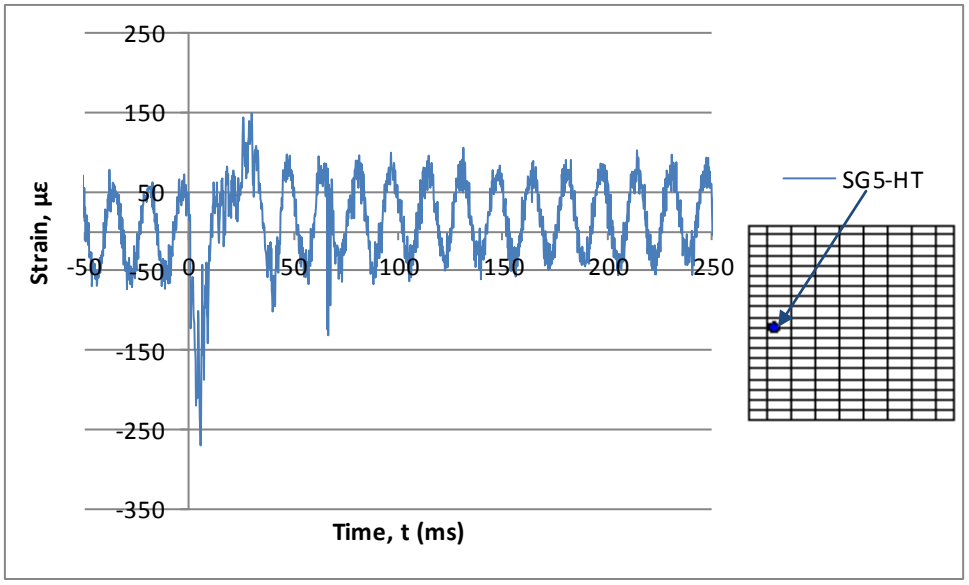


Figure B.42: Test 6 strain-time history for Gauge SG5-HT of Wall 2

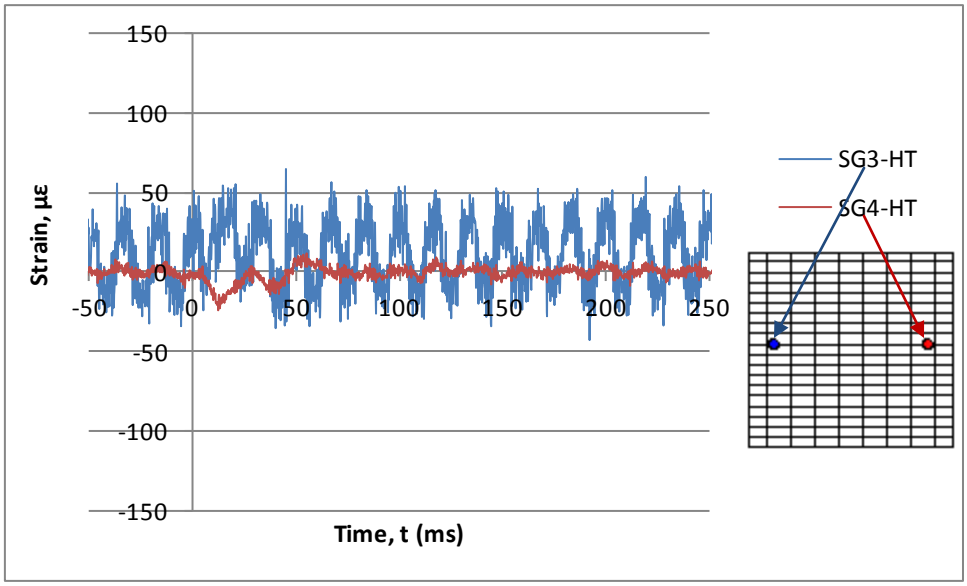


Figure B.43: Test 1 strain-time histories for Gauges SG3-HT and SG4-HT of Wall 2

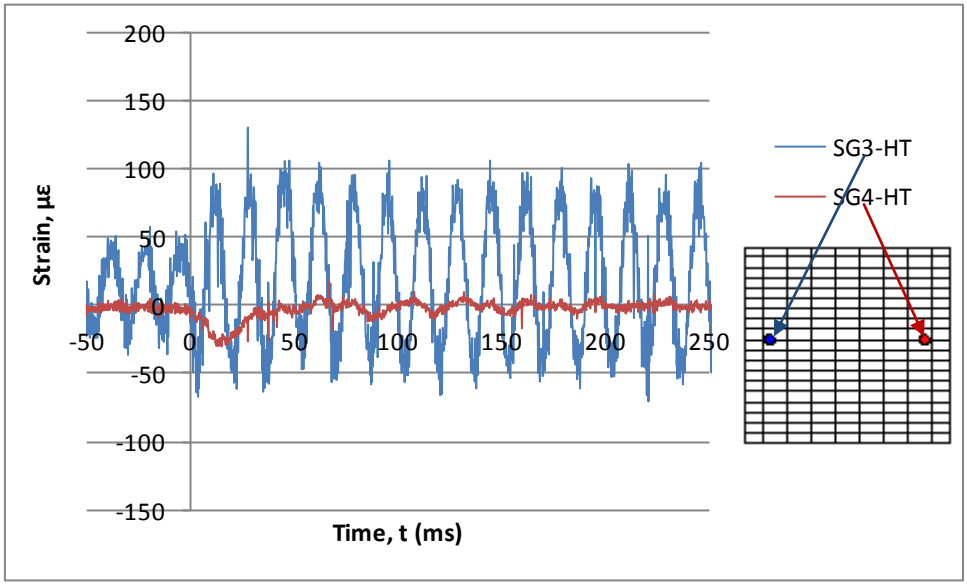


Figure B.44: Test 2 strain-time histories for Gauges SG3-HT and SG4-HT of Wall 2

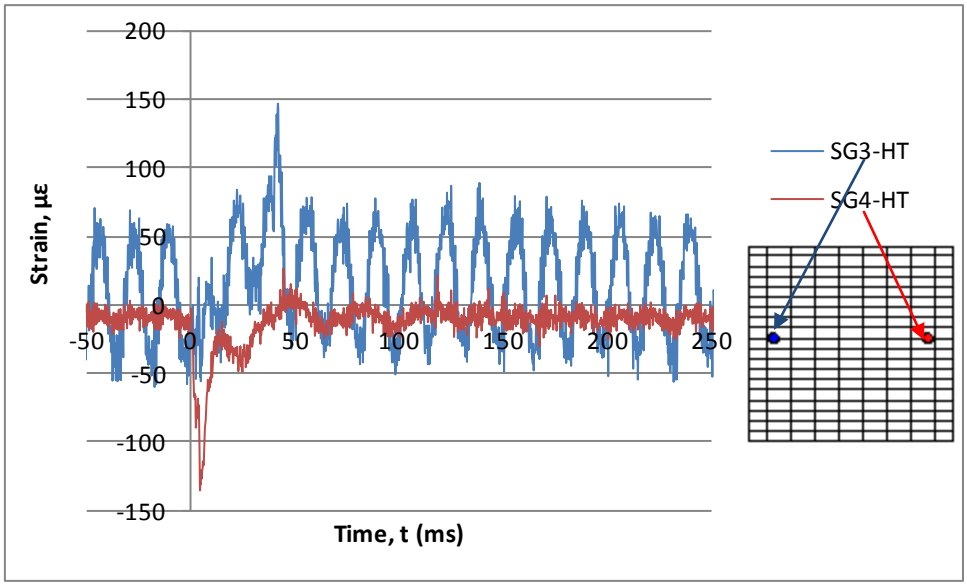


Figure B.45: Test 3 strain-time histories for Gauges SG3-HT and SG4-HT of Wall 2

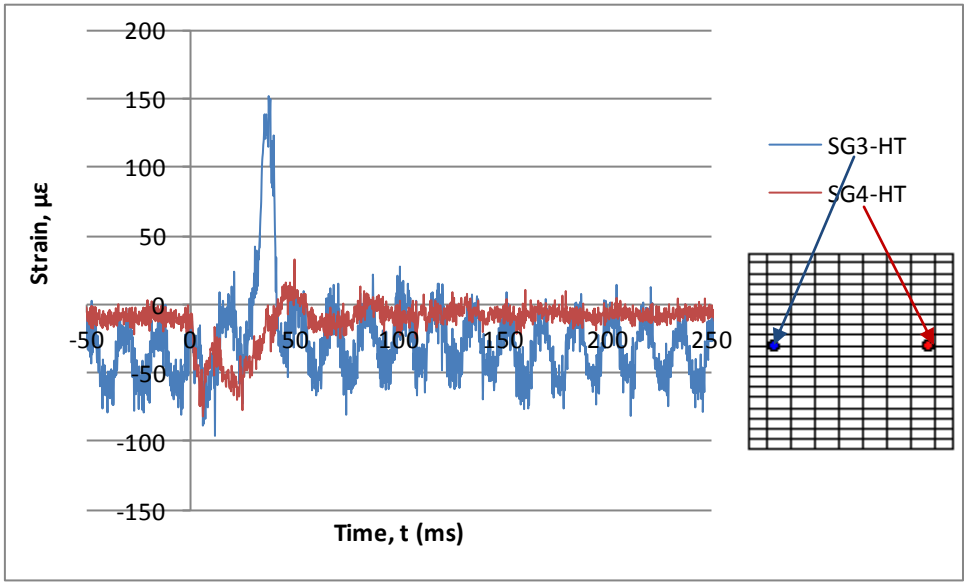


Figure B.46: Test 4 strain-time histories for Gauges SG3-HT and SG4-HT of Wall 2

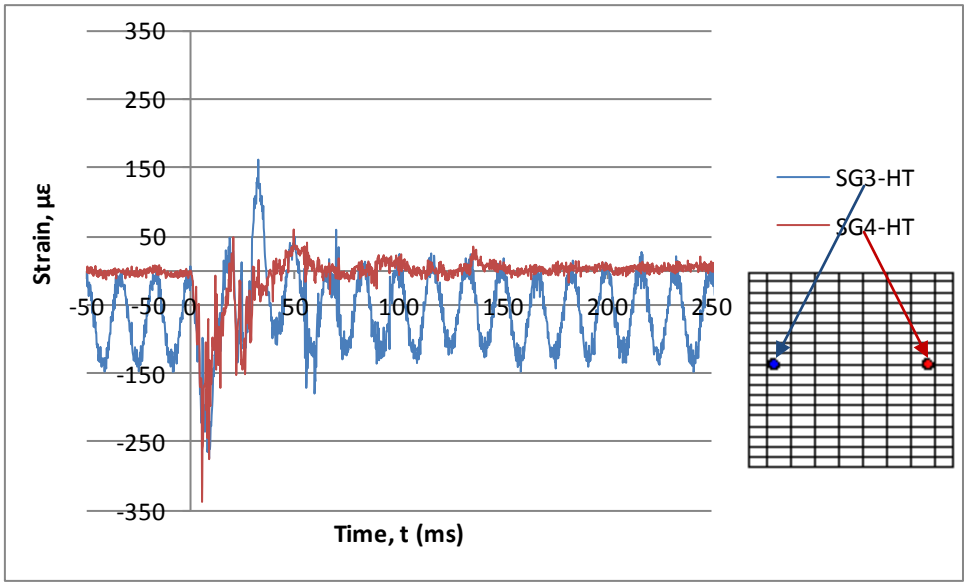


Figure B.47: Test 5 strain-time histories for Gauges SG3-HT and SG4-HT of wall 2

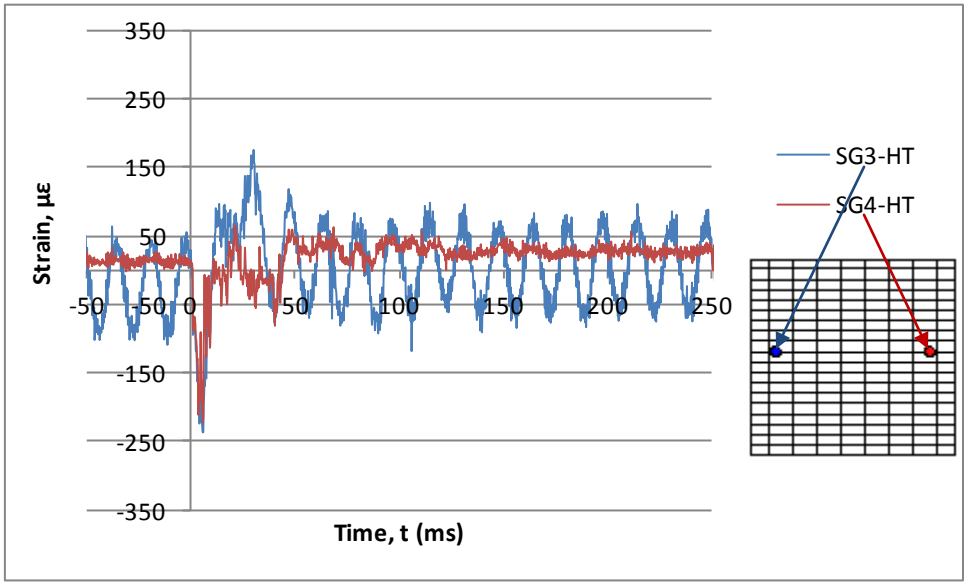


Figure B.48: Test 6 strain-time histories for Gauges SG3-HT and SG4-HT of Wall 2

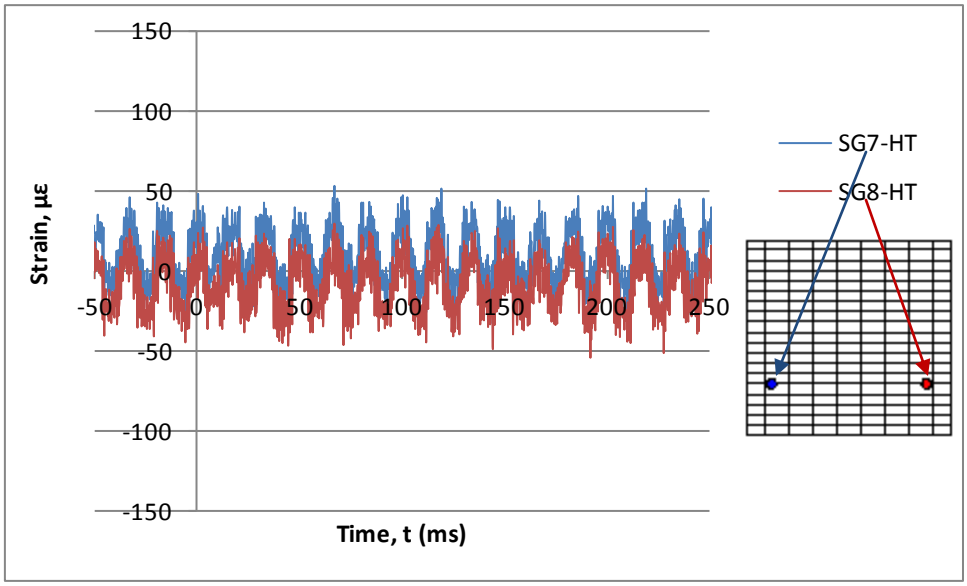


Figure B.49: Test 1 strain-time histories for Gauges SG7-HT and SG8-HT of Wall 2

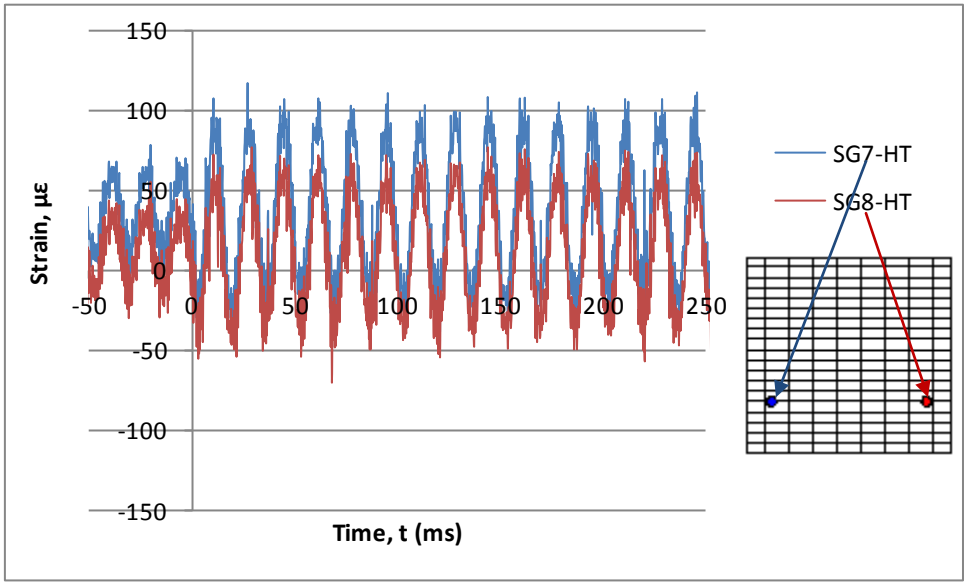


Figure B.50: Test 2 strain-time histories for Gauges SG7-HT and SG8-HT of Wall 2

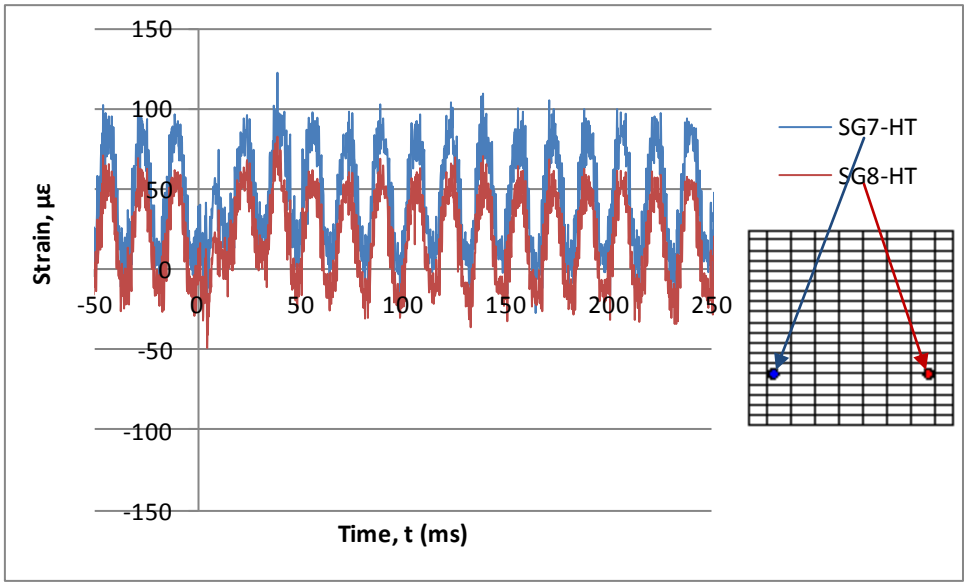


Figure B.51: Test 3 strain-time histories for Gauges SG7-HT and SG8-HT of Wall 2

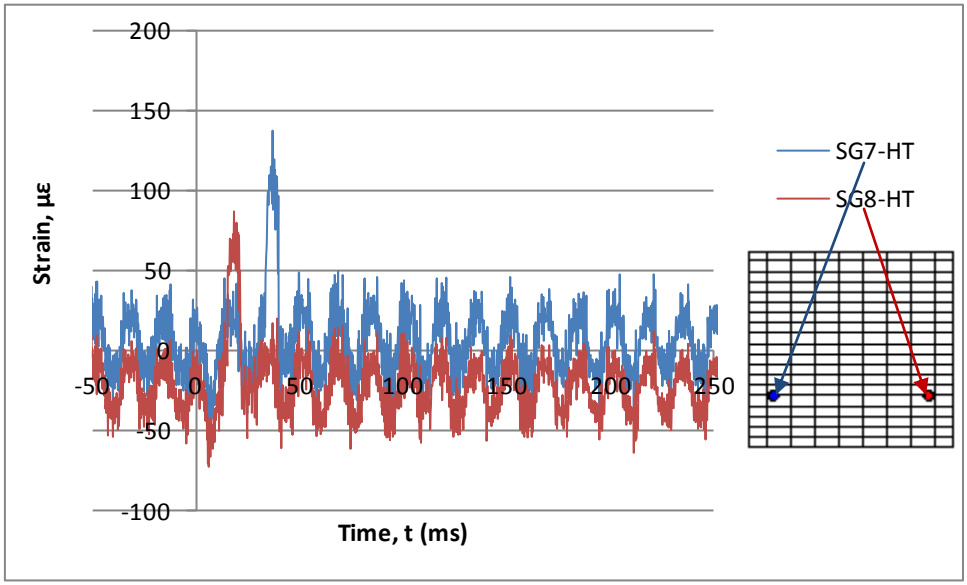


Figure B.52: Test 4 strain-time histories for Gauges SG7-HT and SG8-HT of Wall 2

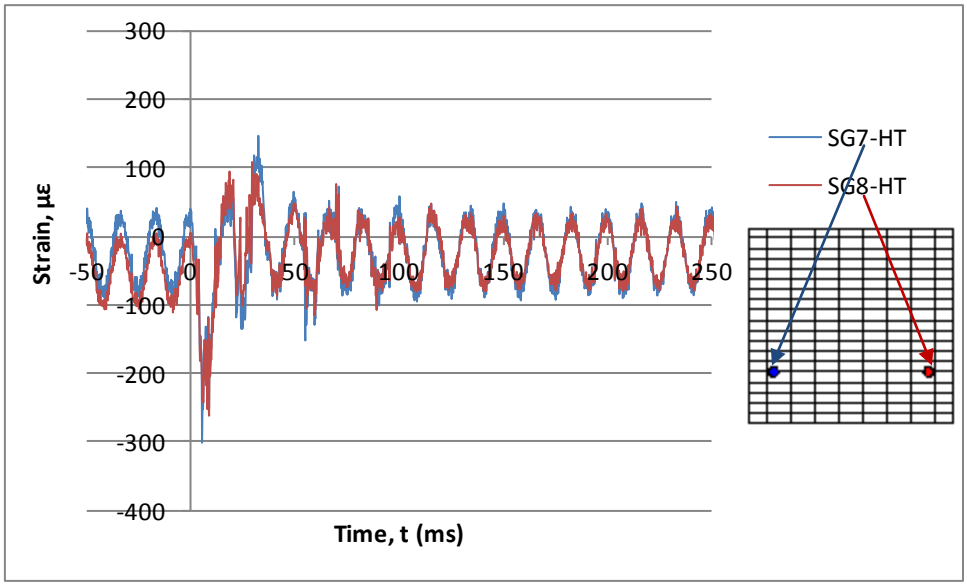


Figure B.53: Test 5 strain-time histories for Gauges SG7-HT and SG8-HT of Wall 2

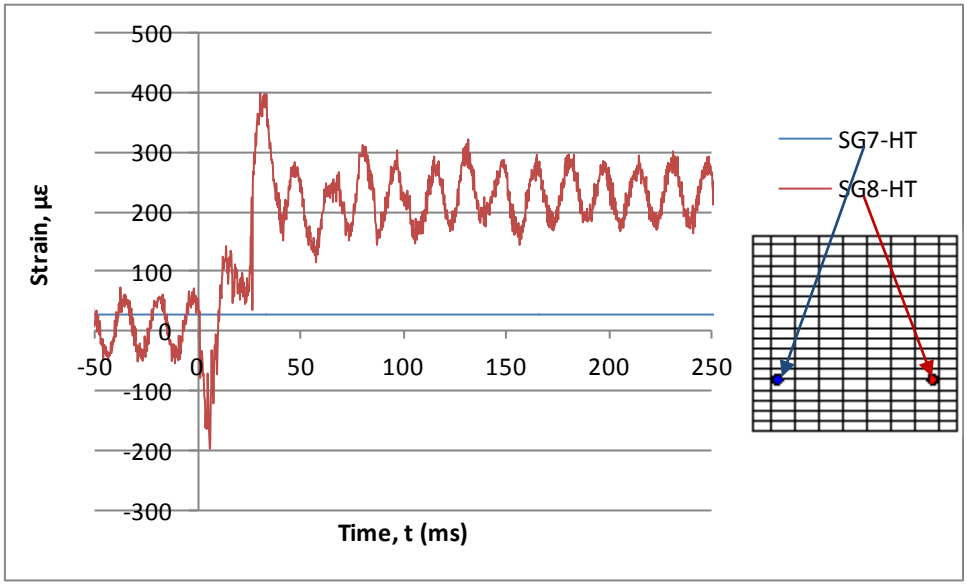


Figure B.54: Test 6 strain-time histories for Gauges SG7-HT and SG8-HT of Wall 2

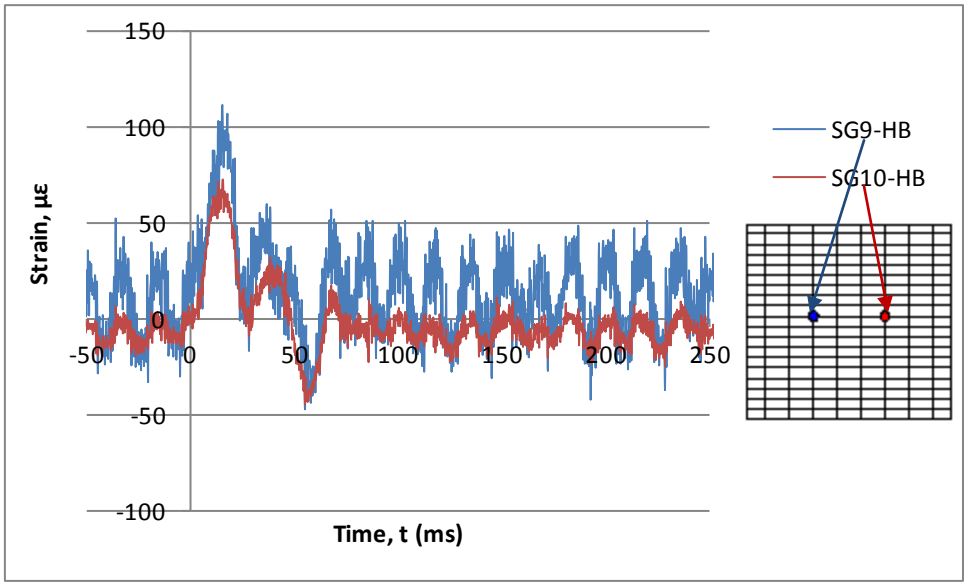


Figure B.55: Test 1 strain-time histories for Gauges SG9-HB and SG10-HB of Wall 2

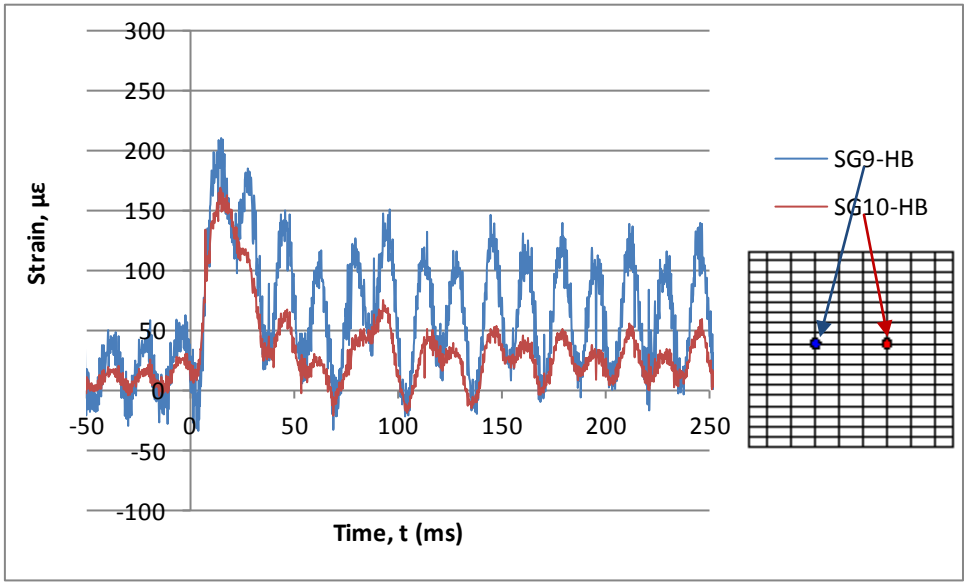


Figure B.56: Test 2 strain-time histories for Gauges SG9-HB and SG10-HB of Wall 2

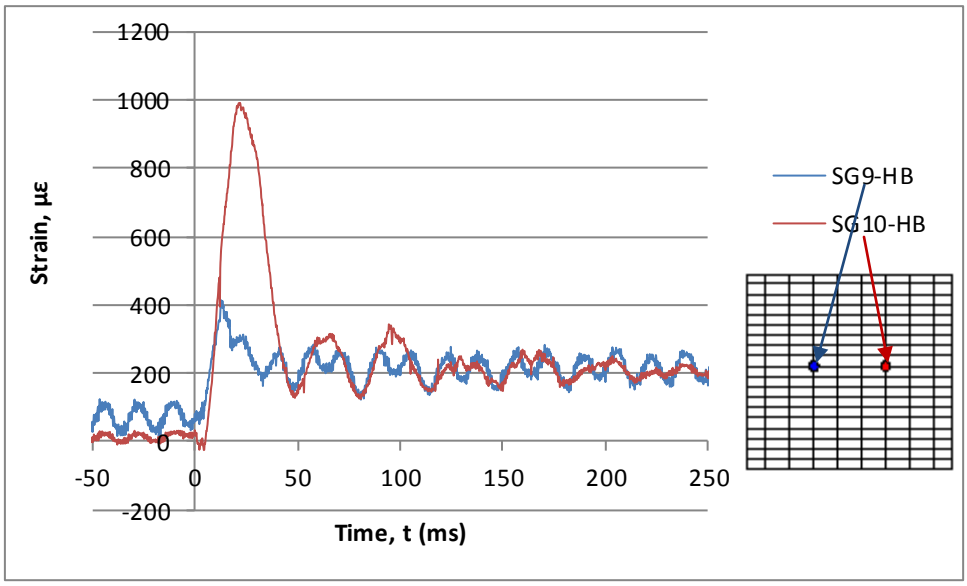


Figure B.57: Test 3 strain-time histories for Gauges SG9-HB and SG10-HB of Wall 2

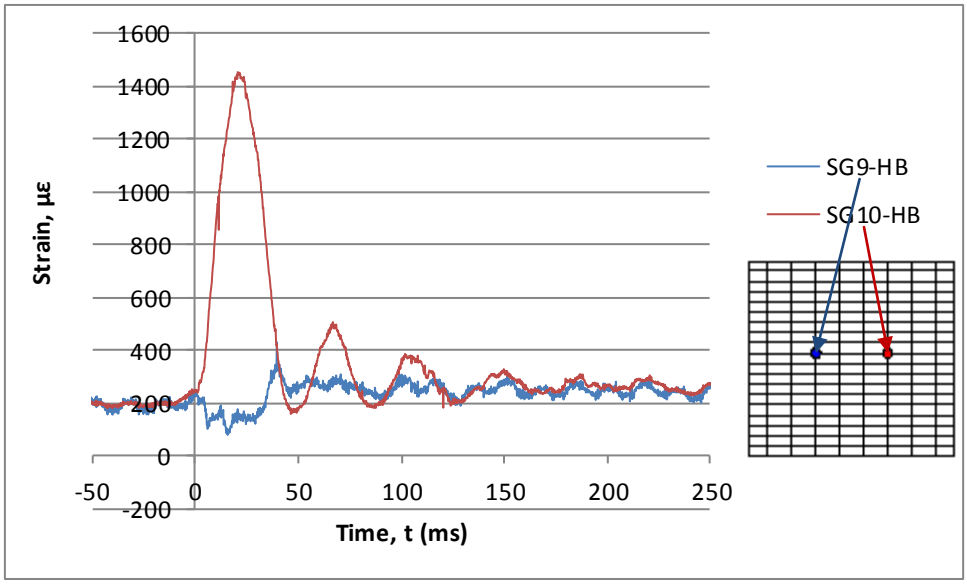


Figure B.58: Test 4 strain-time histories for Gauges SG9-HB and SG10-HB of Wall 2

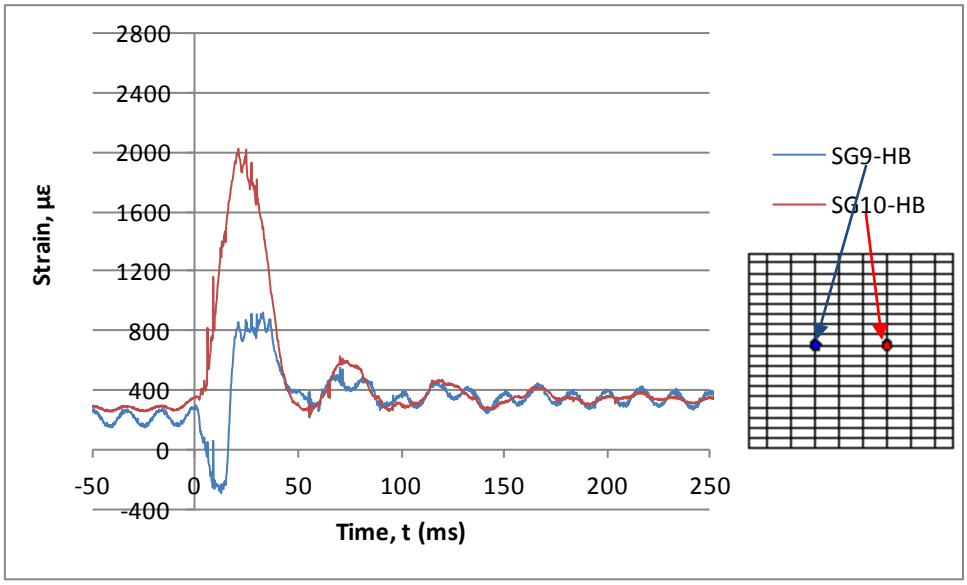


Figure B.59: Test 5 strain-time histories for Gauges SG9-HB and SG10-HB of Wall 2

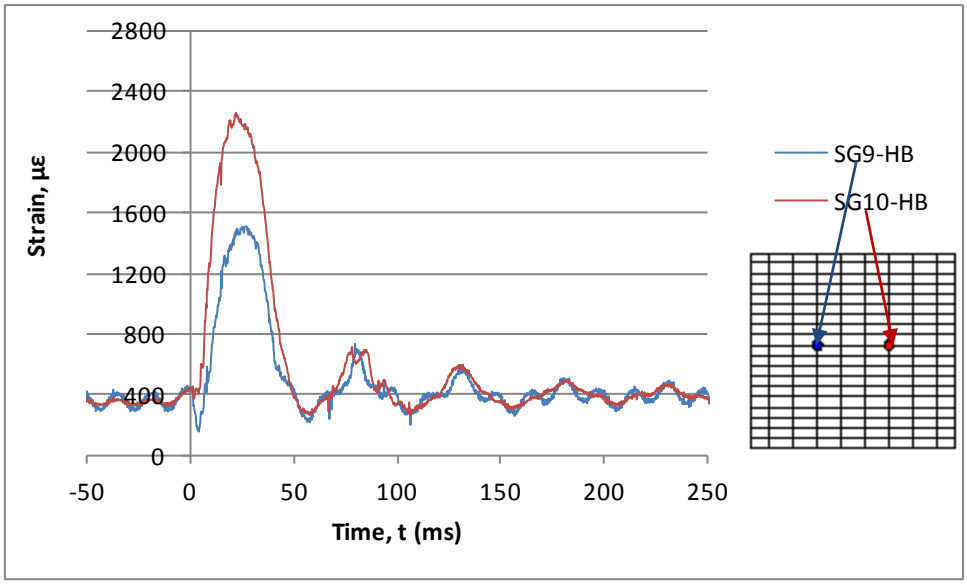


Figure B.60: Test 6 strain-time histories for Gauges SG9-HB and SG10-HB of Wall 2

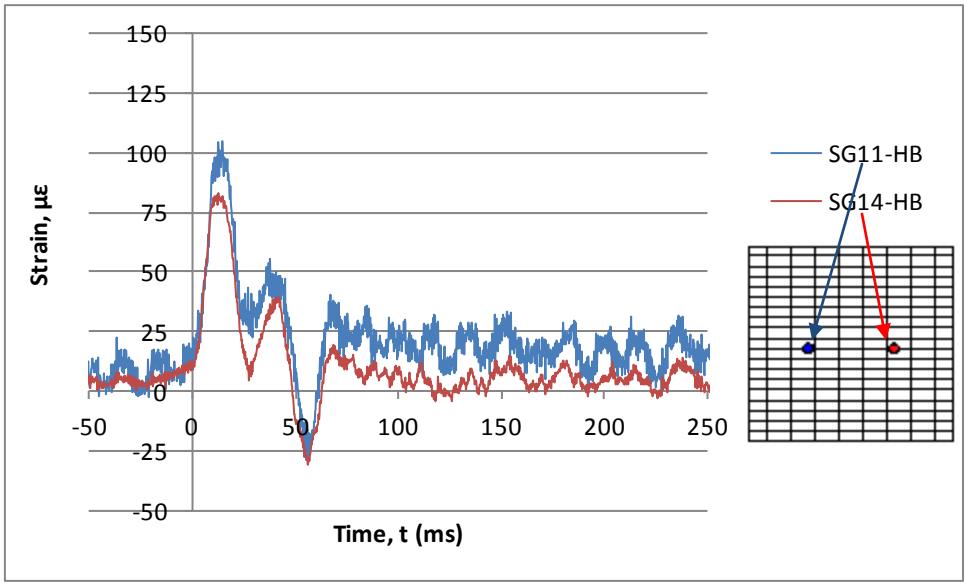


Figure B.61: Test 1 strain-time histories for Gauges SG11-HB and SG14-HB of Wall 2

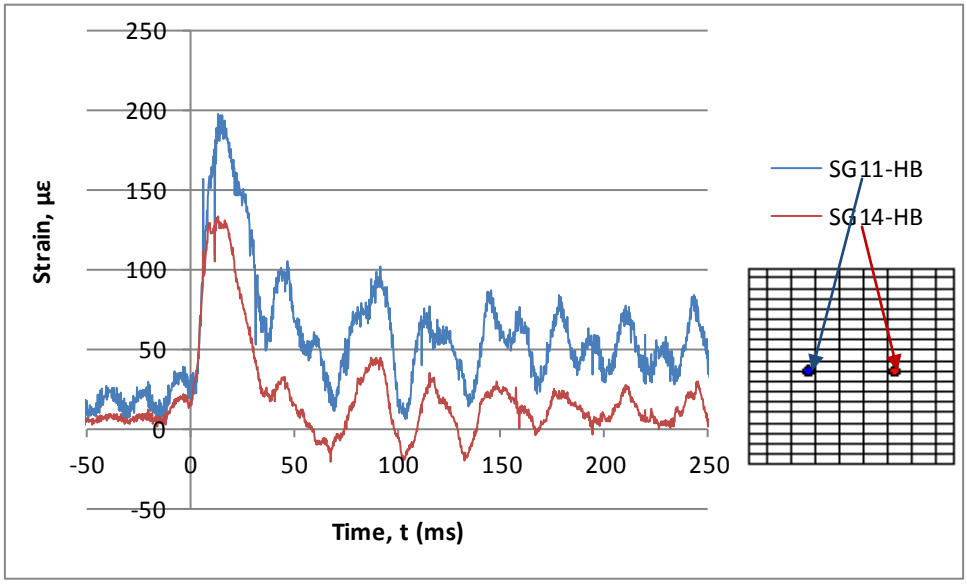


Figure B.62: Test 2 strain-time histories for Gauges SG11-HB and SG14-HB of Wall 2

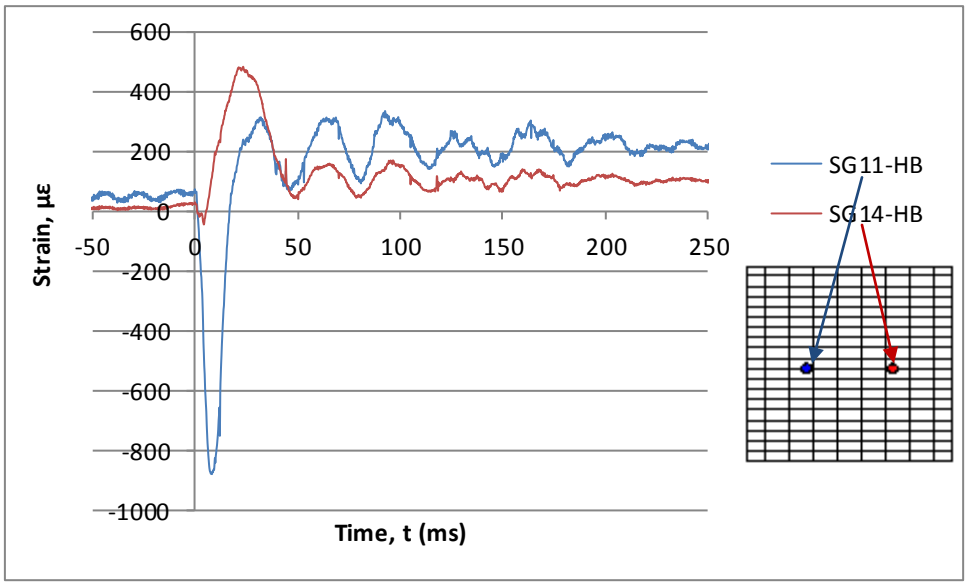


Figure B.63: Test 3 strain-time histories for Gauges SG11-HB and SG14-HB of Wall 2

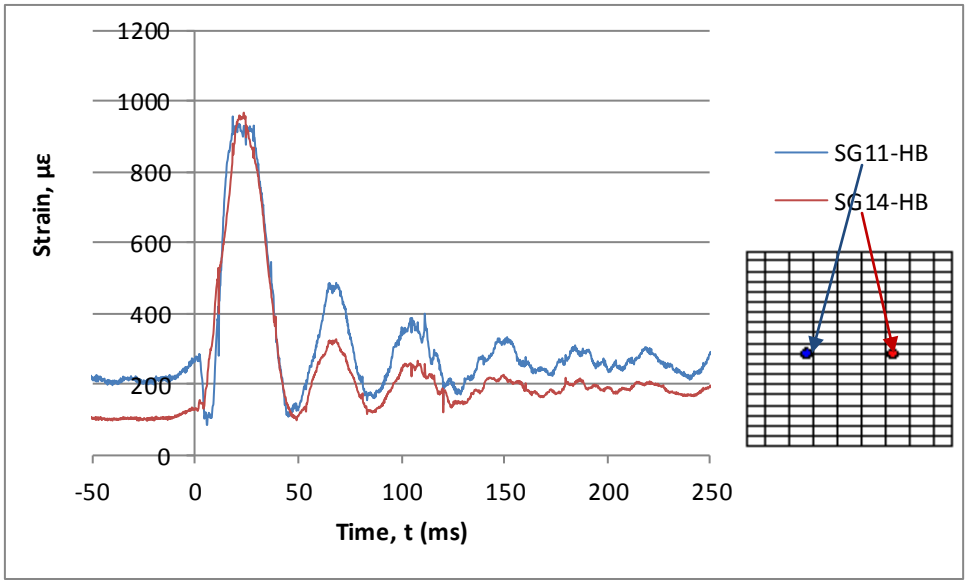


Figure B.64: Test 4 strain-time histories for Gauges SG11-HB and SG14-HB of Wall 2

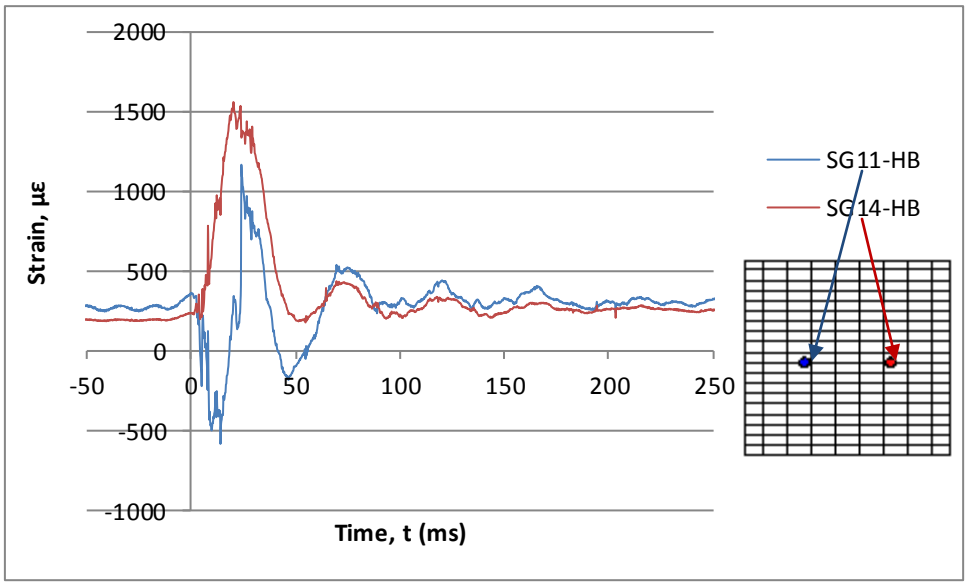


Figure B.65: Test 5 strain-time histories for Gauges SG11-HB and SG14-HB of Wall 2

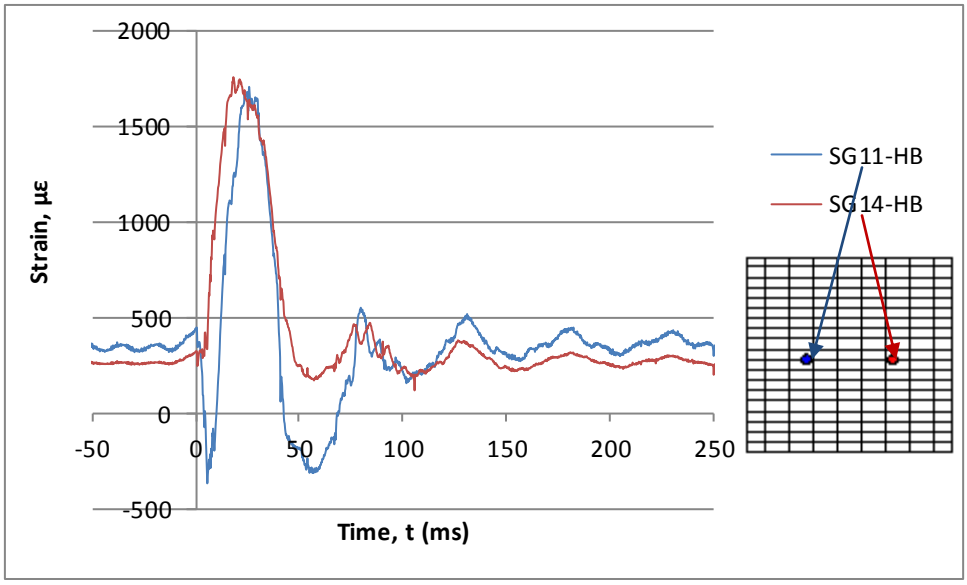


Figure B.66: Test 6 strain-time histories for Gauges SG11-HB and SG14-HB of Wall 2

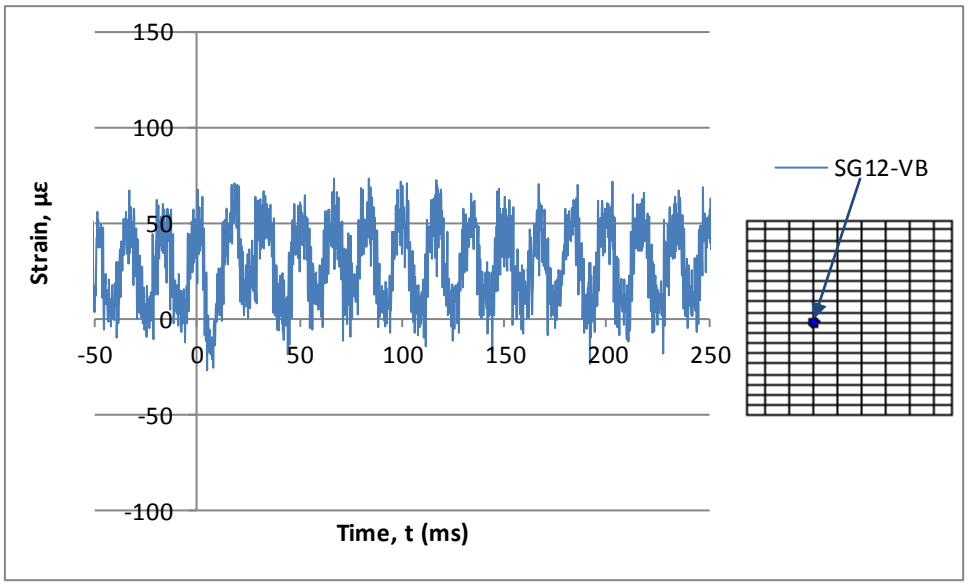


Figure B.67: Test 1 strain-time history for Gauge SG12-VB of Wall 2

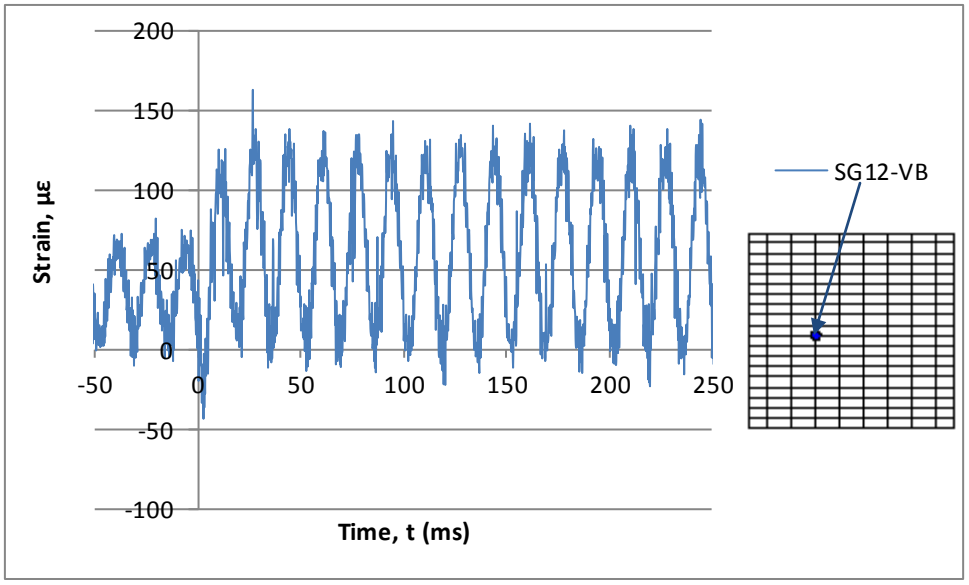


Figure B.68: Test 2 strain-time history for Gauge SG12-VB of Wall 2

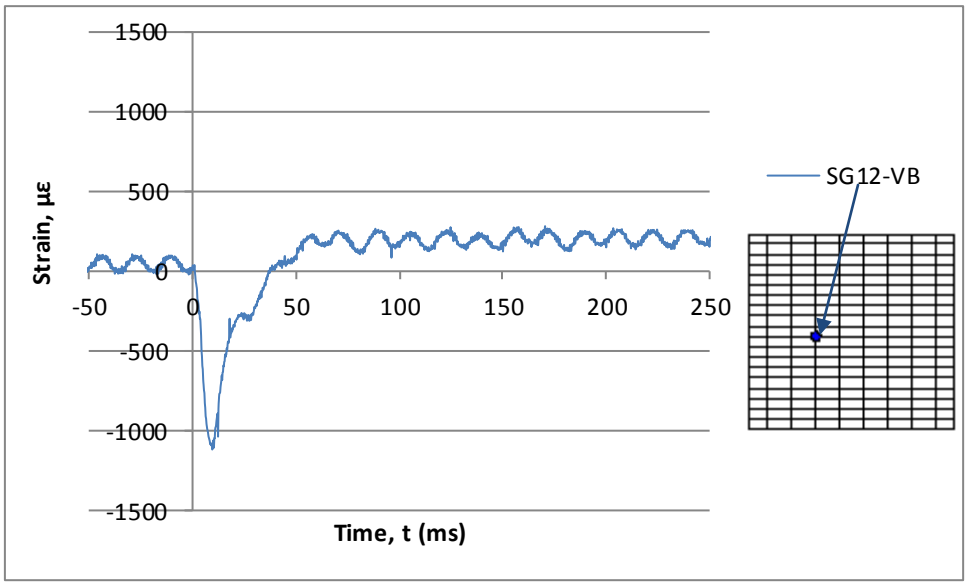


Figure B.69: Test 3 strain-time history for Gauge SG12-VB of Wall 2

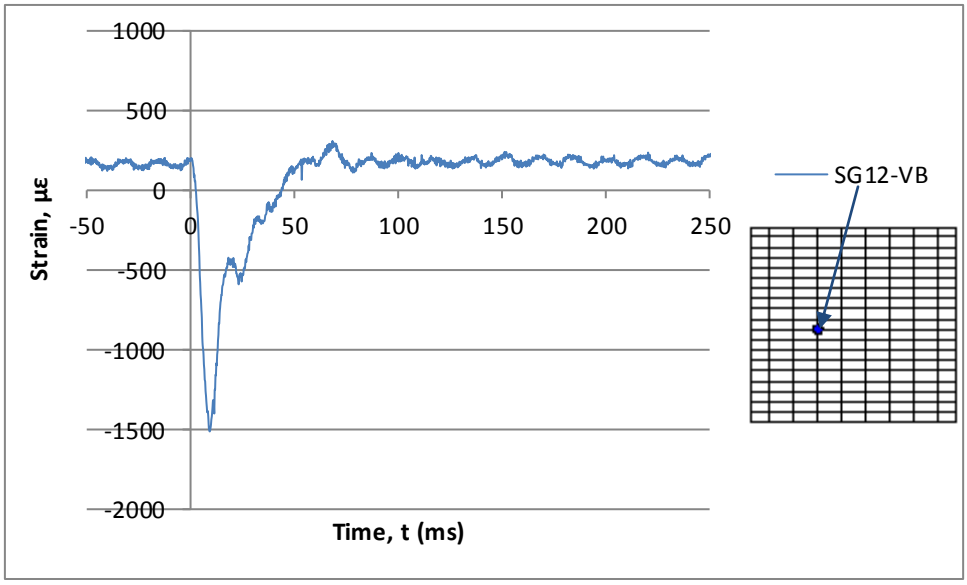


Figure B.70: Test 4 strain-time history for Gauge SG12-VB of Wall 2

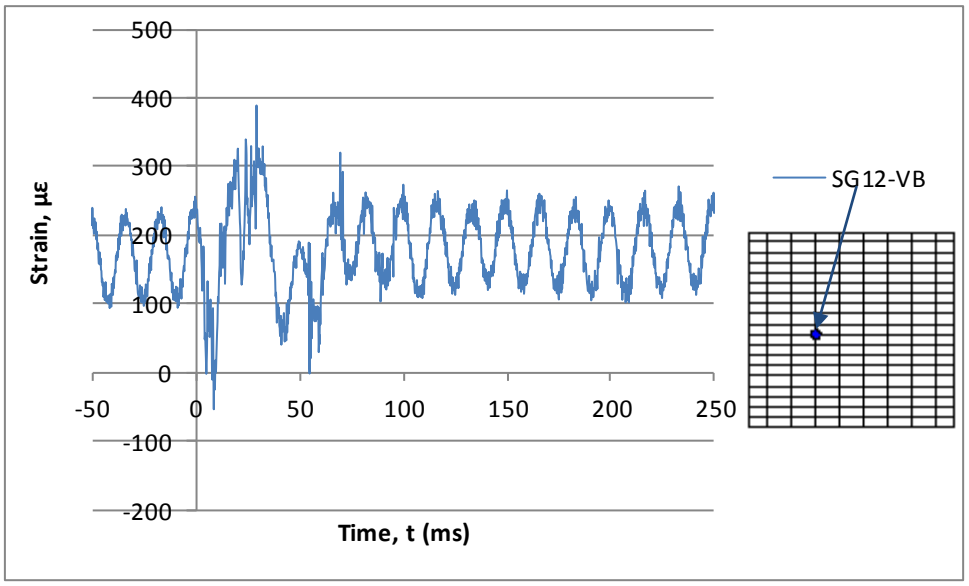


Figure B.71: Test 5 strain-time history for Gauge SG12-VB of Wall 2

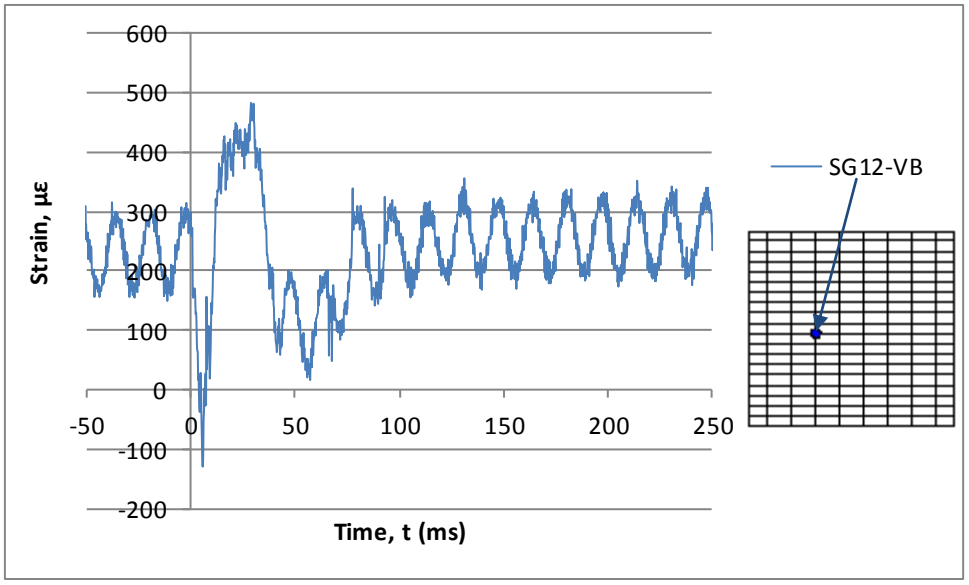


Figure B.72: Test 6 strain-time history for Gauge SG12-VB of Wall 2